Quantum-gas microscopy of strontium Bose- and Fermi-Hubbard systems

Sandra Buob

A thesis submitted in fulfilment of the requirements for the degree of Doctor of Philosophy in Photonics

Thesis supervisor: Prof. Dr. Leticia Tarruell

UNIVERSITAT POLITÈCNICA DE CATALUNYA
BARCELONATECH

ICFO - Insitut de Ciències Fotòniques
UPC - Universitat Politècnica de Catalunya

October, 2024

Thesis committee:

Prof. Dr. Tilman Esslinger	Institute for Quantum Electronics, ETH Zürich
Prof. Dr. Christian Groß	Institute of Physics, Eberhard Karls Universität Tübingen
Dr. Pablo Loza-Alvarez	ICFO - The Institute of Photonic Sciences

Substitute examiners:

Dr. Maria Moreno-Cardoner	Department of Physics, Universitat de Barcelona
Prof. Dr. Morgan W. Mitchell	ICFO - The Institute of Photonic Sciences

Abstract

Ultracold atoms have proven to be a valuable asset to study and understand complex quantum many-body systems in a well-controlled setting. In particular, quantum-gas microscopes provide unprecedented access to local observables and allow one to investigate those systems at the level of each individual particle, giving new insights on their behaviour. While so far most of these microscopes used alkali atoms, the distinct properties of alkaline-earth atoms, in particular strontium, combined with quantum-gas microscopy are expected to shed new light on a broad variety of many-body problems. This thesis describes the realization of single-site-resolved imaging for both bosonic and fermionic strontium atoms in a Hubbard-regime optical lattice, which unlocks the possibility to study novel types of Bose- and SU(N) Fermi-Hubbard systems.

An essential step in ultracold-atom experiments is the preparation of a quantum degenerate cloud. In the first part of this thesis, we discuss the methods we have implemented in our apparatus to achieve this goal. We developed a new resonant-shielding method to double the atom number during the first cooling stage in a broad-linewidth blue magneto-optical trap. During the second cooling stage in a narrow-linewidth red magneto-optical trap, the hyperfine structure of the fermionic atoms adds additional challenges, which are addressed by mixing the hyperfine states with an additional laser for efficient trapping and cooling. After the laser-cooling stages, we perform evaporative cooling in a far red-detuned optical potential before loading the atoms into a two-dimensional optical lattice. The lattice laser operates at the clock-magic wavelength of strontium (813.4 nm) which will enable high-precision measurements in future experiments.

To image the individual atoms in the optical lattice, we place a high-NA objective in close vicinity to the atoms. We demonstrate single-atom resolution for bosonic and fermionic strontium and successfully reconstruct the lattice occupation for both of them, reaching fidelities as high as 96 %. For the bosonic ^{84}Sr atoms, we induce fluorescence on the blue broad-linewidth transition and simultaneously perform attractive Sisyphus cooling on the red narrow-linewidth transition. Moreover, combining this imaging method with momentum-space detection, we observe the matter-wave interference arising from the phase coherence of the Bose-Hubbard superfluid. For the fermionic ^{87}Sr atoms, we image with the red transition only, which allows us to obtain for the first time for a fermionic alkaline-earth atom both single-atom resolution and spin-resolved detection.

This thesis has combined, for the first time, quantum-gas microscopy with ultra-

cold strontium and its distinct spectral properties. This platform should enable a broad range of future studies. For the bosons, it unlocks investigation of the single-atom-resolved dissipative Bose-Hubbard systems and the exploration of collective atom-photon scattering in ordered atomic arrays. For the fermions, the spin-dependent single-atom detection provides the ideal setting for investigations of antiferromagnetic correlations in SU($N \leq 10$) Fermi-Hubbard systems and the realization of exotic magnetic phases.

Resumen

Los átomos ultrafríos han demostrado ser un recurso valioso para el estudio y la comprensión de sistemas cuánticos de muchos cuerpos en un entorno controlado. En particular, los microscopios de gases cuánticos proporcionan un acceso sin precedentes a observables locales y permiten investigar esos sistemas a nivel de cada partícula individual, ofreciendo nuevas perspectivas sobre su comportamiento. Aunque hasta ahora la mayoría de estos microscopios han utilizado átomos alcalinos, se espera que las propiedades distintivas de los átomos alcalinotérreos, en particular el estroncio, combinadas con la microscopía de gases cuánticos, arrojen nueva luz sobre una amplia variedad de problemas de muchos cuerpos. Esta tesis describe la realización de imágenes con resolución de átomo único de la red para estroncio bosónico y fermiónico en una red óptica en régimen de Hubbard. Este resultado abre la posibilidad de estudiar nuevos tipos de sistemas de Bose-Hubbard y Fermi-Hubbard SU(N).

Un paso esencial en los experimentos de átomos ultrafríos es el de preparar una nube cuántica degenerada. En la primera parte de esta tesis, discutimos los métodos implementados en nuestro aparato para lograr este objetivo. Hemos desarrollado un nuevo método de protección sobre una transición en que duplica el número de átomos en la primera etapa de enfriamiento, la trampa magneto-óptica azul sobre la transición ancha. Durante la segunda etapa de enfriamiento en una trampa magneto-óptica roja sobre la línea estrecha, la estructura hiperfina de los átomos fermiónicos presenta nuevos desafíos, que abordamos mezclando los estados hiperfinos con un láser adicional para lograr un atrapamiento y enfriamiento eficiente. Después de las etapas de enfriamiento láser, realizamos enfriamiento por evaporación en una trampa dipolar antes de cargar los átomos en una red óptica bidimensional. El láser de la red opera a la longitud de onda mágica para la transición reloj del estroncio (813.4 nm), lo que permitirá mediciones de alta precisión en futures experimentos.

Para tomar imágenes de los átomos individuales en la red óptica, colocamos un objetivo de microscopio de alta apertura numérica a poca distancia de los átomos. Demostramos la detección de átomos individuales para estroncio bosónico y fermiónico, y reconstruimos la ocupación en la red para ambos, alcanzando fidelidades de hasta un 96 %. Para el isótopo bosónico de ^{84}Sr, inducimos fluorescencia en la transición ancha azul y simultáneamente realizamos enfriamiento atractivo de Sísifo en la transición estrecha roja. Además, mediante la combinación este método y la detección en el espacio de momentos, conseguimos observar la interferencia de la onda de materia que surge de la coherencia de fase del superfluido de Bose-Hubbard. Para los átomos

fermiónicos de ^{87}Sr, utilizamos solo la transición roja para la fluorescencia, lo que nos permite obtener por primera vez tanto resolución de átomos individuales como detección del estado de espín en átomos alcalinotérreos.

Esta tesis ha combinado, por primera vez, la microscopía de gases cuánticos con el estroncio ultrafrío y sus propiedades espectrales distintivas. Esta plataforma habilita una amplia variedad de futuros estudios. Para los bosones, permite la investigación de sistemas Bose-Hubbard disipativos con detección de átomos individuales así como la exploración de la interacción colectiva de átomos y fotones en matrices ordenadas de átomos. Para los fermiones, la detección individual de átomos y su estado de espín proporciona el entorno ideal para investigar las correlaciones antiferromagnéticas en sistemas SU($N \leq 10$) de Fermi-Hubbard y la realización de fases magnéticas exóticas.

Resum

Els àtoms ultrafreds han demostrat ser un recurs valuós per l'estudi i la comprensió de sistemes quàntics de molts cossos en un entorn controlat. En particular, els microscopis de gasos quàntics proporcionen un accés sense precedents a observables locals i permeten investigar aquests sistemes a nivell de cada partícula individual, oferint noves perspectives sobre el seu comportament. Malgrat que fins ara la majoria d'aquests microscopis han utilitzat àtoms alcalins, s'espera que les propietats distintives dels àtoms alcalinoterris, en particular l'estronci, combinades amb la microscòpia de gasos quàntics, aportin nova llum a una àmplia varietat de problemes de molts cossos. Aquesta tesi descriu la realització d'imatges amb resolució d'un sol punt de xarxa per a àtoms d'estronci bosònics i fermiònics en una xarxa òptica al règim de Hubbard. Aquest resultat desbloqueja la possibilitat d'estudiar nous tipus de sistemes de Bose-Hubbard i Fermi-Hubbard SU(N).

Un pas essencial en els experiments d'àtoms ultrafreds és la preparació d'un núvol quàntic degenerat. A la primera part d'aquesta tesi, discutim els mètodes implementats al nostre aparell per aconseguir aquest objectiu. Hem desenvolupat un nou mètode de protecció en ressonància que duplica el nombre d'àtoms a la primera etapa de refredament, la trampa magneto-òptica blava de transició ampla. Durant la segona etapa de refredament en una trampa magneto-òptica vermella de línia estreta, l'estructura hiperfina dels àtoms fermiònics presenta nous reptes, que abordem barrejant els estats hiperfins amb un làser addicional per atrapar i refredar els àtoms eficientment. Després de les etapes de refredament làser, realitzem refredament per evaporació en una trampa dipolar abans de carregar els àtoms en una xarxa òptica bidimensional. El làser de la xarxa opera a la longitud d'ona màgica per a la transició rellotge de l'estronci (813.4 nm), que permetrà mesures d'alta precisió en experiments futurs.

Per prendre imatges dels àtoms individuals a la xarxa òptica, col·loquem un objectiu de microscopi d'alta obertura numèrica a poca distància dels àtoms. Hem demostrat la detecció d'àtoms individuals per a estronci bosònic i fermiònic, i hem reconstruït l'ocupació a la xarxa per a ambdós, assolint fidelitats de fins a un 96 %. Per a l'isòtop bosònic de ^{84}Sr, hem induït fluorescència en la transició ampla blava i simultàniament hem realitzat refredament atractiu de Sísif en la transició estreta vermella. A més, mitjançant la combinació d'aquest mètode i la detecció en l'espai de moments, hem aconseguit observar la interferència de l'ona de matèria que sorgeix de la coherència de fase del superfluid Bose-Hubbard. Per als àtoms fermiònics de ^{87}Sr,

només hem utilitzat la transició vermella per a la fluorescència, cosa que ens permet obtenir per primera vegada tant la resolució d'àtoms individuals com la detecció de l'estat d'espín en àtoms alcalinoterris.

Aquesta tesi ha combinat, per primera vegada, la microscòpia de gasos quàntics amb l'estronci ultrafred i les seves propietats espectrals distintives. Aquesta plataforma habilita una àmplia varietat d'estudis en el futur. Per als bosons, desbloqueja la investigació de sistemes Bose-Hubbard dissipatius amb detecció d'àtoms individuals, així com l'exploració de la interacció col·lectiva d'àtoms i fotons en matrius ordenades d'àtoms. Per als fermions, la detecció individual d'àtoms i el seu estat d'espín proporciona l'entorn ideal per investigar les correlacions antiferromagnètiques en sistemes SU($N \leq 10$) de Fermi-Hubbard i la realització de fases magnètiques exòtiques.

List of Publications

The work in this thesis has led to the following publications:

- Jonatan Höschele, Sandra Buob, Antonio Rubio-Abadal, Vasiliy Makhalov, and Leticia Tarruell. *Atom-Number Enhancement by Shielding Atoms From Losses in Strontium Magneto-Optical Traps.* Phys. Rev. Appl. **19**, 064011 (2023).
- Sandra Buob, Jonatan Höschele, Vasiliy Makhalov, Antonio Rubio-Abadal, and Leticia Tarruell. *A Strontium Quantum-Gas Microscope.* PRX Quantum **5**, 020316 (2024).

ORCID ID: 0000-0003-4067-7502

Contents

Chapter 1

Introduction

Quantum many-body systems of interacting particles exhibit rich phase diagrams and numerous interesting physical properties. Besides the fundamental interest in those complex systems, understanding the emergence of collective phenomena in quantum many-body systems can be essential for real-life applications. An evident example is high-T_c superconductivity. It was discovered by J. G. Bednorz and K. A. Müller in 1986 [1] and awarded the Nobel prize one year later. Despite the effort put into understanding and describing it [2, 3, 4], there are still many open questions surrounding the phenomena. In addition, the ceramics exhibiting high-T_c superconductivity are brittle and have to be cooled well below room temperatures, to around 100 K [5]. That makes it challenging to form wires or coils, somehow limiting the real-life application of such materials. Understanding the process leading to high-T_c superconductivity may provide insight in those problems and an approach to solutions.

Besides superconductivity, there is a plethora of interesting phases emerging in condensed matter physics. Many of those can be traced back to the complex quantum many-body nature of the electrons populating a crystal structure. As P. W. Anderson describes it in his article *"More Is Different"*: *The ability to reduce everything to simple fundamental laws does not imply the ability to start from those laws and reconstruct the universe* [6]. In order to comprehend the mechanisms underlying those phases and phase transitions arising in condensed matter, it is invaluable to consider models that are reduced to the essential processes causing them. For example band theories, such as the tight-binding model, describe individual electrons moving in the crystal structure of the solid. Although, they disregard interactions, they succeed in the description of simple metallic and insulating phases, but schematically fail in other cases. For instance, the tight-binding model predicts Mott insulating materials to be conductors. This is because their insulating nature arises as a result of the interaction between the electrons. While a metallic phase arises in the regime where it is energetically favorable for the electrons to delocalize over the full crystal and thus tunnel between sites, in the Mott insulating phase the interaction between the electrons dominates and makes it energetically favorable for the electrons to stay as far from each other as possible, only occupying their respective ionic core.

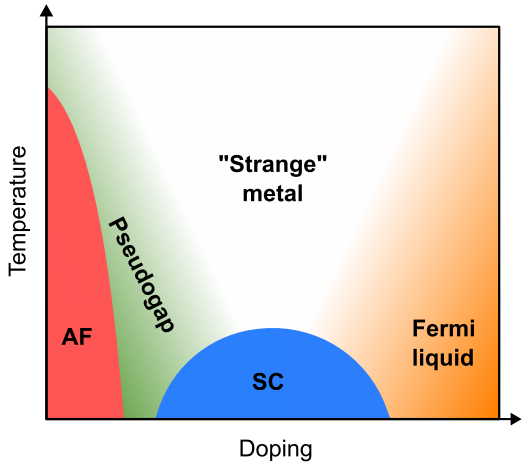

Figure 1.1: Conjectured phase diagram of the two-dimensional Fermi-Hubbard model. The half-filled system at small temperatures is in an antiferromagnetic (AF) phase. Upon increasing the doping various other phases are expected to emerge. Of particular interest is the high-T_c superconducting (SC) dome in the center of the phase diagram present also in cuprates [13]. The phase diagram is adapted from [18].

The transition of a system from a metal to a Mott insulator is captured by the Hubbard model [7, 8, 9, 10]. It is one of the most popular models of solid state physics [11] and is a key motivation for this thesis. It describes the motion and dynamics of strongly correlated quantum particles in a discrete periodic potential, such as the collective behavior of electrons in a perfect crystal. Beyond its most basic version, it can easily be modified to account for even more complex phenomena than the aforementioned Mott insulator [12]. For example, adding long-range interactions to the model resembles the Coulomb interactions of electrons, or introducing density-dependent tunneling can lead to the emergence of charge-density waves. Furthermore, it is hypothesised that in two spatial dimensions the model might hold the key to understand high-T_c superconductivity [13]. As displayed in the conjectured phase diagram of the Hubbard model in Fig. 1.1, high-T_c superconductivity arises at low temperature upon doping a system in the antiferromagnetic regime. This brings us to another area of great interest and captured by the Hubbard model: quantum magnetism. It arises from exchange interactions which couple the electrons through their spins and in the strong coupling limit, it can be described by the celebrated Heisenberg model [14, 15]. In the presence of geometrical frustration, such as in triangular or kagome lattice geometries, it is expected to lead to even more interesting phases such as spin liquids [16, 17].

Analytic solutions of the Hubbard Hamiltonian exist only for few specific scenarios, for example in the one-dimensional case [19]. Even though numerically there are many powerful methods to tackle the problem, such as quantum Monte-Carlo [20], dynamic mean-field theory [21] or exact diagonalization [22, 23] to name a few, they still have their limits. The Hilbert space grows exponentially with the number of constituents in

the system. Therefore for higher dimensional systems, increasing number of particles, complex geometries of the crystal structure, frustrated spin systems and dynamical problems, even the most powerful classical supercomputers reach their limits [24, 25]. Performing quantum simulations, as it has been suggested by Feynman [26], can complement the numerical methods and provide deeper understanding, eventually leading to adjusted theoretical approaches [27]. A quantum simulator does not need to be a universal quantum computer to provide insight into complex quantum many-body systems. Instead, it is sufficient to simulate and study one particular problem, comparable to a wind-channel that allows to simulate the air flow around various objects and thus providing a fundamental understanding of one particular feature [25]. The basic principle is to realize a well controlled system of particles following the laws of quantum mechanics and implementing the Hamiltonian of the desired model. By measuring the system properties and dynamics one is able to understand quantitatively the realized model. There are various experimental platforms available for quantum simulations among which trapped ions [28, 29, 30], quantum dots [31, 32], superconducting circuits [33, 34, 35], photons [36, 37], nuclear spins [38, 39, 40] and neutral atoms [41, 42, 43]. Besides simulating condensed matter physics, quantum simulations find application in various other research areas such as atomic physics, quantum chemistry, high-energy physics, and even cosmology [44].

Ultracold neutral atoms, which are the system employed in this thesis, present a resourceful platform for quantum simulation [41, 42]. They exploit the different properties of atomic species, for example their energy level structure, their electronic or nuclear spin degree of freedom or the interactions between the atoms. Additionally, these systems are highly tunable through laser light or magnetic fields, which allow one to manipulate the states of the atoms. For example, interfering laser beams form a periodic, optical potential for the atoms. The depth depends on the power and the wavelength of the laser beams. Optical lattices filled with atoms resemble electrons in a crystal. Moreover, there are atoms following bosonic as well as fermionic statistics, thus further extending the possibilities of ultracold atom quantum simulators.

As theoretically proposed in the work of D. Jaksch *et al.* [45] those systems allow simulation of Mott insulating phases. Soon after this proposal was published, it was demonstrated in an experiment for bosonic rubidium atoms in a three-dimensional optical lattice by M. Greiner *et al.* [46]. Six years later, two groups demonstrated the metal-to-Mott-insulator transition described by the Fermi-Hubbard model with two-spin-component fermions of potassium atoms [47, 48]. But the capacity of ultracold atoms goes beyond. Quantum simulations of various phases of the Hubbard model have been studied successfully. For example, antiferromagnetic spin correlations of femionic systems were demonstrated [49] and later also long-range antiferromagnetic order [50], triangular lattices were implemented presenting a superfluid to Mott insulator transition [51] and were used as a platform to study classical magnetism [52], topological phenomena arising in the Haldane model have been studied [53] and a minimalistic version of a fractional quantum Hall state was realized in a system of two ultracold atoms [54, 55]. Additionally, non-equilibrium phenomena have been investigated with ultracold atoms. Some notable examples are quantum thermalization

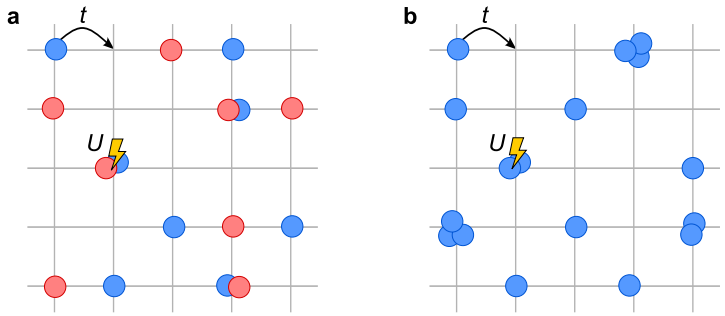

Figure 1.2: Schematic representation of a Hubbard system. **a** In the Fermi-Hubbard model with two spin states, red and blue, the Pauli exclusion principle prohibits identical particles to occupy the same lattice site. The tunneling t of a particle from one site to another is indicated by an arrow. The interaction energy U describes the energy cost of having two particles in the same lattice sites. **b** For the Bose-Hubbard model the t and the U describe the same processes as in the fermionic case. However, due to the bosonic nature of the particles it is possible for identical particles to occupy the same lattice site.

through entanglement [56] or many-body localization in one-dimensional lattices [57] and in a two-dimensional lattice [58].

This thesis focuses on the realization of a quantum-gas microscope of bosonic and fermionic strontium with the goal to realize quantum simulations of the Bose- and Fermi-Hubbard models. To this end, we will exploit the peculiar properties of strontium in order to realize and study various complex quantum many-body systems. In the following sections, we present an overview of the models we are interested in and discuss the realization of ultracold atom quantum simulators, in particular quantum-gas microscopes. We present a brief summery of the properties and the resulting applications of strontium and its benefits in the realization of a quantum-gas microscope.

1.1 The Hubbard model

The Hubbard model, in its standard form, describes interacting fermionic particles with spin 1/2 moving in a periodic potential, see Fig. 1.2a. In second quantization, the Hubbard Hamiltonian consists of two summands:

$$\hat{H}_{\mathrm{FH}} = \underbrace{-t \sum_{\langle j,l\rangle,\sigma=\uparrow,\downarrow} \left(\hat{c}^{\dagger}_{j,\sigma}\hat{c}_{l,\sigma} + \mathrm{h.c.}\right)}_{\text{tunneling term}} + \underbrace{U \sum_{j,\sigma\neq\sigma'} \hat{n}_{j,\sigma}\hat{n}_{j,\sigma'}}_{\text{interaction term}} \tag{1.1}$$

where the sum over $\langle j,l\rangle$ is restricted to pairs of nearest neighbors in the lattice, and the spin indices $\sigma,\sigma' \in \{\uparrow,\downarrow\}$ are the two different spin states. The tunneling parameter $t>0$ describes particles hopping between different lattice sites. The creation and annihilation operators $\hat{c}^{\dagger}_{j,\sigma}$ respectively $\hat{c}_{l,\sigma}$ fulfill the fermionic anticommutation relation $\{\hat{c}_{j,\sigma},\hat{c}^{\dagger}_{l,\sigma'}\} = \delta_{\sigma,\sigma'}\delta_{j,l}$. The repulsive on-site interaction $U>0$ describes the

energy cost of having two particles in the same lattice site. Due to the Pauli exclusion principle, only particles of different spin $\sigma \neq \sigma'$, are allowed to occupy the same site. The number operator $\hat{n}_{j,\sigma} = \hat{c}^\dagger_{j,\sigma}\hat{c}_{j,\sigma}$ refers to the number of atoms with spin σ in the j-th lattice site.

The Fermi-Hubbard model has a bosonic counterpart, the Bose-Hubbard model [59]. The creation and annihilation operators of the Bose-Hubbard model fulfill the canonical commutation relation $[\hat{b}_j, \hat{b}^\dagger_l] = \delta_{j,l}$ which results in

$$\hat{H}_{\mathrm{BH}} = -t \sum_{\langle j,l \rangle} \left(\hat{b}^\dagger_j \hat{b}_l + \mathrm{h.c.} \right) + \frac{U}{2} \sum_j \hat{n}_j \left(\hat{n}_j - 1 \right). \tag{1.2}$$

The two models are described in the same fashion with tunneling and interaction terms, see Fig. 1.2b.

Over the years, a variety of effective Hamiltonians have been developed which originate from the Hubbard model and describe specific limits of a system [12]. Therefore, they allow one to investigate particular phases and phase transitions of those limits. One example is the limit of strong interaction $U/t \gg 1$ where double occupancy is suppressed due to the large energy cost U of having two particles in the same site. In a spin-1/2 fermionic system at half-filling[1] only magnetic interactions are relevant in the limit of strong interaction. The relevant energy scale is the superexchange energy $J = 4t^2/U$. It describes spin-exchange through a second order tunneling process [60]: Two neighboring lattice sites are occupied by two different spins, $|\uparrow,\downarrow\rangle$ or $|\downarrow,\uparrow\rangle$. The two states are coupled through virtual states $|\uparrow\downarrow,0\rangle$ or $|0,\uparrow\downarrow\rangle$, which are at a higher energy given by U. Thus the process of exchanging two spins, $|\uparrow,\downarrow\rangle \rightarrow |\downarrow,\uparrow\rangle$, is a second order tunneling process through a virtual state and scales with a magnitude $\sim t^2/U$. The system can then be expressed by the Heisenberg model which is derived from the Hubbard model [14]:

$$H_{\mathrm{HM}}(N=2) = \frac{J}{2} \sum_{\langle jl \rangle} \hat{S}^z_j \hat{S}^z_l + \frac{J}{4} \sum_{\langle jl \rangle} \left(\hat{S}^+_j \hat{S}^-_l + \hat{S}^-_j \hat{S}^+_l \right) \tag{1.3}$$

for two spin states, with the spin lowering operator $\hat{S}^+_j = c^\dagger_{j,\uparrow} c_{j,\downarrow}$ and the spin raising operator $\hat{S}^-_j = c^\dagger_{j,\downarrow} c_{j,\uparrow}$, and the z-component of the total spin angular momentum operator $\hat{S}^z_j = \frac{1}{2}\left(c^\dagger_{j,\uparrow} c_{j,\uparrow} - c^\dagger_{j,\downarrow} c_{j,\downarrow} \right)$

The ground state of the SU(2) Heisenberg model with antiferromagnetic exchange interaction $J > 0$ is a singlet of total spin zero, as stated by Marshall's theorem [14]. Although this does not imply that the ground state is ordered in a checkerboard pattern, there is a strong tendency for that [61]. In Fig. 1.3a, we represent the antiferromagnetic order of an SU(2) Heisenberg model by alternating the two spin states (red and blue) in the lattice.

So far, we have specifically considered two different spin states $|\uparrow\rangle$ and $|\downarrow\rangle$. If we allow $\sigma \in \{1, 2, ..., N\}$, we obtain a generalization of Eq. (1.1) with N different

[1] Half-filling refers to a system where there are as many particles as lattice sites, but half of them are in one spin state and the other half are in the other spin state.

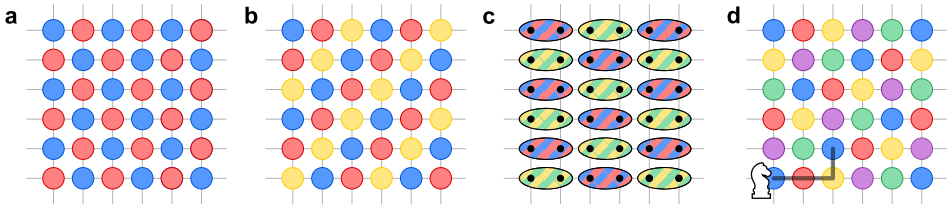

Figure 1.3: The ordering of spin flavors arising in a SU(N)-Heisenberg model. **a** For $N = 2$, the two spin states are alternating and form the typical antiferromagnetic pattern. **b** For $N = 3$, the three-sublattice phase shows diagonal strips of the different spin flavors as shown in the work of T. A. Tóth *et al.* [73]. **c** Dimerization arises for SU($N = 4$) where each dimer consists of two colors, and the pair of colors alternate similar to the antiferromagnetic pattern in SU(2). It is presented in the work of P. Corboz *et al.* [74]. **d** For SU($N = 5$), the spins order in a (chess) knight-move pattern which is explained in the works by P. Nataf *et al.* and T. Botzung *et al.* [75, 23].

spin states, corresponding to the SU(N) Fermi-Hubbard model [62]. This generalized version of the Hubbard model is motivated by various research areas. One example is elementary particle theory where quantum chromodynamics is a SU(3) theory that includes three flavors of quarks. This idea led to the Nobel prize for M. Gell-Mann in 1969. Moreover, SU(N) models with $N > 2$ also find applications in condensed matter physics, for example in multi-valley semiconductors exhibiting the quantum Hall effect [63, 64] or in high-T_c superconductors [65, 66, 67, 14]. Ultracold atom experiments have a great capacity of realizing and studying such systems [68], as demonstrated already in various systems [69, 70, 71, 72]. To this end, they exploit the nuclear spin of the atoms in systems with total electronic spin zero, because the interactions between different nuclear spin states are equal and there are no spin-exchange collisions.

For an SU(N) system, the resulting quantum Heisenberg model describes the interaction between spin states for N different spins [14],

$$H_{\mathrm{HM}}(N) = \frac{J}{N} \sum_{\langle jl \rangle} \sum_{\sigma\sigma'} \hat{S}_j^{\sigma\sigma'} \hat{S}_l^{\sigma'\sigma} \tag{1.4}$$

where the spin states are σ and σ'. This is a generalized form of Eq. (1.3) for the case of SU($N = 2$). The spins $\sigma = 1, 2$ are typically described as $\sigma = \uparrow, \downarrow$, and the spin flip terms are given by $\hat{S}_j^{12} = \hat{S}^+ = c_{j,1}^\dagger c_{j,2}$ and $\hat{S}_j^{21} = \hat{S}^- = c_{j,2}^\dagger c_{j,1}$ [14].

Finding the ground state of SU($N > 2$) Heisenberg systems is not a trivial problem. Numerical methods have revealed the ground states for small values of N. Namely, the SU(3)-Heisenberg model in a cubic lattice has a ground state of a three-sublattice phase [73], see Fig. 1.3b, rather than a two-sublattice phase that would resemble the checkerboard pattern of the SU(2)-Heisenberg antiferromagnet. Further, in a SU(4)-Heisenberg model dimerization is predicted on the square lattice and each dimer consists of a pair of flavors which are different from the adjacent pair [74], see Fig. 1.3c. In the case of $N = 5$ spin flavors, the spins are expected to order as displayed in Fig. 1.3d, where the same spins arrange in the pattern of the knight move in chess. This was found from exact diagonalization of the SU(N)-Heisenberg model

[75]. The complexity further increases when considering the more general discussion of the SU(N)-Fermi Hubbard model. For large N values, M. Hermele *et al.* [76] predicted a chiral spin liquid ground state. The complexity increases even further for different lattice geometries as presented recently by T. Botzung and P. Nataf [23].

1.2 Quantum simulations of Hubbard models with ultracold atoms

A rich platform for quantum simulations of the Hubbard model are ultracold atoms in optical lattices. The optical lattice simulates the periodic potential given by the ionic cores in a solid. It is generated by interfering laser beams. Their geometry can vary in dimension and shape depending on the spatial arrangement of the interfering beams [77]. Typical lattice spacings are between 250 nm to 1 µm, which is related to the wavelength of the laser light. Due to the larger lattice spacing and the large mass of the atoms, the magnitudes of the energy scales of the ultracold atom experiments become much smaller compared to solids, and hence we require temperatures on the order of nanokelvin in order to operate in the same energy regime. To this end, the creation of quantum degenerate gases of atoms was a key step to be able to simulate the Hubbard model. Bose-Einstein condensates were first achieved [78, 79] and degenerate Fermi gases of various species followed shortly after [80, 81, 82, 83, 84]. Loading those ultracold clouds adiabatically into an optical lattice provides a convenient starting point to realize systems with the desired small temperatures.

1.2.1 Quantum-gas microscopy

Considering that the Hubbard model describes particles moving in a periodic potential, observing these particles individually may unravel open questions on the complex quantum many-body physics that the Hubbard model describes [43]. That is the idea behind quantum-gas microscopy. A high-resolution optical imaging system is combined with a quantum-gas experiment, enabling the detection and resolution of individual atoms in an optical lattice in the Hubbard regime.

In 2009, W. S. Bakr *et al.* [85] demonstrated for the first time quantum-gas microscopy in the Bose-Hubbard regime. Shortly afterwards, the localization of the atoms in the Mott insulating phase was directly observed with single-site resolution [86]. For the quantum phase transition, a comparison between the probability distribution of the atoms and the phase coherence measurement became possible and was presented in [87]. While this was done with bosonic atoms, five years later fermionic atoms were also detected with single-atom resolution [88, 89, 90]. The implementation of spin-resolved imaging on top of single-atom resolution gave access to studies of spin correlations in two-component Fermi-Hubbard system in one- and two-dimensions and over the distance of few lattice sites [91, 92, 93]. Additionally, the demonstration of long-range antiferromagnetic order in the Fermi-Hubbard regime was observed with single-atom resolution [50]. This is an excellent starting point to investigate other phases of the Fermi-Hubbard model, for example engineering doping by introducing

holes in an antiferromagnetic spin system [94, 95] and observing their pairing [96], which is believed to be the key mechanism behind high-T_c superconductivity. Further studies have been carried out investigating the effect of effective magnetic fields [97], transport in Fermi-Hubbard systems [98, 99], the formation and behavior of magnetic polarons which are quasi particles in the doped Fermi-Hubbard system [100, 101] and many more.

The quantum-gas microscopes for fermionic atoms listed above are either with potassium ^{40}K or with lithium ^{6}Li. In my thesis, I extend the existing toolbox of quantum-gas microscopes by adding strontium. In particular, single-atom-resolved imaging for both bosonic and fermionic strontium is demonstrated, with a first proof-of-principle of spin resolution for two of the ten spin states of the fermionic isotope.

1.3 Strontium: properties and applications

There are four stable isotopes of strontium, three bosonic and one fermionic, making it a promissing atom for quantum-gas microscopy of both Bose- and Fermi-Hubbard systems. As an alkaline-earth atom, it has the two-valence electrons which form a spin-singlet in the ground state. There are broad- and narrow-linewidth transitions. The most popular broad-linewidth transition is in the blue spectrum at 461 nm and excites the singlet of the ground state to an excited singlet state. The most popular narrow-linewidth transition for laser cooling is at 689 nm, in the red spectrum, and excites the singlet state of the ground state to a triplet state. Exploiting the transitions with their vastly different linewidths allows to perform efficient laser cooling to quantum degeneracy [102]. This achievement made continuous Bose-Einstein condensation possible and paves the way towards atom lasers [103]. Moreover, the closed two-level system of the narrow-linewidth transition at 689 nm finds various applications. Optical tweezers experiments exploit the transition for fluorescence imaging and simultaneous cooling [104].

Strontium has several metastable states, arising as a result of the dipole-forbidden singlet-to-triplet transitions. Strontium atomic clocks benefit in particular from the ultra-narrow transition to the so called clock state [105]. Additionally, there are magic wavelengths at which the light shift of the ground and the excited state are equal [106]. This provides a great tool for high-precision experiments [107]. For example, optical atomic clocks are able to detect the gravitational redshift across few millimeters [108] and optical tweezers of strontium exploiting the clock state provide a convenient system to realize quantum simulations with Rydberg states [109]. The fermionic isotope has a nuclear spin of $I = 9/2$ resulting in ten different spin states, which all interact the same with each other. That is why strontium is an excellent candidate for SU($N \leq 10$) Fermi-Hubbard physics. Additionally, it is interesting for quantum information processing based on nuclear spin qubits [110].

Because of the list of the above properties and their possible applications, a strontium quantum-gas microscope complements the existing list of quantum-gas microscopes and adds new opportunities to the field of quantum simulation. The use of a magic-wavelength optical lattice sets the stage for high precision measurements. The

SU(N) nature of the fermionic isotope is a great tool to study SU(N) quantum magnetism with $N \leq 10$. Combining the single-atom resolution with spin resolution as it has been demonstrated in tweezers experiments [110], has great potential to study antiferromagnetic ordering for more than two spin states.

Furthermore, the optical lattice of a strontium experiment can easily have smaller lattice spacing than the transition linewidth. Those subwavelength optical lattices pose a promising setting for studies of collective atom-photon interactions [111]. In such experiments, one can consider the atoms as dipole emitters which absorb and emit the near-resonant light. If the distance in an array of such dipoles is smaller than the transition wavelength, collective phenomena are enhanced which can lead to constructive (superradiance) or destructive (subradiance) interference. The change in linewidth of the emission has been observed in the subradiant scattering phenomena presented in the form of an atomic mirror with rubidium atoms [112]. Moreover, the phenomena of subradiance can be exploited for storing and manipulating light [113, 114].

1.4 Thesis outline

This thesis presents the realization of a strontium quantum-gas microscope for simulations of both Bose- and Fermi-Hubbard models. We prepare a cloud of ultracold strontium applying the cooling techniques established in most strontium experiments, but demonstrate a new loss-shielding scheme to increase the magneto-optical trap atom number. Our apparatus can prepare bosonic as well as fermionic clouds. We then load the atoms into a two-dimensional, square optical lattice which will allow us to simulate Bose- or Fermi-Hubbard models. By placing a high numerical aperture objective close to the atoms we unlock single-site-resolved imaging. For the bosonic isotope, we exploit the broad-linewidth transition to scatter photons, which are subsequently captured in the objective and detected on an EMCCD camera. The recoil heating is addressed by attractive Sisyphus cooling on the red transition similar to the one applied in optical tweezers [115, 109]. For the fermionic isotope, we image with the red transition only, performing imaging and cooling simultaneously. This method has enabled us to obtain first images of two different spin states and paves the way towards SU($N \leq 10$) Fermi-Hubbard physics.

The chapters of this thesis are structured in the following way:

- Chapter 2 presents the properties of strontium relevant for this thesis and its level diagram. An overview of the experimental apparatus is explained alongside with the cooling sequence used to produce ultracold atoms of the different isotopes of strontium. It focuses in particular on the bosonic ^{84}Sr and the fermionic ^{87}Sr isotope. We present a detailed discussion on the repumper lasers which are required for efficient laser cooling. We elaborate on a new scheme that we have developed, consisting of a resonant shielding of losses in the blue magneto-optical trap to enhance the atom number. The second cooling stage is the red magneto-optical trap. We discuss its peculiarities for the bosonic and

the fermionic isotopes. In the last part, we present the crossed optical dipole trap and the light sheet trap which we use to evaporatively cool the atoms to quantum degeneracy in the bosonic case.

- Chapter 3 describes in detail the setup and the geometry of our fourfold optical lattice. We discuss the basics of optical lattices for the simulation of the Hubbard model. We compare a twofold versus a fourfold interference for the realization of a square optical lattice and describe the optical setup. We present the calculation of the band structure and the lattice parameters. Additionally, we discuss a spatially dependent parametric heating method used to determine the trapping frequency of the optical lattice.

- Chapter 4 describes quantum-gas microscopy of bosonic ^{84}Sr. It discusses the setup of the microscope and the procedure to get single-atom-resolved imaging of the bosonic isotope. We present the imaging performance in particular the resolution and the fidelity. The cooling method applied to counteract the recoil heating is attractive Sisyphus cooling. Besides a discussion on its performance, we present the spatial dependence of the cooling method and exploit it to characterize the trapping frequency of the harmonic confinement. We conclude the chapter by presenting the detection of a superfluid in the quantum-gas microscope. We study the superfluid interference peaks and determine their visibility.

- Chapter 5 presents quantum-gas microscopy of the fermionic isotope ^{87}Sr. We explain the limitations for imaging of the fermions using the blue transition for fluorescence. We discuss the hyperfine structure and the spin-dependent polarizability of the trapping laser light. We then demonstrate imaging of the fermionic isotope, exploiting the narrow-linewidth transition. We characterize the resolution and the fidelity. In the last part, we show our first results of spin resolved imaging exploiting the spin-dependent light shift of the narrow-linewidth transition. We discuss current challenges of this scheme and future perspectives for the spin-resolved imaging of SU(N) Fermi-Hubbard systems with $N > 2$.

- Conclusion and outlook 6: We conclude and summarize the work presented in the thesis and discuss possible future research directions opened by this work.

Chapter 2

Preparation of ultracold strontium clouds

This chapter presents our ultracold strontium apparatus which allows us to work with the bosonic and the fermionic isotopes. It gives an overview of the apparatus and the capturing and cooling methods: laser cooling on the blue and the red transition before evaporative cooling in the optical dipole trap. We start by explaining some key properties of strontium. Then present an overview of the atomic source which consists of a strontium oven, a two-dimensional magneto-optical trap (MOT) and a short Zeeman slower. After pushing the atoms into the science chamber, we trap them by means of a the three-dimensional blue MOT. In this context, we compare different repumping schemes to recover atoms leaking into a metastable state and we present our method to double the number of atoms in the blue MOT by resonant shielding on the narrow-linewidth red transition. The blue MOT is loaded into a red MOT. We point out the challenges of the narrow-line cooling on the red transition, in particular for the fermionic isotope. In the last part the optical dipole trap potential will be explained and how we reach quantum degeneracy for the bosonic isotope after evaporative cooling.

The results presented were achieved in a team effort together with my PhD colleague Dr. Jonatan Höschele, and the postdocs Dr. Vasiliy Makhalov and Dr. Antonio Rubio Abadal, supervised by Prof. Dr. Leticia Tarruell. While the design of the vacuum chamber and the laser system was done by David Jacobs, Dr. Jonatan Höschele and Prof. Dr. Leticia Tarruell, the assembling of both was a team effort where myself and Dr. Vasiliy Makhalov joined. The repumper laser setup as well as design and the assembling of the optical dipole trap was done by myself with assistance from my colleagues. The results presented in Sec. 2.2.3 are published in [116].

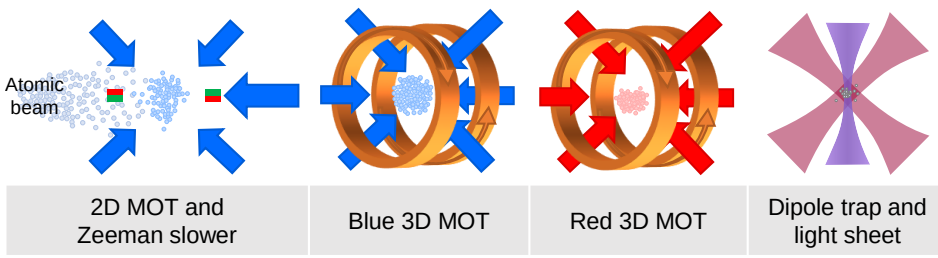

Figure 2.1: Schematic of the cooling sequence. The different steps of our cooling sequence are displayed. We start with a two-dimensional magneto-optical trap (2D MOT) and a Zeeman slower using the blue light at 461 nm represented by the blue arrows. The second step is a three-dimensional magneto-optical trap (3D MOT) on the blue transition followed by a red 3D MOT operated at 689 nm. The magnetic field gradient is generated by a set of coils (orange circles) in anti-Helmholtz configuration. The last cooling step is evaporation in a combination of a crossed dipole trap (red) and a tightly focused light sheet beam (purple).

2.1 Experimental apparatus and cooling sequence

The goal of our experiment is to load quantum degenerate clouds of strontium into an optical lattice to realize the Hubbard model and study it by means of single-site-resolved imaging. To this end, our experimental apparatus is designed to prepare ultracold clouds of bosonic ^{84}Sr or fermionic ^{87}Sr atoms. To reach quantum degeneracy, we exploit the two main laser cooling transitions of strontium, the blue and the red one, as well as evaporation, see Fig. 2.1. In doing so, we follow a similar protocol as presented in the demonstrations of the first strontium Bose-Einstein condensates [117, 118]. Atoms which are ejected from an oven are slowed down by a Zeeman slower and captured in a two-dimensional magneto-optical trap (2D MOT). A resonant beam pushes the atoms into the science chamber where they are recaptured by a three-dimensional magneto-optical trap (3D MOT) operated on the blue transition. The atoms are further cooled in a 3D MOT operated on the red transition, before they are loaded into the far red-detuned optical dipole trap. A tightly focused light sheet beam adds additional confinement. From there, quantum degeneracy is reached through evaporative cooling in the combined optical dipole and light sheet trap. We can switch between different isotopes by adjusting the frequencies of the lasers applied for laser cooling.

Reaching quantum degeneracy with ultracold atoms requires a particular vacuum environment in order to have a controlled system with negligible atom losses. To this end, our vacuum chamber consists of two parts: the source and the science chamber. These have different vacuum qualities and are separated by a differential pumping tube. The source chamber with the strontium oven operates at high vacuum, with pressures around 10^{-8} mbar, see Fig. 2.2a. The science chamber consists of a small glass cell[1] in which the quantum simulation experiments are carried out, see Fig. 2.2b.

[1] Custom uncoated quartz cell, 20 mm × 17 mm × 67 mm with wall thickness 3.5 mm

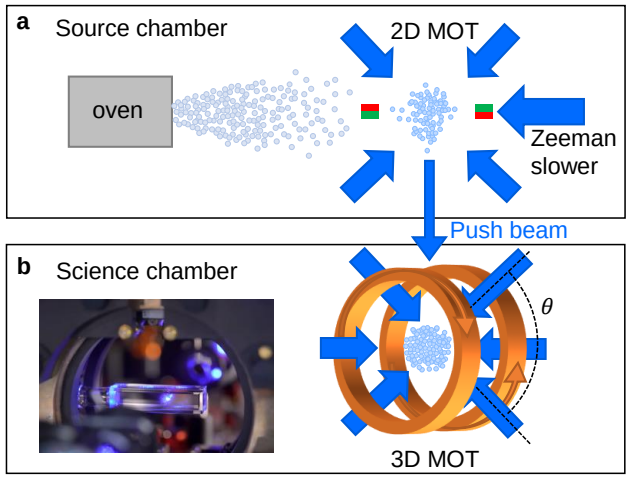

Figure 2.2: Schematic explanation of the experimental apparatus. **a** The source chamber contains the strontium oven which ejects atoms that are then captured in a two-dimensional magneto-optical trap (2D MOT). Permanent magnets (red-green rectangles) generate the magnetic field gradient, and four beams are applied to capture the atoms. Additionally, a Zeeman slower beam, counterpropagating to the atomic beam slows it down and facilitates the capture in the 2D MOT. A resonant laser beam pushes the atoms through a differential pumping tube into the science chamber **b** which is a small glass cell (see photo) surrounded by a pair of coils. Operated in anti-Helmholtz configuration, they generate the magnetic quadrupole field for the three-dimensional magneto-optical trap (3D MOT). The MOT beams propagating through the coils are perpendicular to the other four beams, which enclose an angle $\theta \approx 60°$, as shown in the schematics.

It is an ultra-high vacuum environment with pressures around 10^{-11} mbar.

The design of the vacuum chamber and the optics setup for the cooling and trapping lasers is discussed in detail in the PhD thesis of J. Höschele [119] and in the master's thesis of D. Jacobs [120]. Therefore, this chapter focuses on the cooling sequence as presented in Fig. 2.1. Here, we start the discussion with some key properties of strontium and the different isotopes as well as the energy level diagram with the optical transitions relevant for this thesis. In a second part, we describe the capturing and preparation of the atoms for further cooling in the blue 3D MOT.

2.1.1 Stable isotopes of strontium

Strontium has four stable isotopes, three bosonic and one fermionic, see Tab. 2.1. As for all alkaline-earth elements, the isotopes with an even mass number follow bosonic statistics, and the ones with odd, such as ^{87}Sr, are fermionic. The number of electrons for strontium is even due to the two valence electrons and the otherwise completely filled inner shells. Thus the number of protons is even too and for the bosonic isotopes, also the number of neutrons has to be even. The spins in the nucleus

(Japan cell)

Isotope	Nuclear spin I	Natural abundance	Scattering length	Quantum degeneracy
^{84}Sr	0	0.56(1) %	122.7(3) a_0	2009 [117, 118]
^{86}Sr	0	9.86(1) %	823(24) a_0	2010 [121]
^{87}Sr	9/2	7.00(1) %	96.2(1) a_0	2010 [82, 83]
^{88}Sr	0	82.58(1) %	$-1.4(6)$ a_0	2010 [122]

Table 2.1: Strontium properties of the four stable isotopes. The only fermionic isotope is ^{87}Sr. The natural abundance is the typical ratio of the isotopes in a strontium source [123]. The scattering length [124] is given in a_0 which is the Bohr radius. Quantum degeneracy has been reached with all of these isotopes.

arrange in antiparallel spin pairs which results in zero nuclear spin for the three bosonic isotopes [125]. In contrast, the fermionic isotope has a nuclear spin of $I = 9/2$. Since the two valence electrons form a singlet in the ground state, the total electron angular momentum is $J = 0$. This results in $N = 2I + 1 = 10$ spin states which have the same interaction due to the decoupling from the electronic state and the absence of hyperfine interaction. Consequently fermionic strontium exhibits SU($N = 10$) symmetry [126, 127, 68].

Quantum degenerate gases have been realized for all four stable isotopes. The first one was ^{84}Sr [117, 118], which has a beneficial scattering length of 122.7(3) a_0 for evaporative cooling, with a_0 the Bohr radius. During evaporative cooling, which is the last step to reach quantum degeneracy [128, 78, 79], the atoms have to interact with each other in order to thermalize. For strontium the scattering length given in Tab. 2.1 is fixed since it has two-valence electrons in singlet configuration and thus there are no magnetic Feshbach resonances that would allow us to change the interaction [129]. For the fermionic isotope the scattering length is comparable to the one of ^{84}Sr and the mixture of the different spin states makes the rethermalization during evaporative cooling to quantum degeneracy efficient [82, 83]. Because of the large scattering length of ^{86}Sr, the density of the atomic cloud has to be low to avoid three-body losses in order to create a Bose-Einstein condensate [121] and the small scattering length of the most abundant isotope ^{88}Sr requires to be sympathetically cooled together with ^{87}Sr [122].

2.1.2 Optical transitions

Strontium has two valence electrons which gives rise to an interesting energy level diagram, see Fig. 2.3. In the ground state $5s5s\,^1S_0$ the two valence electrons form a singlet. The transition at 461 nm conserves the singlet and has a broad linewidth of $\Gamma_{\mathrm{blue}}/2\pi \approx 30.5$ MHz. Exciting the ground state to a triplet state is a dipole forbidden transition and requires a spin flip which is the reason for the narrow linewidth of $\Gamma_{\mathrm{red}}/2\pi \approx 7.4$ kHz for the transition to $5s5p\,^3P_1$, also referred to as intercombination

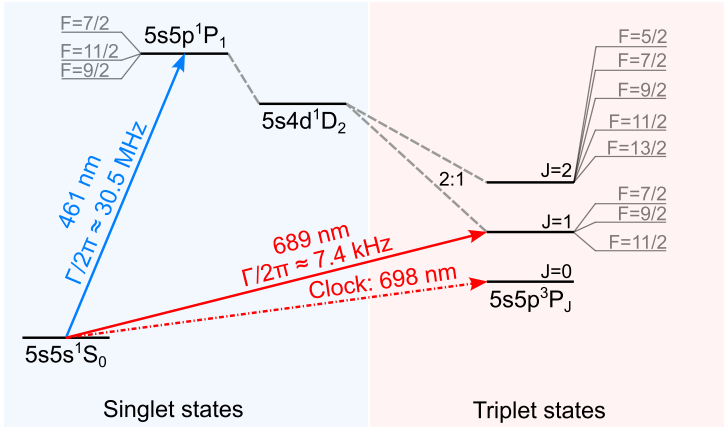

Figure 2.3: Level diagram of strontium. There are singlet and triplet states which depend on the alignment of the spins of the two valence electrons, they are indicated by the blue respectively red shaded background. The two main transition for laser cooling of strontium are the blue one at 461 nm and the red one at 689 nm, given with their respective linewidth Γ. The clock transition at 698 nm is highly forbidden for the bosonic isotopes and it has a linewidth on the order of millihertz for the fermionic isotope. The hyperfine splitting for the fermions into the different F-states, with $|I - J| < F < I + J$, are indicated with the frequency shifts listed in Tab. 2.4. The intermediate D-state is a decay channel of the $^1\mathrm{P}_1$ state into one of the $^3\mathrm{P}_J$ states, for $J = 1, 2$, with a ratio of $2 : 1$.

Transition	**Linewidth** Γ	I_{sat}	T_{D}	T_{recoil}
$^1\mathrm{S}_0 \xrightarrow{461\,\mathrm{nm}} {}^1\mathrm{P}_1$	$2\pi\times 30.5\,\mathrm{MHz}$	$41\,\mathrm{mW/cm^2}$	$\approx 720\,\mu\mathrm{K}$	$\approx 1\,\mu\mathrm{K}$
$^1\mathrm{S}_0 \xrightarrow{689\,\mathrm{nm}} {}^3\mathrm{P}_1$	$2\pi\times 7.4\,\mathrm{kHz}$	$2.96\,\mu\mathrm{W/cm^2}$	$\approx 180\,\mathrm{nK}$	$\approx 460\,\mathrm{nK}$

Table 2.2: Parameters for the two laser cooling transitions of strontium. The saturation intensity is I_{sat}, the Doppler temperature is $T_{\mathrm{D}} = \hbar\Gamma/(2k_{\mathrm{B}})$, and the recoil temperature is $T_{\mathrm{recoil}} = \hbar k^2/(mk_{\mathrm{B}})$, where k is the wavevector, m is the mass of the atoms, k_{B} is the Boltzmann constant and $\hbar$ is the reduced Planck constant.

Isotope	$^1\mathbf{S}_0$ - $^1\mathbf{P}_1$	$^1\mathbf{S}_0$ - $^3\mathbf{P}_1$
^{84}Sr	$-270.8\,\mathrm{MHz}$	$-351.49\,\mathrm{MHz}$
^{86}Sr	$-124.8\,\mathrm{MHz}$	$-163.81\,\mathrm{MHz}$
^{87}Sr	$-46.5\,\mathrm{MHz}$	$-62.15\,\mathrm{MHz}$
^{88}Sr	0	0

Table 2.3: Isotope shifts of the optical transitions of strontium relevant for laser cooling [123]. The values are given with respect to the transition of ^{88}Sr.

Hyperfine state	$^1\mathbf{P}_1$	$^3\mathbf{P}_1$	$^3\mathbf{P}_2$
$F = 5/2$			+2371.28 MHz
$F = 7/2$	+37 MHz	+1414.12 MHz	+1597.14 MHz
$F = 9/2$	-23 MHz	+283.86 MHz	+618.65 MHz
$F = 11/2$	-6 MHz	-1179.29 MHz	-551.55 MHz
$F = 13/2$			-1898.05 MHz

Table 2.4: Hyperfine splitting of ^{87}Sr in the singlet ^{1}P$_1$ state and the triplet states ^{3}P$_1$ and ^{3}P$_2$ obtained from [125]. Their values are given with respect to an assumed $I = 0$ state. The values of ^{3}P$_1$ are consistent with the transition frequencies listed in [123]. Further details are presented in Appx. A.1.

line. These two transitions, called blue and red due to the color of the laser light, are convenient for laser cooling of strontium. The different linewidth results in orders of magnitude differences in their temperature limits, see Tab. 2.2. This results in vastly different temperatures for the magneto-optical traps of the two transitions. Operated on the blue transition the 3D MOT reaches millikelvin temperatures, while in contrast the red 3D MOT reduces the temperature of the atoms to microkelvin.

The resonances for these two transitions shift at the order of megahertz for different isotopes, see Tab. 2.3. Additionally, the fermionic isotope has a hyperfine structure, with different energies for the different F states, see Tab. 2.4. Interestingly, the hyperfine splitting of the ^{1}P$_1$ state is at the same order as the linewidth of the blue transition, while the ^{3}P$_1$ has a splitting several orders of magnitude larger than its narrow linewidth such that the hyperfine states on the red transitions can be excited independent from each other.

As it is displayed in Fig. 2.3, the blue transition is not closed. There is a decay channel through an intermediate D-state into the triplet states. The ratio of atoms decaying from the ^{1}P$_1$ state into the ^{1}D$_2$ state is approximately 1 : 20000 [130, 131, 115]. Atoms that decay into the ^{3}P$_1$ state, return to the ground state in around 100 µs. In contrast, the ^{3}P$_2$ state is a metastable state and has a lifetime of several minutes [132, 133]. Additionally, atoms in this state are magnetically trapped [134] which makes it a convenient reservoir state to accumulate atoms during a blue magneto-optical trap which has been applied in the first ^{84}Sr Bose-Einstein condensate [117, 118]. The same technique is exploited in experiments of mixtures, as for example with ^{88}Sr and ^{87}Sr shown in [122]. This magnetically trapped metastable state is not unique to strontium, but exists for various other atoms as well [135].

Furthermore, in Fig. 2.3 the clock transition is indicated at 698 nm. It is exploited for the most precise atomic clocks up to date [105]. For bosons this transition is strictly dipole forbidden, only by applying strong magnetic fields the transition can be addressed as a result of mixing with other excited states [136, 137]. For the fermions,

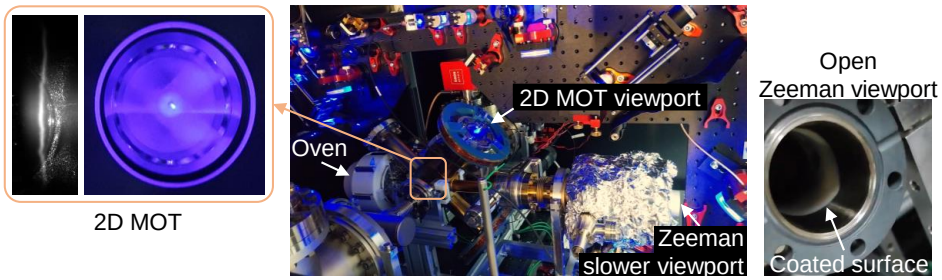

Figure 2.4: Photographs of the source chamber. The Zeeman slower and the four 2D MOT viewports are placed far away from the oven, shown in middle picture. The coils surrounding the viewports of the 2D MOT allow us to adjust the zero of the magnetic field gradient which is generated by permanent magnets. Pictures of the 2D MOT are displayed on the left, from top as a bright line respectively from side as a small white spot in the center of the picture. The Zeeman slower viewport is heated up in order to avoid coating of the sapphire window and thus covered with isolation material. When opening the window (picture on the right) the effectiveness of the heating can be seen through the sharp edge of the coating inside the vacuum tube.

it has a theoretically predicted linewidth Γ_{clock} on the order of 10^{-3}Hz [133] and has been exploited in metrology [108] and quantum computing [110].

2.1.3 From the atomic source to the science chamber

Our source of strontium atoms is an oven filled with solid strontium and operated at around 550 °C. This temperature is significantly higher than the ones used for rubidium or potassium sources due to the small vapor pressure of strontium compared those alkali atoms. The vaporized atoms leave the oven through a microcapillary array which creates a collimated atomic beam inspired by the designs of [138, 139]. As displayed in Fig. 2.2a the atoms ejected from the oven are slowed down by means of a short Zeeman slower (approximately 11 cm) which facilitates efficient capturing in the two-dimensional magneto-optical trap (2D MOT), see Fig. 2.2a [140, 141]. The magnetic field is generated by permanent magnets arranged around the vacuum chamber as discussed in detail in [119]. The Zeeman slower exploits the residual field of the quadrupole magnetic field of the 2D MOT. Both the Zeeman slower and the 2D MOT laser beams are operated at the blue transition of strontium, at 461 nm. The broad linewidth of this transition allows efficient capturing of the atoms by addressing a large range of velocity classes. On a more technical note, the viewports in the source chamber need to be protected from coating with strontium, which is highly reactive with glass surfaces [142]. For the 2D MOT, we place the viewports far from the atoms at 45° with respect to the atomic beam, see Fig. 2.4. The Zeeman slower beam propagates antiparallel to the atomic beam, therefore its viewport is in direct line of sight of the oven. To avoid its coating we continuously heated it up to 400 °C. When we opened the Zeeman slower viewport to fix a leak, we discovered that the interior of the tube was coated up to a sharp line, see Fig. 2.4, this indicates that the heating

is indeed necessary and reliable.

From the 2D MOT, we push the atoms with a resonant laser beam through the differential pumping tube into the science chamber. For an efficient transfer, the centering of the 2D MOT in front of the differential pumping tube is crucial. Even though the chamber is designed such that this should be the default scenario, for a first alignment it was useful to have two pairs of coils around the 2D MOT viewports producing bias fields, which allowed us to shift the zero of the quadrupole magnetic field and thus move the position of the trapped atoms.

In the science chamber, the atoms are then trapped in the small glass cell using a three-dimensional MOT with six beams and a pair of coils in anti-Helmholtz configuration, see Fig. 2.2b. From there, we cool the atoms to quantum degeneracy which is the starting point for our quantum simulation experiments. The quartz glass cell is uncoated and has an internal volume of $60 \times 13 \times 10\,\mathrm{mm}^3$ with a wall thickness of 3.5 mm. This small size has the advantage that we can place the objective for the microscope outside vacuum and yet close to the atoms. However a drawback is that the atomic flux into the glass cell is limited. Since the 2D MOT has a temperature of few millikelvin, the atoms pushed to the science chamber diverge while travelling to the science chamber. The distance between the 2D MOT and the 3D MOT is 71 cm long and the glass cell which has an opening of 10 mm diameter. Thus, we are losing more than 90 % of the atoms that are pushed from the 2D MOT. In future upgrades of the experiment, we advice to shorten the distance between the two chambers. Nonetheless, the spacious design with a large cylinder connecting the glass cell with the non-evaporable getter (NEG) pumps[2] is favorable for efficient pumping speed to reach the desired ultra-high vacuum environment.

2.2 Blue 3D MOT: reducing losses with repumping and shielding

The atoms that are pushed into the glass cell are captured in a three-dimensional magneto-optical trap (3D MOT), see Fig. 2.1. In this section, we present a short overview of this so-called blue 3D MOT. We discuss the challenge arising from the fact, that the blue transition is not closed, see Fig. 2.3. Atoms that leak into the metastable states can be recovered through one of the various repumping transitions available which will be compared in the first part of this section. In the second part, we present the atom number enhancement through resonant shielding on the narrow-linewidth red transition and we conclude with a short description of the Doppler cooling applied in the last stage of the blue MOT.

2.2.1 Blue 3D MOT

For strontium the blue 3D MOT is commonly called "blue" due to the wavelength 461 nm being in the blue spectrum. Its broad linewidth of $\Gamma_{\mathrm{blue}}/2\pi \approx 30.5\,\mathrm{MHz}$

[2]SAES Getter: NEXTorr D 500–5

allows the capturing of a large range of velocity classes, additionally, the high photon scattering rate makes capturing efficient. The temperature limit of the blue MOT is given by the Doppler temperature $T_D = \hbar\Gamma_{blue}/(2k_B) \approx 720\,\mu K$ where $\hbar$ is the Planck constant and k_B is the Boltzmann constant.

In our case, the blue MOT is set up with three beams and their retro-reflection plus a set of coils in anti-Helmholtz configuration placed around the glass cell, see Fig. 2.2b. The horizontal beams passing through the coils are orthogonal to the other four beams entering diagonally. The angle θ between these diagonal beams is around 60°, which will enable us to place the objective of the high-resolution imaging system close to the glass cell without clipping the MOT beams (see Ch. 4). The beams have a radial $1/e^2$ waist of $\sim$3.88 mm and around 3.5 mW power per beam. For the bosonic isotope ^{84}Sr we typically use $-1.5\,\Gamma_{blue}$ detuning and a magnetic field gradient of 56 G/cm. For the fermions we found empirically that larger gradients (73 G/cm) and further detuned blue light ($-1.9\,\Gamma_{blue}$) results in higher atom number.

Having many atoms in the blue MOT is crucial because it is the starting point of the cooling process to quantum degeneracy. During each consecutive step some of the atoms are lost. Consequently efficient repumping is key to a good performance of the blue MOT. Additionally, the resonant shielding during the blue MOT increases the number of atoms further.

2.2.2 Repumpers for the blue MOT

The blue MOT transition from $^1S_0$ to $^1P_1$ is not fully closed. Atoms excited on this transition have a finite chance to fall into an intermediate D-state. Different ratios for the probability are reported in literature, 1 : 50000 [143, 144, 145] or 1 : 20000 [130, 131, 115]. From the D-state, they decay with a ratio of 2:1 into either the $^3P_1$ or the $^3P_2$ state. While the atoms form the $^3P_1$ state fall back into the ground state on a short time scale of hundreds of microseconds, the $^3P_2$ state is a metastable state with lifetimes of around 500 s [146] and requires a repumping laser to recover the atoms. There are various transitions for strontium to repump the atoms back to the ground state $^1S_0$ [147]. A summary of some of the options can be found in Tab. 2.5 and is displayed in Fig. 2.5. All of those come with their advantages and disadvantages which will be discussed in the following.

Before diving into the sea of repumpers, one should say that some experiments use the metastable state as a reservoir [117, 122]. The $^3P_2$ state is magnetically sensitive such that atoms are magnetically trapped in the quadrupole field of the MOT [134], see Sec. 2.1.2. Only after the blue MOT and before the next cooling stage the atoms are recovered from the metastable state with a flash of repumper light. However, in our experiment we repump continuously during the blue MOT for two reasons: on the one hand, the small glass cell requires large magnetic field gradients in order to avoid collisions of the atoms in the magnetic trap with the glass cell walls. But at those gradients the efficiency of the blue MOT to capture atoms which are pushed into the science chamber decreases. On the other hand, accumulating atoms in the reservoir can take several seconds [117] and thus increases the time of an experimental cycle.

Wavelength	**Transition**	**Groups (Ref.)**
497 nm	$5s5p\,^3P_2 \rightarrow 5p5d\,^3D_2$	LENS [148]
403 nm	$5s5p\,^3P_2 \rightarrow 5s6d\,^3D_2$	IQOQI [147], UCSB [149]
3012 nm	$5s5p\,^3P_2 \rightarrow 5s4d\,^3D_2$	Rice [150]
481 nm	$5s5p\,^3P_2 \rightarrow 5p5p\,^3P_2$	Rice [151], USTC [152]
+ 474 nm	$5s5p\,^3P_0 \rightarrow 5p5p\,^3P_1$	ICFO [153]
+ 679 nm	$5s5p\,^3P_0 \rightarrow 5s6s\,^3S_1$	ICFO [116]
707 nm	$5s5p\,^3P_2 \rightarrow 5s6s\,^3S_1$	-
+ 679 nm	$5s5p\,^3P_0 \rightarrow 5s6s\,^3S_1$	JILA [154], JILA [145]
+ 483 nm	$5s5p\,^3P_0 \rightarrow 5s5d\,^3D_1$	IISER Pune [155]
+ 2.6 µm	$5s5p\,^3P_0 \rightarrow 5s4d\,^3D_1$	Birmingham [156]
448 nm	$5s4d\,^1D_2 \rightarrow 5s8p\,^1P_1$	UvA [157]

Table 2.5: List of repumper laser wavelengths and transitions used in various different strontium experiments, see also Fig. 2.5. The enhancement in atom number achieved with the blue MOT is of the same order of magnitude for all of them (see text for details) but is also difficult to compare since they are measured in different experiments.

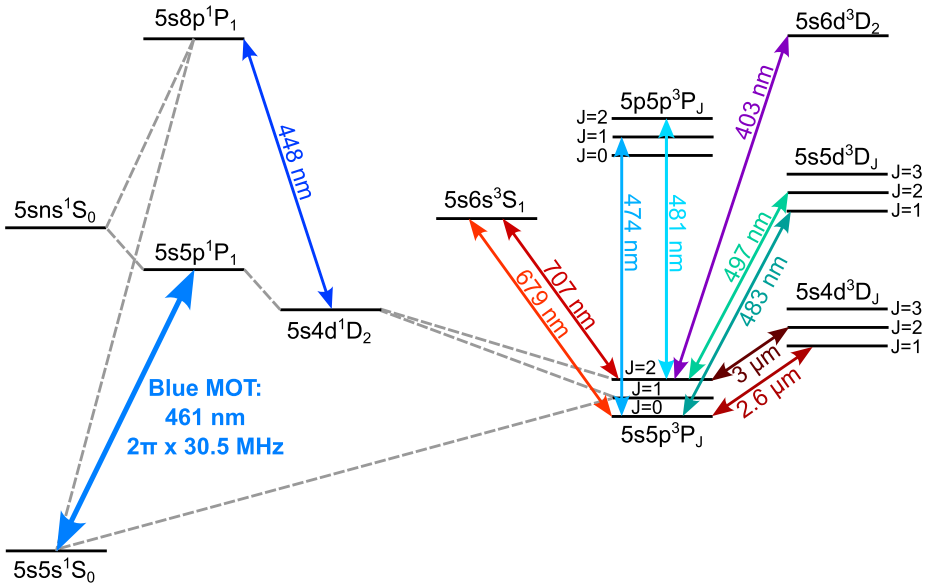

Figure 2.5: A summary of strontium repumping transitions used during the blue MOT ($5s5s\,^1S_0 \rightarrow 5s5p\,^1P_1$ at 461 nm). The repumping transitions are indicated with arrows and their respective wavelength. Details on the different transitions and their references to literature can be found in the text and in Tab. 2.5. Some of the decay channels are indicated with grey dashed lines and the blue MOT transition is highlighted by a thicker arrow.

Repumping through ^3D_J states

There are several repumping transitions operating with one of the ^3D_J states, see Fig. 2.5. Two of them are the $5p5d\,^3D_2$ transition at 497 nm [148, 117] and the $5s6d\,^3D_2$ transition at 403 nm [147, 149, 158]. While repumping with 497 nm provides a factor of 30 enhancement in atom number, an enhancement of 12 was reported for the 403 nm repumper [158]. The difference arises due to more losses into the $5s5p\,^3P_0$ clock state for the shorter wavelength [147]. Choosing the 403 nm over the 497 nm used to be favorable due to the available light sources at the particular wavelengths. Light at 497 nm was generated through frequency doubling of an infrared laser, while laser diodes existed for 403 nm. However, with the recent developments in laser diodes there has been reports of an extended-cavity diode laser able to generate this wavelength [159] which makes the 403 nm even less favorable. Also because close to ultra-violet light suffers from power losses in optical elements more than visible light, making 403 nm even less favorable.

Another option is the mid-infrared transition to $5s4d\,^3D_2$ at 3012 nm. While the enhancement for ^{88}Sr has been measured in the Killian group to be a factor of 10, improvements in the vacuum quality of that experiment resulted in a factor of 25 enhancement for ^{84}Sr [150]. However, this midinfrared wavelength is challenging due to the availability of sources and detectors and the poor transmission properties of viewports [160]. But then again, the large wavelength can be exploit for interesting physics, and could for instance be used to detect Dicke superradiance [161], see Ch. 1 Sec. 1.3.

Repumping through doubly excited states

The wavelength 481 nm excites the atoms from the metastable state $5s5p\,^3P_2$ to the doubly excited state $5p5p\,^3P_2$. While we investigated this repumper laser[3] in our experiment, it is used in the group of Prof. T. Killian at Rice university [151] and has been studied by F. Hu *et al.* in [152]. From the excited state, atoms decay to $5s5p\,^3P_{J=1,2}$ states with a ratio of approximately 3 : 1. There is a small fraction that ends up in the $^3P_0$ state. For the enhancement we have measured around an order of magnitude increase in atom number, while a factor of 20 is reported in [152].

So far, the 481 nm has been reported as a stand-alone solution. In our experiment, we investigate the combination with repumper lasers of the clock state $^3P_0$. On the one hand, we test the transition to the doubly excited level $5p5p\,^3P_1$ with wavelength of 474 nm, reported in [153], as suggested by [152]. We observe a factor 1.3 increase for ^{88}Sr atoms when repumping with 2 mW of 474 nm light compared to only applying the 481 nm repumper. This confirms that the clock state is populated during repumping with 481 nm. It is not clear that this is the highest performance of the transition since in these tests we were limited in power and stability of the frequency of the laser. On the other hand, there is the more common wavelength for repumping the clock state which is at 679 nm. It uses the $5s6s\,^3S_1$ for repumping. For the isotope ^{88}Sr we also

[3] Toptica External cavity diode laser DL pro, with #LD-0488-0060-2

reported on a factor of 1.3 enhancement [116] which appears to be limited by two-body losses. However, for the less abundant isotope ^{84}Sr, we observe a factor of around 5 improvement using powers of several milliwatts on the atoms.

Repumping at 707 nm

The short-lived $5s6s\,^3S_1$ has been explored as repumping transition already by T. P. Dinneen *et al.* in 1999 [154] using 707 nm light. It has a short lifetime of 16 ns and decay channels to all the ^3P_J states, with $J = 0, 1, 2$. This is why it is required to combine it with a repumper laser that recovers the atoms from the clock state $J = 0$. Combining the 707 nm with the previously mentioned 679 nm laser is probably the most common approach for repumping and results in a factor of 10 improvement [154, 145]. Other clock-state repumper lasers have shown even better efficiencies. The combination of the 707 nm with the 483 nm which excites the atoms to the $5s5d\,^3D_1$ state enhances the atom number by a factor of 13 [155]. Another option has shown a factor of 15, with mid-infrared light at 2.6 µm exciting to $5s4d\,^3D_1$ [156].

In our experiment, we have tested the combination of 707 nm laser [4] with a 679 nm laser[5] for ^{84}Sr. Without repumper laser we are not able to detect atoms in absorption imaging. Therefore, we compare the atom numbers for the two red repumpers with the ones obtained by repumping with 481 nm and the 679 nm clock repumper. We find that both methods are comparable in repumping efficiency for the bosonic isotope.

Repumping the intermediate D-state

Atoms cycling on the blue MOT transition fall into the metastable state $^3P_2$ through the $5s4d\,^1D_2$ state, see Fig. 2.5. The lifetime of this intermediate D-state is on the order of 100 µs [162], a time during which the atoms are not addressed by the cooling light. J. Samland *et al.* [157] demonstrate repumping of this intermediate state directly through the higher lying $5s8p\,^1P_1$ state. The majority of atoms either decay back to the $^1D_2$ state or to the ground state with a fraction of around 10 % passing through higher excited $^1S_0$ states. All of the processes involved happen within 100 ns. The performance has been tested on the atomic flux from a 2D MOT, which increased by 60 % when introducing 16 mW of 448 nm repumper light [157].

This transition presents an interesting candidate for repumping during fluorescence imaging on the 461 nm transition, in particular for wavelengths used for optical tweezers where the D-state is anti-trapped, for example 515 nm [115, 163]. However, even though 96 % of the atoms are expected to be repumped efficiently, the remaining percentage will take a slower path or decay to the metastable triplet states.

Repumping of the fermionic isotope

The fermionic isotope with its hyperfine structure poses an additional challenge for efficient repumping. The metastable state $5s5p\,^3P_2$ is split into five hyperfine levels

[4] MOGlabs External cavity diode laser DLC202/HC, with 750LD30.
[5] Toptica External cavity diode laser DL pro, with #LD-0685-0050-AR-1.

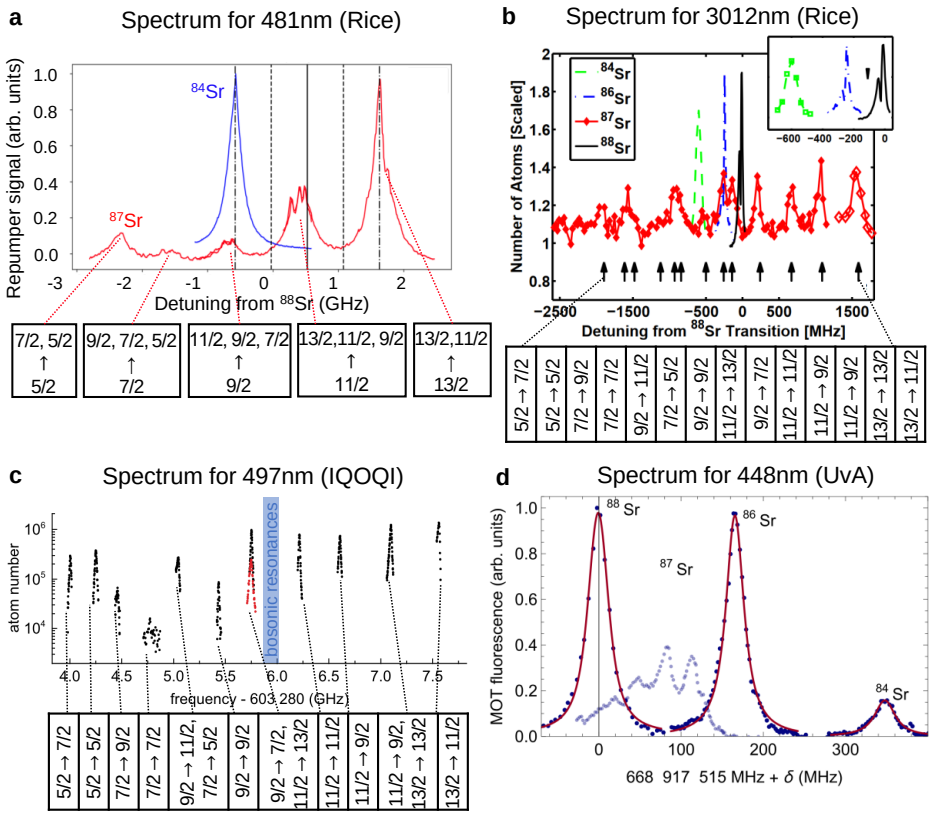

Figure 2.6: Spectroscopy measurements of different repumping transitions from literature. **a** Spectrum of 481 nm for ^{84}Sr and ^{87}Sr discussed in [164]. Applying sidebands with an EOM allows addressing several of the transitions, indicated with the black vertical lines. **b** Spectrum for the 3012 nm repumper transition showing a similar range of few gigahertz [150]. **c** The repumper at 497 nm shows a similar spectral range as in **b**. The relative position of the bosonic isotopes is shown by the blue shaded area [147]. **d** The D-state repumper at 448 nm has an significantly smaller splitting of the hyperfine states in contrast to the other transition [157]. Figures are adapted from [164, 150, 147, 157].

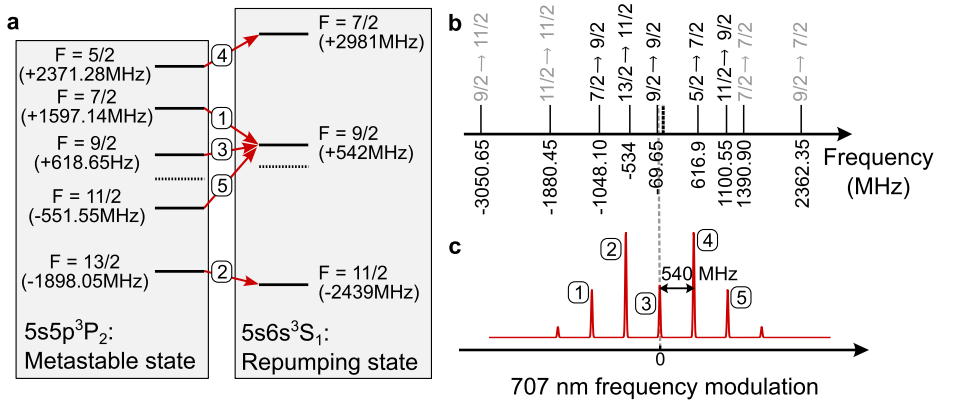

Figure 2.7: Method to repump the fermions with the 707 nm repumper. **a** The states involved in repumping from the $5s5p\,^3P_2$, metastable state, to the $5s6s\,^3S_1$ contains several hyperfine states. Atoms falling into the metastable state during the blue MOT populate all the different hyperfine states $F = 5/2$, $7/2$, $9/2$, $11/2$ and $13/2$, all of which need to be repumped. **b** The possible repumping transitions for the different hyperfine states span a range of around 5 GHz. The values are given with respect to the ^{88}Sr resonance. In order to repump all the F-states, we follow the idea of [165] and use an EOM with a modulation frequency of 540 MHz for the 707 nm laser. A schematic of the spectrum is shown in **c**, it allows the repuming of all the hyperfine levels from the metastable state via the transitions indicated with arrows in **a**. This figure is adapted from [165] and [125].

with quantum number $F = 5/2$, $7/2$, $9/2$, $11/2$ and $13/2$ spanning a range of few gigahertz, see Tab. 2.4. For efficient repumping it is crucial to address all of these transitions. Spectroscopy measurements for different repumping wavelengths have been performed in other groups and reported in literature, see Fig. 2.6. In order to repump efficiently it is not necessary to address all possible transitions. Instead, it is sufficient to excite each of the F-states of the metastable state.

The spectrum of the 481 nm repumper, presented in [164], shows that for this transition the hyperfine splitting in the metastable state dominates the spectrum. In Fig. 2.6a, there are five peaks corresponding to the five hyperfine states and they exhibit a small substructure arising from the hyperfine splitting of the doubly excited state, see for example the peak corresponding to $F = 11/2 \rightarrow F' = 13/2$, $11/2$, $9/2$. The full range of the spectrum covers around 4.5 GHz. In order to repump the different states and also different isotopes in mixture experiments, in the Killian group at Rice University, they use an electro-optical modulator (EOM) with a modulation frequency around 550 MHz [164], however this does not cover the full spectrum.

The repumping spectrum at 3012 nm (Fig. 2.6b) and the one at 497 nm (Fig. 2.6c) span a range of around 3.5 GHz [150, 147]. Covering the full spectrum with an EOM will be challenging in particular because the excitation of the $F = 5/2$ and the $F = 13/2$ are on opposite ends of the transition, see 2.6b and c. In conclusion, these three transitions are not great options if it is about recovering all of the atoms from the metastable state.

A different story applies when repumping from the intermediate D-state directly. Even though the $5s4d\,^1D_2$ state has also five hyperfine states, the spectrum for the fermions spans only around 150 MHz [157], see Fig. 2.6d. Therefore, repumping for the fermions is expected to be simpler because the spectral range can be covered more easily, but this has yet to be tested.

In our experiment, we exploit the 707 nm repumper laser for the fermions together with the 679 nm clock repumper. The clock state $^3P_0$ has no hyperfine levels and therefore does not require modulation of the repumper laser. The splitting of the hyperfine levels for the metastable state $^3P_2$ and the repumper state $^3S_1$ are shown in Fig. 2.7a with the frequency shift with respect to an assumed bare state calculated by S. Stellmer in [125]. T. Yang *et al.* studied the relative frequencies for the excitations of all the different hyperfine states with respect to the 707 nm-repumping transition of ^{88}Sr. In their work [165], they present a modulation scheme with an EOM to repump all the F-states of the metastable state, see Fig. 2.7b and c. Following their example, we implement an EOM[6] with a frequency generator[7] modulated at 540 MHz which allows us to excite all the hyperfine states of $^3P_2$ with at least one transition. This method allowed us to detect five million atoms in the blue MOT for the fermions, while we would not detect any signal in absorption without repumper lasers.

Conclusion

Considering the different results on repumping stontium atoms which have been presented during the past years there are various options performing comparably. To consider are the specific applications of the experiment and on a more technical side the required lasers. The option of having an external cavity laser diode is an advantage because it makes the experiment simpler. Furthermore, it is preferable to have rather only one than two repumper lasers. However, we have seen that while 481 nm works well by itself, the gain we achieved by adding the clock repumper laser was significant in our experiment. In the end, we compared the atom number when using the 481 nm repumper with the clock repumper at 679 nm versus using the two red 707 nm repumper with the clock repumper. In both cases we detect around 3×10^6 atoms, thus we conclude that both repumping schemes are equally suitable for our application.

For the fermionic isotope, the same transitions as for the bosonic ones are an option. Addressing all the hyperfine states presents an additional challenge. But if the atom number is not a limiting factor, repumping just one or two F-states can be sufficient. We have seen that the best choice for us is to repump all the hyperfine states with the 707 nm transition. In this way we achieved around 5×10^6 atoms, where we also were shielding the atoms from losses during the blue MOT as discussed in the following section.

[6] QUBIG resonant electro-optic phase modulator, PM-Sr_0.54
[7] Windfreak SynthNV with frequency range 34MHz - 4.4GHz, max power 19dBm

2.2.3 Resonant shielding during the blue MOT

Increasing the number of atoms without additional complexity of an experiment is a desirable goal, especially to reach quantum degeneracy in compact systems. Improvements can be achieved by building more efficient sources [138, 166, 165, 141] or implementing strategies to reduce losses. This is particularly relevant for the laser cooling steps involving the blue transition because it is not closed, see Fig. 2.3. As discussed in the previous section, adding repumper lasers on carefully chosen transitions allows to increase the atom number, but the additional lasers can be a costly solution, they increase the complexity of the experiment and they are limited in their efficiency. Another method is to accumulate the atoms in a reservoir state. As discussed in Sec. 2.1.2, there is a magnetically trapped state at $^3P_2$ which has been exploited as a reservoir in the first realization of strontium Bose-Einstein condensates [117, 118]. However, this comes at the expense of increased cycle time. To develop other methods, we can gain inspiration from alkali atoms where a so-called dark spot MOT was used to reduce losses [167, 168]. In a small region of the MOT, the atoms are put in a hyperfine ground state which does not interact with the trapping light, therefore the name dark spot MOT. This allows to overcome the density limit of the MOT caused by collisions between ground state and excited state atoms and radiation pressure of re-emitted photons form trapped atoms. This method cannot be directly transposed to strontium due to the lack of a hyperfine structure in the ground state of the bosonic strontium isotopes. But one can find another scheme which also uses reduction of losses by storing the atoms in another state. We call it shielding and it uses an excited state of the ^3P_J manifold.

To put it briefly, during the blue MOT we address the atoms with the narrow-linewidth transition (689 nm) on resonance. By exciting the atoms into the $^3P_1$ state we shield them from losses of the blue transition and consequently enhance the atom number by a factor of two. The advantages of this method are that it does not require new lasers, no long accumulations in reservoir states and is also not density dependent. In the following section, a schematic explanation of the shielding effect is presented and the efficiency is quantified through characterization of loading and loss rates in different configurations, including different strontium isotopes and changing repumper configurations. A detailed theoretical explanation of our method can be found in the PhD thesis of J. Höschele [119]. The results of this section are presented in our publication [116].

Dynamic study of resonant shielding

The shielding effect can be understood by looking at the dynamics displayed in Fig. 2.8. The measurement displays a state dependent detection for ^{88}Sr where the total atom number in the system is measured through absorption imaging and the number of atoms cycling on the blue transition is given through blue fluorescence detected with a photomultiplier[8] and a 461 nm interference filter placed in front of it. In a first stage,

[8] Photosensor module H107021-210 with PMT from Hamamatsu, spectral range 230 nm - 700 nm

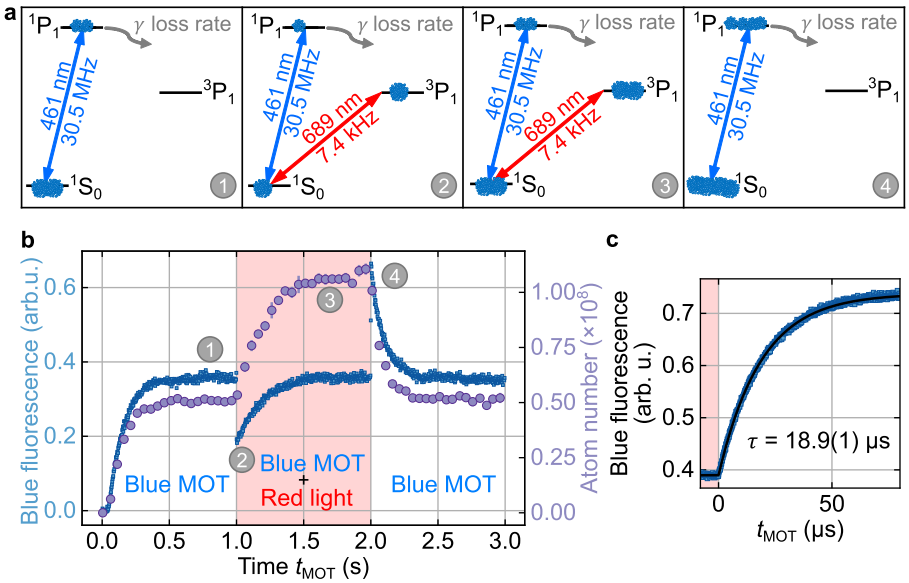

Figure 2.8: Dynamics measurement of the resonant shielding for ^{88}Sr. **a** Schematic explanations of the processes leading to the signal shown in b and c. **b** The fluorescence signal measured versus time provides information about atoms cycling on the blue MOT transition and the total atom number in the system is measured by means of absorption imaging. During the time $t_{\mathrm{MOT}} = 1\,\mathrm{s}$, the blue MOT is loaded and both fluorescence and atom number reach a steady state because the atoms cycling on the blue transition are exposed to losses (loss rate γ), see the schematic (1). Switching on red light on resonance (2) excites half of the atoms into the $^3P_1$ state, thus reducing the fluorescence signal without affecting the total atom number. After $t_{\mathrm{MOT}} = 2\,\mathrm{s}$ the steady state for the shielded blue MOT is reached, the fluorescence signal is at the same value as at $t_{\mathrm{MOT}} = 1\,\mathrm{s}$, but the total atom number is doubled due to atoms populating the $^3P_1$ state, see (3). **c** A sudden switch off of the red light causes these atoms to decay and return to cycling on the blue transition which results in a burst of fluorescence, see also (4). We fit the rise of the fluorescence signal exponentially and find a time constant of 18.9(1) µs which is comparable to the lifetime of the excited state 21.28(3) µs [169]. The measurement was performed with continuously loading of the MOT and constantly repumping the $^3P_2$ state.

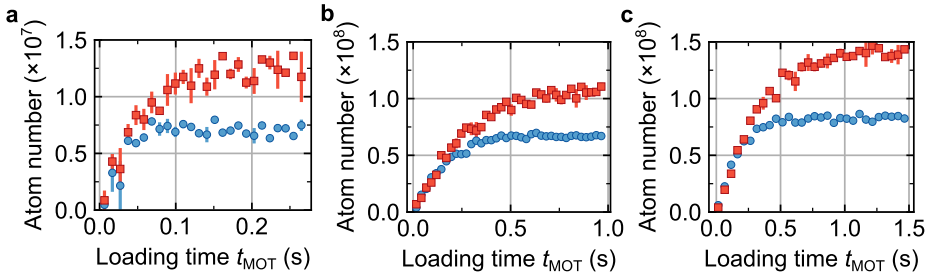

Figure 2.9: Loading curves for ^{88}Sr in three different density regimes by applying different repumping configurations. **a** No repumper lasers (enhancement of $\eta \approx 1.76$), **b** Repumping $^3P_2$ with 481 nm ($\eta \approx 1.64$) and **c** repumping additionally with 474 nm the $^3P_0$ state ($\eta \approx 1.74$). The shielding was not optimized in this measurement, and yet the enhancement performs comparably for all three configurations.

Red	Loading rate	Loss rate
✗	$2.4(3) \times 10^8\,\mathrm{s}^{-1}$	$34(5)\,\mathrm{s}^{-1}$
✓	$2.4(2) \times 10^8\,\mathrm{s}^{-1}$	$19(2)\,\mathrm{s}^{-1}$

Table 2.6: Loading and loss rate for ^{88}Sr without repumping lasers. The values correspond to the data shown in Fig. 2.9a fitted with Eq. (2.2). The loading rate is the same with and without the red shielding light, but the losses decrease to around $19\,\mathrm{s}^{-1}$.

we load the atoms into the continuously repumped blue MOT without red light. The atoms pushed into the science chamber cycle on the blue transition while some of them are lost. Within $t_{\mathrm{MOT}} = 1\,\mathrm{s}$ a steady state is reached, where the fluorescence signal as well as the total atom number saturate. At this time, we switch on the red light on resonance. Some of the atoms in the blue MOT start cycling on the red transition, which causes a decrease in the fluorescence signal but no change in atom number. Since we are still loading atoms into the MOT, eventually the fluorescence signal recovers but along with it the atom number enhances by a factor of $\eta = 2.08(15)$. From the fluorescence signal we can estimate that 47(1) % of atoms are in the $^3P_1$ state. Then at $t_{\mathrm{MOT}} = 2\,\mathrm{s}$ we suddenly switch off the red light. A flash in the fluorescence signal arises and the atom number starts decreasing. We attribute this to the decay of atoms from the $^3P_1$ back to the ground state and therefore being exposed to the blue transition. To confirm this theory, we fit the flash of the fluorescence signal exponentially and find a time constant $\tau = 18.9(1)\,\mu\mathrm{s}$, which is compatible with the lifetime of the $^3P_1$ excited state of $21.28(3)\,\mu\mathrm{s}$ [169], see Fig. 2.8c. This is evidence that the atoms are doubled because of the excitation into the $^3P_1$ state where they are no longer exposed to the losses associated with the blue cooling transition.

Loading and loss rates

For more quantitative statements about the atom number enhancement in the blue MOT, we describe the change in atom number N over time by means of a rate equation:

$$\frac{dN(t)}{dt} = L - (\gamma + \beta n_c)N(t). \tag{2.1}$$

The loading rate L depends on the capture efficiency of the blue MOT and consequently also the performance of the 2D MOT and the pushing into the science chamber (Fig. 2.2). Here, we have considered that the atoms experience losses of two types: one-body, indicated by the loss rate γ and corresponding to the atoms leaking into the D-state (Fig. 2.3) and two-body indicated by the loss rate β [170], and corresponding to light-assisted collisions which depend on the MOT density n_c. If we don't apply repumper lasers during the MOT loading, we reduce the density n_c and the two-body losses can be neglected, thus Eq. (2.1) simplifies to

$$\frac{dN(t)}{dt} = L - \gamma N(t). \tag{2.2}$$

For a detailed theoretical discussion including high-density regimes and two-body losses we refer to the appendix of our publication [116] and the PhD thesis of J. Höschele [119].

We fit a blue MOT loading curve, see Fig. 2.9a, which was measured without repumper lasers, to the rate equation Eq. (2.2). The results for the loading and the loss rate are summarized in Tab. 2.6. Indeed the loss rate is the main cause of the change in atom number while the loading rate stays constant whether we use the red shielding effect or not.

Furthermore, we confirm that the enhancement η of the shielding arises independent from the nature of the losses as expected [170, 116]. To this end, we probe the loading of the MOT in different density regimes which effectively means different loss regimes. The low-density blue MOT from Fig. 2.9a has an enhancement consistent compared to the high-density MOT where we repump the atoms form the metastable state, see Fig. 2.9 b. Adding a repumping laser for the clock state does not alter the result either, see Fig. 2.9c. The shielding frequency and intensity in these particular measurements was not optimized which is why the enhancement is less than the one reported in [116]. However, the shielding proves to be resistant against overall drifts of the system as all three curves in Fig. 2.9 reveal comparable enhancement values despite the vastly different densities in the trap.

Shielding for different isotopes

We observe shielding for all the stable isotopes of strontium. The least abundant among the four is ^{84}Sr, however, it is a preferable candidate for Bose-Einstein condensation due to its favorable scattering properties [124, 171, 117]. We can compare its loading curve with the one of ^{88}Sr, see Fig. 2.10. We achieve an atom number enhancement of $\eta = 1.85(2)$ comparable to the one of ^{88}Sr. This increase in atom number

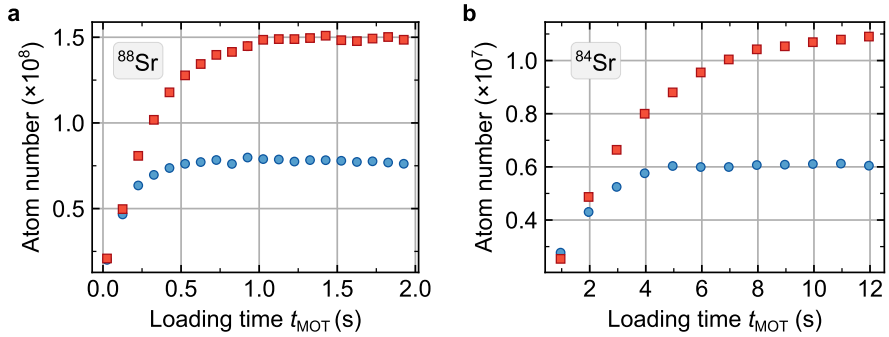

Figure 2.10: Shielding for bosonic isotopes. **a** The most abundant isotope ^{88}Sr with 481 nm and 679 nm repumpers. We observe an enhancement of $\eta \approx 1.94$. **b** For ^{84}Sr with both repumpers we measure an enhancement of $\eta \approx 1.84$, see also [116]. The differences in final atom number and loading time can be traced back to the natural abundance, which is 82.58(1) % for ^{88}Sr and 0.56(1) % for ^{84}Sr, see Tab. 2.1.

is conserved in the consecutive cooling steps all the way to the optical dipole trap and thus sets improved initial conditions for evaporative cooling to quantum degeneracy.

Finally, we demonstrate the shielding for the fermionic isotope which is an interesting candidate for experiments of SU($N \leq 10$) physics thanks to its large nuclear spin of $I = 9/2$, see Sec. 2.1.1. The nuclear spin is also responsible for the hyperfine structure that splits the $^3P_1$, which is used for the resonant shielding. All three hyperfine states can shield the atoms from losses in the blue MOT. As shown in Fig. 2.11, we combine the effect of shielding in the $F = 11/2$ state with the one of $F = 9/2$ and increase the atom number accordingly. Those two transitions are commonly present in fermionic strontium experiments, as they are required for the following cooling stages, see Sec. 2.3.

Modulation of the shielding laser frequency has not shown any benefit, see Fig. 2.12 for ^{87}Sr. Our understanding is that since we intensity-broaden the transition by oversaturating it, the modulation is not adding to the shielding. More power would be needed to increase the effect further, especially for the fermionic isotope where the m_F-states in the MOT magnetic field are split due to the Zeeman effect (Appx. A.1) and we have observed better enhancement for the less Zeeman-split state $F = 9/2$.

Conclusion

For the shielding, we exploit the six beams used for the red MOT cooling stage, described in the next section. But a single beam with comparable intensity would be sufficient. The intensity of all six beams is $8.3 \times 10^4\, I_{s,\,red}$, with $I_{s,red} = 2.96\,\mu W/cm^2$, for beams with radial $1/e^2$ beam waist of around 2.16 mm and 3 mW power per beam. This leads to intensity broadening and allows us to shield the atoms over the full range of the blue MOT. In J. Höschele's Ph.D. thesis [119], further measurements are discussed which confirm that it is indeed a resonant effect.

There are two constraints of our shielding method. On the one hand, the loading time increases through the shielding. This is because the loading rate of the blue

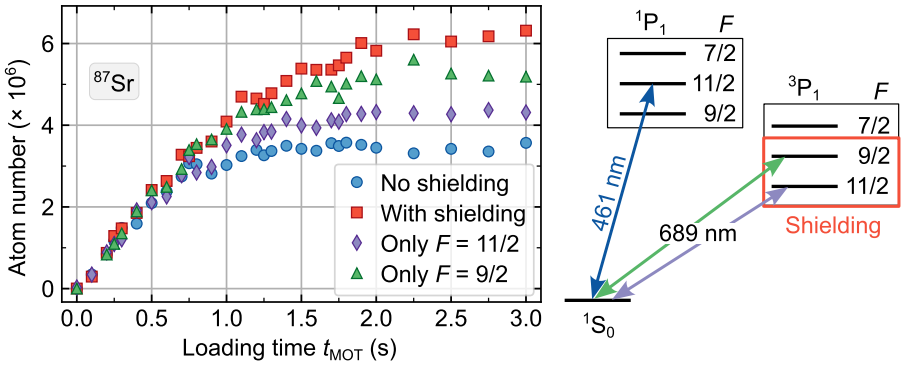

Figure 2.11: Loading curves of fermionic ^{87}Sr for different shielding configurations. The loading rate is similar for all four curves. The final atom number increases by adding red light for the $F = 11/2$ hyperfine state (purple diamonds) and even more if we use instead the $F = 9/2$ (green triangles), which is due its smaller Zeeman broadening (Appx. A.1). Applying the two at the same time accumulates the effects of both (red rectangles).In these curves, we apply three repumper lasers 481 nm, 679 nm and 707 nm, which is not required but resulted in the largest atom number.

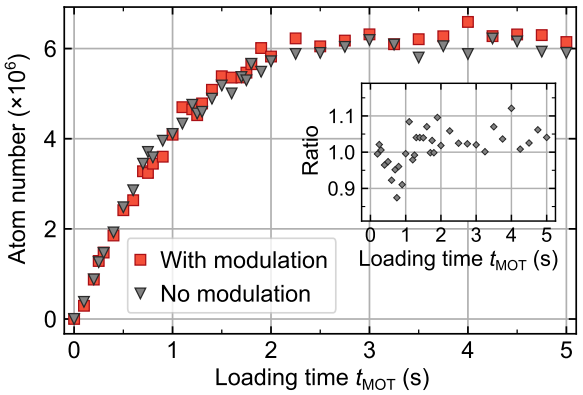

Figure 2.12: Modulating the red laser during shielding of the fermionic isotope ^{87}Sr. We compare the loading into the blue MOT with a modulation of the 689 nm light (red rectangles) to no modulation (back triangles). We modulate the frequency around resonance with an amplitude of 10 MHz peak-to-peak, and a modulation frequency of 20 kHz. The inset shows the ratio between shielding with and without modulation. The effect is not significant.

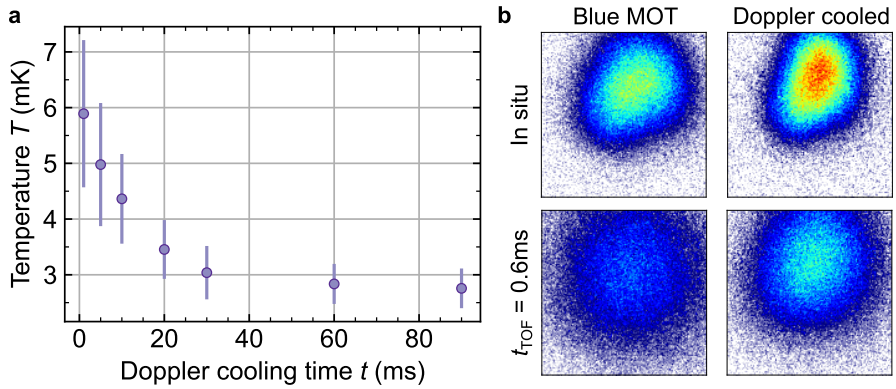

Figure 2.13: Temperature of the blue MOT extracted from time of flight measurements after a final Doppler cooling stage. From the expansion of the cloud detected in the absorption images we estimate the temperature reached for different durations of the Doppler cooling stage. The large error bars arise due to the difference in horizontal and vertical expansion times t. Doppler cooling reduces the temperature of the atoms by few millikelvin resulting in better transfer into the red MOT, see main text. On the right, example absorption images ($2.5 \times 2.5\,\mathrm{mm}^2$) are displayed, with in situ and 0.6 ms time of flight (TOF) before and after Doppler cooling.

MOT stays the same only the loss rate is reduced through resonant shielding on the red transition. On the other hand, experiments that rely on metastable state reservoir will not benefit form shielding. Their goal is to load many atoms into the metastable state such that their performance depends on the losses through the D-state into the metastable states. Despite those limitations, the effect has great potential. Most strontium experiments have already implemented the red laser because it is used for further laser cooling. It is therefore a simple way to double the atom number in the experiment.

2.2.4 Doppler cooling in the blue MOT

Above we have discussed how we improve the atom number in the blue MOT. In addition, it is desirable to reach low temperatures in this stage because it reduces atom losses in the transfer to the next cooling stage. While sub-Doppler cooling cannot be applied for bosonic strontium due to the lack of a hyperfine structure in the ground state, we can exploit the peculiarities of the Doppler cooling. The temperature and density of atoms trapped in a blue MOT can be further reduced by decreasing the intensity and the absolute value of the detuning of the blue MOT beams. The temperature limit is given by the Doppler temperature $T_\mathrm{D} = \hbar\Gamma_\mathrm{blue}/(2k_\mathrm{B}) \approx 720\,\mu\mathrm{K}$, which is proportional to the linewidth of the transition $\Gamma_\mathrm{blue} \approx 2\pi \times 30.5\,\mathrm{MHz}$, see Tab. 2.2.

We study the result of this decrease by measuring the temperature of the blue MOT, see Fig. 2.13. If we keep the blue MOT parameters constant, we measure temperatures around 7.5 mK from the vertical expansion during a short time of flight

of around 1 ms. If we linearly decrease the detuning of the blue MOT from $-1.5\,\Gamma_{\mathrm{blue}}$ to $-1.0\,\Gamma_{\mathrm{blue}}$ and at the same time linearly reduce the power to zero, while leaving the magnetic quadrupole field constant, we can reduce the temperature to around 3 mK while the atom number does not change. We find that 30 ms for the ramp is enough to reduce the temperature. We achieve a transfer of 600 000 atoms into the next cooling step, the red MOT, in contrast to around 300 000 atoms without the linear decrease of the blue light parameters. While this is for the bosonic isotope ^{84}Sr, we find a similar decrease in temperature for the fermions, where we measure around 3.3 mK in the blue MOT and 1.7 mK after Doppler cooling.

2.3 Red MOT: from milli- to microkelvin

Following the blue MOT is a so called red MOT, see Fig. 2.1. The name stems from the laser wavelength used which is with 689 nm in the red spectrum. The transition is the same as we use for the shielding in Sec. 2.2.3 and excites an atom from the ground state $5s5s\,^1S_0$ to the excited state $5s5p\,^3P_1$. The temperatures that can be achieved with the two different MOT transitions are several orders of magnitude different. While we measure few millikelvin for the ^{84}Sr blue MOT, we find microkelvin cold clouds for the red one. This arises due to the orders of magnitude difference in their linewidths, see Tab. 2.2. For the blue MOT this results in a temperature limit for the MOT given by the Doppler temperature $T_{\mathrm{D}} = \hbar\Gamma_{\mathrm{blue}}/(2k_{\mathrm{B}})$. For the red transition, the Doppler temperature is around 4100 times smaller, in fact it is even smaller than the red recoil temperature ($T_{\mathrm{recoil}} = \hbar^2 k_{\mathrm{red}}^2/(mk_{\mathrm{B}})$, with $k_{\mathrm{red}} = 2\pi/\lambda_{\mathrm{red}}$). Therefore, the temperature limit for the red MOT is the recoil temperature, more specifically $T_{\mathrm{recoil}}/2$. This makes the red MOT a powerful tool to reach low temperatures and thereby prepare the atoms for the following cooling step of evaporative cooling, which will be presented in Sec. 2.4.

In this section, the challenges and benefits arising from the narrow-linewidth transition will be discussed. To this end, we discuss first the broadband red MOT and the method of sawtooth waveform adiabadic passage used to capture the relatively hot atoms from the blue MOT with the red light. Then, we explain the challenges of the single-frequency red MOT used to reach microkelvin temperatures. They arise, on the one hand, from the narrow-linewidth of the transition and, on the other hand, from the splitting of the substates in the hyperfine levels of the fermionic isotope.

2.3.1 Broadband red MOT

The kilohertz linewidth of the red transition is too narrow to capture the atoms from the millikelvin cold blue MOT. To circumvent this issue, the frequency of the red MOT is broadened by means of frequency modulation which allows us to address more velocity classes, as it overcomes the different Doppler shifts. Thus the capture efficiency of the red MOT increases.

One method that exploits frequency modulation in a more involved scheme is the sawtooth waveform adiabatic passage (SWAP) method [172, 173]. It uses the two-level

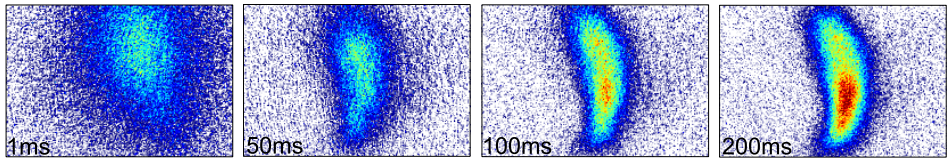

Figure 2.14: Cooling process of ^{84}Sr atoms in a broadband red MOT showing snapshots at different times of the cooling. The cooling is achieved by applying a 20 kHz sawtooth frequency modulation to the frequency carrier of the red MOT beams with 4 MHz peak-to-peak amplitude, 2.05 MHz red-detuned from resonance. The elongated shape most likely arises as a result of the anisotropic magnetic field gradient from the quadrupole as well as an imbalance in the MOT beam powers. The four absorption images have all the same color scale and display an area of $3.7 \times 2.5\,\mathrm{mm}^2$.

system between the ground state and the $m_J = 0$ magnetic Zeeman sublevel of the $^3\mathrm{P}_1$ state. Two counterpropagating beams are frequency modulated with a sawtooth waveform swept across resonance. An atom absorbs a photon from the beam antiparallel to its motion and is deexcited through stimulated emission with the beam from the opposite direction. In this way, the momentum of the atom is reduced by two photon recoils during one sweep, see the PhD thesis of M. A. Norcia [174] for a detailed explanation. The SWAP method combined with a magnetic field gradient, a so called SWAP MOT [174], no longer benefits from the stimulated emission but still makes use of the sawtooth waveform in contrast to a triangular one. In the study of the SWAP cooling in a MOT by S. Snigirev *et al.* [175] they discuss how the sawtooth method is more robust and efficient than a triangular waveform for the broadband red MOT.

In our experiment, we cool more atoms with the sawtooth waveform compared to the triangular one, but we are not crossing the resonance during the SWAP MOT. We modulate the frequency with a sawtooth at 20 kHz with a peak to peak amplitude of 4 MHz and the center frequency −2.05 MHz from resonance. We investigate the shape of the atomic cloud during the broadband red MOT by taking absorption images at different times, see Fig. 2.14. For this measurement we set the magnetic field gradient to 5.4 G/cm and we keep the power of the red MOT beams constant at around 3 mW per beam. We see how the cloud gets denser with longer times and we find that the number of atoms does not change during the process.

Typically, the broadband red MOT lasts 150 ms during which we reduce the power of the red from the initial 3 mW to around 1 mW per beam with 2.16 mm $1/e^2$ Gaussian beam waist. Then we switch off the modulation to operate the MOT with a single frequency. In the past, we have been operating a 20 ms broadband MOT followed by 20 ms during which we reduce the modulation amplitude and shift the zero towards resonance, also reducing the power. We ended with a 100 ms single frequency stage. We have seen that the performance for both methods is comparable. However, the first one mentioned is simpler to optimize as there are less parameters involved and it only consists of the broadband and the single frequency stages.

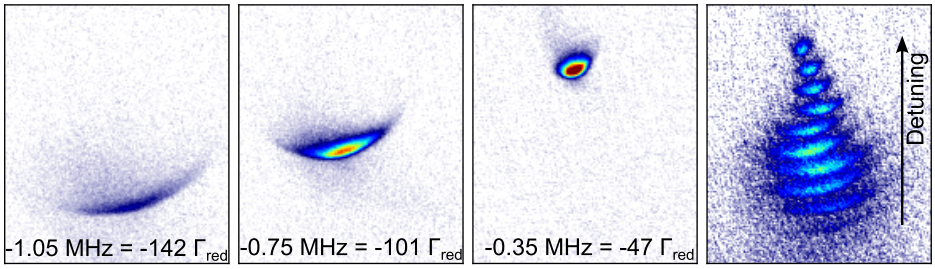

Figure 2.15: A single frequency red MOT of ^{84}Sr at different detunings, indicated in the bottom corner of the absorption images. This is at a gradient of 5.4 G/cm, with 150 ms of broadband stage before going to single frequency for a duration of 30 ms. In the most right image sequential single frequency red MOTs at different detunings are displayed, which where obtained in different realizations of the experiment. It shows how the red MOT shifts its position and shape when stepping the detuning closer to resonance. The picture shows normalized red MOTs in order to have same brightness for display purposes. The dimension of the pictures in real space is $2.1 \times 2.5\,\mathrm{mm}^2$.

2.3.2 Single-frequency red MOT

Finally, the microkelvin temperature of the red MOT is reached through narrow-line cooling [176, 177, 178] after switching off the frequency modulation. For the bosonic ^{84}Sr atoms, the resonance changes spatially due to the Zeeman shift caused by the magnetic field gradient, see Fig. 2.16a. We address the atoms on the narrow-linewidth transition $\Gamma_{\mathrm{red}} \approx 2\pi\times 7.4\,\mathrm{kHz}$ with a beam that is hundreds of kilohertz red-detuned from resonance. Due to the narrow-linewidth, the atoms are only cooled in the shell of the magnetic field gradient where they are near-resonant with the MOT beams, see Fig. 2.16a. Furthermore, the acceleration due to gravity is comparable to the one from scattered photons. Therefore, the atoms in the red MOT are affected by gravity and populate the bottom of the trap, which results in the typical half moon shape of the bosonic red MOT, displayed in Fig. 2.15. This figure also shows nicely how the position and the shape of the red MOT are affected by the detuning. Approaching resonance moves the atoms closer to the magnetic field zero and reduces the radius of the cooling shell.

2.3.3 Fermionic red MOT

The fermionic isotope ^{87}Sr has ten spin states arising from the nuclear spin $I = 9/2$, see Sec. 2.1.1. This provides fascinating properties for quantum simulation experiments, however, it makes the experiment, and particularly its laser cooling, more challenging. For the blue transition the hyperfine states are split by only tens of megahertz. This is on the order of the linewidth of the blue transition, such that the performance of the blue MOT is comparable to the one of the bosonic isotope. For the red MOT, the three hyperfine states of the $^3\mathrm{P}_1$ excited state, $F = 7/2$, $9/2$ and $11/2$, are split by around 1 GHz. Thus, they can be addressed individually.

In the $F = 11/2$ of the $^3\mathrm{P}_1$ state, which is used for the red MOT, the Zeeman

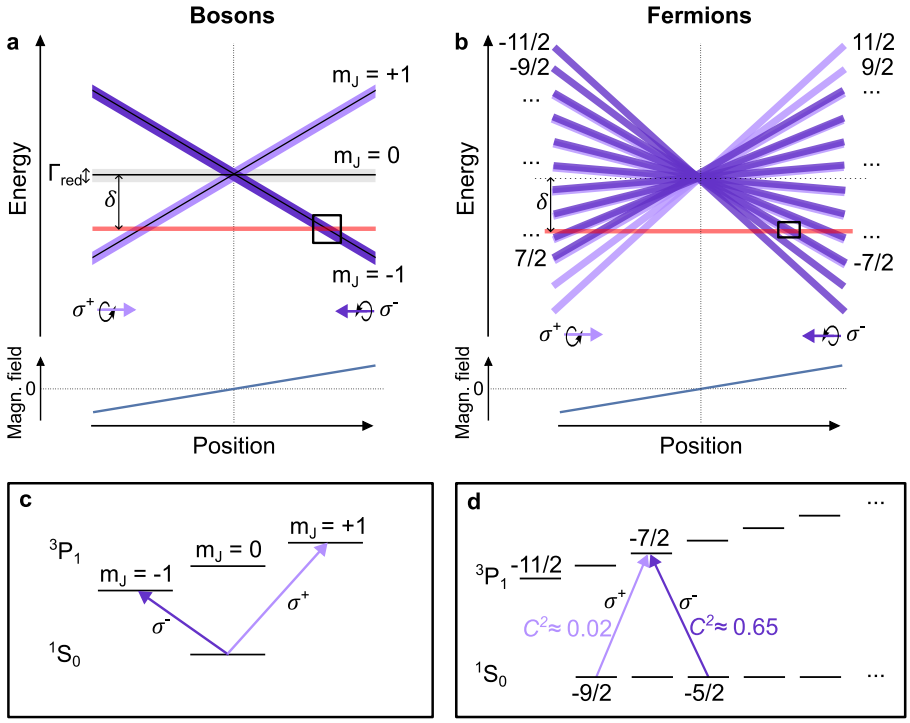

Figure 2.16: The narrow linewidth red MOT shown in a simplified schematic for the bosons **a** and for the fermions **b**. For the bosonic isotope the three m_J states of the $^3P_1$ state are Zeeman split due to the magnetic field gradient, see **c**. The linewidth Γ_{red} which is displayed by the thickness of the m_J-levels in **a**, is smaller than the detuning δ. Consequently, the atoms are addressed only in a small range away from the zero magnetic field value. In the fermionic case **b** and **d**, the excited state has sublevels $m_F = \pm 11/2, \pm 9/2, ..., \pm 1/2$, which are split while the ground state is basically degenerate. As a result, depending on the m_F state of an atom it can be pushed towards or away from zero. For example an atom on the right side of the trap (in the black box) will be excited with σ^+ if it is in $m_F = -9/2$ or with σ^- if it is in $m_F = -5/2$, see **d**. The squared Clebsch-Gordan coefficient C^2 describes the coupling between the different m_F-states of the ground and the excited state.

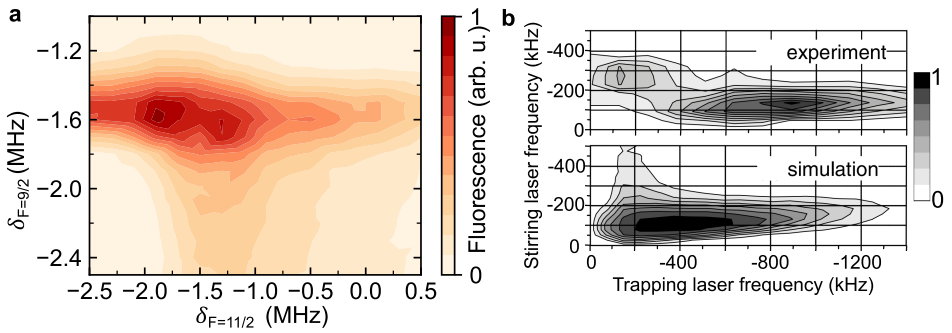

Figure 2.17: The fermionic red MOT depending on the frequency detuning of the trapping ($F = 11/2$) and the stirring ($F = 9/2$) transitions. **a** The measurement was performed with fluorescence imaging and shows the detunings δ_F of the different hyperfine states $F = 11/2$ used for the red MOT and $F = 9/2$ used for stirring. **b** Compared to the simulation and the experiment of T. Mukaiyama *et. al* [179] we find the optimum frequencies at larger detunings. But similar to their report, we also observe that the $F = 11/2$ transition has a larger frequency range where it performs efficiently compared to the $F = 9/2$ of the stirring transition, which is understood by the different splitting of the m_F states for the two hyperfine states, see the Zeeman splitting discussed in Appx. A.1. **b** was adapted from [179].

splitting lifts the degeneracy of the $m_F = -11/2, -9/2, ..., 11/2$ states. Consequently, as displayed in Fig. 2.16b, it is not possible to address all the spin states at the same place with the same frequency. Additionally, some of the atoms are repelled from the trap, as they absorb photons of the beam coming from the *wrong* direction. In a braodband MOT, or in the SWAP MOT, this is not a problem because of the frequency broadening and the probability of the different transitions [174]. The broadened red MOT light addresses all the m_F-transitions, but the probability of the transitions depends on the coupling given by the Clebsch-Gordan coefficient, see Appx. A.2. As displayed in Fig. 2.16d, the transition from $m_{F_g} = -5/2$ to the excited state $m_F = -7/2$ with σ^- is more probable than the excitation of $m_{F_g} = -9/2$ with σ^+ polarized light. Considering all the Clebsch-Gordan coefficients of the m_F-transitions, we find that on average the atoms experience a force towards the center of the trap.

However, in a single frequency fermionic red MOT, we no longer address all the transitions over the full extend of the atomic cloud due to the large splitting in the excited hyperfine state. This means that not all states will be trapped. To still cool the atoms efficiently, we change the spin state of the atoms during the red MOT, mixing them, such that the atoms are likely to populate spin states that can be addressed by the red MOT light. To this end, a stirring beam is implemented [179] which excites the atoms to the $F = 9/2$ state, mixing the spin states and acting as molasses cooling.

We scan the frequency of the stirring laser versus the one of the trapping laser while detecting the number of atoms in fluorescence, see Fig. 2.17. We find that the trapping laser has a larger frequency range where we detect a signal compared to the stirring. This is understood by the vastly different response to the magnetic field given by the different g-factors ($g_{F=11/2} = 3/11$ and $g_{F=9/2} = 2/33$), see Appx. A.1.

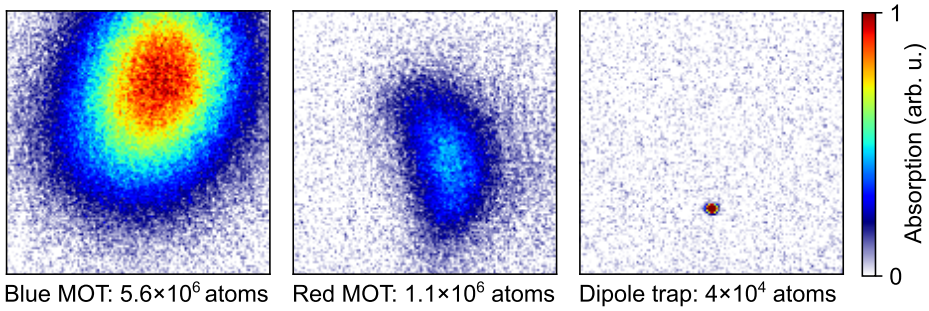

Figure 2.18: Cooling process of the fermions. The temperature reduces from around 2 mK in the blue MOT to 2 µK after the loading of the red MOT into the optical dipole trap.

A similar behavior has been observed in [179] where they studied and discussed the effect of the stirring beam on the fermionic red MOT.

This splitting of the m_F-states through the magnetic field is the reason why the fermions don't arrange in a shell-like shape as the bosons. The single frequency red MOT of the fermions addresses the atoms in the full area of the trap. The cloud has rather an elliptical shape with the edges defined by the magnetic field and the detuning of the laser, see Fig. 2.18.

2.4 Optical dipole trap and light sheet

Strontium can be laser cooled all the way to quantum degeneracy as has been shown by S. Stellmer *et. al* [180]. This reduces vastly the cycle time, but increases the complexity of the experiment through adding extra laser beams such as a dimple and a transparency beam. While this is convenient for the realization of continuous Bose-Einstein condensates or atom lasers [103], in our experiment we follow a different approach.

After reaching microkelvin temperatures in the single-frequency red MOT we load them into a optical dipole trap and a light sheet beam (Fig. 2.1). We improve the transfer from the red MOT to the dipole trap by adjusting the frequency of the red light in order to cool the atoms in the trap. Furthermore, the magnetic field sensitivity of the red MOT allows us to move its position in the desired direction by means of a bias magnetic field. This affects the shape of the red MOT insignificantly since the detuning is not changed. It is a convenient method to align the dipole trap with the red MOT. Once the atoms are in the optical dipole trap, we add the light sheet potential in order to achieve a strong vertical confinement. The potentials of these two traps are discussed in this section and the full cooling sequence to a quantum degenerate cloud is presented for the bosonic isotope ^{84}Sr.

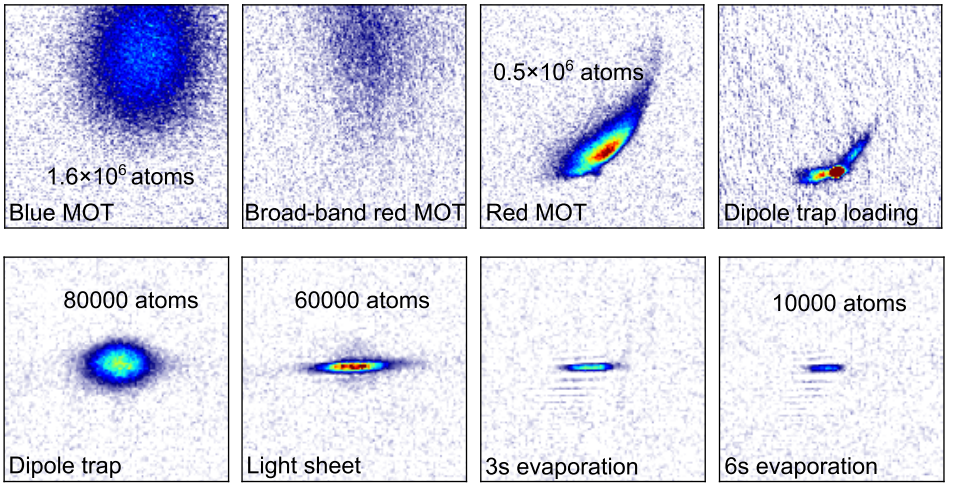

Figure 2.19: In situ absorption images of the different cooling steps on the way to a ^{84}Sr BEC. The top row shows the MOT cooling stages until the loading into the optical dipole trap, the color scale is the same for the four images and the images have a real size of $2.5 \times 2.5\text{mm}^2$. The bottom row displays the optical dipole trap and the light sheet with two evaporation steps. The real size of the images are $0.75 \times 0.75\text{mm}^2$. Since again the color scale is kept constant, it is clear that during evaporation we reduce the atom number. While these are not the optimum atom number of the experiment, it gives an idea of the evolution of the atomic cloud.

2.4.1 Optical dipole trap

The optical dipole trap is created by two in-plane laser beams perpendicular to each other and far-detuned from resonance at $\lambda_\text{L} = 1064\,\text{nm}$. The potential, which the atoms experience, depends on the polarizability α and the intensity $I_j(\vec{r})$ of the two beams as follows

$$V_\text{dip}(\vec{r}) = -V_0(\alpha)(I_1(\vec{r}) + I_2(\vec{r})) + mgz \tag{2.3}$$

where the last term takes into account gravity, with m the mass of a strontium atom, g the acceleration due to gravity and z the vertical position of the atoms. The value of V_0 is proportional to the polarizability and can be described as

$$V_0(\alpha) = \frac{3\pi c^2}{2}\left[\frac{1}{\omega_\text{blue}^3}\left(\frac{\Gamma_\text{blue}}{\omega_\text{blue}-\omega_\text{L}} + \frac{\Gamma_\text{blue}}{\omega_\text{blue}+\omega_\text{L}}\right) + \frac{1}{\omega_\text{red}^3}\left(\frac{\Gamma_\text{red}}{\omega_\text{red}-\omega_\text{L}} + \frac{\Gamma_\text{red}}{\omega_\text{red}+\omega_\text{L}}\right)\right] \tag{2.4}$$

where we consider the blue 461 nm and the red 689 nm transitions with their respective linewidths $\Gamma_\text{blue/red}$ and frequencies $\omega_\text{blue/red}$, and $\omega_\text{L} = 2\pi c/\lambda_\text{L}$ is the frequency of the laser, where c is the speed of light [181].

Furthermore the intensity of the two crossed laser beams I_1 and I_2 is given by the formula for a Gaussian beam. Here an example for a beam propagating along x:

$$I(x,y,z) = \frac{2P}{\pi}\frac{1}{w_y(x)}\frac{1}{w_z(x)}\exp\left(-2\frac{y^2}{w_y(x)^2}\right)\exp\left(-2\frac{z^2}{w_z(x)^2}\right). \tag{2.5}$$

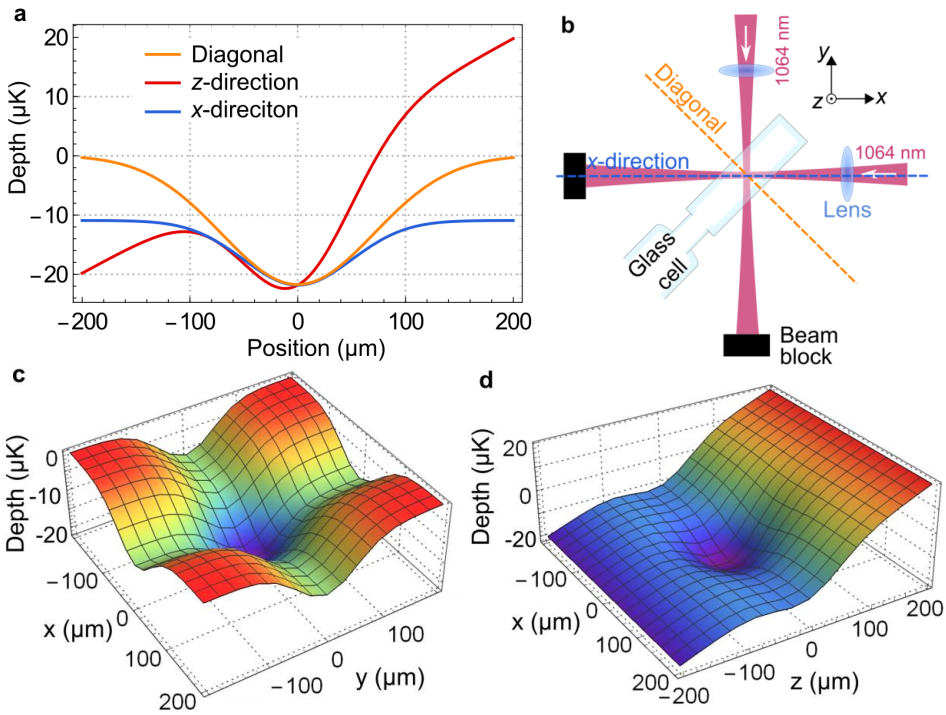

Figure 2.20: Potential created by the crossed optical dipole trap. **a** Depth in microkelvin in different directions of the trap, for 3.3 W per beam. **b** Setup of the optical dipole trap where we indicate the different directions plotted in **a**. We focus the beam with a lens of focal length $f = 200\,\text{mm}$ to a beam waist of 100 µm ($1/e^2$ Gaussian beam waist) and block them afterwards (black rectangle). **c** The beams realize channels of lower potential in their propagation direction. **d** In z-direction the potential is tilted due to gravity.

The intensity maximum $I(\vec{0}) = \frac{2P}{\pi w_{y0} w_{z0}}$ depends on the power P and the beam waists w_{y0} and w_{z0} in y- and $z-$direction, respectively. The waist function is

$$w_j(x) = w_{j0}\sqrt{1 + \left(\frac{x\lambda}{\pi w_{j0}^2}\right)^2}, \text{ where } j = y, z.$$

The beam waist w_{j0} is the radius of the beam at its focus corresponding to an intensity decrease of $1/e^2$ compared to its maximum value.

Applying those formulas, we can calculate the depth of the trapping potential used to load the red MOT atoms into the dipole trap where we use the parameters of our experiment. The 1064 nm light stems from a Nd:YAG laser[9] with a total output power of 25 W. We split the light into two paths and use acousto-optic modulators[10], on the one hand to control the laser power sent to the atoms, and on the other hand to shift the frequency of the two dipole trap beams by several tens of megahertz with respect to each other in order to avoid interference between the two beams. After passing the light through a photonic crystal fiber[11] we focus the two beams to the position of the atoms which are at this stage trapped in the red MOT. The beam waist is around 100 µm (focused with a lens[12] of 200 mm focal length).

We typically for the dipole trap with around 3.3 W per beam, which results in a total trap depth of around 20 µK, see Fig. 2.20. However, along the direction of the beam (for example along x-direction, see Fig. 2.20b), the relative depth is around 10 µK. This is because of the incoming beam, which creates a channel of lower potential, which is nicely displayed in a surface plot as shown in Fig. 2.20c. Furthermore, the effect of gravity reduces the total depth by tilting the full potential in vertical z-direction, see Fig. 2.20d.

The loading process of the dipole trap from the red MOT can be seen in Fig. 2.18 for the fermions ^{87}Sr and in Fig. 2.19 for the bosonic isotope ^{84}Sr.

2.4.2 Light sheet potential

On top of the optical dipole trap we add a light sheet beam at the clock-magic wavelength of 813.4 nm, see Fig. 2.1. This beam is generated by titanium-sapphire (Ti:Sa) laser[13], which is shared between the light sheet beam and the optical lattice (discussed in the following Ch. 3). At powers of only 270 mW, we reach a trap depth of 50 µK due to the beam waist of approximately 3.5 µm×60 µm. These waists are achieved by focusing an elliptical beam with a aspheric lens[14] of focal length f = 31.25 mm into the glass cell. Details on the setup of the light sheet beam are presented in the PhD thesis of J. Höschele [119].

[9] Mephisto MOPA 25 W Laser System
[10] Intraaction ATM-802DA6 modulator
[11] NKT Photonics LMA-PM-15, 2 m, SMA-905/SMA-905 6 mm steel
[12] Lens UVFS Plano-Convex, focal length 200 mm (LA4102-C, Thorlabs)
[13] Sirah Matisse CS laser system pumped by Millenia eV25W, MOS-2BB optics set
[14] Precision Aspheric Lens , TECHSPEC 25 mm diameter, 0.40 Numerical Aperture, Uncoated (Edmund Optics)

The tight vertical confinement of the light sheet beam finds its main application in the confinement of the atoms into a two-dimensional plane in order to create a two-dimensional optical lattice, see Ch. 3. We can determine the trap frequencies of the light sheet beam from the second derivative of the trapping potential in Eq. (2.3)

$$\omega_j^2 = \frac{1}{m}\frac{\partial^2 V_{\mathrm{dip}}}{\partial r_j^2} \tag{2.6}$$

where we assume a harmonic confinement and $r_j = x$, y or z, allowing us to calculate the trap frequency in a given direction, with m the mass of the atoms. We have measured the trap frequencies by means of parametric heating, which is presented in [119], and we extracted the light sheet beam waists from the measurement which revealed the exact values of the waists in vertical direction $w_v = 3.480(1)\,\mu\mathrm{m}$ and in horizontal direction $w_h = 57.2(1)\,\mu\mathrm{m}$ [119].

We do not load the atoms from the red MOT directly into the light sheet beam due to their small spatial overlap, see Fig. 2.19 where the red MOT is around 0.8 mm wide which is two orders of magnitude larger than the 3.5 µm vertical beam waist of the light sheet beam. Instead, we first load the dipole trap, which has a better spatial overlap due to the 100 µm beam waist, then switch off the red light and add the light sheet potential. As displayed in Fig. 2.19, the vertical width of the atomic cloud shrinks upon loading into the light sheet potential and we show around 60 000 trapped bosonic atoms. While this is not the maximum atom number of our experiment, it is still sufficient to perform evaporation in the dipole trap plus light sheet potential. Besides, the use for the two-dimensional confinement for the lattice, which will be discussed in detail in Sec. 3.2.2, it has also an advantage for evaporative cooling, as discussed in the following section.

2.4.3 Evaporative cooling

Once the atoms are in the optical dipole plus light sheet trap, we start evaporative cooling. We present here a brief explanation with some key results, but refer the reader to the PhD thesis of J. Höschele [119] for a detailed discussion of the process and the characterization of the ^{84}Sr Bose-Einstein condensate.

The initial trap frequencies of the light sheet beam are $\omega_x \approx 2\pi\times 239\,\mathrm{Hz}$, $\omega_y \approx 2\pi\times 377\,\mathrm{Hz}$ and $\omega_z \approx 2\pi\times 6.5\,\mathrm{kHz}$, while the ones of the dipole trap alone are around 105 Hz in horizontal direction and 150 Hz in vertical direction. During 10 s, we reduce the power of the optical dipole trap exponentially to zero and the one of the light sheet beam to a finite small value of $\sim 6\,\mathrm{mW}$. This results in a final trapping potential of 1 µK depth and $\omega_x \approx 2\pi\times 36\,\mathrm{Hz}$, $\omega_y \approx 2\pi\times 56\,\mathrm{Hz}$ and $\omega_z \approx 2\pi\times 1\,\mathrm{kHz}$.

We measure the expansion of the atoms after releasing them from the final potential of the light sheet beam. In Fig. 2.21 we observe that during 13 ms time of flight the atomic cloud shows the typical asymmetric expansion expected for a Bose-Einstein condensate that has been released from an anisotropic trap. At the end of this stage there are typically 5000 atoms in the ultracold atomic cloud. To get a better overview of the condensation process, in Fig. 2.22, which shows the atoms after 7 ms

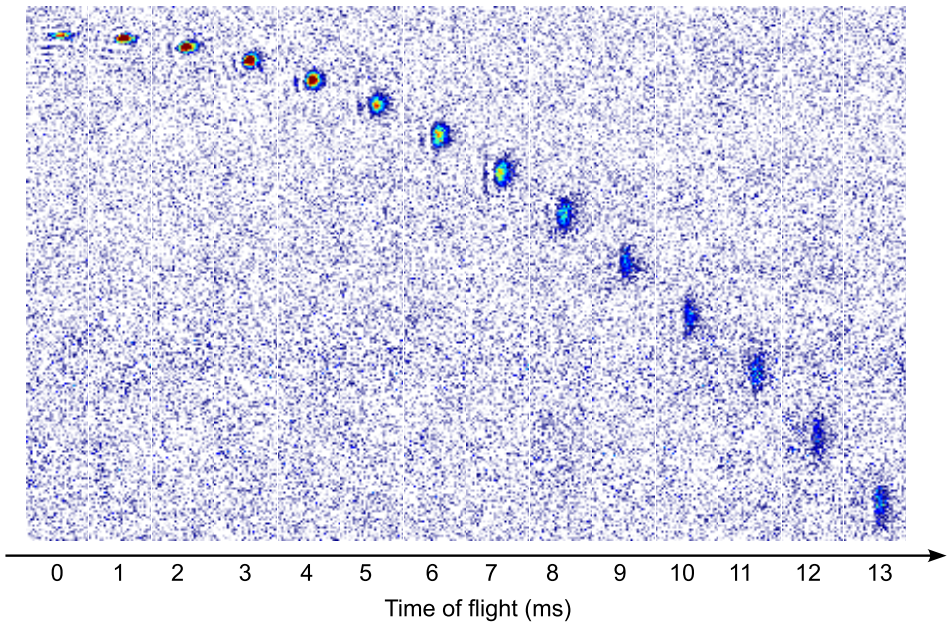

Figure 2.21: Time of flight after evaporatively cooling ^{84}Sr atoms in the dipole trap plus light sheet. We measure around 5000 atoms and can observe the asymmetric expansion of the cloud while in free fall after releasing from the trap.

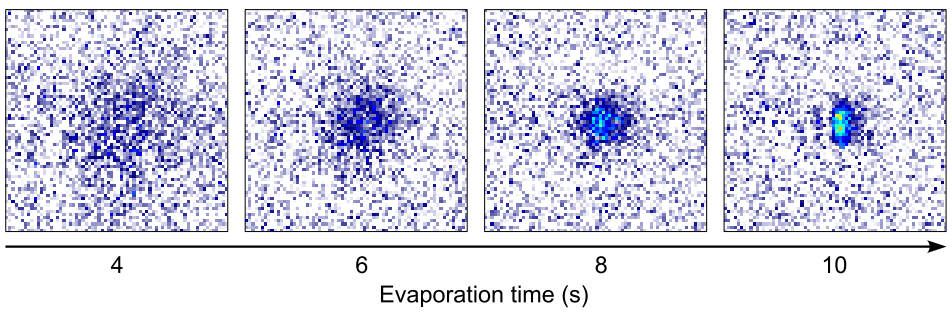

Figure 2.22: The atomic cloud gets denser and denser while evaporatively cooling. The images are taken by means of absorption after a 7 ms time of flight. The field of view is $0.26 \times 0.26\,\mathrm{mm}^2$.

time of flight at different times during the evaporation process. The thermal could at $t_{\mathrm{evap}} = 4\,\mathrm{s}$ turns into a Bose-Einstein condensate after $t_{\mathrm{evap}} = 10\,\mathrm{s}$ of evaporation. For the fermionic atoms, we have performed evaporative cooling as well, but we have not confirmed quantum degeneracy of the atoms at this point.

2.5 Conclusion

We discussed the cooling sequence of our ultracold strontium experiment. Starting from the oven and the 2D MOT with the Zeeman slower, the atoms are pushed into the glass cell and captured by the blue MOT. We discussed the various repumper transitions available for strontium and concluded with our application of a repumper laser at 481 nm combined with the 679 nm clock repumper for the bosonic isotope. However, we discussed the motivation to use a different combination for the fermionic atoms, namely 707 nm with the same colck repumper at 679 nm, which we implemented in our experiment because the frequency modulation to address all the hyperfine states is simpler for this repumper transition. We highlighted the atom number enhancement which we have achieved through resonant shielding on the narrow-linewidth red transition during the blue magneto-optical trap.

We continued the discussion with the red magneto-optical trap and the challenges arising due to the narrow-linewidth of the transition and the hyperfine splitting of the fermionic atoms. We explained the solutions of using a braodband and a single-frequency cooling stage, and showed the performance of the fermionic red magneto-optical trap when addressing different hyperfine states. In the last part, we introduced the crossed optical dipole trap at 1064 nm and the tightly focused light sheet beam at 813.4 nm, which combined present the optical potential for evaporative cooling. While the quantum degeneracy of the fermionic atoms has yet to be demonstrated, we have realized a Bose-Einstein condensate of ^{84}Sr.

Chapter 3

Fourfold optical lattice

This chapter addresses the design and the physics of the optical lattice used in our experiment. We present a brief overview of optical lattices in general and discuss some of their key features. We present the geometry arising from the fourfold interference of our optical lattice in contrast to a twofold interference lattice. We explain the bow tie configuration of our optical lattice setup, which we use to overlap one initial lattice beam four times with itself to realize the fourfold interference. The atom in the lattice are vertically confined into a two-dimensional plane by means of a tightly focused, elliptical light sheet beam. Furthermore, we present the band structure of our optical lattice and discuss the effect of experimental imperfections on the energy of the different bands. We end the chapter with a demonstration of spatially dependent parametric heating detected with the microscope, which arises due to the harmonic confinement of the optical potential.

The work presented in this chapter was a team effort together with my PhD colleague Dr. Jonatan Höschele, the postdocs Dr. Vasiliy Makhalov and Dr. Antonio Rubio Abadal, and supervised by Prof. Dr. Leticia Tarruell. The design of the optical lattice and the implementation in the apparatus was done by myself. The calculations of the band structure were initially done by Marc Miranda Riaza, a master student in the theory group of Prof. Dr. Alessio Celi, co-supervised by Prof. Dr. Leticia Tarruell.

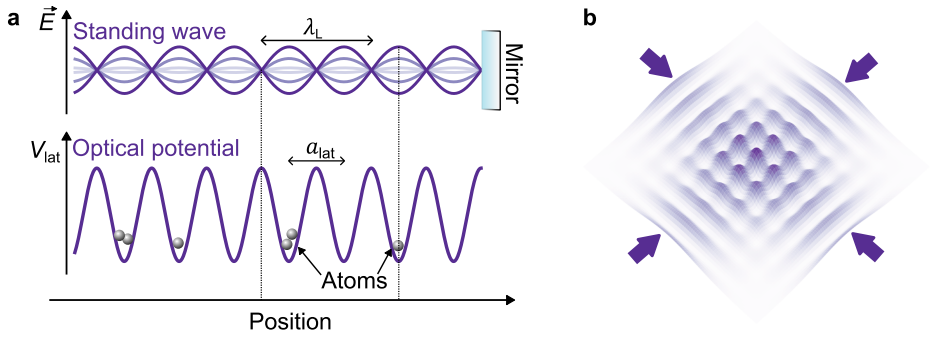

Figure 3.1: Creation of optical lattice with interfering laser beams. **a** One-dimensional lattice formed by the retroreflection of a laser beam at wavelength λ_L. The interference forms a standing wave with nodes and anti-nodes, shown for the electric field component $\vec{E}$ of the laser beam (top). Due to the ac Stark shift, the atoms experience this standing wave as a periodic potential V_{lat} (bottom) with a lattice spacing $a_{lat} = \lambda_L/2$. In the case of a far red-detuned laser, the atoms are attracted to the intensity maxima, which correspond to the anti-nodes (see dashed lines). **b** A two dimensional lattice potential, formed from the interference of two pairs of laser beams, indicated by the four arrows.

3.1 Optical lattices and Hubbard models

Optical lattices are an important tool for quantum simulations, as they are the key ingredient to realize Hubbard models. Their strength compared to solid-state systems lies in the high tunability of parameters such as the tunneling between lattice sites, the on-site interactions, but also the countless lattice geometries that can be realized [182, 77, 183]. In this section, the fundamental concepts of optical lattices are discussed. To this end, we present the connection to the Hubbard parameters and discuss different lattice geometries, as well as the dependence of the potential on the atomic state. This is relevant to excite an atom on the ultra-narrow-linewidth transition to the clock state $^3P_0$ in the lattice potential.

3.1.1 Basics on optical lattices

Optical lattices are commonly created by interfering laser beams. As discussed in the previous chapter in Sec. 2.4.1, the trapping potential for an atom in a light field arises due to the ac Stark shift [181]. It depends on the polarizability and the intensity of the laser light, see Eq. (2.3) and (2.4). The interference of the laser beams gives rise to a periodic intensity distribution and thus a periodic optical potential. For instance, a one-dimensional optical lattice can be formed by a single retroreflected beam that interferes with itself, see Fig. 3.1a. The interference pattern derived from the electric field components is

$$I(x) = 2\epsilon_0 c \left| \sum_{j=1}^{2} \vec{E}_j(x) \right|^2 \sim \left| \mathcal{E}_1 \exp^{-ikx} + \mathcal{E}_2 \exp^{ikx} \right|^2 = 4\mathcal{E} \cos^2(kx) \qquad (3.1)$$

where $\vec{E}_j(x)$ describes the counterpropagating beams which, in this example, have the same amplitude $\mathcal{E}_1 = \mathcal{E}_2 = \mathcal{E}$. The wavevector $k = 2\pi/\lambda_L$ depends on the wavelength of the laser λ_L. Here, ϵ_0 is the vacuum permittivity and c is the speed of light. We find that the periodic potential derived in Eq. (3.1) has a lattice spacing of $a_{lat} = \lambda_L/2$, see Fig. 3.1a.

To create a two-dimensional lattice, the one-dimensional interference pattern is extended by adding a second retroreflected beam, perpendicular to the first. Their frequency detuning should be large enough ($\gtrsim 10\,\mathrm{MHz}$), such that the two perpendicular beams do not interfere with each other. The resulting intensity pattern is schematically shown in Fig. 3.1b. By adding a third retroreflected beam perpendicular to the first two, the two-dimensional lattice becomes a three dimensional one.

3.1.2 Hubbard parameters

The optical lattice and the properties of the atoms determine the tunneling t and the on-site interaction U of the Hubbard model (Eq. (1.2)). We express the two parameters in terms of the Wannier functions $W_n(\mathbf{r}-\mathbf{R}_j)$ which form an orthonormal single-particle basis. They depend on the band n and the distance between the position $\mathbf{r}$ and the lattice site $\mathbf{R}_j$ [42]. For the lowest band, the Wannier functions are centered around the lattice site $\mathbf{R}_j$ and for sufficiently deep lattices they are tightly localized, and only the overlap with nearest-neighbor lattice site is relevant. The tunneling is then given by

$$t_{ij} = \int W_0^*(\mathbf{r}-\mathbf{R}_i)\left[\frac{-\hbar^2}{2m}\nabla^2 + V_{\mathrm{lat}}(\mathbf{r})\right] W_0(\mathbf{r}-\mathbf{R}_j)\mathrm{d}\mathbf{r}$$

and $\mathbf{R}_i$ is the lattice site adjacent to $\mathbf{R}_j$ because of the tight-binding approximation. The tunneling can also be extracted from the Fourier transform of the energy eigenvalues $w_{\mathbf{q}}$, which are obtained from the band structure of the lattice [184]:

$$t_{ij} = \frac{1}{N}\sum_{\mathbf{q}} \hbar w_{\mathbf{q}} e^{-i\mathbf{q}(\mathbf{R}_j-\mathbf{R}_i)}\,. \tag{3.2}$$

This will enable us to determine the tunneling parameter t from the band structure calculated in Sec. 3.3.

The expression of the on-site interaction in terms of Wannier functions is

$$U = g\int |W_0(\mathbf{r})|^4 \mathrm{d}\mathbf{r}$$

where the coupling strength g depends on the scattering length and the mass of the atoms. In the specific example of a three-dimensional lattice the value is $g = 4\pi\hbar^2 a_s/m$ [185]. For some atomic species, such as alkali atoms, the scattering length and thus the interaction can be tuned by means of Feshbach resonances [186, 129]. In the case of ^{84}Sr this value is fixed at $a_s \approx 123 a_0$ (Tab. 2.1), with a_0 the Bohr radius, due to the singlet formed by the two valence electrons in the ground state which prevent Feshbach resonances. However, in a two-dimensional lattice, the interaction can be modified to some extent by means of the vertical trapping frequency ω_z, since $U \sim \sqrt{\omega_z}$ [185, 184].

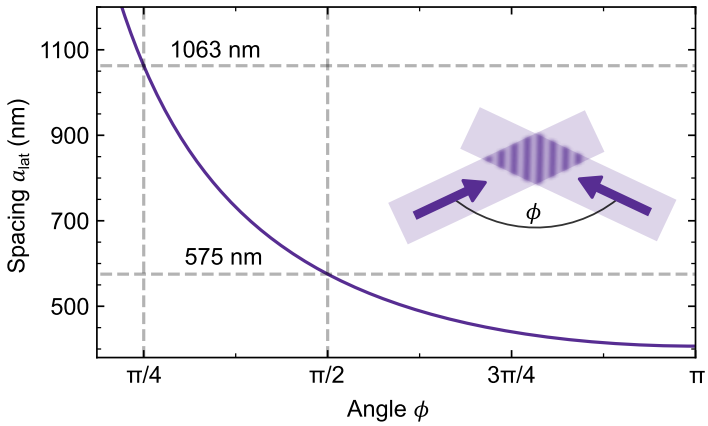

Figure 3.2: Spacing of one dimensional optical lattice at wavelength $\lambda_L = 813.4\,\text{nm}$. Following Eq. (3.4), we show the lattice spacing $a_{lat}(\phi)$ for two beams with an angle ϕ as shown in the inset. For a retroreflected beam, the spacing is half the lattice wavelength. The dashed lines indicate the spacing at $\phi = \pi/2$ and $\pi/4$.

The depth of optical lattices is typically expressed in terms of the recoil energy

$$E_r = \frac{\hbar^2 k^2}{2m} = \frac{h^2}{(2m\lambda_L^2)} \tag{3.3}$$

which is the characteristic energy scale of the lattice potential, because it depends on the mass m of the atoms and the wavevector $k = 2\pi/\lambda_L$ and allows the comparison of energy regimes between different experiments despite the different atomic species or lattice lasers.

Instead of the laser wavelength often the lattice spacing is used in its definition which is half of the wavelength in the case of a square optical lattice formed by two retroreflected beams. We chose to define the recoil energy as given in Eq. (3.3), because the lattice spacing depends on the geometry of the optical lattice and is not constant for a given laser wavelength. This dependence of the lattice spacing on the arrangement of the beams manifests already in a simple one-dimensional optical lattice created by two interfering laser beams with an angle ϕ between the two beams. In Eq. (3.1), we have assumed the two beams are counterpropagating, $\phi = \pi$. If we change this angle, the lattice spacing increases following the formula

$$a_{lat} = \frac{\lambda_L}{2} \frac{1}{\sin \phi/2} \tag{3.4}$$

which is displayed in Fig. 3.2.

3.1.3 Features of optical lattices

Lattice geometries

Various optical lattices have been realized and studied in the past. For example, the first ultracold atom Mott insulators, bosonic as well as fermionic, were realized in

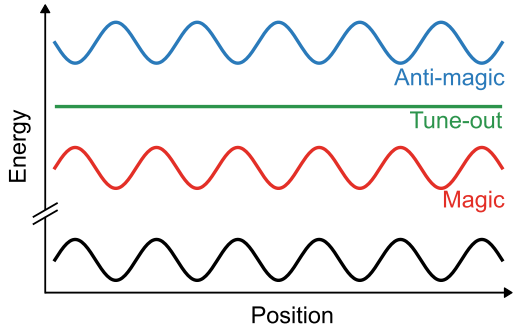

Figure 3.3: Examples for state dependent lattices. At magic wavelength the ground state (black) has the same light shift as the excited state (red). Tune-out (green) means that the state does not experience a light shift at the given wavelength. Anti-magic is realized with two tune-out wavelengths, and has the same light shift in the ground and excited state but with opposite sign [187, 188]. The figure is from [189].

three-dimensional simple cubic optical lattices [46, 47, 48]. By adjusting the angles between the lattice beams, as discussed in Fig. 3.2, the geometry of the lattice can be altered and triangular lattices can be formed for instance by overlapping three beams with an angle $\phi = 120°$ between each of the beams [51, 52]. Playing with the interference between the individual standing waves of the lattice beams unlocks additional tunability of the optical lattice geometry. Moreover, adding extra beams along one or several of the existing lattice beams allows to create superlattices, for example tunable double well potentials [190, 191]. This also allows for a simple method to tune the geometry of the optical lattice, simply by varying the power or the frequency of the additional laser beam. In this way, optical lattice experiments achieved tunable geometries for example from a square, over a triangular, a honeycomb to a checkerboard lattices [192]. Furthermore a tunable Lieb lattice [193] and a tunable kagome lattices [194] have been realized in a similar fashion by generating the lattice from two sets of laser beams to form the tunable geometry by adjusting the respective depth of the lattices. Multifrequency lattices allow fast changes of the geometry and have been realized recently [195]. More exotic lattices can be realized by interfering a number of laser beams [196] which permits the simulation of quasicrystals [197], a system with long-range order but without periodicity.

For quantum-gas microscopy, it is convenient to work with two-dimensional lattices because they can be positioned in the imaging plane of the objective. However, three-dimensional lattices work as well, and then only one plane of the lattice is imaged after the atoms in the other plans have been removed [90]. In the first quantum-gas microscope the lattice was created with a lithographically produced holographic mask which allows to realize different geometries depending on the chosen mask, however, the presented system used a square geometry for the lattice [85].

State dependent lattices

Apart from the lattice spacing, the wavelength of the lattice laser determines also the light shift and thus the depth of the potential at a given intensity. Moreover, if an atom is excited to a higher electronic state, it will typically experience a different light shift compared to the ground state. This is a method that has been exploited in Sisyphus cooling [198, 199] and will be addressed in the following chapters (Ch. 4 and Ch. 5). The effect is captured by the polarizability which varies for different electronic states of the atoms, see Appx. B.

An example for strontium where the ground state polarizability α_g is smaller than the excited-state polarizability α_e is at 813.4 nm between the ground state $^1S_0$ and the excited state $^3P_1$ [109]. In this case, the potential of the excited-state lattice will be deeper compared to the lattice of the ground state. The same two states can have the opposite relation for example at 515 nm [115, 163] or at 1040 nm [200]. Other state dependent lattices can have anti-trapped states such as $^1P_1$ at 515 nm which is a challenge for imaging in optical tweezers [163].

The wavelength at which two particular states have the same polarizability and thus the same light shift is called magic wavelength [106], see Fig. 3.3. They are a powerful tool in the context of precision metrology [107]. Typically magic for one transition is not magic for another, but there can be several magic wavelength corresponding to different transitions. For example the wavelength 813.4 nm, which we use in our optical lattice, is the clock-magic wavelength of strontium [201], having the same light shift for the clock state $^3P_0$ and the ground state $^1S_0$. There are other magic wavelength for the clock state, for example blue-detuned around 390 nm [202]. Magic wavelengths corresponding to the $^3P_1$ state are for example 915 nm [203], around 515 nm [115, 163] and near 473 nm [204].

Furthermore, there are so called tune-out wavelength where the state does not experience a light shift at all [205, 206]. Combining two tune-out wavelengths in a clever way allows to realize anti-magic lattices where $\alpha_g = -\alpha_e$, see Fig. 3.3. This can be useful for quantum computing and gate operations [187, 188].

3.2 Fourfold optical lattice

The two-dimensional square optical lattice used in our quantum-gas microscope is a result of a fourfold interference. It is realized with a bow tie optical lattice setup where four laser beams are all interfering with each other. This is in contrast to a twofold optical lattice where only the two counter propagating beams interfere, see Fig. 3.4. While both reveal a square geometry of the optical lattice, the lattice spacing as well as the potential landscape are different. In this section, the twofold and fourfold optical lattices will be compared. Additionally, the lattice setup and the two-dimensional confinement of the optical lattice will be discussed.

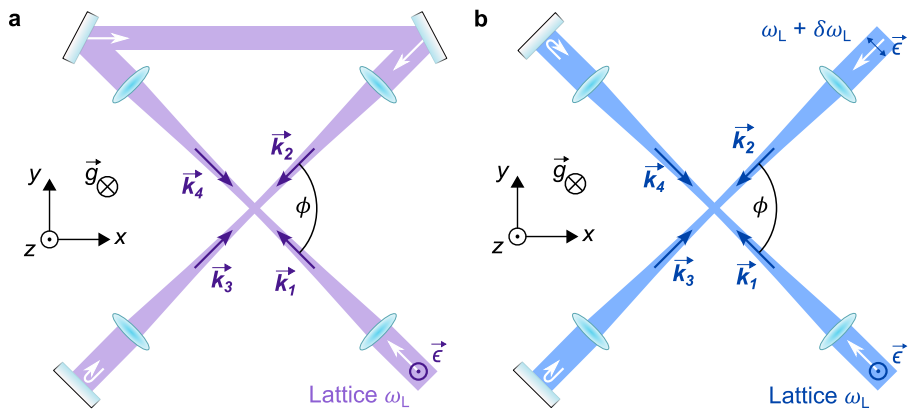

Figure 3.4: Comparison between fourfold and twofold optical lattice. **a** A fourfold optical lattice realized with a bow tie setup where the beam is four times overlapped with itself. The beam is vertically polarized $\vec{\epsilon}$ such that all four beams interfere with each other. **b** Twofold interference with two retroreflected beams where $\vec{k}_1$ interferes only with $\vec{k}_4$ and $\vec{k}_2$ interferes only with $\vec{k}_3$ which is a result of the frequency difference $\delta\omega_L$ on the order of megahertz between the two beams. The setup can have fourfold interference if the two beams have parallel polarization and the same frequency, but in that case the relative phase of the two lattices needs to be set to the correct value.

3.2.1 Twofold versus fourfold interference

The relationship between the intensity of interfering laser beams and the lattice potential is discussed in Sec. 3.1.1. We extend it here to the interference pattern related to two-dimensional square optical lattices. Typically, there are four beams employed, but the lattice potential varies if all four are interfering with each other (fourfold interference) or only the two counterpropagating ones (twofold interference) [207].

Having two orthogonal retroreflected beams, interfering independent from each other, results in an intensity

$$\begin{aligned} I(\vec{r}) &\sim |\vec{E}_1 + \vec{E}_4|^2 + |\vec{E}_2 + \vec{E}_3|^2 = \\ &= 4\mathcal{E}\cos^2\left(k\left[-x\cos\left(\phi/2\right) + y\sin\left(\phi/2\right)\right]\right) + \\ &+ 4\mathcal{E}\cos^2\left(k\left[x\cos\left(\phi/2\right) + y\sin\left(\phi/2\right)\right]\right) \end{aligned} \tag{3.5}$$

which is the sum of the intensity of two one-dimensional lattices, compare Eq. (3.1). Here, we ignore the time dependence for simplicity. The beam configuration is displayed in Fig. 3.4 and we assume $\mathcal{E}_j = \mathcal{E}$ and $|\vec{k}_j| = k$ for $j \in \{1, 2, 3, 4\}$. The coordinate system is chosen in a way that the beams are propagating diagonally, which will be convenient for the lattice potential arising from the fourfold interference.

If all four beams are interfering with each other,

$$I(\vec{r}) \sim \left|\sum_{j=0}^{4} \vec{E}_j\right|^2$$

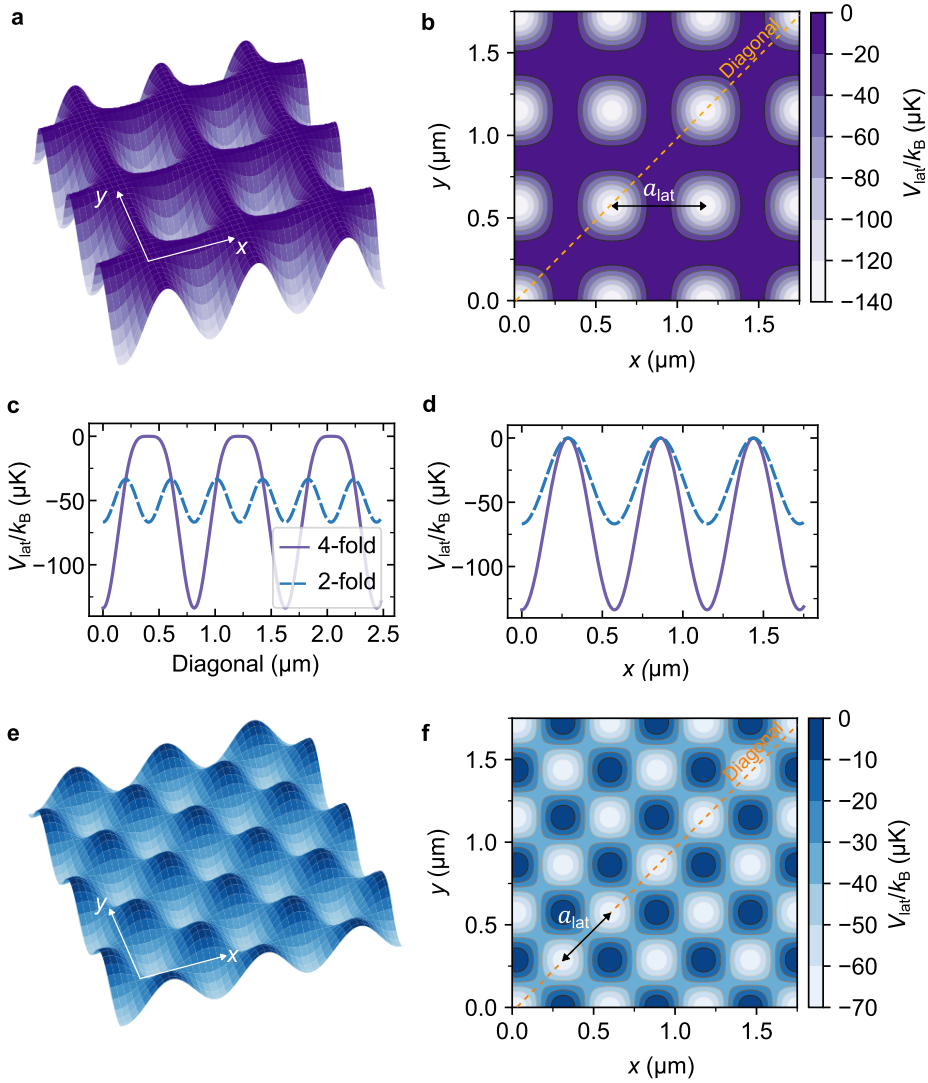

Figure 3.5: Comparison between fourfold and twofold lattice potential. **a**, **b** The fourfold potential in a 3D plot and in a contour plot show the lattice sites surrounded by a zero potential. The coordinate system in Fig. 3.4 is chosen, such that the lattice sites are aligned with the coordinate system. **e**, **f** The potential of a twofold lattice with the same intensities in the four beams as in the fourfold case are shown in a 3D plot and as a contour plot, respectively. The nearest-neighbors are along the diagonal axis and the density of minima is higher for the twofold lattice due to the smaller lattice spacing compared to the fourfold lattice. **c**, **d** Direct comparison of the fourfold (top: **a**, **b**) and twofold (bottom: **e**, **f**) potentials, along the diagonal axis and along the x-direction.

an additional term arises in the intensity

$$\begin{aligned} I(\vec{r}) \sim\ & 4\mathcal{E}\cos^2\left(k\left[-x\cos\left(\phi/2\right)+y\sin\left(\phi/2\right)\right]\right)+ \\ & +4\mathcal{E}\cos^2\left(k\left[x\cos\left(\phi/2\right)+y\sin\left(\phi/2\right)\right]\right)+ \\ & +8\mathcal{E}\cos\left(k\left[-x\cos\left(\phi/2\right)+y\sin\left(\phi/2\right)\right]\right)\cos\left(k\left[x\cos\left(\phi/2\right)+y\sin\left(\phi/2\right)\right]\right) \end{aligned} \tag{3.6}$$

accounting for the interference of beams $\vec{k}_1$ and $\vec{k}_4$ with $\vec{k}_2$ and $\vec{k}_3$. The beam arrangement in Fig. 3.4a has the shape of a bow tie and is formed with one single beam. It is possible to create fourfold interference with two independent beams as displayed in Fig. 3.4b, but then they have to match in frequency and polarization. Additionally, active phase stabilization is required in a setup of two independent beams in order to have a stable lattice potential. [207]

The potential arising form the fourfold and the twofold interference are shown in Fig. 3.5. The lattice sites in the fourfold potential are aligned with the axis of the coordinate system, while in the twofold they are along the directions of the lattice beams. Also, the depth of the potential is different, which is captured in Eq. (3.5) and Eq. (3.6). The maximum of the fourfold interference is twice as large compared to the twofold interference. This affects the depth of the optical lattice such that the fourfold is twice as deep as the twofold with the same intensity in the lattice beams for both cases, see Fig. 3.5d. Additionally, the energy distribution is different, in particular, the lattice sites in the fourfold case are deeper but they are surrounded by plateaus of zero potential energy (Fig. 3.5a), while the twofold lattice reveals a non-flat landscape in between lattice sites (Fig. 3.5). More specifically, the potential an atom has to overcome to hop between neighboring lattice sites is the maximum depth of the potential in the fourfold lattice, but it is only half of the maximal depth of the twofold lattice, see Fig. 3.5. Further, the lattice spacing in the fourfold lattice is $a_{\mathrm{lat}} = \lambda_{\mathrm{L}}/\sqrt{2}$, but for the twofold it is $a_{\mathrm{lat}} = \lambda_{\mathrm{L}}/2$. This is the reason why we define the recoil energy (Eq. (3.3)) not with the lattice spacing but instead with the wavelength.

3.2.2 Optical setup

Our optical lattice operates at the clock-magic wavelength of strontium at 813.4 nm because it will allow us to operate the ultra-narrow-linewidth clock transition which is useful for various applications for example storage of the different fermionic spin states as demonstrated by [110], to exploit spin-orbit coupling [209], or to perform ultra-precise spectroscopy of many-body phases [210, 211, 212]. To this end, we use a titanium-sapphire (Ti:Sa) laser[1] with around 8 W at 813 nm, which is around the highest power available at this wavelength. The light is shared between the lattice and the light sheet beam (Sec. 2.4.2). The wavelength of the Ti:Sa laser is tunable and can also be adjusted to the magic wavelength of the $^3\mathrm{P}_1$ state at 915 nm.

For quantum-gas microscopy, in particular, the imaging of the atoms, it is crucial to realize deep optical lattice potentials, in order to keep the atoms trapped despite

[1] Sirah Matisse CS laser system pumped by Millenia eV25W, MOS–2BB optics set, tuneable from 730 nm to 930 nm

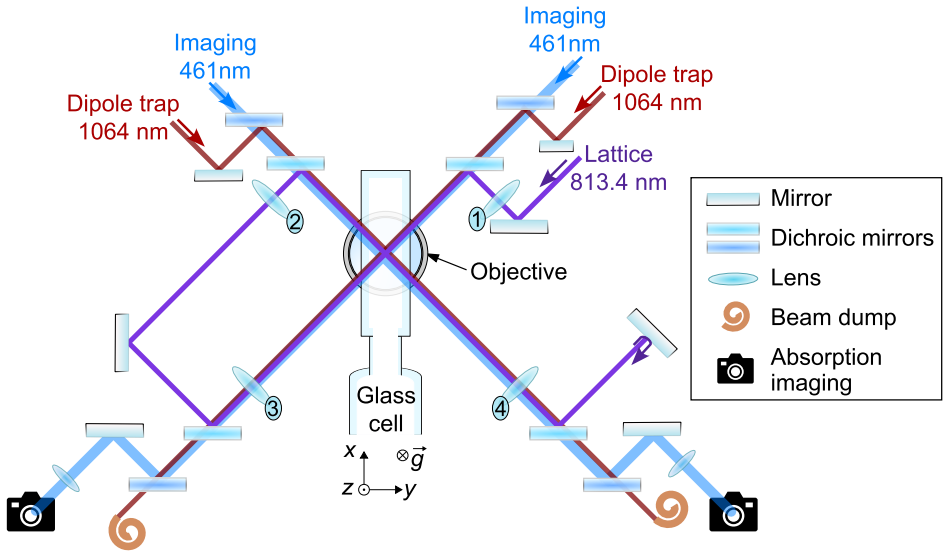

Figure 3.6: Setup of the optical lattice. The lattice beam passes four times through the glass cell. It is focused with four lenses of $f = 200\,\mathrm{mm}$. The distance between the second and the third lens is $2f$, and the distance between the fourth lens and the retroreflecting mirror is f. The lattice beams are combined with the dipole trap beam and the imaging beam used for absorption imaging. The objective is below the glass cell and the lattice lays in the $x - y$ plane.

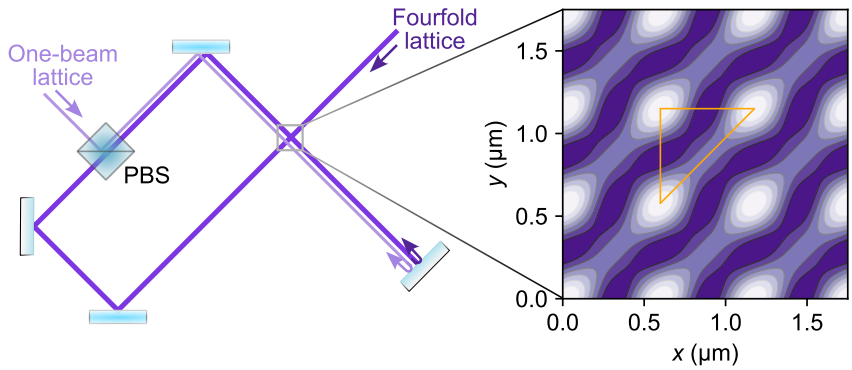

Figure 3.7: Beam configuration for a triangular optical lattice. In the setup in Fig. 3.6, we have placed a polarizing beam splitter cube (PBS), which will allow us to overlap the lattice with an additional retroreflected laser beam. This beam will modify the geometry of optical lattice and as discussed in [208], should allow us to realize triangular lattice geometries, as displayed in the right part in a schematic contour plot.

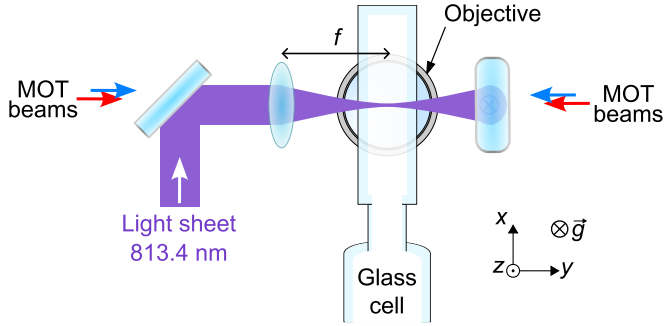

Figure 3.8: Setup of the light sheet beam. The light sheet is realized by focusing a elliptical beam with an aspheric lens of focal length $f = 31.25\,\mathrm{mm}$ into the glass cell. Since it propagates in y-direction, which is the same as two of the MOT beams for the blue as well as the red MOT, we have to combine them with a dichroic mirror. After passing the glass cell, the light sheet beam is reflected downwards into a beam dump.

the recoils heating from the imaging photons. For this reason, we setup a fourfold optical lattice for our quantum-gas microscope. This allows us make optimal use of the power available from our Ti:Sa laser by sending the same beam four times through the glass cell forming a bow tie shape, see Fig. 3.4a.

The lattice beams are overlapped with the optical dipole trap and the absorption imaging path as shown in Fig. 3.6. We designed the setup such that the most important beams are reflected in order to preserve the beam shape and wavefront. Consequently, the lattice beams are always reflected on the custom dichroic mirrors[2]. The dipole trap beams are reflected at the input when combined with the imaging beam[3], but then transmitted[4] and sent to a beam dump, see Fig. 3.6. The imaging beams are transmitted before passing through the glass cell, but after separating from the lattice beam, they are reflected and detected by a camera[5].

The lattice beams are circular and focused into the glass cell by means of four lenses with 200 mm focal length. Due to spatial constrains, we decided to use two different lenses, one is focusing only the lattice beam[6] and the second one is shared between the absorption imaging and the lattice beam[7], thus they have slighly different specifications. The lenses are in focal distance from the center of the glass cell. The distance between the second and the third lens is twice the focal length and from the last lens to the retroreflecting mirror the distance measures one focal length.

[2]Dichroic mirrors, high transmission for several relevant strontium wavelength 461 nm, 689 nm, 698 nm, 671 nm and the dipole trap at 1064 nm. Reflectivity for 813 nm and 915 nm above 99.9 % for s-polarized light (Laseroptik), for the transmission and reflection curves see Appx. C.

[3]Shortpass Dichroic Mirror, 900 nm Cutoff (DMSP900, Thorlabs)

[4]Longpass Dichroic Mirror, 950 nm Cut-On (DMLP950L, Thorlabs)

[5]Flir CMLN–13S2M_CS

[6]Plano-Convex Lens, TECHSPEC 25 mm diameter and 200 mm focal length, NIR-I Coated (Edmund Optics)

[7]UV Plano-Convex Lens, TECHSPEC 50 mm diameter and 200 mm focal length, VIS-NIR Coated (Edmund Optics)

The vertically polarized beams enter the glass cell with 45° angle. Due to the uncoated glass cell, the transmission through its wall is $T = 0.86$ which we determined experimentally. This results in power losses for each consecutive lattice beam. In particular, the first beam is reduced by T, the second one by T^3 because the initial beam passes three times through the glass cell wall, see Fig. 3.6, and so on. This is a disadvantage, in particular for a bow tie configuration because the last beam will travel seven times through the glass cell wall. One way to correct for the losses is by adjusting the polarization such that effectively all beams contribute to the interference with the same intensity. However, while the losses are relevant for the values of the Hubbard parameters, we have not been limited by them in our experiment. An advantage of the bow tie configuration, besides the recycled power, is that no phase stabilization is required because the beam is retroreflected on the last mirror, and thus the phase of all four interfering beams is stable with respect to each other.

Furthermore, we have the option to upgrade our square geometry to a triangular one. The lattice setup has an additional beam splitter cube installed, which is shown in Fig. 3.7. If we insert an additional laser beam through the cube, we can tune the geometry of our optical lattice by varying the depth of the additional one-beam lattice and we can enter a regime, where the potential as a triangular geometry, see Fig. 3.7. This will be useful for investigations of frustrated systems with two spin components [208].

Two-dimensional confinement

To confine the lattice in a two-dimensional plane we add a light sheet beam, tightly focused perpendicular to the lattice, described in Sec. 2.4.2 and in detail in the Ph.D. thesis of J. Höschele [119].

The light sheet beam is made out of an elliptical beam which is focused into the glass cell with an aspheric lens[8] of focal length $f = 31.25\,\mathrm{mm}$. It propagates along y-axis, perpendicular to the glass cell, see Fig. 3.8. We overlap the light sheet beam with the MOT beams using the same dichroic mirror as for the optical lattice. In order to have a collimated MOT beam passing the glass cell, we adjust their beam shape to correct for the aspheric lens of the light sheet.

The vertical trap frequency ω_z achieved with the light sheet beam is relevant for the on-site interaction parameter of the physics lattice but also for the performance of the fluorescence imaging process, which is discussed in Ch. 4. We use the Lamb-Dicke parameter to identify the confinement of the light sheet:

$$\eta = \sqrt{\frac{\omega_r}{\omega_z}} = \sqrt{\frac{h\pi}{\omega_z m \lambda^2}}\,. \tag{3.7}$$

The recoil frequency ω_r depends on the wavelength λ and the mass of the atom m. The vertical trap frequency ω_z depends on the intensity of the light sheet beam. With a beam waist of $3.5\,\mu\mathrm{m}\times 60\,\mu\mathrm{m}$ and around 300 mW power we achieve a trap frequency

[8] Precision Aspheric Lens , TECHSPEC 25 mm diameter, 0.40 Numerical Aperture, Uncoated (Edmund Optics)

of $\omega_z \approx 2\pi \times 6.5\,\mathrm{kHz}$ (see Sec. 2.4.2), and the Lamb-Dicke parameter for the red transition at $\lambda = 689\,\mathrm{nm}$ is with $\eta \approx 0.9 < 1$, which is important for the processes involved in single atom imaging [203].

3.3 Band structure of the fourfold optical lattice

The band structure describes the energy levels of electrons in a solid and their band gaps. In the same fashion the band structure of an optical lattice can be calculated in an ultracold atom experiment. From the band structure we can then compute the Hubbard parameters, discussed in Sec. 3.1. In this section, we present the calculation of the band structure of our fourfold optical lattice. Additionally, we will present the dependence of the energy levels on different parameters of the interfering laser beams. In particular, we will consider power imbalance and misalignment of the beams because it will allow us to determine the tunneling and the interaction parameters for the real experimental setup.

3.3.1 General lattice potential

For the calculation of the band structure, we consider an optical lattice arising from four beams with different powers and the angle between the two pairs of counterpropagating beams given by a variable ϕ, see Fig. 3.4a. In Eq. (3.6), we assumed the four beams have all the same powers. However, since our fourfold lattice consists of one beam passing four times through the glass cell and the uncoated wall transmits only 86 % of the power it is important to consider the losses in the calculations of the band structure and later the Hubbard parameters. We write the electric field corresponding to the four beams with amplitudes $\mathcal{E}_j$, where $j \in \{1, 2, 3, 4\}$, where the beams are labeled as displayed in Fig. 3.4a and they are all vertically polarized such that the electric field component reads

$$\begin{aligned}
\vec{E}_1 &= \mathcal{E}_1 \hat{e}_z \exp\left(-ik\left[-x\cos\left(\phi/2\right) + y\sin\left(\phi/2\right)\right]\right) \\
\vec{E}_2 &= \mathcal{E}_2 \hat{e}_z \exp\left(-ik\left[-x\cos\left(\phi/2\right) - y\sin\left(\phi/2\right)\right]\right) \\
\vec{E}_3 &= \mathcal{E}_3 \hat{e}_z \exp\left(-ik\left[x\cos\left(\phi/2\right) + y\sin\left(\phi/2\right)\right]\right) \\
\vec{E}_4 &= \mathcal{E}_4 \hat{e}_z \exp\left(-ik\left[x\cos\left(\phi/2\right) - y\sin\left(\phi/2\right)\right]\right)
\end{aligned} \tag{3.8}$$

where we neglect the time dependence of the electric field and also the Gaussian beam envelope. The intensity of those four beams interfering with each other is

$$\begin{aligned}
I(\vec{r}) \sim |\sum_{j=0}^{4} \vec{E}_j|^2 = \\
&= \mathcal{E}_1^2 + \mathcal{E}_2^2 + \mathcal{E}_3^2 + \mathcal{E}_4^2 + \\
&+ \left(2\mathcal{E}_1\mathcal{E}_2 + 2\mathcal{E}_3\mathcal{E}_4\right)\cos\left(2ky\sin\left(\phi/2\right)\right) + \\
&+ \left(2\mathcal{E}_1\mathcal{E}_3 + 2\mathcal{E}_2\mathcal{E}_4\right)\cos\left(2kx\cos\left(\phi/2\right)\right) + \\
&+ 2\mathcal{E}_1\mathcal{E}_4\cos\left(2k\left[-x\cos\left(\phi/2\right) + y\sin\left(\phi/2\right)\right]\right) + \\
&+ 2\mathcal{E}_2\mathcal{E}_3\cos\left(2k\left[x\cos\left(\phi/2\right) + y\sin\left(\phi/2\right)\right]\right)
\end{aligned} \tag{3.9}$$

	$n' = n-1$	$n' = n$	$n' = n+1$
$m' = m-1$	$-s\frac{\mathcal{A}_2\mathcal{A}_3}{\mathcal{I}_{\max}}$	$-s\frac{\mathcal{A}_1\mathcal{A}_2+\mathcal{A}_3\mathcal{A}_4}{\mathcal{I}_{\max}}$	$-s\frac{\mathcal{A}_1\mathcal{A}_4}{\mathcal{I}_{\max}}$
$m' = m$	$-s\frac{\mathcal{A}_1\mathcal{A}_3+\mathcal{A}_2\mathcal{A}_4}{\mathcal{I}_{\max}}$	$-s\left(1-\frac{\mathcal{A}_1^2+\mathcal{A}_2^2+\mathcal{A}_3^2+\mathcal{A}_4^2}{\mathcal{I}_{\max}}\right)$	$-s\frac{\mathcal{A}_1\mathcal{A}_3+\mathcal{A}_2\mathcal{A}_4}{\mathcal{I}_{\max}}$
$m' = m+1$	$-s\frac{\mathcal{A}_1\mathcal{A}_4}{\mathcal{I}_{\max}}$	$-s\frac{\mathcal{A}_1\mathcal{A}_2+\mathcal{A}_3\mathcal{A}_4}{\mathcal{I}_{\max}}$	$-s\frac{\mathcal{A}_2\mathcal{A}_3}{\mathcal{I}_{\max}}$

Table 3.1: Hamiltonian matrix elements $\langle n', m'|\, V_{\text{lat}}\, |n, m\rangle$ of the lattice potential in the plane-wave basis. The amplitudes of the electric fields $\mathcal{E}_j$ are proportional to $\mathcal{A}_j$, which describes the attenuation in each of the four beams with $j \in \{1, 2, 3, 4\}$. The depth of the lattice $s = V_0/E_{\text{r}}$ is given in terms of the recoil energy $E_{\text{r}} = h^2/(2m\lambda^2)$, where $\lambda = 813.4\,\text{nm}$. The parameter $\mathcal{I}_{\max}$ describes the maximum of the unitless interference pattern, see text.

which can be reduced to Eq. (3.6) when assuming all intensities to be equal. With this equation, we can readily calculate the lattice potential considering the power losses on the glass cell and include different alignments of the lattice beams by changing the angle $\phi = \pi/2 \pm \delta\phi$ between the lattice beams.

3.3.2 Band structure calculation

The band structure of the optical lattice is determined by the eigenvalues of the Hamiltonian

$$\hat{H} = \frac{\hat{\mathbf{p}}^2}{2m} + V_{\text{lat}}(\hat{\mathbf{r}})\,. \tag{3.10}$$

The potential $V_{\text{lat}}(\hat{\mathbf{r}})$ is proportional to the intensity we have calculated in Eq. (3.9). We rewrite the potential in terms of recoil energy using the lattice depth $s = V_0/E_{\text{r}}$:

$$V_{\text{lat}}(x, y) = s\left(1 - \frac{\mathcal{I}_{\text{fourfold}}}{\max\{\mathcal{I}_{\text{fourfold}}\}}\right) \tag{3.11}$$

where $\mathcal{I}_{\text{fourfold}}$ is the unitless interference pattern obtained from Eq. (3.9). Its maximum value $\max\{\mathcal{I}_{\text{fourfold}}\} = \mathcal{I}_{\max} = 16$ if all four beams have the same power.

We determine the eigenstates of the Hamiltonian numerically [208]. To this end, we compute the Hamiltonian matrix elements in the plane-wave basis $|\mathbf{q}, n, m\rangle \sim \exp^{i\mathbf{r}(\mathbf{q}+n\mathbf{b}_x+m\mathbf{b}_y)}$, where $\mathbf{b}_{x,y}$ is the lattice vector in reciprocal space and $\mathbf{q}$ is the quasimomentum in the first Brillouin zone. The non-zero matrix elements arising from the potential part are displayed in Tab. 3.1.

Additionally, we write the kinetic part of the Hamiltonian in terms of the recoil energy by applying a change of variables $x \to \tilde{x} = kx$ and $y \to \tilde{y} = ky$ such that

$$\frac{\hat{\mathbf{p}}^2}{2m} = -\frac{\hbar^2}{2m}\nabla^2_{x,y} = -\frac{\hbar^2 k^2}{2m}\nabla^2_{\tilde{x},\tilde{y}} = -E_R\nabla^2_{\tilde{x},\tilde{y}} \tag{3.12}$$

and the kinetic momentum only adds to the diagonal term of the Hamiltonian, for $n' = n$ and $m' = m$:

$$\langle \mathbf{q}, n, m| - \nabla^2_{\tilde{x},\tilde{y}}\, |\mathbf{q}, n, m\rangle = (q_x + 2n\cos(\phi/2))^2 + (q_y + 2m\sin(\phi/2))^2 \tag{3.13}$$

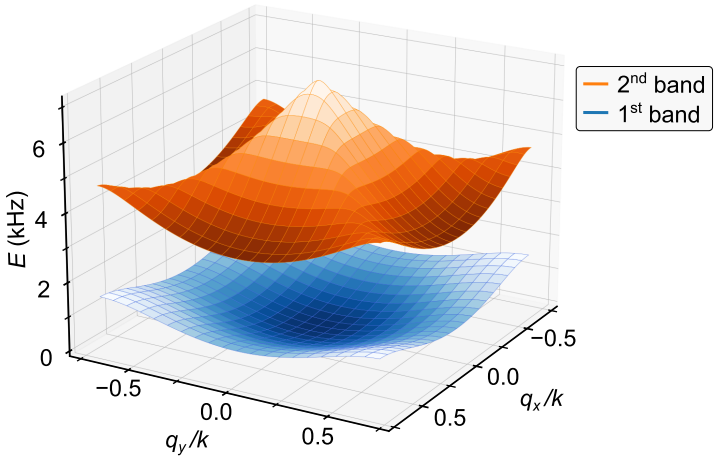

Figure 3.9: First and second band of the fourfold optical lattice. We calculate the band structure with exact diagonalization for a lattice depth of $V_0 = 2.3\,E_\mathrm{r}$. The four beams all have equal intensity and are perpendicular to each other. The tunneling parameter is then $t = h\times 188\,\mathrm{Hz}$ and the interaction parameter $U = h\times 121\,\mathrm{Hz}$ for a vertical confinement of 1.1 kHz.

In the numerical calculation of the eigenvalues and eigenvectors of the Hamiltonian we use a cutoff N_cutoff such that we include $(2N_\mathrm{cutoff}+1)^2$ states for each quasimomentum. Furthermore, the two-dimensional Brillouin zone is discretized into a grid of 101×101 sites. Diagonalization of the Hamiltonian then provides the band structure of the fourfold lattice, shown in Fig. 3.9 for the first and the second band of a two-dimensional, fourfold optical lattice at lattice depth $V_0 = 2.3\,E_\mathrm{r}$ and with a vertical confinement $\omega_z = 2\pi\times 1.1\,\mathrm{kHz}$. The tunneling is typically derived from the Wannier functions. However, as explained in Eq. (3.2), the tunneling is given by the Fourier transformation of the band structure eigenvalues [184]. Therefore, once we determine the band structure with the method described above, we can compute the tunneling in this way, which is a simpler method than dealing with complex lattice structures. For instance, for the band structure shown in Fig. 3.9, we find the tunneling parameter $t = h\times 188\,\mathrm{Hz}$. The interaction parameter is calculated assuming a harmonic approximation for the 2D lattice potential and using the vertical trap frequency given by the light sheet (Sec. 3.2.2). Specifically, for the 2D lattice plane, we find the harmonic confinement that minimizes the energy, which has been shown in [213] to provide a good estimate for U as compared to spectroscopic measurements. For the band structure of Fig. 3.9 with a vertical confinement of 1.1 kHz, we find the interaction parameter $U = h\times 121\,\mathrm{Hz}$. The ratio $t/U = 1.55 \gg 0.06$ which is indeed in the Hubbard regime [214]. These specific parameters will be relevant in the following chapter in Sec. 4.4 where we discuss the experimental detection of a superfluid with the microscope.

The band structure calculation presented here is performed following the procedure described in the master's thesis of M. Miranda, a master student in our group, who developed a theoretical model of our optical lattice and its potential expansions [208].

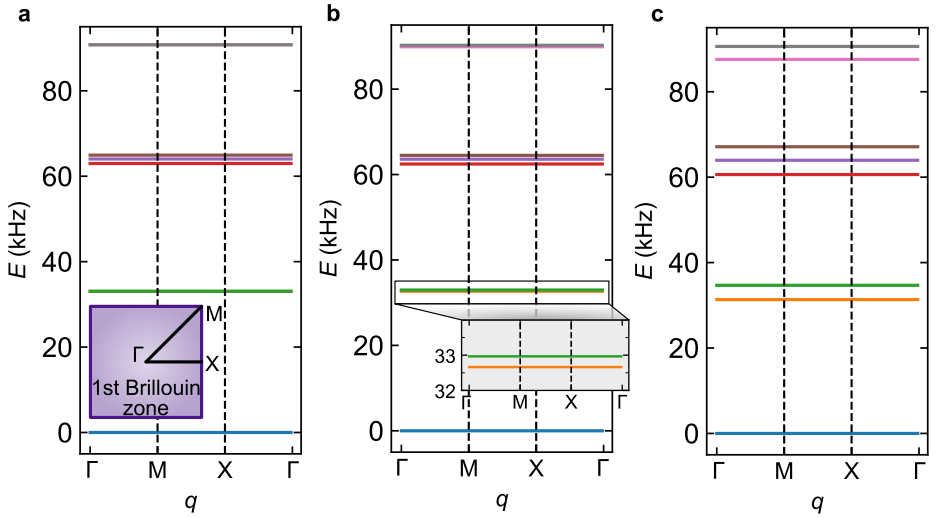

Figure 3.10: Band structures of a $50\,E_\mathrm{r}$ deep lattice in the first Brillouin zone. **a** The band structure for a fourfold optical lattice at $50\,E_\mathrm{r}$ with perpendicular beams and equal power in all of the beams. **b** The power of the beams is reduced by 14 % each time it passes the glass cell, such that the last beam, after passing the glass cell seven times is at 0.86^7 of the initial power. It splits the first excited band into two with 0.3 kHz energy difference. **c** The angle between the beams is at $\phi = 96°$ (measured in the experiment, see Sec. 4.2.2), which causes a splitting of the lowest bands by around 3 kHz.

3.3.3 Lattice parameter dependence

A challenge of a fourfold optical lattice is the power imbalance between the four lattice beams. Since we create the lattice with one beam overlapping four times with itself, each consecutive beam will have reduced power, see Sec. 3.2.2. We compute the band structure of a fourfold optical lattice at $50\,E_\mathrm{r}$ and compare it to the condition given in our experiment.

In Fig. 3.10, the energy of the bands is shown with respect to the quasimomentum q in the first Brillouin zone. The power losses due to the reflections on the uncoated glass cell split the bands by hundreds of Hertz, see Fig. 3.10b. In comparison, the angle between the lattice beams has a larger effect on the splitting. In our experiment, we measured an angle between the beams of $\phi = 96°$ (Fig. 3.4), which results in a 3 kHz splitting of the lowest band, see Fig. 3.10c.

In the Hubbard regime with $V_0 = 2.3\,E_\mathrm{r}$, discussed in Fig. 3.9, the combination of the power attenuation and the alignment of the lattice beams affect the on-site interaction only mildly, it differs by less than 3 % compared to the ideal scenario. However, the tunneling becomes direction dependent: $t_x = h\times 161\,\mathrm{Hz}$ and $t_y = h\times 222\,\mathrm{Hz}$.

To gain a deeper understanding of the effect of the power losses, we compare the losses we have in our system, corresponding to a 86 % transmission with an extreme scenario of only 50 % transmission through the glass cell. In Fig. 3.11, we see that the lattice sites in x-direction form a chain which is separated from the neighboring

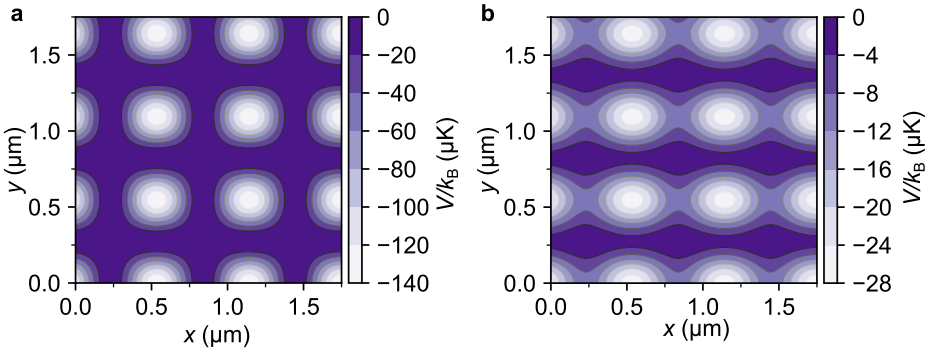

Figure 3.11: Effect of power losses in the lattice beams. **a** The lattice potential for a transmission of 86 % through the glass cell wall, and 96° angle between the lattice beams. **b** Calculation of the potential for more significant power losses of 50 % transmission in the glass cell walls. The potential displays chains in x-direction and is around five times shallower.

sites in y-direction. This is a expensive method in terms of laser power to change the lattice geometry.

3.4 Parametric heating in a microscope

Parametric heating is a common method to measure the trap frequency of optical dipole traps and optical lattices [215, 216, 217]. Its basic principle is captured in the physics of driven oscillators, such as a child playing on a swing [218]. If the child crouches and stands up with the natural frequency of the swing, the motion of the child drives the oscillation and the swing swings higher every turn. For parametric heating, a small modulation is applied to the lattice. If the modulation frequency is twice the trap frequency, vibrational states are excited which induces heating or losses of atoms in the system. The term, parametric heating or parametric excitation refers to the modulation of a parameter causing heating or excitation of the system. In this section, we present the parametric heating performed in the fourfold optical lattice of our quantum-gas microscope, and how we extract the trap frequency. Further, we compare it to the energy of the different bands.

3.4.1 Spatially dependent parametric heating

For the parametric heating measurements, we prepare a cold, but not quantum degenerate, cloud of ^{84}Sr atoms, see Fig. 3.12. The atoms are prepared in the crossed optical dipole trap and the light sheet is ramped up to a depth of around 50 µK. We perform a short evaporation of 5 s during which we exponentially reduce the dipole trap and the light sheet in order to decrease the temperature of the cloud. Then, we increase the light sheet potential to approximately 1.6 µK depth and a vertical trap frequency ω_z of around $2\pi \times 1.1$ kHz before loading the optical lattice. We set the lattice potential at different depths for different measurements of parametric heating

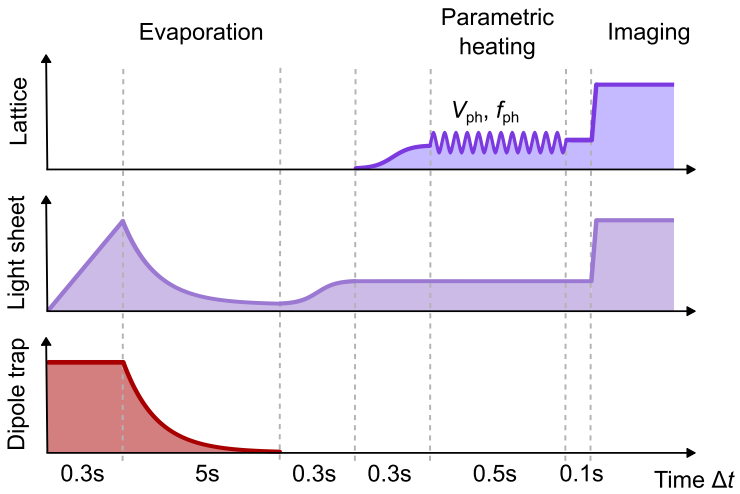

Figure 3.12: Protocol for parametric heating showing optical lattice, light sheet and dipole trap power. After loading the ^{84}Sr atoms into the optical dipole trap and ramping up the light sheet beam power, we perform a 5 s evaporation to reduce the temperature of the atoms. We load the thermal cloud into an optical lattice and modulate the intensity of the trapping potential during 500 ms before increasing the lattice and the light sheet power for imaging. The modulation frequency f_{ph} as well as the depth of the lattice $V_{\mathrm{lat}} = V_{\mathrm{ph}}$ can be varied to measure the trap frequency of the potential.

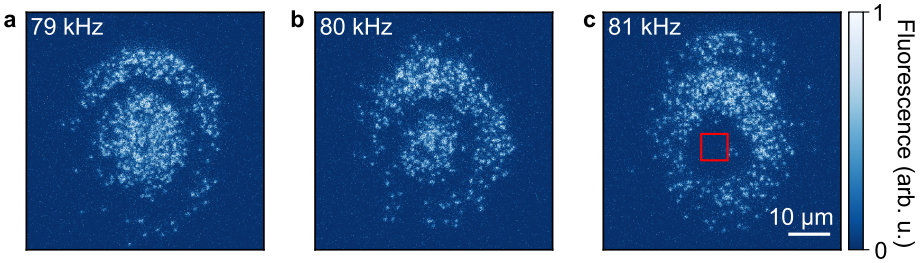

Figure 3.13: Fluorescence of atoms in the optical lattice after parametric heating. The granular structure is due to the single atom resolution, see Ch. 4. The lattice is around 69 E_{r} deep and is modulated at different frequencies **a** 79 kHz, **b** 80 kHz and **c** 81 kHz. The region of interest used to analyse the trap frequency in Fig. 3.14 is indicated by the red square in **c**. The ring shrinks from one shot to the next due to changing the frequency of the lattice intensity modulation.

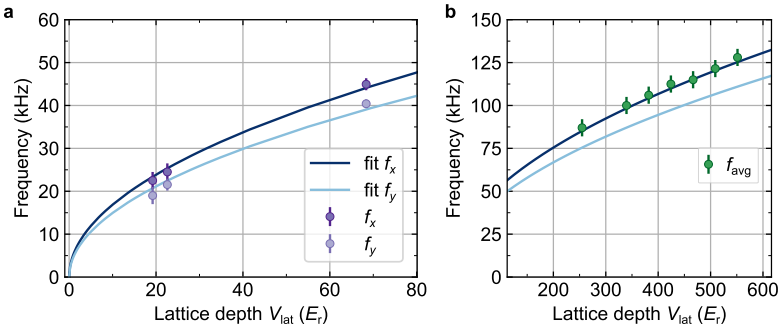

Figure 3.14: Parametric heating resonances used to calibrate the lattice depth. **a** Fit of the resonances to the trap frequencies of the fourfold lattice. Due to difference of the potential in x and y-direction arising from the intensity imbalance and the alignment of the lattice beams, the trap frequencies f_x and f_y are different. For the lattice beams, we assume a Gaussian beam waist of 90 µm and attenuation due to reflections on the glass cell $R \approx 0.14$ (transmittance: $T \approx 0.86$). We add an additional attenuation factor for each of the beams as fit parameter, which corrects additional power losses or misalignment as well as imperfections in the polarization or uncertainty in the beam waist. We find the attenuation of each beam from the fit: $a_1 \approx 0.95$ $a_2 \approx 0.98$ $a_3 \approx 0.77$ and $a_4 \approx 0.88$. **b** Comparison of the fit of f_x and f_y obtained in **a** to the average frequency measured for resonances at deeper lattice potentials f_{avg}, which were not included in the fit. The heating at this depth is not sensitive to the substructure of the bands and instead just displays one broad resonance.

and modulate the power of the beam with 12 % to 16 % of its value V_{ph} during 500 ms. We detect the atoms that survived the heating by means of fluorescence imaging in a deep optical lattice and light sheet potential with single site resolution as it will be discussed in the quantum-gas microscopy chapter (Ch. 4).

The periodic lattice potential is subject to the harmonic potential arising due to the Gaussian beam profile of the tightly focused light sheet beam (3.5 µm $1/e^2$ radial beam waist in vertical direction). This results in a spatial dependence of the trap frequency. The harmonic potential arising from the Gaussian beam profile of the lattice beams has a comparably smaller effect due to the larger beam sizes. In consequence, the resonance frequency observed with parametric heating is spatially dependent. We observe rings where the atoms disappear due to the resonant modulation of the lattice potential, and the radius of the ring changes with the modulation frequency, see Fig. 3.13.

The trap frequency of the optical lattice is estimated for the center of the trap. We scan the modulation frequency and measure the fluorescence signal in the small region in the center of the trap indicated by the red square in Fig. 3.13c. If we match the resonance frequency with the modulation frequency, we heat the atoms in the center and do not detect a fluorescence signal. We repeat the measurement at different lattice depths, namely at 19(1) E_{r}, 23(1) E_{r} and 69(1) E_{r}.

We detect several resonances, which are related to imperfection of the harmonic confinement in the lattice sites arising from the power imbalance and the deviation

from perfect perpendicular alignment. This effect is also captured by the energy levels of the band structure of our fourfold optical lattice, see Fig. 3.10. In order to get an estimate of the optical lattice, we fit the trap frequencies assuming a harmonic confinement in the lattice wells. We apply the specific geometry and parameters of our optical lattice and write the trap frequencies as square root of the Hessian matrix of the lattice potential, see Eq. (3.9). This is important because the lattice potential becomes spatially inhomogeneous when we introduce the power imbalance and the 96° alignment of the lattice beams. We perform a least square fit for the measured trap frequencies where we use the intensity attenuation for each of the beams as free parameter. This allows us to correct the value of the intensity, or deviation in the vertical orientation of the polarization. The fit is displayed in Fig. 3.14 revealing agreement with the measured data, also for higher power which we did not consider for the fit.

The spatially dependent parametric heating might find application in future experiments of state preparations where we can consider implementing a scheme similar to algorithmic cooling presented in [219]. For instance, modulation of the lattice would allow us to modify the lattice occupation.

3.5 Conclusion

In this chapter, we explained the setup for our optical lattice, which forms a bow tie configuration and allows us to overlap one laser beam four times with itself, thus giving rise to a fourfold interference. We presented the differences between our fourfold optical lattice and a twofold optical lattice, where we discussed the change in the geometry and the depth of the lattice wells. With the calculated band structure we studied theoretically the splitting caused by power imbalance and misalignment of the lattice beams. In the experimental setup, the four beams of the lattice vary in power because of the losses in the glass cell wall. We determined the tunneling and the interaction parameters for the lattice used in the following chapter, Ch. 4 Sec. 4.4. We have found that, for a lattice depth of $2.3\,E_\mathrm{r}$ and a two-dimensional confinement of $\omega_z = 2\pi\times 1.1\,\mathrm{kHz}$, we are in fact in the Hubbard-regime, with an interaction $U = h\times 121\,\mathrm{Hz}$ and a tunneling $t = h\times 188\,\mathrm{Hz}$. We concluded the chapter with a demonstration of spatially dependent parametric heating detected in the microscope and used to determine the trapping frequency of the lattice.

Chapter 4

Quantum-gas microscopy in the Bose-Hubbard regime

In this chapter, we present the realization of a strontium quantum-gas microscope in the Bose-Hubbard regime. We discuss the state of the art in quantum-gas microscopy and present an overview of existing quantum-gas microscopes and the techniques implemented to achieve single-atom resolution of different atomic species. Furthermore, we present our imaging setup and the imaging method applied, which we have borrowed from strontium tweezers experiments. We then discuss the imaging performance, the resolution we achieve, the reconstruction of the images to obtain the occupation matrix of the lattice and the pinning fidelity, which describes the hopping and loss events during imaging. In the following part, we delve into our cooling scheme, attractive Sisyphus cooling in the optical lattice, and exploit it to characterize our harmonic trapping potential during imaging. We conclude the chapter by demonstrating the detection of a superfluid in the microscope. To this end, we measure and characterize the interference peaks arising as a result of the phase coherence of our quantum gas.

This work was a team effort between my PhD colleague Dr. Jonatan Höschele, the postdocs Dr. Vasiliy Makhalov and Dr. Antonio Rubio Abadal, supervised by Prof. Dr. Leticia Tarruell. The analysis of the data in Sec. 4.4 was done by myself. In Sec. 4.2, Sec. 4.3 and Sec. 4.4 we discuss the results that were published in [220] more extensively and present additional information and data.

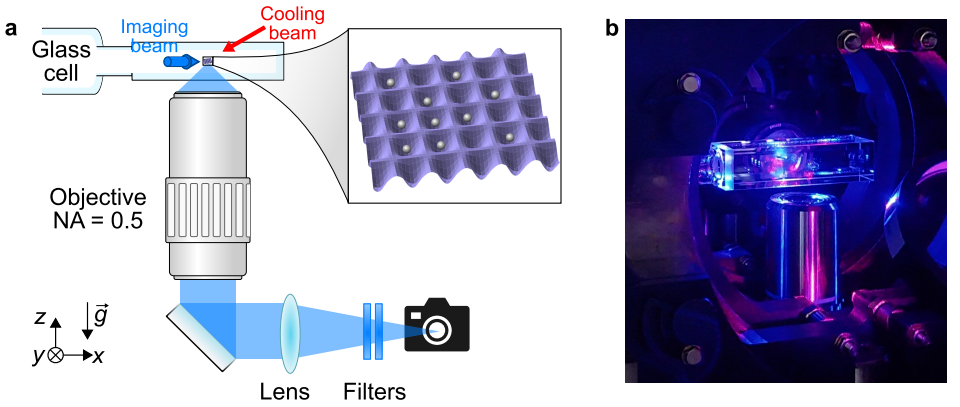

Figure 4.1: Setup of our quantum-gas microscope. **a** Schematic setup of the microscope with the glass cell and the lattice filled with atoms (inset), exposed to an imaging beam (blue arrow) and a cooling beam (red arrow). While we show just one cooling beam, we typically use the six red MOT beams for cooling (Sec. 2.3). The objective placed below the glass cell captures the fluorescence signal of the atoms, and a lens ($f = 500\,\mathrm{mm}$) focuses the image in the camera. Two filters remove light at any undesired wavelength which would cause a background on the images. **b** Photograph of the glass cell and the objective in the lab, while running the experiment. This explains the blue and red lights in the image.

4.1 Microscopy of ultracold atoms

A quantum-gas microscope is an experimental setup capable of detecting quantum gases in optical lattices with single-atom resolution. There are three main components: a quantum gas, typically ultracold atoms in an optical lattice, a high-resolution imaging system, and the imaging light which generates the fluorescence signal of the atoms, see Fig. 4.1. In this section, we discuss the state of the art of quantum-gas microscopy and present an overview of the existing quantum-gas microscopes around the world and the techniques they employ for single-atom resolution. In the second part, our setup is introduced which has the goal of adding strontium to the list of existing quantum-gas microscopes.

4.1.1 State of the art

Quantum-gases in optical lattices have been studied already more than twenty years ago [46]. Also the detection of single atoms in optical lattices is not a recent development [221]. The first realization of an optical lattice system in the Hubbard regime imaged with single-atom resolution was for a quantum gas of rubidium [85]. Since then, other atomic species have been imaged by means of quantum-gas microscopy besides rubidium ^{87}Rb [85, 86, 222, 223, 224, 225]. There are lithium ^{7}Li [226, 227] and cesium ^{133}Cs [228] microscopes for bosonic alkali atoms. For fermionic atoms there are lithium ^{6}Li [97, 229, 230, 231] and potassium ^{40}K [88, 89, 90] microscopes. Non-alkali atoms have been imaged successfully with single-atom resolution

for example with bosonic ytterbium ^{174}Yb [232, 233] and erbium ^{168}Er [234].

To realize the Hubbard model, the ultracold atoms are loaded into optical lattices. Most lattice potentials are the result of interfering laser beams under different angles and with different laser wavelengths, realizing different lattice geometries and spacing. For example, a square lattice with a spacing of 544 nm [232] and of 266 nm [233] have been realized for ytterbium microscopes, and triangular lattices have been demonstrated for rubidium as well as lithium [223, 229]. It is important to notice that the lattice has to operate in two significantly different regimes [235].

On the one hand, there is the so-called physics lattice which is employed to simulate the physics problem at interest, realizing the Hubbard model and studying different regimes and limits. To this end, the atoms should be able to tunnel between lattice sites and interact with each other. On the other hand, there has to be a deep optical lattice that fixes the atoms in their position during the imaging process, which is commonly referred to as pinning lattice. The two regimes are typically realized with the same setup and switching from one to the other involves a change in beam power. However, they can be formed by different beams and even have different lattice spacing [227].

To detect the atoms populating different lattice sites, an imaging resolution on the order of the lattice spacing is required. The most basic configuration is an objective with a high numerical aperture (NA) placed close to the quantum gas, see for example Fig. 4.1a. Depending on the design of the vacuum chamber and the lattice spacing, an objective might not resolve the atoms well enough. Adding a hemispherical lens to the vacuum viewport can increase the NA of the imaging system through solid immersion [236], as it has been realized in several quantum-gas microscope experiments [85, 88, 226, 232]. Another option is to place the objective inside vacuum, which can quickly turn into a "ship in a bottle" problem [234, 237].

Having the quantum-gas in the lattice and the high-resolution imaging system, only the signal to detect the atoms is missing. To achieve that, the atoms are excited with a resonant or near-resonant imaging beam (blue arrow in Fig. 4.1), and the fluorescence photons which arise from the spontaneous decay back into the ground state are used for the detection. The challenging part of this process, is to keep the atoms trapped despite the recoil heating, which arises due to the scattering of the imaging photons from the imaging beam. Therefore, a crucial ingredient of the imaging is to cool the atoms in order to counteract the recoil heating. The cooling methods applied vary depending on the atomic species. For example, polarization gradient cooling has been exploited for the rubidium quantum-gas microscopes [85, 86]. Another method is Raman sideband cooling also applied to rubidium but equivalently used for various other alkali atoms [88, 226, 227, 223, 229, 230]. Electromagnetically induced transparency (EIT) cooling was demonstrated for fermionic potassium quantum-gas microscopes [89, 90]. The cesium quantum-gas microscope uses molasses cooling [228]. For bosonic ytterbium the cooling methods are quite different since the lack of a hyperfine structure rules out sub-Doppler cooling. Realizing a deep optical lattice in the excited state such that cooling is not required [232], or exploiting the narrow-linewidth transition at 556 nm wavelength to perform narrowline optical molasses cooling [233]

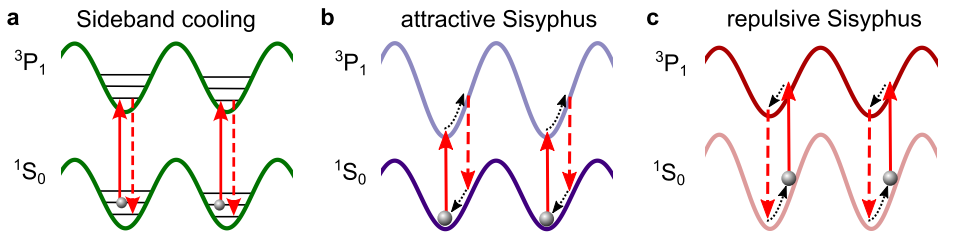

Figure 4.2: Cooling methods for single-atom imaging of strontium. **a** Sideband cooling in a magic potential where the ground state $|g\rangle = |^1\mathrm{S}_0\rangle$ and the excited state $|e\rangle = |^3\mathrm{P}_1\rangle$ experience the same light shift and thus have the same trapping frequency, $\omega_g = \omega_e$. This allows to reduce the motional quantum number through excitation of the red sideband transition (solid arrow) [115, 163, 238]. **b** For attractive Sisyphus cooling [109], the light shift for the ground state is smaller than for the excited state such that $\omega_g < \omega_e$. Atoms in the center of the lattice site are excited by means of 689 nm light. Through spontaneous emission the energy of the atoms is reduced as the emitted photon will be more energetic than the absorbed one due to the steeper potential in the excited state. **c** Repulsive Sisyphus cooling uses the same cooling transition as the other two methods, but the light shift of the ground state is stronger than for the excited state such that $\omega_g > \omega_e$ [115, 200].

are two options that have been explored.

Single-atom imaging of strontium

With the goal to add a strontium to this list of existing quantum-gas microscopes, we present an overview of the methods used in optical tweezers to detect single strontium atoms. The physics goals of optical tweezers experiments differ from the one of optical lattices, however, the methods of single-atom detection can be applied in the same fashion in both systems. Typically, the fluorescence signal is induced by a imaging beam at 461 nm addressing the broad-linewidth transition. For the cooling, to counteract the recoil heating during imaging, a convenient choice is the narrow-linewidth transition at 689 nm which excites the atoms from the ground state $^1\mathrm{S}_0$ to the excited state $^3\mathrm{P}_1$.

There are three different methods commonly used to cool strontium in an optical potential during imaging, see Fig. 4.2. The methods heavily depend on the differential light shifts arising form the trapping light. For example, in the magic condition, where the ground and the excited state experience the same light shift and thus the trapping frequencies are equal ($\omega_g = \omega_e$) [107, 203], resolved sideband cooling during imaging was successfully demonstrated for strontium in optical tweezers [115, 163] and later in optical lattices [238]. If the trapping potential is state-sensitive, Sisyphus cooling can be applied [198, 199]. Repulsive Sisyphus cooling has been demonstrated in optical tweezers experiments [115] and optical lattices [200]. Attractive Sisyphus cooling for strontium was shown in optical tweezers [109] but has not been realized in optical lattices.

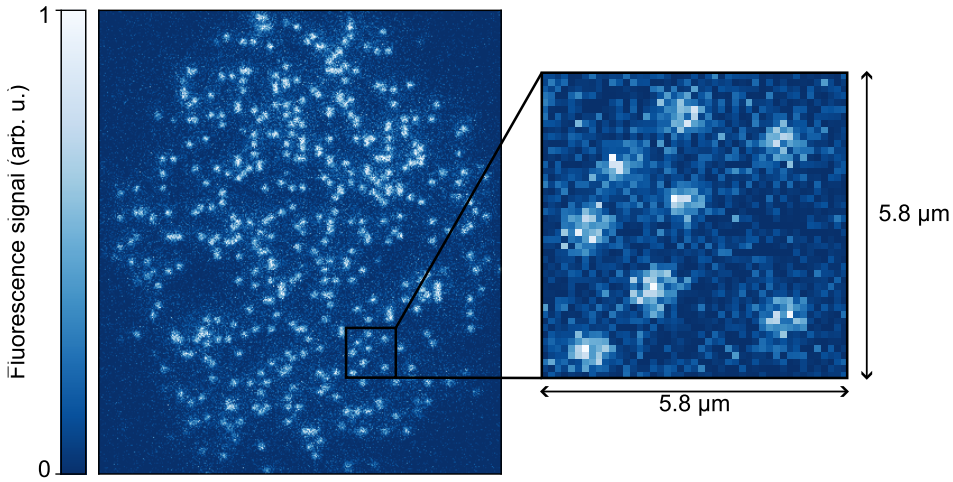

Figure 4.3: Raw fluorescence image of hundreds of ^{84}Sr atoms. A dilute thermal cloud was loaded into an optical lattice. The inset shows around 10×10 lattice sites occupied with eight atoms.

4.1.2 Our strontium microscope

Our strategy to demonstrate quantum-gas microscopy of strontium consists of a square optical lattice, a small glass cell, a high-NA objective and an EMCCD camera, see Fig. 4.1. We exploit blue transition for fluorescence and implement attractive Sisyphus cooling on the red transition to obtain images as in Fig. 4.3.

We trap the strontium atoms in a fourfold optical lattice operated at the clock-magic wavelength $\lambda = 813.4\,\text{nm}$, see Ch. 3. The fourfold geometry leads to a spacing of $\lambda/\sqrt{2} \approx 575\,\text{nm}$. The lattice serves first as physics lattice and then at increased laser power as pinning lattice during imaging. The fourfold geometry allows us to create deeper lattices compared to a twofold interference (Sec. 3.2), which is beneficial in particular for the pinning lattice. We confine the atoms into a two-dimensional plane by means of a vertically tightly focused light sheet beam with a beam waist of 3.5 µm ($1/e^2$ waist in gravity direction).

The science chamber containing the two-dimensional optical lattice is a small uncoated quartz glass cell with internal volume of $60 \times 13 \times 10\,\text{mm}^3$ (length × width × height) and a wall thickness of 3.5 mm, see Fig. 4.1. For the high resolution imaging, we place a custom objective[1] close to the quantum-gas but outside vacuum. The objective has a NA= 0.5 and a focal length $f_{\text{obj}} = 4\,\text{mm}$. The working distance is 15.08 mm and corrected for the 3.5 mm thick wall of the glass cell.

The objective captures the blue fluorescence photons and as shown in Fig. 4.1a they are reflected on a 45° mirror[2], passed through an achromatic lens[3] with a focal

[1] Mitutoyo G Plan Apo 50X Objective, infinity corrected, working distance 15.08 mm through compatible cover glass (thickness 3.5 mm), wavelength range 436−656 nm.

[2] Broadband Dielectric Mirror, 400-750 nm (BB2-E02, Thorlabs)

[3] Achromatic doublet, focal length 500 mm (ACT508-500-A, Thorlabs)

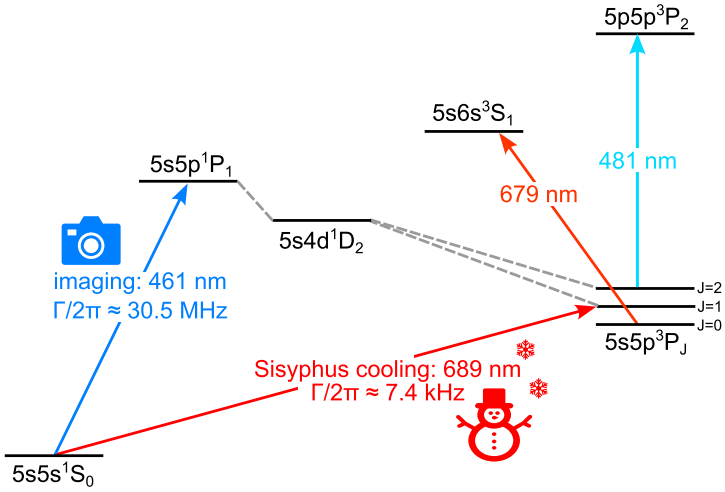

Figure 4.4: Transitions relevant for single-atom imaging. We excite the atoms with the broad-linewidth blue transition (at 461 nm) to obtain the fluorescence signal. Since it is not a closed transition (see grey dashed lines indicating decay channels), we need to apply the two repumper lasers for the $^3P_2$ and the $^3P_0$ states. During imaging we use the narrow-linewidth red transition (at 689 nm) for attractive Sisyphus cooling.

length of $f_{\text{lens}} = 500\,\text{mm}$ and focused on the EMCCD camera[4] (Electron Multiplying CCD). With this imaging system, we achieve a magnification of $\mathcal{M} = 125$. The EMCCD camera has 512×512 active pixels, and the pixel size $p_s^2 = 16\,\mu\text{m} \times 16\,\mu\text{m}$. With our lattice spacing of 575 nm we have 4.5×4.5 pixels per lattice site available.

In order to keep light at undesired wavelengths out of the camera, we add two filters[5] of the same type to select only the desired imaging wavelength.

We chose the blue transition at 461 nm for fluorescence imaging because of the short wavelength and the broad linewidth of $\Gamma_{\text{blue}}/2\pi \approx 30.5\,\text{MHz}$, see Fig. 4.4. To generate the fluorescence photons, we illuminate the atoms with a blue laser beam with an intensity $I \approx 0.6 \times 10^{-3}\, I_{\text{s,blue}}$ and $\delta \approx 2\,\Gamma_{\text{blue}}$ red-detuned from resonance, where $I_{\text{s,blue}} = 41\,\text{W/cm}^2$ is the saturation intensity of the blue transition. The light of the imaging beam propagates in the plane such that there are as few background photons as possible detected on the camera. The polarization is horizontal, which is the optimal condition considering the dipole emission pattern of the scattered photons [137]. We estimate a scattering rate of around 3400 photons per second per atom. We expect to capture around 5.6 % of the total scattered photons, due to the limited collection efficiency of the objective [137] and the losses in the imaging system (see Ch. 5, Tab. 5.3 for details and a comparison with 689 nm light). For a typical image of single bosonic atoms, as shown in Fig. 4.3, we detect around 300 photons per atom during a 3 s exposure. This is less then expected from the numbers stated before. It arises on the one hand, because the atoms leak into the metastable states, from where

[4] Andor 897 Ultra, active pixels 512×512, pixel size $16 \times 16\,\mu\text{m}$.

[5] For blue imaging: 461/5 nm BrightLine® single-band bandpass filter (FF01-461/5-25, Semrock), transmission >90 % at 458−463.5 nm.

we recover them by drive the repumper transitions, see Fig. 4.4 and Sec. 2.2.2. On the other hand, and more importantly, due to the cooling during imaging, the atoms spend less time in the ground state, and thus scatter less blue photons.

We drive the red transition during imaging in order to cool the atoms by means of attractive Sisyphus cooling. As discussed in Sec. 4.1.1, there is also sideband cooling, which requires a magic trapping potential, where the ground state and the excited state have the same trapping frequency (Fig. 4.2a and repulsive Sisyphus cooling which relays on a deeper trapping potential of the ground state in contrast to the excited state, which results in a larger trapping frequency of the ground state compared to the excited state, $\omega_g > \omega_e$, see Fig. 4.2c. In our experiment we exploit attractive Sisyphus cooling where we have a weaker trap in the ground state compared to the excited state, $\omega_g < \omega_e$. The basic principle is displayed in Fig. 4.2b. Atoms are selectively excited near the center of the lattice sites. This is possible thanks to the narrow linewidth $\Gamma_{\mathrm{red}}/2\pi \approx 7.4\,\mathrm{kHz}$ of the transition. Due to their kinetic energy, the atoms will oscillate in the excited state potential until they spontaneously decay back to the ground state. The spontaneous decay is likely to happen away form the trap center. Due to the deeper trapping potential of the excited state, the emitted photon carries part of the energy of the atom, resulting in cooling.

We exploit the existing six red MOT beams for Sisyphus cooling of ^{84}Sr, however, one beam would be sufficient [109]. We set the light on resonance and apply an intensity on the order of $1000\,I_{\mathrm{s,red}}$, where $I_{\mathrm{s,red}} = 2.96\,\mu\mathrm{W/cm^2}$ is the saturation intensity of the red transition. The beams have the same circular polarization as the MOT beams while the magnetic field is parallel to the polarization of the lattice and the light sheet beams.

For efficient in-trap cooling, it is typically required to be in the Lamb-Dicke regime where the Lamb-Dicke parameter $\eta = \sqrt{\hbar\pi/(m\omega\lambda^2)} < 1$ meaning that the trapping frequency dominates the recoil frequency of the scattered photon, see Sec. 3.2.2. While we are well below the limit in x- and y-direction ($\eta_{x,y} \approx 0.2$), the value in z-direction is with $\eta_z \approx 0.9$ rather large in comparison. However, we have observed efficient cooling even with this weak vertical confinement, which is consistent with the results presented in [104] where they demonstrate attractive Sisyphus cooling in shallow optical tweezers.

4.2 Single-atom resolution in the optical lattice

With the setup and methods described above we are able to take images of the ^{84}Sr atoms in the optical lattice. This section addresses the characterization of the resolution in our imaging system by means of the point spread function. The reconstruction of the optical lattice occupation is also discussed. The performance of our imaging is presented by analysing hopping and losses during the detection process.

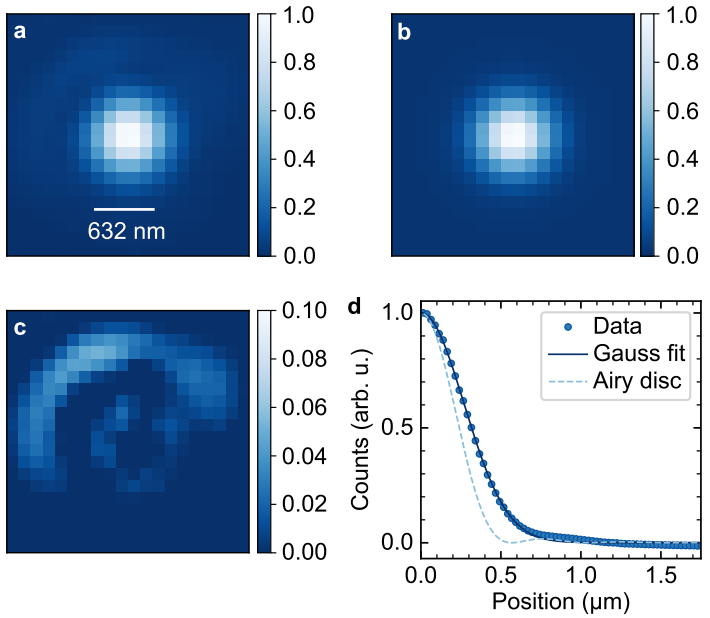

Figure 4.5: Point spread function of our imaging system. **a** Image obtained by averaging over 1187 individual atoms. From the Gauss fit **b**, we find a full width at half maximum of 632(3) nm. The residual in **c** is obtained from the difference of the averaged atoms and the Gaussian fit. The color scale is a tenth of the one in **a** and **b**. **d** The azimuthal average of the point spread function (dots) with the Gauss fit (solid line), which is a good approximation for the signal. The theoretical Airy disc of our imaging system is displayed by the dashed line.

Lattice spacing	575 nm
Imaging wavelength	461 nm
Theoretical Airy disc (FWHM)	562 nm (470 nm)
Experimental Gauss fit FWHM	632(3) nm

Table 4.1: Resolution for imaging with the blue transition of strontium. The theoretical values of the radius of the Airy disc and its FWHM (full width at half maximum) are given using Eq. (4.2). The value of the Gauss FWHM is obtained from fitting the averaged signal of the atoms, see Fig. 4.5.

4.2.1 Resolution and point spread function

The resolution of the imaging system can be characterized by measuring the response to a point source. The resulting point spread function has an intensity profile that follows the Airy function [239]

$$I_{\text{Airy}} = I_0 \left[\frac{2J_1(\rho)}{\rho}\right]^2 \tag{4.1}$$

where the intensity distribution depends on the first order Bessel function $J_1(\rho)$ and ρ is proportional to distance r from the center of the point source. The first zero of Eq. (4.1) determines the size of the Airy disc and can be calculated from the imaging wavelength λ and the NA of the objective:

$$r_0 = 1.22\frac{\lambda}{2\text{NA}}\,. \tag{4.2}$$

The Rayleigh criterion states that if two point sources are more than one Airy disc apart, they can be resolved as two individual points. For this reason, we design the imaging system such that the Airy disc is smaller than the lattice spacing of 575 nm. Having a imaging wavelength $\lambda = 461$ nm and an objective with NA $= 0.5$, the Airy disc is around 562 nm and its full width at half maximum is approximately 470 nm, see Tab. 4.1.

The actual resolution achieved in the experiment is detected from the signal of individual atoms. They can be approximated as point sources emitting photons. Thus, an ideal image of an atom is described by the Airy function (Eq. (4.1)), such that the resolution can be experimentally measured by means of the signal of the atoms. To this end, we load a thermal cloud with few atoms into the optical lattice. We detect individual atoms which are well separated from each other. Averaging 1187 signals of these single atoms and fitting them with a Gaussian function, we find a point spread function with a full width at half maximum (FWHM) equal to 632(3) nm, see Fig. 4.5. Even though this value is larger than the lattice spacing, having the additional information about the lattice geometry still allows us to reconstruct the lattice occupation for the images. In even more extreme cases, where the point spread function

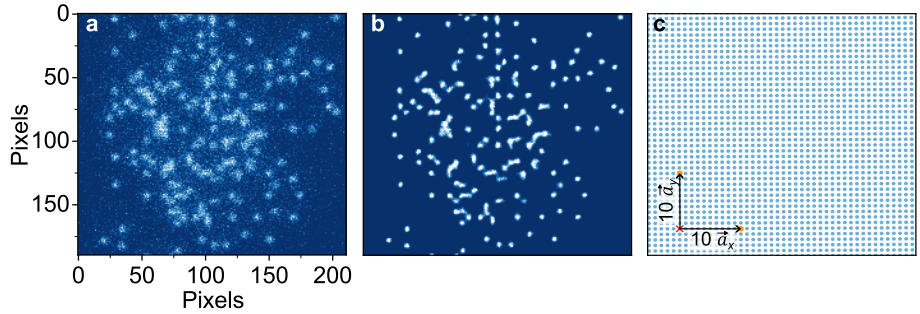

Figure 4.6: Deconvolution and reconstruction of images to obtain the lattice grid. **a** Raw fluorescence signal captured for a dilute cloud of thermal atoms. **b** The raw image is processed by a deconvolution with the point spread function, which results in more distinct point like signals. For the deconvolution, we perform 15 iteration with the Richardson-Lucy algorithm [240, 241]. Through Fourier transformation of the deconvolved image we obtain the lattice vectors $\vec{a}_x$ and $\vec{a}_y$ which allow us to reconstruct the lattice grid shown in **c**. There, the size of the lattice vectors is multiplied by a factor of ten for better visibility. The three images show all the same field of view.

spans over several lattice sites, reconstruction of the lattice occupation through unsupervised deep learning methods has been demonstrated successfully for quantum-gas microscopes [228].

4.2.2 Deconvolution and reconstruction

To obtain information about the microscopic properties of the cloud, the lattice occupation has to be reconstructed from the fluorescence images. In a first step, we process the images by performing a deconvolution with the measured point spread function of Fig. 4.5a. We deconvolve the raw image (Fig. 4.6a) with 15 iterations of the Richardson-Lucy algorithm [240, 241] obtaining images as the one shown in Fig. 4.6b. In an ideal deconvolution the fluorescence signal of the atoms can be traced back to its original point source, removing the resolution limited detection of the imaging system. Applying a 2D Fourier transform on the deconvolved images allows us to calculate the lattice vectors $\vec{a}_x$ and $\vec{a}_y$ which make it possible to reconstruct the lattice grid, see Fig. 4.6c. For a detailed study of the deconvolution and the reconstruction see the Ph.D. thesis of J. Höschele [119].

Knowing the lattice grid, we bin the counts of the single-atom images to each lattice site. The result is the histogram in Fig. 4.7a, which displays the number of photon counts and their occurrence. There are two distinct peaks arising. The one at zero is related to the lattice sites with no atoms, and the one around 300 photons shows the occurrence of lattice sites with atoms. We set the threshold for an occupied or an empty lattice site in between the two peaks and can then obtain the occupation matrix of the image, see Fig. 4.7b. From a double Gaussian fit of the two peaks in the histogram, we find that more than 99.9 % of the occupied lattice sites are above the threshold. In fact, an occupied lattice site will have exactly one atom. This is

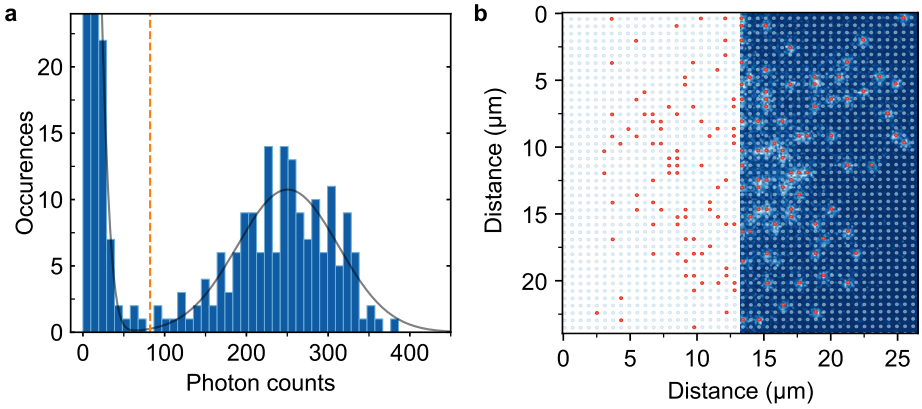

Figure 4.7: Histogram and reconstructed occupation matrix. **a** For each lattice site we count the number of detected photons and plot it in a histogram. The double peak is an indication for the quality of our imaging system, it shows that we can distinguish zero-atoms from one-atom lattice sites. The threshold separating the two regimes is indicated by the red dashed line. **b** Occupation of the lattice with light blue dots representing no atoms, and red dots lattice sites where we detected an atom. For comparison, we overlap half of the matrix with the raw fluorescence image. We converted pixels to distance using the magnification measured (see text).

due to light-assisted inelastic collisions arising form the imaging and the cooling light [242, 243]. If there are two atoms in the same lattice site, the excitation of the atoms increases the interaction energy which leads to the loss of both atoms. In consequence, any lattice site with an even number of atoms, suffers from those losses such that no atom will be left. While in a lattice site with an odd number of atoms, one atom will be left after the collisional losses and will be detected as occupied. This is referred to as parity projection, we only detect even or odd numbers of atoms per lattice site [85, 86].

Additionally, from the lattice vectors of the reconstructed images we extract the magnification and the real lattice spacing. The lattice vectors obtained from the Fourier transformation tell us the distance between two lattice sites in units of pixels given by $\tilde{a}_x$ and $\tilde{a}_y$. The real distance is given through the magnification $\mathcal{M}$ and the pixel size $p_s = 16\,\mu\text{m}$ as

$$a_{x,y} = \frac{\tilde{a}_{x,y}\, p_s}{\mathcal{M}}. \tag{4.3}$$

Furthermore, the lattice spacing can be expressed in terms of the angle α between the lattice beams as

$$a_{x,y} = \frac{\lambda_\text{L}}{2} \frac{1}{\sin \alpha_{x,y}} \tag{4.4}$$

where λ_L is the wavelength of the lattice laser, see Fig. 4.8. Plugging Eq. (4.3) into Eq. (4.4) and applying that $\alpha_x + \alpha_y = 180°$, we find a magnification $\mathcal{M} = 126.7(3)$ for our imaging system. The uncertainty was determined from the uncertainty of defining the lattice vectors from the Fourier transformation.

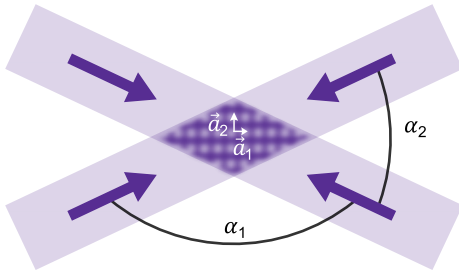

Figure 4.8: Lattice spacing and angles of the lattice beams. For an optical lattice formed by fourfold interference as described in Sec. 3.2 the angle between the beams determines the lattice spacing. Since the counterpropagating beams are overlapped, the angles fulfill $\alpha_1 + \alpha_2 = \pi$.

To conclude, we calculate the lattice spacing in real space $(a_x, a_y) = (608(1)\,\text{nm}, 547(1)\,\text{nm})$ which is anisotropic due to an around 6° deviation of the lattice beams from a perfect perpendicular alignment.

4.2.3 Imaging performance

For reliable imaging of single atoms it is crucial that the atoms are preserved and stay in their lattice sites during imaging. This is why the pinning lattice should be as deep as possible. We analyse the performance of our imaging protocol by taking ten consecutive pictures of the same atomic cloud. In Fig. 4.9a three deconvolved images of a sequence of ten such pictures are presented. The exposure time for each image is 3 s, which is the time of the first picture. Due to time the camera takes to process the image, the second picture was taken at 6.35 s and the last one at 33.15 s. While taking the ten pictures, we expose the atoms continuously with the blue imaging and the red cooling beams. The different colored circles in the pictures indicate atoms in the lattice, losses or hopping events where an atom moved to a new lattice site. While there are 37 atoms lost after 33.15 s of imaging in the last picture, there are only three losses from the first to the second image.

We can gain a better understanding of the evolution by comparing photon counts in each lattice site from one picture to another. Fig. 4.9b compares the first and the second and Fig. 4.9c compares the first and the last image. The plots are separated in four areas given by the threshold between zero-atom and one-atom case. The vertical dashed line is the threshold of image 1, and the horizontal line is the threshold of image 2. Points in the bottom left regime indicate empty lattice sites in both images, and points in the upper right regime indicate lattice sites with an atom in both images. While in Fig. 4.9b most of the points are in these two regimes, there are few lattice sites that have only an atom in one of the two lattice sites. If the atoms are only detected in the first image, that means the atom left the lattice site during imaging, it either got lost or hopped to another lattice site (lower right regime). If photons are only detected in lattice sites of the second image, an atom hopped into this lattice site (upper left regime). Comparing the first and the last image with this method (Fig.

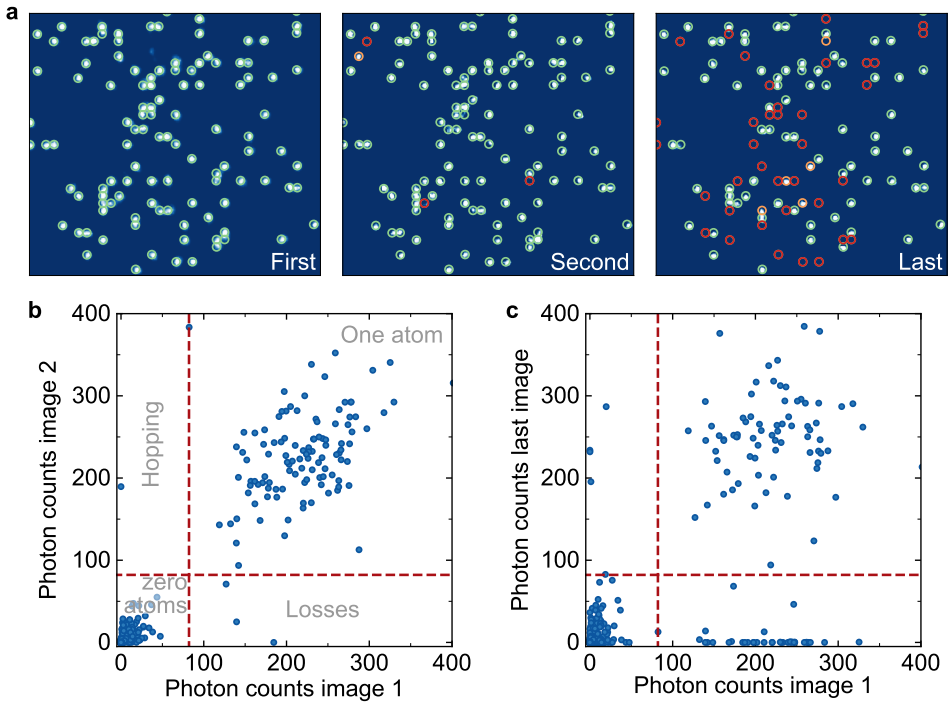

Figure 4.9: Performance of our fluorescence imaging for long imaging times. **a** A series of ten images was taken, with 3 s exposure and a total imaging time of 33.15 s. Shown are the deconvolved images ($51\times38\,\mu m^2$), the first one at 3 s, the second at 6.35 s and then also the last one of the series. The green circles indicate atoms that stay in their lattice site, the red circles are lost atoms and the orange ones atoms that appeared in comparison to the first image. We compare the photon counts at each lattice site for two pictures of the same cloud. The two red dashed lines are threshold between zero and one atom. It splits the **b** and **c** in four areas corresponding to zero-atoms, one-atom, hopping events, or loss of the atom. **b** Comparison of the first and the second picture. **c** Comparison of the first and the last picture. Having the points on a diagonal is an evidence for good imaging performance, as it means that the photon counts per lattice site were comparable in the two images.

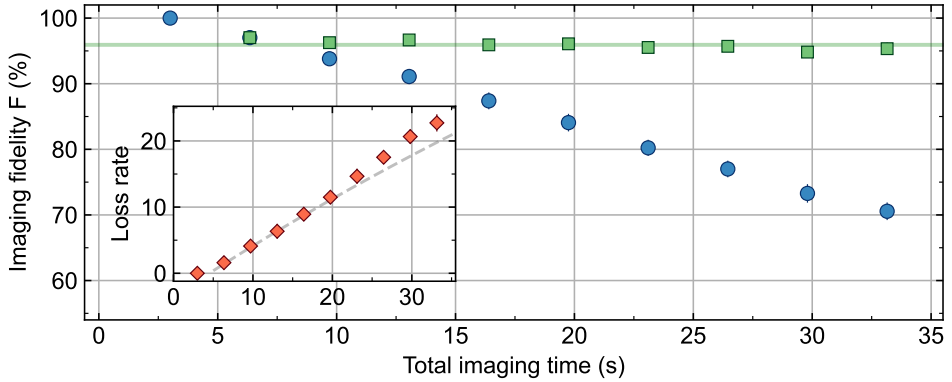

Figure 4.10: Performance of the site-resolved imaging. **a** Pinning fidelity measured as a function of the imaging time where we capture several images of the same cloud during 33.15 s with several repetitions. The blue circles are the evolution of the occupation compared to the first image taken, the error bars indicate one standard error of the mean. We also compare two consecutive images (green squares) and find that the fidelity of consecutive shots averages to around 96 %. The loss rate (inset) is comparable to the losses detected in the optical lattice.

4.9c), we see that still many of the data points are in the two diagonal regimes, with some losses and some hopping events occurring.

To quantify the performance of our imaging, we measure the pinning fidelity alongside loss and hopping rates. The loss rate L represents the ratio of atoms lost during the imaging process. It can be described as

$$L = \frac{\sum_{i,j} m_{ij} - \sum_{i,j} n_{ij}}{\sum_{i,j} m_{ij}} \tag{4.5}$$

where $\mathbf{M} = (m_{ij})$ is the occupation matrix of the first image and $\mathbf{N} = (n_{ij})$ the occupation of the second image. The sum over the matrix elements m_{ij} counts the number of atoms detected in the image.

The hopping rate H describes the ratio of atoms changing their lattice site from one shot to another. Subtracting the occupation of the second image from the first gives zero if there was no atom, or one atom in both images. The difference is $+1$ if the atom was lost in the second image and -1 if the atom hopped into the lattice site in the second image. The hopping can be calculated as the changes of occupation minus the losses and is given as

$$H = \frac{\sum_{i,j} |(m_{ij} - n_{ij})| - (m_{ij} - n_{ij})}{2 \sum_{i,j} m_{ij}}. \tag{4.6}$$

We define the pinning fidelity $\mathcal{F}$ as the ratio of atoms that stay in their exact site from one image to another. It is given by the loss rate (Eq. (4.5)) and the hopping rate (Eq. (4.6)) through

$$\mathcal{F} = 1 - (L + H) \tag{4.7}$$

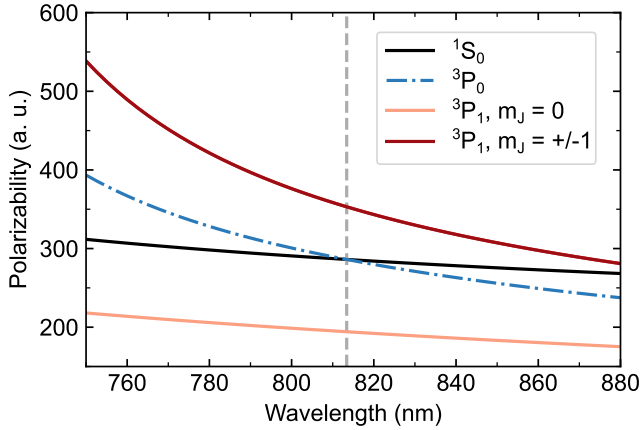

Figure 4.11: Wavelength and state dependent polarizability for the bosonic isotope (see Appx. B, Eq. (B.1)). Our trapping laser operates at 813.4 nm, see dashed vertical line. This is the magic wavelength for the clock state $^3P_0$ (dotted-dashed line), where $\alpha(^1S_0) = \alpha(^3P_0)$. For the $^3P_1$ state, the condition for attractive Sisyphus cooling is fulfilled for $m_J = \pm 1$, while $m_J = 0$ fulfills the criteria for repulsive Sisyphus cooling.

The evolution of the fidelity is shown in Fig. 4.10, and example images were presented in Fig. 4.9. During 35 s of imaging we track the hopping and loss mechanism. We distinguish between pinning fidelity compared to the first image of the series and a comparison between consecutive images. The pinning fidelity during the 35 s of taking images is reduced to around 70 %, however, from one shot to another it stays around 96 %. We find an average hopping between two images of around 1.3(4) % and an average loss rate of around 2.8(7) %, where we have considered 36×36 lattice sites in the analysis. The losses as a function of imaging time, see inset in Fig. 4.10, follow the losses we see in the lattice characterized by an exponential decay constant of $\tau_{\text{loss}} = 130(5)$ s, without blue imaging but with red cooling light. This is evidence that the blue imaging parameters chosen result in negligible losses of the imaging process itself.

4.3 Attractive Sisyphus cooling

A crucial part for high pinning fidelity is the cooling during imaging. The bosonic strontium atoms are cooled by means of attractive Sisyphus cooling, see Fig. 4.2b. To this end, the atoms are excited from the ground state $^1S_0$ to the excited state $^3P_1$ through the narrow-linewidth transition at 689 nm. Due to the stronger trapping in the excited state the atom energy is reduced through spontaneous emission. This section focuses on the cooling spectrum and the phenomena arising due to the narrow-linewidth cooling transition.

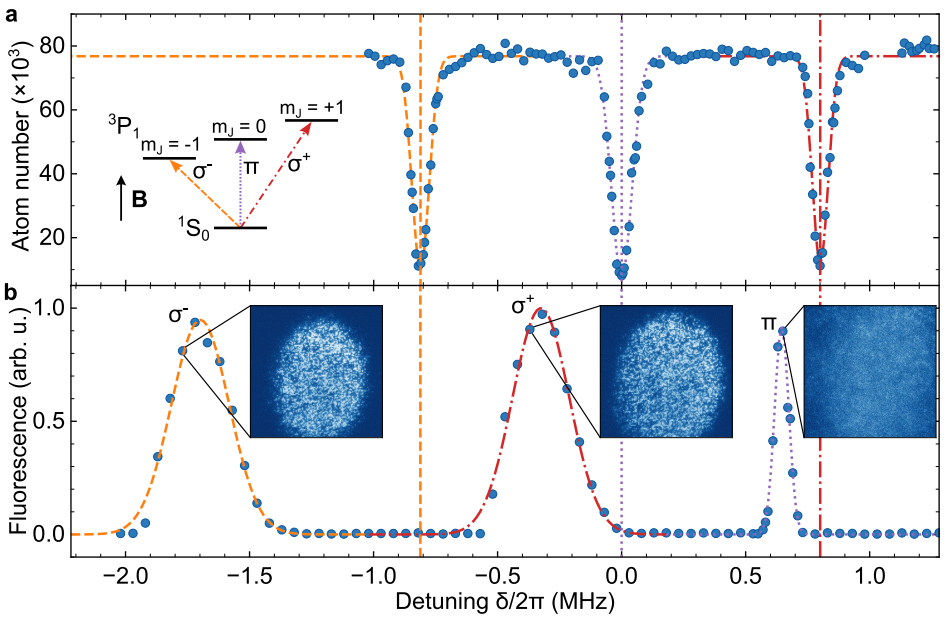

Figure 4.12: Resonances of the red transition for ^{84}Sr. **a** The bare resonances were measured in free space by counting atom numbers from absorption imaging (blue circles) after exposure with red pulse at different detuning δ. The $\sigma^{-/+}$ transitions, corresponding to $m_J = -1, +1$ (orange dashed, and red dotted-dashed lines) are Zeeman split by $\pm 0.8\,\mathrm{MHz}$ around the π resonance ($m_J = 0$, purple dotted line). The inset shows the split m_J states related to the transitions which were detected in the measurement (σ^-, π, σ^+). **b** The fluorescence signal of the single-atom images (blue circles) depends on the performance of the cooling and therefore the detuning δ of the red cooling light. The lattice and light sheet potential shift the resonances. The insets display the fluorescence images at different detunings with full field of view. When exciting the π transition, the images are blurry (around $0.65\,\mathrm{MHz}$ detuning). Both σ transitions show efficient cooling performance and nice single-atom images. The peaks are fitted to three independent Gaussian functions.

4.3.1 Sisyphus cooling spectrum

The excited state has a total electronic angular momentum of $J = 1$. Therefore, under the influence of a non-zero magnetic field, it splits into three non-degenerate substates $m_J = -1, 0, +1$ with different polarizabilities, see Fig. 4.11. The $m_J = \pm 1$ substate has $\alpha_e = 353.9\,\text{a.u.}$[6] and $m_J = 0$ has $\alpha_e = 195.1\,\text{a.u.}$ [137]. Meanwhile, the ground state has no electron spin, and therefore $J = 0$ and the polarizablility is $\alpha_g = 286.0\,\text{a.u.}$ [137].

We perform free space spectroscopy of the Zeeman-split resonances. To this end, we load the atoms into the dipole trap and expose the atoms to the 689 nm light during 0.5 ms while all the trapping potentials are off. We detect the number of surviving atoms in absorption images. We find the three transitions σ^-, π, σ^+ corresponding to $m_J = -1, 0, 1$, see Fig. 4.12a. The bare resonance is given by the magnetic insensitive π transition which we set to zero detuning δ. The magnetic field $\mathbf{B}$ oriented along z-direction is the same that is applied during fluorescence imaging. It shifts the two σ transitions by $\delta/2\pi \approx \pm 0.8\,\text{MHz}$ which is more than 100 times larger than the linewidth of the transition.

When measuring the spectrum of the red cooling frequency by observation of the single-atom images, we find three signals at distinct frequencies, see Fig. 4.12b. The two red-shifted peaks correspond to the $m_J = \pm 1$ states. The shift arises due to the light shift caused by the lattice and light sheet potential. The larger polarizability of the excited state compared to the ground state results in efficient attractive Sisyphus cooling, as shown in the inset of Fig. 4.12b where we observe well resolved individual atoms. The blue-shifted signal around $\delta/2\pi \approx 0.65\,\text{MHz}$ excites atoms to the $m_J = 0$ state which has a weaker trapping potential than the ground state due to its smaller polarizability. Thus the atoms cannot be cooled by means of attractive Sisyphus cooling and the images are blurry and not well resolved. However, the $m_J = 0$ state fulfills the condition for repulsive Sisyphus cooling, see Fig. 4.2, which has been demonstrated in a lattice with a wavelength of 1040 nm [200].

4.3.2 Spatially dependent cooling

As discussed above, Sisyphus cooling is efficient around resonance which depends on the Zeeman splitting and the ac Stark shift arising from the trapping potentials. Consequently, the cooling performance is sensitive to the overall harmonic confinement arising from the tightly focused light sheet and the finite sized lattice beams, see Fig. 4.13, which give rise to a spatially inhomogeneous light shift.

In fact, with the red transition having a linewidth $\Gamma/2\pi \approx 7.4\,\text{kHz}$ we are able to resolve the spatially dependent light shift in our system. The tightly focused light sheet beam changes the light shift notably in the field of view of our imaging system ($64.5 \times 64.5\,\mu\text{m}^2$). It has a beam waists of around 60 µm in plane and 3.5 µm in vertical direction, which results in a Rayleigh length $l_\text{R} = \frac{\pi w_0^2}{\lambda}$ of around 47 µm along the propagation direction, see Fig. 4.14. Additionally, the lattice beams have a beam

[6] a.u. stands for atomic units of the electric polarizablility

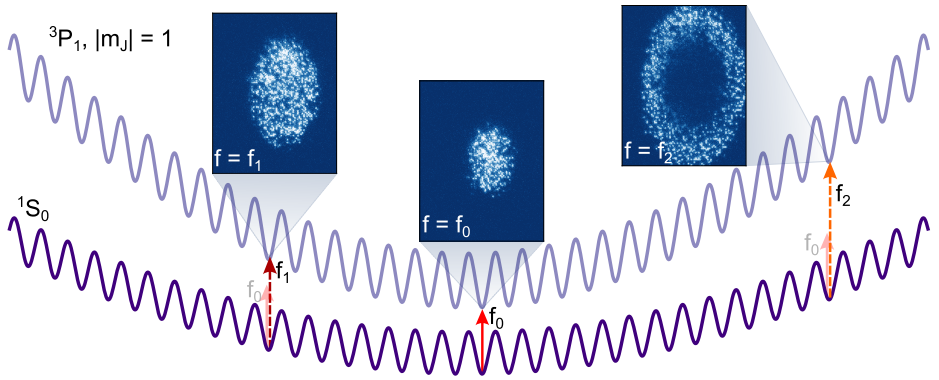

Figure 4.13: Intuitive idea of spatially dependent Sisyphus cooling. The differential light shift of the cooling transition affects the lattice sites, but also the harmonic confinement which arises as the sum of the light sheet potential and the envelope of the lattice potential. The resonance of the cooling transition becomes spatially dependent, as depicted by the different length of the red arrows. The insets show example images ($50\times65\,\mu m^2$) measured at deep confinement with around 1.3 W power in the light sheet beam and around 2 W in each of the four lattice beams. In the center, at $f = f_0$, we only cool a small area. Increasing the frequency to $f_1 = f_0+100\,\mathrm{kHz}$ allows us to cool a larger area. When we set it to $f_2 = f_0+300\,\mathrm{kHz}$, we are no longer cooling the center and observe the atoms occupying a ring shape area which makes the equipotential of the harmonic confinement visible.

waist $\omega_{\mathrm{latt}} \approx 70\,\mu m$ which is comparable to the field of view of our imaging system. The example images in Fig. 4.13 were taken at deep potentials and thus show a strong spatial dependence on the cooling frequency. Typically, we work with weaker trapping in order to cool more homogeneously and image larger areas, as shown in the insets in Fig. 4.12b.

The effect of spatially dependent cooling can be used to investigate the trapping potential. We know that the detunting of the red cooling light is directly related to the light shift between the two transitions: $\delta/2\pi = U_e/h - U_g/h$. The trapping potentials for the ground state U_g and the excited state U_e are given by the formula of the optical dipole trap (see Sec. 2.4):

$$U_{\mathrm{dip}} = -\frac{1}{2\epsilon_0 c}\alpha I(\vec{r}) \tag{4.8}$$

with ϵ_0 the vacuum permittivity, c the speed of light and $I(\vec{r})$ the position dependent intensity. The polarizability α depends on the wavelength and is different for the ground and excited state as discussed in the previous section. The intensity of the laser beams is given by Eq. (2.5) in Ch. 2. For the light sheet it propagates along y-direction with two different beam waists w_{x0} and w_{z0}, resulting in

$$I(x,y,z) = \frac{2P_{\mathrm{LS}}}{\pi}\frac{1}{w_x(y)}\frac{1}{w_z(y)}\exp\left(-2\frac{x^2}{w_x(y)^2}\right)\exp\left(-2\frac{z^2}{w_z(y)^2}\right). \tag{4.9}$$

The optical lattice is a result of fourfold interference as discussed in Sec. 3.2. The

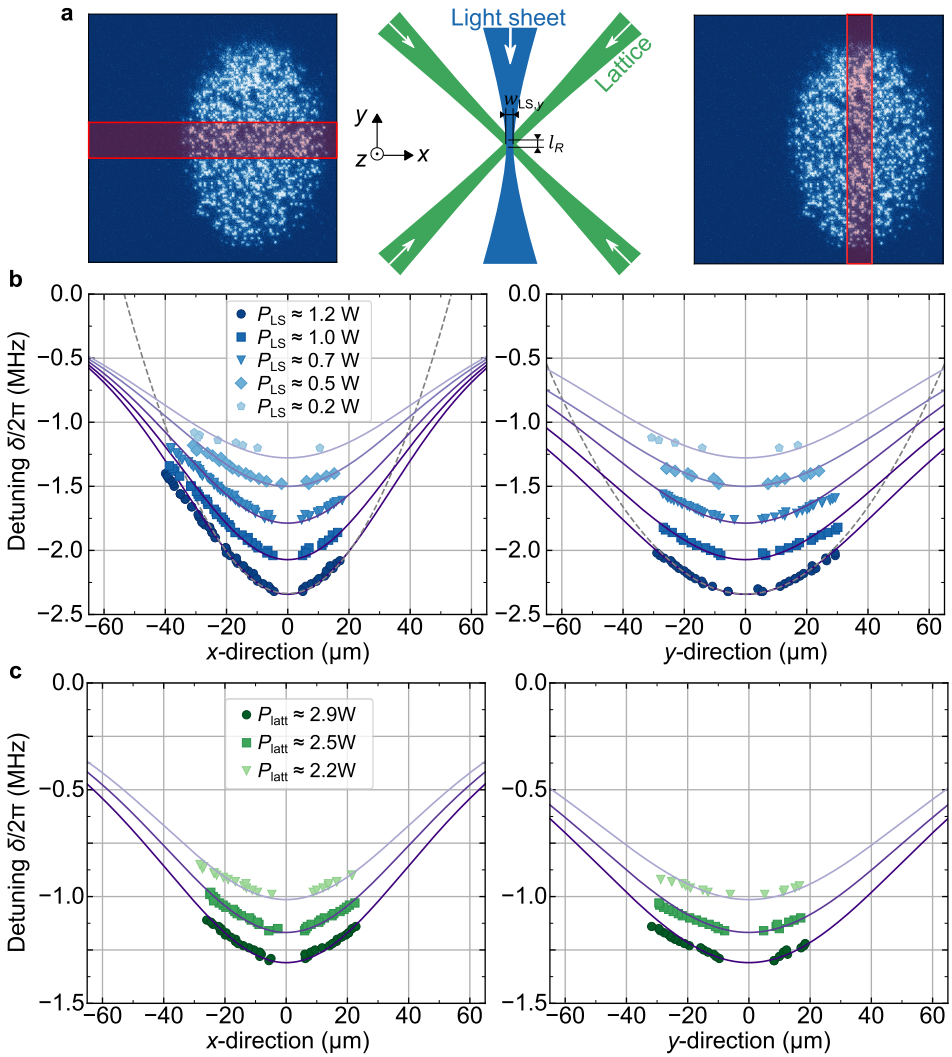

Figure 4.14: Spatially dependent cooling for different trapping potentials. **a** We measure the size of the imaged atoms in x and y-direction (red squares) for different detuning of the red cooling beams. The elliptical shape of the cloud arises due to the anisotropy of the light sheet beam. We indicate the Rayleigh length $l_{\mathrm{R}} \approx 47\,\mu\mathrm{m}$ which has a similar value as the beam waist in y-direction $w_{\mathrm{LS},y}$. **b** At constant lattice power, we change the power of the light sheet. The edge position in x-direction (left) and y-direction (right) are plotted versus the detuning of the red cooling frequency with respect to the Zeeman split bare resonance of the σ^+ transition, see 4.12a. The two-directions are analysed with a combined Gaussian fit. In **b** the light sheet power is a free parameter and we let the remaining parameters vary in a small range: the waist of the lattice beams w_{latt} =70(2) μm, the waists of the light sheet beam $w_{\mathrm{LS},x}$ =57(2) μm, $w_{\mathrm{LS},z}$ =3.5(2) μm and the power of the lattice beams P_{latt} =2.5(5) W. In **c** we measure the light shifts for different lattice powers, thus P_{latt} is the fit parameter and P_{LS} =0.275(25) W varies in a small regime. The dashed grey line in **b** is a harmonic fit to the central part of the trap (±25 μm) for $P_{\mathrm{LS}} \approx 1.2\,\mathrm{W}$.

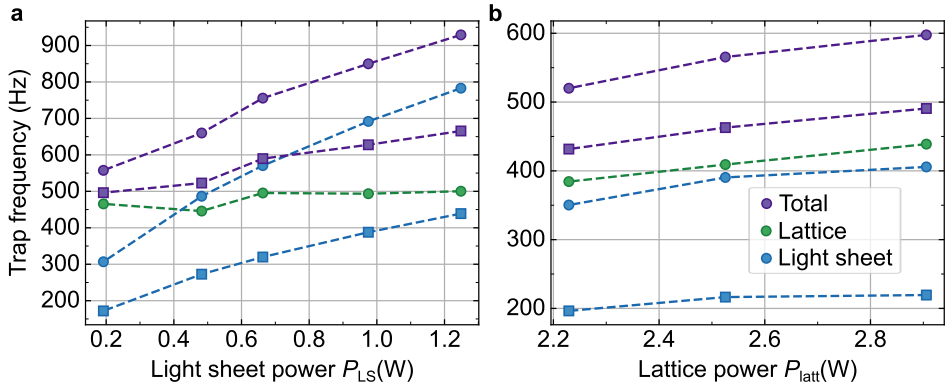

Figure 4.15: Fitted trap frequency from the data in Fig. 4.14. We apply the fitting parameters to the trapping potential functions and calculate the trap frequency as the second derivative of a harmonic potential. **a** Trap frequency as a function of the light-sheet power, keeping the lattice power constant at $P_{\mathrm{latt}} \approx 2.5\,\mathrm{W}$. The lattice trap frequencies in x and y-direction are equal due to the circular shape of the lattice beams. For the light sheet we find different trap frequencies in the different directions, due to its anisotropic shape (see blue circles (f_x) and blue squares (f_y)). **b** Extracted trap frequencies as a function of the lattice power. The low constant value of the light sheet power $P_{\mathrm{LS}} \approx 275\,\mathrm{mW}$ is a factor of uncertainty in the measurement, as the edge of the cloud is not as sharp as it is for deeper light sheet potentials. The dashed lines serve as guides to the eye.

harmonic confinement due to the interfering lattice beams can be calculated as

$$I_{\mathrm{lattice}} = \frac{\epsilon_0 c}{2}\left[\mathcal{E}_1(x,y) + \mathcal{E}_2(x,y) + \mathcal{E}_3(x,y) + \mathcal{E}_4(x,y)\right]^2 \tag{4.10}$$

$$\mathcal{E}_j(\tilde{x},\tilde{y}) = \sqrt{\frac{4}{\pi\epsilon_0 c}\frac{P_j}{w_0^2}}\,\frac{w_0}{w(\tilde{x})}\,\exp\left[-\frac{\tilde{y}^2}{w(\tilde{x})^2}\right] \tag{4.11}$$

where we assume $z = 0$ and $\tilde{x}$, $\tilde{y}$ are chosen with respect to the propagation of the j-th lattice beam. All four beams contribute to the envelope with different powers. This is important due to the losses arising upon the transmission of the beam through the glass cell, which lead to a transmittance $T = 0.86\,\%$ each time the beam passes through the glass cell wall (see Sec. 3.2.2).

As shown in Fig. 4.14, we measure the spectrum of the Sisyphus cooling for different powers of the light sheet beam b or the lattice beams c. Then, we fit the light sheet potential and the envelope of the lattice to the cloud sizes measured for different cooling frequencies. To this end, we cut a slice of the image along x-direction, integrate the signal over y-direction and fit an error function to the edge of the cloud (Fig. 4.14a). We proceed similarly for the y-direction. The cloud is not centered with respect to the image, this enables us to capture more data points in the $-x$-direction. As expected, we observe that for more power, which means deeper potentials, the detuning δ is further from the non-light-shifted resonance of the transition, $\delta = 0$. Moreover, for large light sheet power, we see that towards the edges of the images, the

potential is no longer described by a harmonic potential. Instead the Gaussian beam profile has to be taken into account, see the harmonic fit in Fig. 4.14b at the highest light sheet power.

Knowing the trapping potentials, we extract the trapping frequency in the center of the trap where it can be approximated by a harmonic confinement. In this case, the trap frequency is given by

$$\omega_x^2 = \frac{1}{m}\frac{\partial^2 U}{\partial x^2} \tag{4.12}$$

in x-direction, with m being the mass of the atoms and U the trapping potential. The calculated trapping frequencies are given in Fig. 4.15. When we calculate the trap frequency for varying lattice power, in Fig. 4.15b, the light sheet power is constant at $P_{\mathrm{LS}} \approx 275\,\mathrm{mW}$. We obtain a trap frequency for the light sheet beam of $\omega_x = 2\pi\times 380(30)\,\mathrm{Hz}$ and $\omega_y = 2\pi\times\ 210(20)\,\mathrm{Hz}$. The results are in fair agreement with what we measured for the light sheet via dipole oscillation: $\omega_x = 2\pi\times\ 420(10)\,\mathrm{Hz}$ and $\omega_y = 2\pi\times 252(5)\,\mathrm{Hz}$.

4.4 Microscopy of a ^{84}Sr superfluid

We present the realization of a Bose-Hubbard superfluid in our strontium quantum-gas microscope. While the measurements in the previous sections have been performed with thermal atoms, we load instead a Bose-Einstein condensate into the lattice. For a two-dimensional system like ours, the superfluidity can be preserved if the loading is done adiabatically, and the ratio between tunneling t and on-site interaction U remains $t/U > 0.06$ [214]. To this end, the isotope ^{84}Sr is a convenient choice, despite its low natural abundance of 0.56(1) %[123], because the scattering length of 122.7(3) a_0 [124] facilitates efficient evaporative cooling to quantum degeneracy, see Sec. 2.4. Here we explain the phase coherence of a superfluid and the emergent interference peaks. We present measurements of the momentum distribution and characterization of our superfluid. Demonstrating the presence of a Bose-Hubbard superfluid is an excellent starting point for simulating many-body quantum systems in our setup, although some modifications are still needed in our setup to reach the strongly interacting regime.

4.4.1 Superfluid and phase coherence

The superfluid phase in an optical lattice arises at the limit of weak interaction U compared to the tunneling t, $U \ll t$. In the extreme case of $U = 0$, all bosonic particles are delocalized and are at zero momentum $\vec{k}$ in the lattice, hence can be described by the wavefunction

$$|\Psi_{\mathrm{SF}}\rangle = \frac{1}{\sqrt{N!}}\left(\hat{b}^\dagger_{k=0}\right)^N |0\rangle = \frac{1}{\sqrt{N!}}\left[\frac{1}{\sqrt{N_{\mathrm{lat}}}}\sum_j \hat{b}^\dagger_j\right]^N |0\rangle \tag{4.13}$$

where $|0\rangle$ describes the vacuum state, corresponding to an empty lattice. For large lattices with N_{lat} sites and many particles N, the wavefunction of the ground state

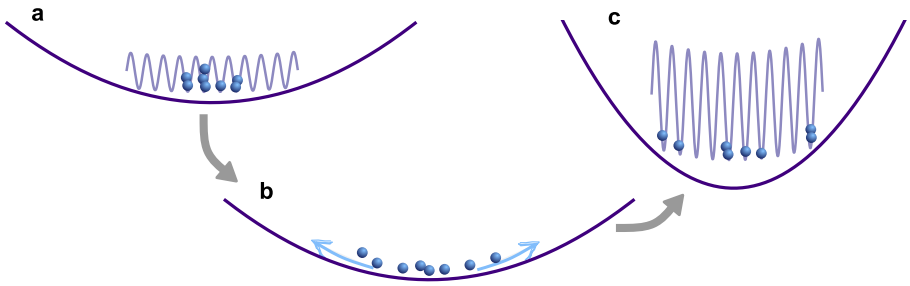

Figure 4.16: In plane expansion in a harmonic potential to gain momentum-space information about the system. **a** The atoms are in a shallow optical lattice confined into a plane by means of the light sheet beam. This gives an overall harmonic confinement to the atoms. **b** After abruptly switching off the lattice potential, the atomic wavefunction expands in the harmonic confinement of the light sheet potential. **c** After an expansion time t_{exp} a sudden switch on of the imaging potential pins the atoms in their position before imaging, which for a superfluid reveals the characteristic interference peaks.

can be written as a product of coherent states $|\alpha\rangle_j$

$$|\Psi_{\mathrm{SF}}\rangle = \prod_j |\alpha\rangle_j = \prod_j \left(e^{-|\alpha|^2/2} \sum_{n=0}^{\infty} \frac{\alpha^n}{\sqrt{n!}} |n\rangle_j \right) \tag{4.14}$$

with $|\alpha|^2 = \langle n \rangle = N/N_{\mathrm{lat}}$ and $|n\rangle_j$ the eigenstate of the number operator of the j-th lattice site in the case of n bosons. Consequently, the probability of having n_j particles in the j-th lattice site is represented by $P(n_j) = \alpha^{2n_j} e^{-\alpha^2}/n_j!$, a Poissonian distribution.

When detecting a superfluid in the lattice by means of a quantum-gas microscope [87], the atomic wave functions collapse and the atoms localize in a particular lattice site following this Poissonian distribution. However, due to parity projection (Sec. 4.2.2) the images reveal an apparently random distribution of filled and empty lattice sites. A convenient method to detect a superfluid phase relies on the long-range phase coherence of the atoms, see Eq. (4.14). Upon free expansion of a superfluid from the lattice, which will reveal its momentum distribution, an interference pattern arises. This has been shown in time of flight measurements [46], where the confining potential was suddenly switched of and the atoms were expanding freely. After a few millisecond an absorption image revealed distinct interference peaks which are directly related to the phase coherence of the initial state.

The challenge of measuring such interference pattern in a quantum-gas microscope is due to the fact that the atoms fall during a time-of-flight and thus move out of the focus of the microscope. To keep them in the focal plane, an in plane expansion can be implemented. To this end, a trapping potential is required which confines the atoms in vertical direction, but not in horizontal direction. However, we perform in-plane expansion with a harmonic trap, similar to the method presented in the work of W. S. Bakr *et al.* [87].

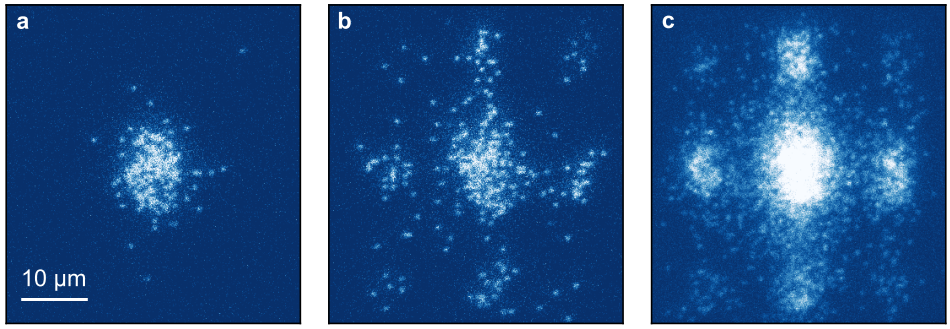

Figure 4.17: Detection of the phase coherence of the Bose-Hubbard superfluid in the optical lattice. **a** The in situ image of the Bose-Einstein condensate loaded into an optical lattice of depth $V_0 = 2.3(1)\,E_r$. **b** Imaging after $t_{\mathrm{exp}} = 2\,\mathrm{ms}$ in-plane expansion (explained in Fig. 4.16) during which the atomic wavefunctions interfere due to their phase coherence between the lattice sites. **c** Higher order interference peaks appear in the corners of the image, when averaging ten images such as the one in **b**.

The method is described schematically in Fig. 4.16. The atoms in the lattice are additionally confined by a harmonic potential (Fig. 4.16a) In our experiment it is given by the tightly focused light sheet beam, such that the confinement in vertical direction ω_z is much larger than the trapping frequencies in the horizontal directions ω_x and ω_y. For the in-plane expansion, the lattice potential is turned off nonadiabatically, but the light sheet is kept on, confining the atoms to a two-dimensional plane (Fig. 4.16b). After the expansion time t_{exp} the imaging potential is switched on, meaning deeper light sheet and lattice potentials (Fig. 4.16c) and collapsing the atomic wavefunctions and pinning the atoms in their current location for fluorescence detection.

Having the harmonic trap with trapping frequencies ω_x, $\omega_y \ll \omega_z$ enables us to map the initial momentum of the atoms at $t_{\mathrm{exp}} = 0$ to the spatial distribution at an expansion time t_{exp} equal to a quarter of the oscillation period $T_{x,y} = 2\pi/\omega_{x,y}$ [244, 245]. Intuitively, this can be understood by considering a particle oscillating in a harmonic confinement. It starts from the center of the trap with an arbitrary velocity climbing up the potential, after a quarter of the period it will turn around and move back towards the center. It will be back in the center after half the period and start moving towards the opposite maximum. This implies that after $t_{\mathrm{exp}} = T/4$ the initial momentum is reflected in the current position of the particle.

If the atoms are initially in a superfluid phase, the atomic wavefunctions interfere with each other during the in-plane expansion because of the phase coherence, see Eq. (4.14). The resulting images show interference peaks as we have detected with our ^{84}Sr quantum-gas microscope, see Fig. 4.17. The vertical confinement of this data is $\omega_z = 2\pi\times 1.1(1)\,\mathrm{kHz}$ and the lattice depth is $V_0 = 2.3(1)\,E_{\mathrm{r}}$. The recoil energy is $E_{\mathrm{r}} = h^2/2m\lambda \approx h\times 3.6\,\mathrm{kHz}$ with $\lambda = 813.4\,\mathrm{nm}$ which we chose due to the fourfold interference of our optical lattice, see Ch. 3. In contrast to the absorption images after time of flight, this method of in-plane expansion with a harmonic trap works well also for low atom numbers (few hundred in our case) because the single atoms

are detected with the microscope.

Despite the momentum to density mapping discussed before, in the measurement of Fig. 4.17 we collapse the atomic wavefunction already at $t_{\mathrm{exp}} = T_x/8$. This is due to the sharp momentum distribution in the case of a superfluid which results in the occurrence of a sharp density-distribution at $t_{\mathrm{exp}} = T/4$. Because of parity projection which only allows to detect whether there is an even (0 or 2 atoms) or an odd (1 atom) number of atoms per lattice site, imaging at $T/4$ results in higher number of atoms per lattice site, such that less atoms will be detected compared to the total atom number in the system. In order to avoid those high-density peaks, we set the expansion time to $t_{\mathrm{exp}} = T_x/8$ in order to observe the superfluid interference peaks in Fig. 4.17.

4.4.2 Evolution of interference peaks

During the in-plane expansion the atoms evolve in the harmonic potential, oscillating around the center. We can track the distance of the peaks from the center of the cloud versus the expansion duration t_{exp}. We fit the distance in x- and in y-direction with two independent sinusoidal-function as shown in Fig. 4.18. We find that the evolution of the interference peaks in the two different directions differ in oscillation frequencies. This is a result of the anisotropic confinement of the light sheet potential. Indeed, we find that the oscillation frequency agrees with the trapping frequency of the light sheet and is $\omega_{x,\mathrm{exp}} = 2\pi\times 62.0(7)$ Hz respectively $\omega_{y,\mathrm{exp}} = 2\pi\times 38.8(8)$ Hz for the weak confinement used during the in-plane expansion.

4.4.3 Visibility and lattice depth dependence

The visibility is a measure that allows quantitative statements about the phase coherence properties of the superfluid in the optical lattice. For absorption images, the density of atoms in the peaks is compared to the density along the diagonal where no peak arises [246]. In a quantum-gas microscope experiment, instead of the density we can directly detect the atom number N in the different regions [87] and the visibility can be defined:

$$\mathcal{V} = \frac{N_{\mathrm{max}} - N_{\mathrm{min}}}{N_{\mathrm{max}} + N_{\mathrm{min}}} \tag{4.15}$$

where N_{max} is the atom number in the region of the peak, and N_{min} in the diagonal region [247]. Because of the anisotropy of the light sheet, the interference peaks expand differently in the two orthogonal directions. Thus, we use an ellipse (see orange dashed line in Fig. 4.19) on which we place the areas to analyse the occupation N_{max} and N_{min}. The radii of this ellipse are given by the distance of the interference peaks from the center of the cloud, where the radius in vertical direction is larger than the one in horizontal direction, $r_y > r_x$. For the areas in which we measure the occupations N_{max} and N_{min}, we use circles with a radius of 30 pixels, which corresponds to an area of around 45 µm^2 in real space. As shown in Fig. 4.19, we observe distinct interference peaks with visibilities above $\mathcal{V} > 0.7$ up to lattice depths of $V_0 \approx 3.5\, E_{\mathrm{R}}$.

Furthermore, we measure the visibility versus different lattice depths. We find that above $4E_{\mathrm{r}}$ lattice depth the phase coherence disappears rapidly, see Fig. 4.20. This

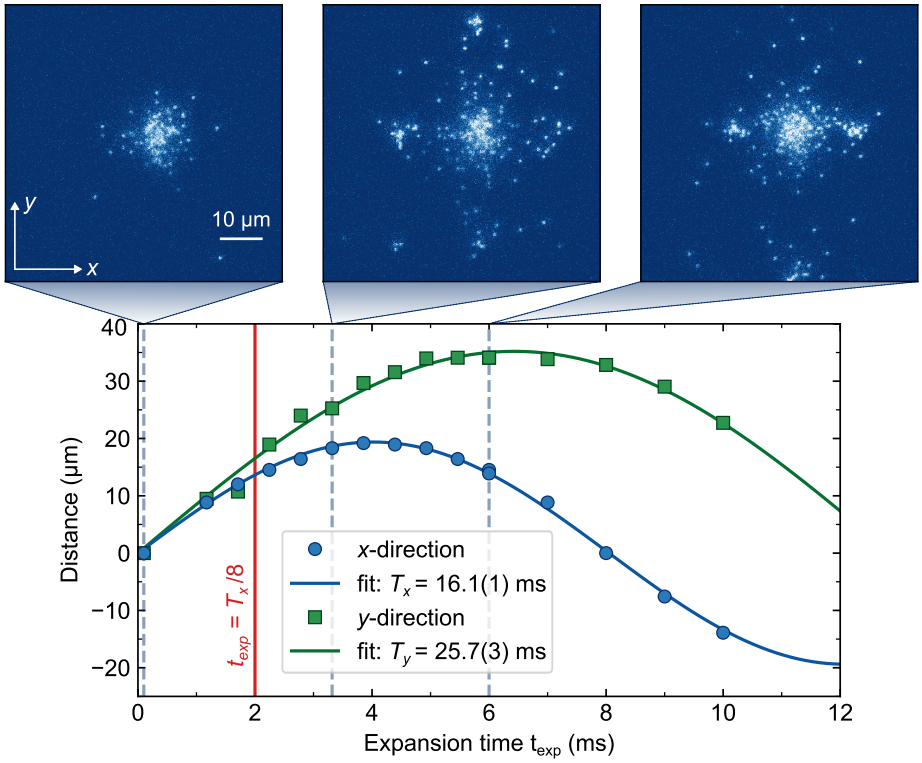

Figure 4.18: Time dependent in-plane expansion of a superfluid in a harmonic trap. The atoms are released from a $V_0 = 2.3(1)E_\mathrm{r}$ deep optical lattice. The position of the superfluid peaks oscillates around the center with a period $T_x = 16.1(1)\,\mathrm{ms}$ and $T_y = 25.7(3)\,\mathrm{ms}$, along the x- and y-direction, respectively. The difference in the two directions arises due to the evolution of the atoms in the anisotropic potential of the light sheet. Three examples are shown at different times, see vertical dashed lines. While at 0.1 ms no peaks are visible (first image), at 6 ms (third image) the upper peak in vertical direction is outside the field of view and the ones in horizontal direction are returning to the center. At the time $t_\mathrm{exp} = T_x/8 \approx 2\,\mathrm{ms}$, indicated with a vertical red line, we take the pictures of Fig. 4.17.

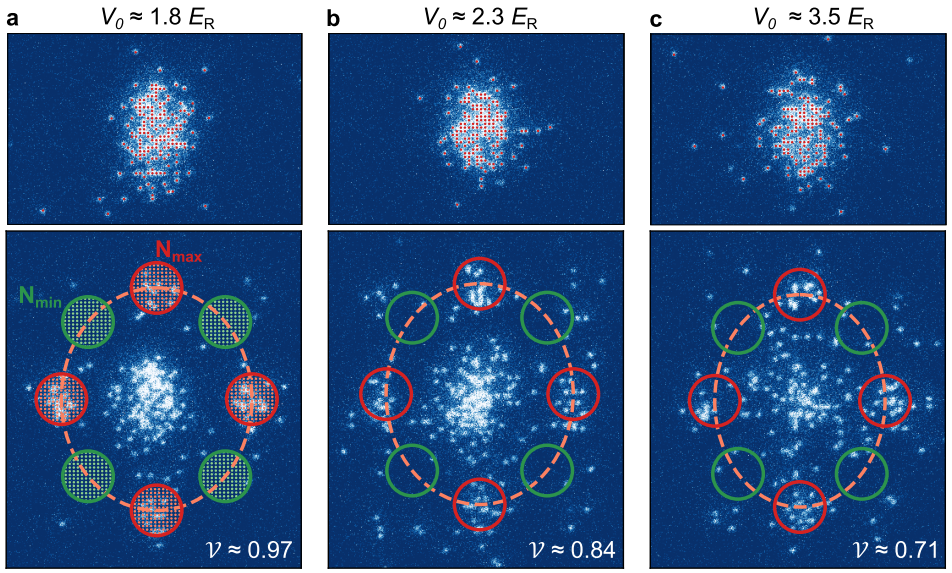

Figure 4.19: Analysis of the visibility in the superfluid interference measurements. The top row in **a-c** shows the in situ superfluid at different lattice depths V_0. The images were successfully reconstructed and detected atoms are indicated with red dots. The bottom row shows examples of superfluid interference peaks with the visibility $\mathcal{V}$ of the specific image. **a** The lattice sites in the areas of interest for the calculation of the visibility are indicated with small dots. After reconstruction and obtaining the occupation matrix, we count the atoms in the red ($N_{\max}$) and green ($N_{\min}$) circles to calculate the visibility $\mathcal{V}$, see Eq. (4.15). The circles have a radius of around 30 pixels which corresponds to an area of 45 µm^2.

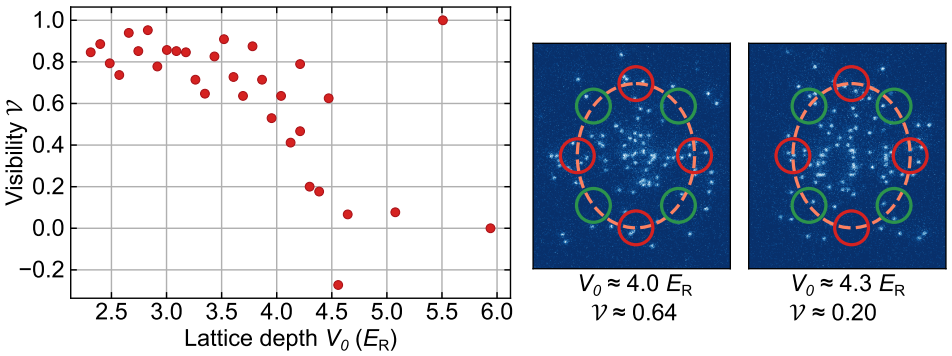

Figure 4.20: Visibility at different lattice depths. We measure the superfluid peaks for $t_{\text{exp}} = 2$ ms and analyse the visibility. Below $4E_r$ the visibility is above 0.7, and the images show distinct superfluid interference peaks, see Fig. 4.19 for examples. For deeper lattices the phase coherence gets lost which is evident by the decrease of the visibility and can be seen in the two examples on the right. For even deeper lattices, the atoms expand thermally and many of them are lost, consequently the values of the visibility above $4.5E_r$ are no longer meaningful, as we may detect one individual atom in the red circles and none in the green (visibility at $5.5E_r$).

cannot be the superfluid to Mott insulator transition. Given our vertical confinement of $\omega_z = 2\pi \times 1.1(1)\,\mathrm{kHz}$, in the case of a symmetric lattice, we would expect a Mott insulator for lattices deeper than $8\,E_\mathrm{r}$. If we take the losses on the glass cell surface into consideration, this value would increase. For example, as discussed in Sec. 3.3.3 in a symmetric lattice at $2.3\,E_\mathrm{r}$ the tunneling is $t = h \times 188\,\mathrm{Hz}$ and the interaction is $U = h \times 121\,\mathrm{Hz}$. Considering the power attenuation due to reflections at the glass cell, and including the exact angle between the lattice beams we find asymmetric tunneling $t_x = h \times 161\,\mathrm{Hz}$ and $t_y = h \times 222\,\mathrm{Hz}$ and a reduced interaction of $U = h \times 119\,\mathrm{Hz}$.

At a lattice depth $V_0 = 4E_\mathrm{r}$ the on-site interaction is $U \approx 160\,\mathrm{Hz}$, due to the rather week vertical confinement. In order to achieve a regime where the interaction is dominating over the tunneling, in particular $t/U > 0.06$ [214], the tunneling would have to be around 10 Hz, which corresponds to the $8\,E_\mathrm{r}$ mentioned above. We believe that the loss of phase coherence that we observe stems from improper thermalization and technical heating sources, for example low frequency noise in the lattice beams can heat the atoms. Adding a vertical lattice for larger confinement in vertical direction and thus increased trapping frequency ω_z will be the solution to this issue in the future.

4.5 Conclusion

We successfully added quantum-gas microscopy of ^{84}Sr to the list of existing quantum-gas microscopes. We demonstrated single-site-resolved imaging in a clock-magic optical lattice. To this end, we have studied the performance of our imaging system. The point spread function is with 632(3) nm larger than expected according to the resolution limit of our imaging system. A deconvolution of the raw images with the point spread function enabled us to reconstruct the lattice vectors using Fourier transformation. From the lattice vectors we determined the magnification $\mathcal{M} = 126.7(3)$ of our imaging setup and the angles between the lattice beams, which deviate around 6° from a perfect perpendicular alignment.

We measured hopping and loss rates during imaging, which revealed a pinning fidelity of $\mathcal{F} \approx 96\,\%$. The losses arise mostly from the losses in the lattice and are not affected by the scattering of imaging photons. To counteract recoil heating due to the imaging photons, we have realized attractive Sisyphus cooling in a lattice. The narrow-linewidth of the red transition, which we use for the cooling, combined with the harmonic confinement of our optical trap results in spatially dependent Sisyphus cooling. We have exploited this phenomena to characterize our trapping potential and estimated the trap frequencies for the light sheet potential and the lattice potential independently.

We presented the detection of a superfluid in our strontium quantum-gas microscope. The phase coherence of the atoms in the superfluid phase reveals interference peaks after an in-plane expansion in a harmonic trap, for a system with Bose-Hubbard parameters $U = h \times 121(3)\,\mathrm{Hz}$ and $t = h \times 188(8)\,\mathrm{Hz}$ for interaction and tunneling respectively. Furthermore, we observed the disappearance of the interference pattern for deeper lattice potentials, which we attribute to technical reasons. We concluded that the realization of a homogeneous unit-filled Mott insulator requires a larger interaction

U, which we will achieve in the future by installing a vertical lattice to increase the vertical trapping frequency.

Chapter 5

Single-atom-resolved imaging of fermionic strontium

This chapter discusses the single-atom-resolved imaging of ^{87}Sr. We present the challenges that arise when imaging fermionic strontium with its large nuclear spin of $I = 9/2$. We discuss the reason why imaging with blue fluorescence and red cooling, as done for the bosonic isotope ^{84}Sr, fails for the fermions. A careful study of the polarizabilities and the differential light shifts of the fermionic hyperfine substates reveals a way to address this challenge by exploiting the red narrow-linewidth transition for fluorescence and cooling simultaneously. We present the performance of the imaging of the fermions compared to the imaging of the bosons. Moreover, we demonstrate first results of spin-resolved imaging by means of the red transition only, involving two different spin states.

The work of this chapter was a team effort between myself and my colleagues Carlos Gas, Dr. Jonatan Höschele, Dr. Antonio Rubio Abadal and Prof. Dr. Leticia Tarruell. The data analysis presented in this chapter has been carried out by myself with assistance from my colleagues.

5.1 Motivation

As discussed in the introduction of this thesis, the interest in having a quantum-gas microscope of ^{87}Sr arises due to the large nuclear spin of $I = 9/2$ and the emergent SU($N \leq 10$) symmetry [248, 68]. The ten different spin states arising in the ground state interact all with the same strength because they emerge from a purely nuclear spin. This provides a rich platform to study exotic magnetic phases and long-range correlations between the N spin states as discussed theoretically for the SU(3) [73], the SU(4) [74] and the SU($N \geq 5$) Heisenberg models [76, 75]. More generally, it is of great interest to study the SU($N \leq 10$) Fermi-Hubbard system for example to investigate out-of-equilibrium SU(N) Heisenberg systems [249] or to explore thermodynamic properties of the SU(N) Fermi-Hubbard model [250], because these systems can provide understanding of the essential features of real material such as high-T_c superconductivity. Some of the aspects of those systems have already been studied. For instance, SU(6) Hubbard systems where Mott insulators have been realized [69] and short-range antiferromagnetic correlations have been observed [71]. More recently thermometry of SU($N \leq 6$) systems was also performed [72]. However, none of those experiments had single-atom resolution and long-range antiferromagnetic order (as observed in SU(2) Fermi-Hubbard systems [50]) was not achieved.

Furthermore, the long-lived clock state ^{3}P$_0$ combined with the nuclear spin, provides a rich platform for quantum computing. The different spin states can form qubits and the clock state can be used to store and even move these spin qubits as proposed by A. J. Daley *et al.* [187]. In the work of K. Barnes *et al.* [110], which uses optical tweezers arrays of strontium, they exploit the storage in the clock state during the read-out of the different spin qubits. The tools of storing and transporting can be exploited in the realization of tunneling gates in a fermionic quantum processor, as theoretically proposed in [251], but not realized experimentally so far. Combined with interaction gates by means of Rydberg excitations, this unlocks a powerful apparatus for quantum many-body systems.

An important addition in the investigations of these research directions would be single-atom-resolved imaging and additionally spin resolution because it could give insight into long-range magnetic correlations and related phenomena [235]. That is the topic of this chapter. We present our first images of single ^{87}Sr atoms in an optical lattice. Furthermore, we demonstrate a first spin-resolved detection of the fermionic atoms, involving two different spin states.

5.2 The challenge of imaging fermions

While the ten different spin states of ^{87}Sr are a valuable asset for studies of quantum-many body systems, they constitute at the same time a challenge for imaging. In contrast to the bosonic isotope presented in Ch. 4, strontium has numerous hyperfine states F with $2F + 1$ substates: $m_F = -F, -F + 1, ..., F - 1, F$. For the ground state ^{1}S$_0$, since $J = 0$, there is only $F_g = 9/2$, which has ten m_{F_g} substates. For the excited states ^{1}P$_1$ and ^{3}P$_1$, with $J = 1$, there are three hyperfine states

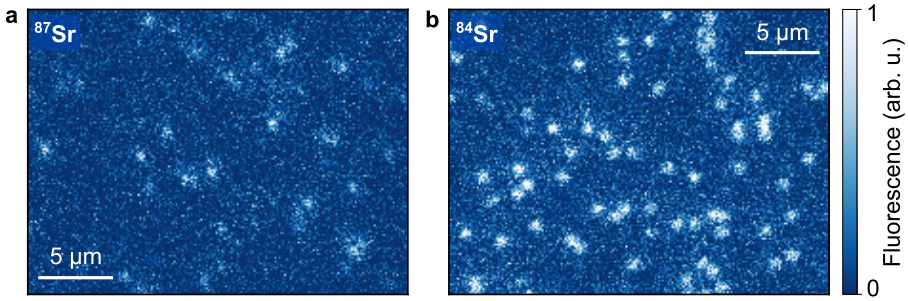

Figure 5.1: Blue fluorescence imaging of ^{87}Sr in comparison with ^{84}Sr. **a** With the blue fluorescence imaging of the fermionic isotope only a few of the atoms are well detected, but most of them are blurry and seem to have been lost during imaging. In this image, the exposure time is 10 s and the magnetic field is perpendicular to the lattice polarization. We use one blue beam to induce fluorescence and six circularly polarized red beams from six different directions to address the $F = 11/2$, and the same for the $F = 9/2$ excited hyperfine state. **b** For comparison, the bosonic atoms show great signal-to-noise ratio when imaged on the blue transition with 10 s exposure while performing attractive Sisyphus cooling on the red transition as discussed in Ch. 4. Both images have the same color scale in arbitrary units.

$F_e = 7/2$, $9/2$ and $11/2$. Upon applying an external field, magnetic or light fields, the energy of the m_F substates shift, with the energy shifts that vary for the different m_F. This is problematic for laser cooling (Sec. 2.3.3) and single-atom-resolved imaging, as discussed in this section. In the following, we explain the challenges of single-atom-resolved imaging of ^{87}Sr and the connection to the different polarizabilities of the hyperfine substates. We present the method, which we implement to achieve our first single-atom resolved images of the fermionic isotope ^{87}Sr.

5.2.1 Blue imaging of fermionic strontium

For single-atom-resolved imaging of ^{87}Sr, a straightforward approach is to image them in the same fashion as the bosonic atoms ^{84}Sr, discussed in Ch. 4. To summarize, for the bosonic isotope ^{84}Sr we generate a fluorescence signal by means of a blue imaging beam at 461 nm. Simultaneously, we perform attractive Sisyphus cooling on the red transition at 689 nm by addressing the ^{3}P$_1$ $|m_J| = 1$ excited state. At the same time, the repumper lasers recover atoms that leak into the metastable states (see Sec. 2.2.2).

Equivalently, we can induce fluorescence for the fermionic ^{87}Sr atoms with an imaging beam at 461 nm. The splitting of the hyperfine states of the ^{1}P$_1$ excited state does not affect the performance because it is too small compared to the linewidth of the blue transition, $\Gamma_{\text{blue}}/2\pi \approx 30.5$ MHz (see Appx. A.1). For the red transition, the hyperfine states can be addressed individually, because the hyperfine splitting is around 1 GHz, which is several orders of magnitude larger than the linewidth of the transition, $\Gamma_{\text{red}}/2\pi \approx 7.4$ kHz. During laser cooling in the red MOT, we exploit this fact to address the $F = 11/2$ for the red MOT and the $F = 9/2$ for the stirring

independently, see Sec. 2.3.3. For the imaging process, we can use these two hyperfine states for cooling. The problem is that the light shift induced by the optical lattice splits the m_{F_e} states of the excited $^3P_1$ state and the energy shift varies for the different substates. Consequently, each spin state m_{F_g} requires a different frequency to perform efficient cooling during imaging. Cooling only one of the spin states fails due to the blue fluorescence. The broad linewidth of the blue transition is not sensitive to the m_F substates, and neither is the repuming transition. Thus, the blue fluorescence imaging mixes the population of the spin states. This means, during imaging, we have to cover the full spectrum of all the m_F states with the red transition for efficient cooling, and cannot chose a particular resonance. However, this might lead to heating of the atoms with the red photons, because the cooling frequency for one state does not fulfill the cooling condition for another and therefore causes likely heating for the other spin states. It is important to note, that besides attractive Sisyphus cooling which we use for the bosonic isotope, also repulsive Sisyphus cooling [200] and sideband cooling [238] have been demonstrated for strontium in an optical lattice. However, it is unfeasible to find one frequency that cools all the sublevels of the hyperfine state efficiently.

If, despite these challenges, we try to image ^{87}Sr with the same method as for the bosonic isotope, we want to address as many spin states as possible. To this end, we apply the six red MOT beams and the six stirring beams to address both the $F = 11/2$ and the $F = 9/2$ hyperfine states. The beams are circularly polarized and enter the glass cell from six different direction, this results in not well-defined polarization of the red light, exciting all possible transitions σ^-, π and σ^+. During imaging, the atoms are trapped in a pinning lattice confined in vertical direction by means of the light sheet beam, as it is done for the bosons.

We obtain images as displayed in Fig. 5.1a. It shows individual fermionic atoms detected with this blue imaging method. But despite the 10 s exposure, which for the bosonic strontium resulted in excellent signal to noise ratio (see for example: Fig. 5.1b), the fermionic signal varies significantly in intensity. This leads to blurry dots in the images. We understand that this is the result of losing the atoms due to heating. The red light fails to efficiently counteract the recoil heating of the blue imaging photons.

5.2.2 Polarizability and spin-dependent light shift

When explaining the imaging of ^{87}Sr atoms with the blue fluorescence signal, we have mentioned that the light shift splits the m_{F_e} states of the red transition and as a result, we cannot cool the atoms efficiently. The light shift is the result of the trapping potential generated by the optical lattice beams and the light sheet beam. It is proportional to the total intensity and the polarizability [181]. The intensity simply depends on the parameters of the laser light such as beam waist, power and their interference. In contrast the polarizability α describes the interaction between the trapping light and the atom and thus depends on the atomic states, the wavelength, in particular the detuning from resonance, and the polarization of the trapping light with respect to the quantization axis [252]. Therefore, the polarizability varies for different

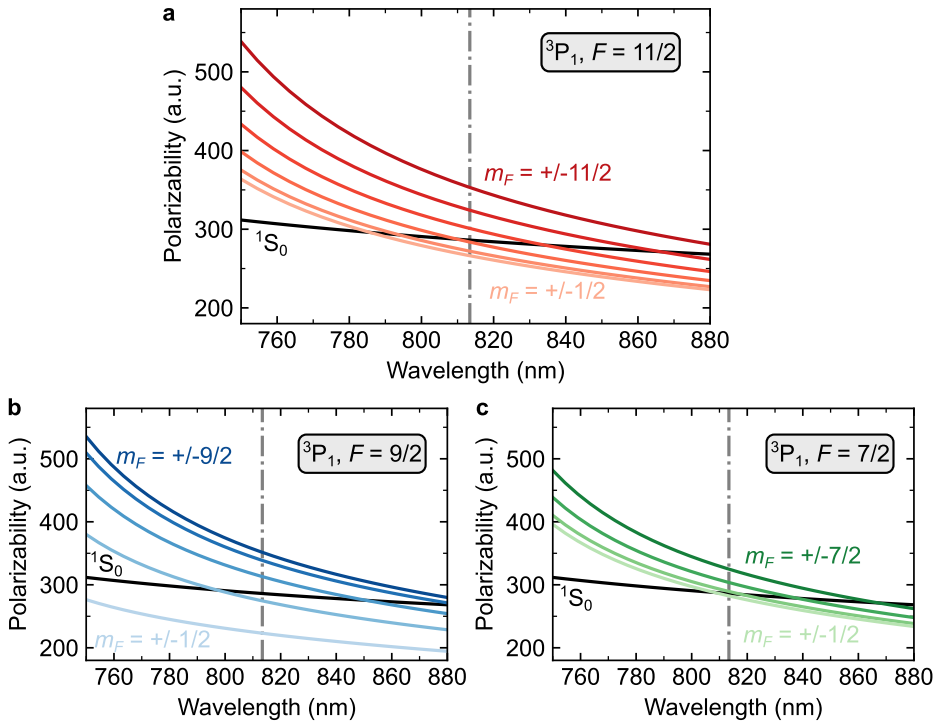

Figure 5.2: Polarizability for hyperfine states of fermionic strontium. **a** Polarizability (in atomic units a. u.) of $^3\mathrm{P}_1$ in the $F = 11/2$ hyperfine state compared to the ground state $^1\mathrm{S}_0$. Only the $|m_F| \geq 7/2$ have larger polarizability than the ground state, thus fulfill the condition for attractive Sisyphus cooling. **b** For the hyperfine state $F = 9/2$ the polarizabilities of the m_F levels are more split compared to $F = 11/2$. **c** For the $F = 7/2$, the polarizabilities lie closer together and near the one of the ground state.

$^3P_1$ $F = 11/2$	α (a.u.)	Light shift	Diff. light shift
$\lvert m_F\rvert = 11/2$	353	−4.37 MHz	−0.83 MHz
$\lvert m_F\rvert = 9/2$	324	−4.01 MHz	−0.47 MHz
$\lvert m_F\rvert = 7/2$	301	−3.72 MHz	−0.18 MHz
$\lvert m_F\rvert = 5/2$	283	−3.51 MHz	0.03 MHz
$\lvert m_F\rvert = 3/2$	272	−3.36 MHz	0.17 MHz
$\lvert m_F\rvert = 1/2$	266	−3.29 MHz	0.25 MHz

Table 5.1: The polarizabilities and light shifts of the $^3P_1$ $F = 11/2$ excited state. The polarizabilities are given in atomic units (a.u.). The light shifts in the center of a lattice site are calculated assuming a fourfold optical lattice (Ch. 3) for 2.5 W power per beam and a beam waist of 70 µm, which is around the values we typically have in the pinning lattice. We include the losses due to transmission through the uncoated glass cell (see Ch. 3) but we disregard the effect of the light sheet. The ground state experiences a light shift of around −3.54 MHz due to a polarizability of 286 a.u. and the differential light shift is the difference between the light shift of the excited m_F state and the ground state.

m_F substates, in the same way as it varies for different m_J states in the bosonic case (Sec. 4.3). We can calculate the different polarizabilites and the resulting light shifts for a given trapping potential. In this section, we present the results of those calculations and we refer to Appx. B for the formulas and details of the calculation.

We study the polarizabilities of the excited state $^3P_1$ used for cooling on the red transition. The polarizabilities for the three hyperfine states are displayed in Fig. 5.2, emphasizing the reason why the cooling during the blue imaging fails. The m_{F_e} states have vastly different polarizabilities which results in different light shifts. Since the ground state has only a nuclear spin and zero total angular momentum $J = 0$, it would require large fields to split the substates. Thus, we can assume that the m_{F_g} states are degenerate. This justifies the comparison between the excited m_{F_e} states and the ground state, as displayed in Fig. 5.2.

For the hyperfine state $F_e = 11/2$ for example, the polarizabilities of $|m_{F_e}| \geq 7/2$ are larger than the one of the ground state, and thus attractive Sisyphus cooling works. But for the other m_{F_e} states, where $|m_{F_e}| \leq 5/2$, repulsive Sisyphus cooling has to be applied. The other hyperfine states show similar splitting of the substates with the difference that $F_e = 9/2$ has a wider spread in polarizability and $F_e = 7/2$ has a narrower spread compared to $F_e = 11/2$.

Besides the cooling method, the different polarizabilities also split the m_{F_e} states, such that their resonance frequencies vary. As a result, it is challenging to address all of them with the correct frequency for efficient cooling. At the intensity which we use during imaging in the pinning lattice we obtain a light shift of around −3.54 MHz for the ground state, and between −3.29 MHz and −4.37 MHz for the excited state,

see Tab. 5.1. The differential light shift is calculated as the difference between the ground state and the excited state light shift. It describes the shift of the resonance frequencies when exciting the different substates of the $^3P_1$ $F = 11/2$ hyperfine state. We find that the difference between the largest and the smallest differential light shift is approximately 1 MHz. With a transition linewidth of 7.4 kHz it becomes a challenge to address all the m_F states at the same time and additionally at the correct frequency for efficient cooling. In particular, the cooling frequency for one m_F state may cause heating for another states.

This explains why imaging ^{87}Sr with blue fluorescence and red cooling fails. Furthermore, we have gained insight into the light shifts of the red hyperfine states, providing a tool box for possible solutions. In particular, we have seen that Sisyphus cooling can work for some of the m_F states. However, the light shift does not split the m_F states sufficiently to excite them independently from each other and we have to additionally split the states by means of a magnetic field.

Zeeman splitting

If the atoms are exposed to a magnetic field, the m_F states of the hyperfine state F split as a result of the the Zeeman effect. The frequency shift of the m_F states depends on the magnetic field and the g_F factor, which varies for different hyperfine states. For small magnetic fields of a few Gauss the dependence is linear (Appx. A.1).

It is important to notice that the polarization of the trapping light together with the magnetic field determines the quantization axis [163]. With a magnetic field parallel to the light polarization, the two effects add up and the energy shift of the m_F states are the sum of the light shift and the Zeeman shift. However, changing the angle between the magnetic field and the polarization of the light affects the energy shift. Due to the change in the quantization axis, the eigenstates of the polarization operator change resulting in different polarizabilities. This applies to both fermionic and bosonic isotopes. While this can be a nuisance for the formulation of the problem, it is an advantage as well. For the bosons there is a magic angle between the polarization of the trapping light and the magnetic field at which 813.4 nm is a magic wavelength for $^1S_0$ and $^3P_1$ ($m_J = 0$) [203]. Moreover, also m_J is no longer well defined if the angle between the magnetic field and the polarization changes, as discussed in [163]. For the following discussion, for simplicity, we are only considering magnetic fields aligned with the polarization of the trapping light and thus the energy shifts of the magnetic and the light field simply add up.

5.2.3 Scheme to image ^{87}Sr

The different polarizabilities α_{m_F} of the hyperfine state F prevent efficient cooling on the red transition, as it has been done for the bosons. However, as Fig. 5.2 shows, there are m_F levels that fulfill the condition for attractive Sisyphus cooling, i.e. with a polarizability larger than the ground state polarizability, while others are in the repulsive Sisyphus regime. If we image solely on one particular transition, cooling would indeed be effective. For this approach, we need to prepare the atoms in a

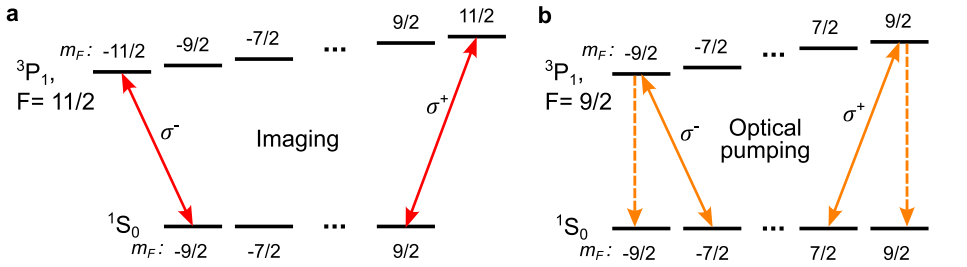

Figure 5.3: Red imaging for fermionic strontium. **a** Cycling transitions between the ground state at $m_{F_g} = \pm 9/2$ and the excited hyperfine state $F_e = 11/2$ to $m_{F_e} = \pm 11/2$. **b** Optical pumping by means of the $F_e = 9/2$ hyperfine state with circular polarized light in order to prepare the $m_{F_g} = \pm 9/2$ states which can be used for imaging.

specific spin state, ideally $|m_{F_g}| = 9/2$ as we explain below. To this end, generating the fluorescence signal with the blue transition is unsuitable because the broad linewidth and the repumping lasers transfer atoms into other m_F states that cannot be cooled, see Sec. 5.2.1.

Consequently, we avoid the blue transition and image on the red transition only, performing cooling and fluorescence at the same time as it has been shown for bosonic ^{88}Sr in optical tweezers [104]. The idea is to prepare a cloud of atoms in the $m_{F_g} = \pm 9/2$ and use the $F_e = 11/2$ for imaging by exciting the atoms with circularly polarized light to the $m_{F_e} = \pm 11/2$, similar to the techniques used in ytterbium tweezers [253]. The benefit of this choice is that the transition is closed such that excited atoms will naturally return to $m_{F_g} = \pm 9/2$, see Fig. 5.3a. To address the states independently from each other, we apply a magnetic field and split the m_{F_e} levels through the Zeeman splitting. To prepare the imaging, we optically pump the atoms into either the $m_F = -9/2$ state or the $m_F = +9/2$ state. To this end, we exploit the $F_e = 9/2$ hyperfine state given that it has a small Zeeman splitting. For circular polarized light on resonance, the atoms are pumped into $m_{F_g} = -9/2$ with σ^- polarized light or into the $m_{F_g} = +9/2$ with σ^+ polarized light, as shown in Fig. 5.3b.

We expect this imaging method to apply equivalently for both the $m_{F_g} = -9/2$ and the $m_{F_g} = +9/2$ spin state. This opens an interesting possibility of imaging a SU(2) system on the red transition with the two spin states being $m_F = -9/2$ and $m_F = +9/2$ state. We will address this in Sec. 5.4

5.3 Single-atom resolution of ^{87}Sr

Following the plan described in the previous section, we overcome the challenges of the state-dependent polarizabilities and obtain single-atom images of the fermionic isotope ^{87}Sr, see Fig. 5.4a.

In this section, we explain the imaging configuration and we present the results of imaging the fermionic isotope using the red transition for fluorescence and cooling simultaneously. We discuss the change in resolution due to the longer imaging wave-

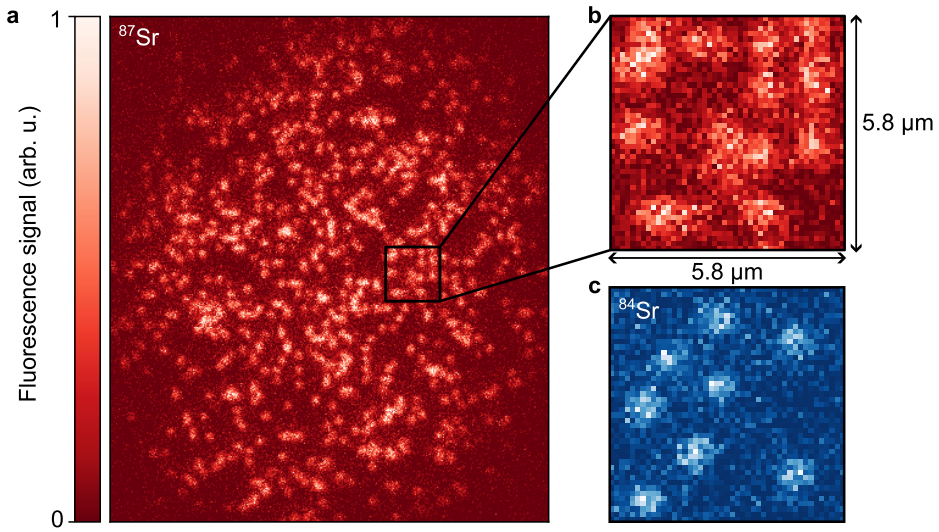

Figure 5.4: Single-atom images of a thermal cloud loaded into the lattice. **a** Hundreds of single fermionic ^{87}Sr atoms imaged on the red transition. **b** Around 10×10 lattice sites from the area indicated in **a**. To distinguish it from the previous images we chose a red colormap due to the red fluorescence for imaging. **c** Image of 10×10 lattice sites of the bosonic ^{84}Sr atoms imaged on the blue transition, see Fig. 4.3. While the size of the image is the same as in **b**, the signal of the atoms is smaller due to the higher spatial resolution of the blue imaging.

length and present the reconstruction and the fidelity of the new imaging method.

5.3.1 Imaging setup

Imaging fermionic strontium on the red transition at 689 nm requires one beam for pumping and a second one to induce the fluorescence of the atoms, see Fig. 5.3. Additionally, we need a well defined quantization axis, in order to drive the pumping and imaging transitions in the right direction, towards $m_{F_g} = -9/2$, or possibly also $m_{F_g} = +9/2$

The schematic of the red imaging configuration is shown in Fig. 5.5. The magnetic field and the polarization of the trapping light determine the quantization axis and consequently the direction and the polarization of the red light. We apply a magnetic field in the vertical direction parallel to the linearly polarized light of the lattice and the light sheet beam. The amplitude of the magnetic field is limited to around 2 G in our experiment due to heating of the z-bias coils. It Zeeman-splits the m_{F_e} states by around 750 kHz and allows us to address the different m_F states individually. However, it is not sufficient to fully suppress off-resonant scattering. This will be addressed in a future upgrade of the coils generating the magnetic field, with which we plan to attain fields an order of magnitude larger.

We apply circularly polarized light σ^- to pump the atoms into the $m_{F_g} = -9/2$ state. It is important to have well defined polarization in order to achieve clean optical

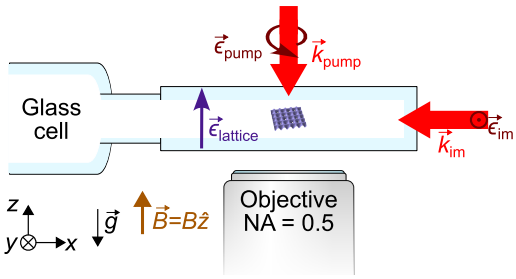

Figure 5.5: Red beam configuration for imaging the fermions ^{87}Sr. The polarization of the lattice beams is oriented along the z-axis, as well as the constant magnetic field $\vec{B}$. For optical pumping of the spin states a beam enters the glass cell vertically and has circular polarization $\vec{\epsilon}_{\text{pump}}$. For imaging, we use a beam from the back of the glass cell with linear polarization in the plane $\vec{\epsilon}_{\text{im}}$, such that it addresses σ^- and σ^+ transitions equally.

pumping of the atoms. For this reason, we install a beam with circular polarization propagating vertically through the glass cell parallel to the polarization of the lattice and the magnetic field, see Fig. 5.5. We separate optical pumping and imaging processes such that the pump beam entering the objective is blocked by a shutter in front of the camera. In this way we prevent exposure of the camera chip. To optically pump the atoms into the $m_{F_g} = 9/2$, we change the direction of the circular polarization to σ^+ by means of adding a $\lambda/2$-wave plate in the beam path using an optomechanical slider[1].

The fluorescence signal results from excitation to the $F_e = 11/2$ hyperfine state from $m_{F_g} = -9/2$ using σ^- polarized light, see Fig. 5.3a. The beam inducing fluorescence should not enter the objective to avoid background photons on the camera sensor during imaging. Therefore, we send a beam along x-direction into the glass cell, see Fig. 5.5. It has linear polarization, perpendicular to the lattice polarization and the magnetic field, resulting in both σ^- and σ^+ polarizations, allowing us to image on the $|m_{F_g} = +9/2\rangle \rightarrow |m_F = +11/2\rangle$ transition as well.

In comparison to the blue imaging setup in Fig. 4.1a, we exchange the filters in front of the camera from blue to red filters[2]. The objective, the mirrors and the lens remain the same and consequently the magnification $\mathcal{M} \approx 125$ is the same as for the blue imaging described in Ch. 4.

5.3.2 Resolution and point spread function

A comparison between the images of the fermionic isotope taken with red fluorescence (Fig. 5.4b) and the images of the bosonic isotope taken with blue fluorescence (Fig. 5.4c) shows that the signal of the atoms in the red imaging is larger than in the blue imaging. It is the result of the lower resolution of the red imaging, arising due to a

[1] Dual-Position Slider (ELL6-SM1-Threaded, Thorlabs)

[2] For red imaging: 690/8 nm BrightLine® single-band bandpass filter (FF01-690/8-25, Semrock), transmission >90 % at 686−694 nm.

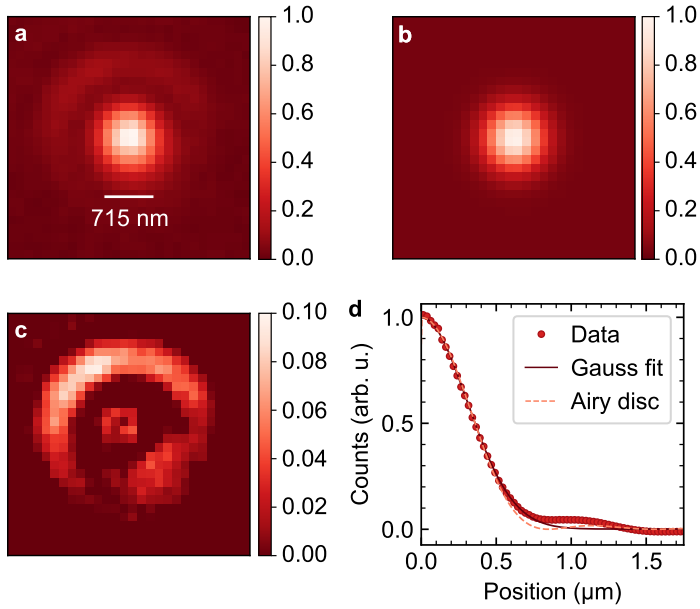

Figure 5.6: Point spread function of red imaging measured with fermionic atoms. **a** The normalized point spread function is obtained from averaging the signal of 162 single atoms. **b** Fitting a two-dimensional Gaussian function to the averaged atom signal, we find a full width at half maximum of 715(10) nm. **c** The residual is calculated as the difference of the averaged atoms and the Gaussian fit. **d** The azimuthal average of the atom signal is fitted with a Gaussian, and shown in comparison to the theoretical Airy function, see Eq. (4.1).

	Blue imaging	**Red imaging**
Imaging wavelength	461 nm	689 nm
Theoretical Airy disc r_0 (r_{FWHM})	562 nm (470 nm)	841 nm (703 nm)
Experimental Gauss fit FWHM	632(3) nm	715(10) nm

Table 5.2: Resolution comparison for blue vs. red imaging. The lattice spacing is 575 nm and the objective has a NA = 0.5. The expected radius of the Airy disc r_0 and its full width at half maximum r_{FWHM} for the red imaging is larger than for the blue due to the difference in the imaging wavelength. The measured value of the red imaging is closer to the expected FWHM of the Airy disc compared to the blue one. The blue imaging was performed with bosonic strontium, the red with fermionic strontium.

natural limit related to the longer wavelength of the red light $\lambda_{\text{red}} \approx 689\,\text{nm}$ compared to the blue one $\lambda_{\text{blue}} \approx 461\,\text{nm}$. In particular, the Rayleigh criterion discussed in Sec. 4.2.1 gives a theoretical limit for the resolution through the radius of the Airy disc $r_0 = 1.22\frac{\lambda}{2\text{NA}}$, with the numerical aperture of our objective NA = 0.5, see Eq. (4.2) Therefore, the longer wavelength λ_{red} results in a larger radius of the Airy disc and thus a lower theoretical resolution, presented in Tab. 5.2.

Experimentally, the lower resolution is captured in the point spread function (PSF). We determine the PSF of the red imaging in the same fashion as the one of the blue. We capture images of dilute thermal clouds, overlap and average the detected atoms and perform a Gaussian fit to extract the full width at half maximum (FWHM). The two-dimensional Gaussian fit of the 162 averaged atom signal has a FWHM of 715(10) nm, see Fig. 5.6. We compare the result of the fit to the FWHM of theoretical size of the Airy disc, which is around 703 nm.

Interestingly, the measured point spread function of the red imaging varies only by few nanometers from the expected FWHM of the Airy disc, in contrast to the blue imaging where the difference is more than 100 nm, see Tab. 5.2. The discrepancy for the blue imaging is probably due to a combination of optical aberrations and of the spread of the atomic wave packet [137]. A thermal spread of the atomic wave packet arises due to the increasing temperature of the atoms caused by the recoil heating with the blue photons during imaging [137]. The scattering of the red imaging photons has a simultaneous cooling effect, thus it is reasonable to assume that the atoms remain colder during the imaging process compared to the blue imaging.

5.3.3 Fidelity and photon count

Despite the lower resolution, the reconstruction of the atoms in the lattice still works efficiently. The image shown in Fig. 5.7a was exposed for 3 s, and after deconvolution of 30 iterations with the Richardson-Lucy algorithm [240, 241], we obtain the occupation matrix in the same way as for the blue imaging of the bosons, see Sec. 4.2.2. The histogram in Fig. 5.7b reveals two distinct peaks indicating the distinguishability of having no atom in a lattice site or having one atom. We identify atoms at a given lattice with a fidelity of 96.6 % based on the overlap of the Gaussian fits for both beams.

For red imaging and 3 s exposure we detect on average around 2500 photons per atom. The simultaneous cooling and imaging on the red transition allows us to saturate the transition and thus scatter more than 10 000 photons per second. As explained in Tab. 5.3, we detect around 7 % of the total scattered photons, which corresponds to 2100 photons per atoms during 3 s exposure. These values are of the same order of magnitude compared to other microscopes, see for example [85, 88, 89, 90].

In comparison to the blue imaging, we detect an order of magnitude more photons per atom, see Fig. 4.7. This is because in the blue fluorescence scheme, the number of blue photons scattered is limited by the efficiency of the red attractive Sisyphus cooling which has to counteract the recoil heating. In that case, we induce fluorescence with a blue beam around $2\Gamma_{\text{blue}}$ detuned from resonance and an intensity of around

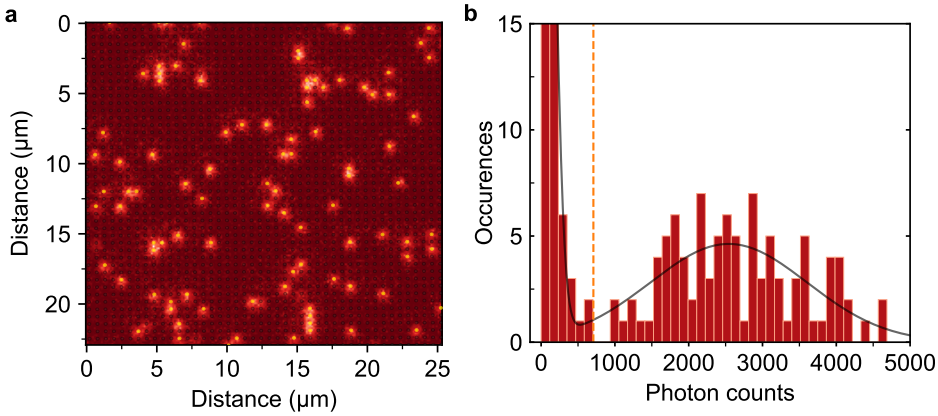

Figure 5.7: Reconstruction of lattice site occupation and histogram for red imaging of the fermionic atoms. **a** Raw image of the fermions with 3 s exposure time is overlapped with the occupation matrix (black and orange dots). The pixel size is converted into real distance in micrometers, and the full size is around 44×44 lattice sites. We image on the $m_{F_g} = -9/2$ to $m_{F_e} = -11/2$ transition, which is red-detuned from all the other spin states. **b** Histogram with photon counts for the raw image shown in **a**. In comparison to the blue imaging of the bosons, we collect about an order of magnitude more photons for the red imaging (see text).

	461 nm	689 nm
Glass cell (uncoated)	92 %	92 %
Objective collection efficiency	9.4 %	9.4 %
Objective transmission	85 %	90 %
Three mirrors	97.3 %	97.9 %
Achromatic lens	99.7 %	99.6 %
Filters	95 %	99 %
Quantum efficiency of CCD	82.9 %	92 %

Table 5.3: Transmission efficiencies of the different elements in the imaging system for blue 461 nm and red 689 nm imaging. The values stem from the specifications of each element. The filters are exchanged from one to the other imaging method. See Sec. 4.1.2 for detail on the elements of the setup.

$10^{-3} I_{\mathrm{sat}}$, with I_{sat} the saturation intensity of the blue transition. In this way, we reduce the numbers of scattered photons to around 3400 photons/s and we detect around 300 photons per atom during 3 s exposure due to the losses in the imaging system, see Tab. 5.3 and Sec. 4.1.2.

The higher number of scattered photons per second for the red imaging compared to the blue facilitates implementing shorter imaging times. However, it comes at the cost of a lower resolution. This may be unfavorable in measurements with smaller lattice spacing and it requires more resilient reconstruction algorithms such as those using machine learning techniques [228]. In conclusion, whether or not the the bosonic isotope will profit from red imaging depends on the specific goal of the experiment. For the fermionic isotope, imaging on the blue transition appears to be unfeasible. Instead we benefit from higher photon counts, which enabled us to perform red imaging with 1 s exposure. This is advantageous for a faster cycle time in the experiment, and might be very beneficial when taking spin-resolved images as discussed in the next section.

5.4 Spin-resolved imaging of ^{87}Sr

The implementation of spin-resolved imaging is a desirable goal to investigate spin correlations and spin ordering for large N systems, where numerical simulations reach their limits [73, 74, 75, 23]. With ^{87}Sr, it has been demonstrated in optical tweezers for two spin states exploiting the clock state [110]. The fundamental idea behind that scheme is to image one spin state while all the others are stored in the long-lived clock state $^3\mathrm{P}_0$. Afterwards, another spin state is brought to the ground state while the others are stored again. A disadvantage of this method is the narrow-linewidth clock laser required to address the ultra-narrow-linewidth transition between $^1\mathrm{S}_0$ and $^3\mathrm{P}_0$. Additionally, large magnetic fields are required, to split the m_F substates of the clock state sufficiently to address the transitions independently [126]. Moreover, inelastic photon scattering from the 813.4 nm lattice beams is expected to limit the lifetime of the atoms in the clock state [254], thus reducing the detection fidelity for the stored atoms.

A different approach is to exploit the narrow-linewidth transition at 689 nm. We can exploit the splitting of the m_{F_e} states to address the different m_{F_g} states independently, see Fig. 5.3. A similar scheme has been presented for ytterbium tweezers experiments with two spin states in the ground state $^1\mathrm{S}_0$ $F = 1/2$ [253]. In this section we will discuss the possibility of adding spin-resolved detection to our imaging scheme and discuss the limitations arising. On top of that, we will present our first results of spin-selective imaging of ^{87}Sr.

5.4.1 Imaging protocol

As presented in Fig. 5.4, we can image fermionic strontium with single-atom resolution in the optical lattice. However, since we exploit the closed transition between $|^1\mathrm{S}_0, F_g = 9/2, m_{F_g} = -9/2\rangle$ and $|^3\mathrm{P}_1, F_e = 11/2, m_{F_e} = -11/2\rangle$ for imaging, we actually image only one spin state: $m_{F_g} = -9/2$. If we add imaging on the other closed

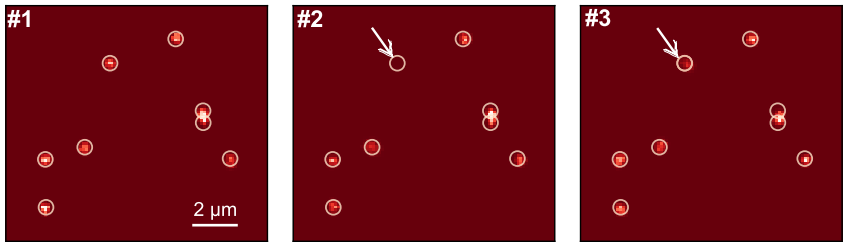

Figure 5.8: Sequence of three consecutive images showing spin transfer. The images show the deconvolution (30 iterations with the Richardson-Lucy algorithm [240, 241]) of fermions in the lattice, imaged with 3 s exposure. The three consecutive images show an atom disappearing in the second image and reappearing in third one, see arrows. Most probably, the atom was transferred into another spin state where it could not be imaged and eventually returned back into the imaged state.

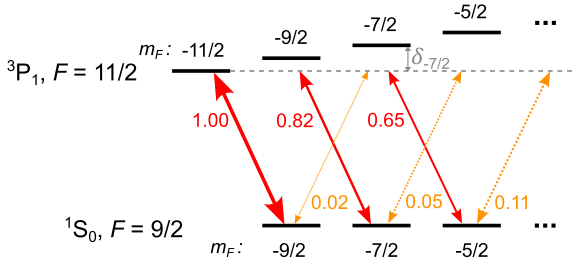

Figure 5.9: Imaging transition for $F_e = 11/2$ with squared Clebsch-Gordan coefficients. When addressing the $|F_g = 9/2, m_{F_g} = -9/2\rangle \rightarrow |F_e = 11/2, m_{F_e} = -11/2\rangle$ transition for imaging, there is a non-zero probability that atoms are excited to the $m_{F_e} = -7/2$. The probability is small and if an atom is brought to a different spin state, it is likely to return immediately to $-9/2$ because the Clebsch-Gordan coefficients favor excitations on the σ^- transition towards $m_{F_g} = -9/2$. Additionally, the Zeeman splitting lifts the degeneracy such that the transitions are detuned by δ from resonance, see for example $m_{F_e} = -7/2$.

transition between $|^1S_0, F_g = 9/2, m_{F_g} = +9/2\rangle$ and $|^3P_1, F_e = 11/2, m_{F_e} = +11/2\rangle$, we can already image two different spin states $m_F = -9/2$ and $m_F = +9/2$, without implementing a clock laser in the experiment. In theory this scheme can easily be extended to more than just two spin states. The goal is to prepare atoms in a chosen set of spin states through optical pumping [255], and load them into the optical lattice in the Hubbard regime. We will image the spin states corresponding to $m_{F_g} = -9/2$ and $m_{F_g} = +9/2$ on their closed transition, see Fig. 5.3a. Afterwards, we will pump another m_{F_g} state into one of the $m_{F_g} = \pm 9/2$ states and image again. We will repeat this process until all the spin states in the system have been detected.

The experimental application presents some challenges, demonstrated in Fig. 5.8. There, we observe individual atoms in a lattice with small population. We capture a sequence of several images with less than 1 s exposure time. As shown in Fig. 5.8, an atom disappears in one picture and reappears in the next one, which seems like the atom is blinking. Because this arises in very sparsely filled lattice with less then 10 atoms within 400 lattice sites, we can rule out hopping as the cause. The effect can be explained through the transfer into another spin state, which cannot be detected on the chosen imaging transition.

There are two possible processes responsible for this spin transfer. On the one hand, our imaging light drives Raman transitions between the different spin states [253] because the imaging light has $\sigma^{\pm}$ contributions, see Fig. 5.5. The Raman Rabi frequency is proportional to $1/\delta_{m_F}$ which allows us to reduce the effect by increasing the detuning δ_{m_F}. However, the splitting between the different m_{F_e} state is limited by the magnetic field we can create in z-direction. In our experiment, the z-coils cannot create fields larger than 2 G and also only for short times due to heating of the coils. On the other hand, the energy difference between the different m_{F_e} states may not be sufficient to suppress off-resonant scattering. In consequence, the atoms can be transferred to another spin state by off-resonant scattering of the light with opposite polarization, as shown in Fig. 5.9. Having said that, the Clebsch-Gordan coefficients of the $F_e = 11/2$ favor the imaging transition (see Appx. A.2 for the values of the Clebsch-Gordan coefficients). For example, the squared Clebsch-Gordan coefficient between $|m_{F_g} = -9/2\rangle \rightarrow |m_{F_e} = -11/2\rangle$ is $C^2 = 1$ which is significantly larger than the one between $|m_{F_g} = -9/2\rangle \rightarrow |m_{F_e} = -7/2\rangle$ which is $C^2 = 0.02$, see Fig. 5.9 and Appx. A.2.

Both scattering processes can be reduced if we split the sublevels of the hyperfine state further. To this end, we will install a new set of coils to achieve magnetic fields about an order of magnitude larger than the current ones and increase the Zeeman splitting between the m_{F_e} levels from around 760 kHz at 2 G to around 7.6 MHz at 20 G.

Additionally, the larger splitting will allow us to optimize the optical pumping, into carefully chosen spin states. Furthermore, the probability of off-resonant scattering of atoms in other $|m_{F_g}| \neq 9/2$ spin states will be reduced (see Fig. 5.9), which should improve the performance of the spin-resolved imaging.

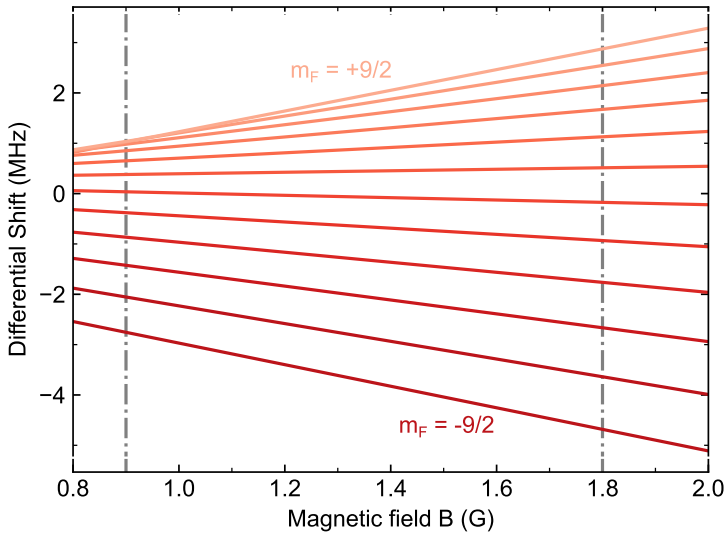

Figure 5.10: Magnetic field dependent differential energy shift. We calculate the differential energy shift for different magnetic fields, considering a light field intensity corresponding to the depth of our fourfold optical lattice (Sec. 3.2). The combination of the Zeeman and the light shift results in smaller splitting for $m_{F_e} < 0$ compared to $m_{F_e} > 0$. The vertical, dashed lines indicate magnetic fields used for imaging in Fig. 5.11.

5.4.2 Proof-of-principle demonstration of spin resolution

From the discussion in Sec. 5.2, we know that a closed transition is required for imaging, and the polarizabilites should fulfill the Sisyphus cooling prerequisite. This is the case for both $|m_{F_g} = \pm 9/2\rangle \rightarrow |m_{F_e} = \pm 11/2\rangle$ transitions with σ^- or σ^+ polarization, respectively. The images in Fig. 5.4 and Fig. 5.7 were taken for atoms in the $m_{F_g} = -9/2$ spin state because this transition is red-detuned from the other m_{F_g} states, and calculating the light shifts, we find that it is more separated from the neighboring states in comparison to $m_{F_g} = +9/2$, see Fig. 5.10. Nonetheless, imaging the $+9/2$-spin state works as well for large enough magnetic fields.

We prepare a cloud of fermionic atoms in the fourfold optical lattice confined in the vertical direction by means of the light sheet, as for the bosons. We optically pump the atoms by means of the $F_e = 9/2$ excited state to increase the population in the $-9/2$ and the $+9/2$-spin states, however our optical pumping is not fit to have only the two spin states occupied. We generate a fluorescence signal of the atoms in the $-9/2$-spin state by exposing them to 689 nm-light with the frequency matching the $|m_{F_g} = -9/2\rangle \rightarrow |m_{F_e} = -11/2\rangle$ transition (Fig. 5.11a). To this end, we split the m_{F_e} states by applying a magnetic field B_z of around 0.9 G. Afterwards, for imaging the $+9/2$-spin state, we increase the magnetic field to 1.8 G, in order to split the states sufficiently, see Fig. 5.10. The spin states are not altered by the adiabatic increase of the magnetic field, which is aligned parallel to the lattice light polarization and does not change direction. Exciting the atoms on the $|m_{F_g} = +9/2\rangle \rightarrow |m_{F_e} = +11/2\rangle$

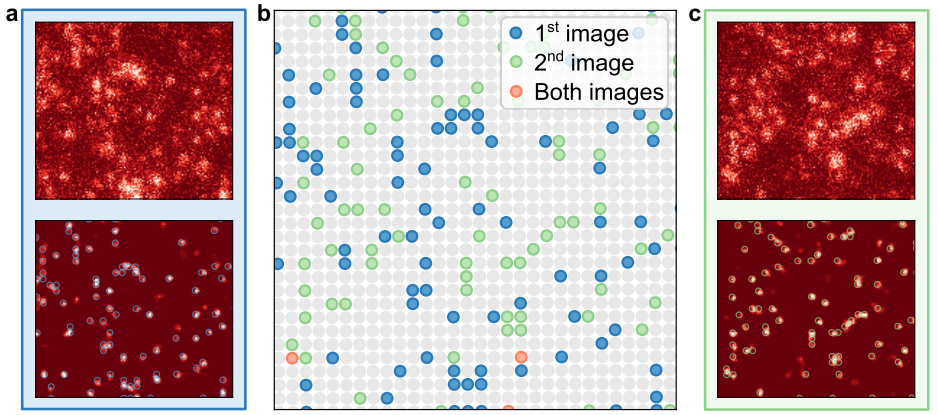

Figure 5.11: Imaging of two different spin states by means of the red transition. **a** Raw (top) and reconstructed (bottom) images of fermions in the $m_{F_g} = -9/2$ state. The imaging frequency is set to the $|F_g = 9/2, m_{F_g} = -9/2\rangle \rightarrow |F_e = 11/2, m_{F_e} = -11/2\rangle$ transition and the exposure time is 1 s. **c** A second image was taken in the same experimental run on the $|F_g = 9/2, m_{F_g} = +9/2\rangle \rightarrow |F_e = 11/2, m_{F_e} = +11/2\rangle$ transition, showing atoms populating the $m_{F_g} = +9/2$ state. **b** The occupation matrices of the two images shows atoms detected in the first image with blue dots and atoms detected in the second image with green dots. The reconstruction does not detect all bright points and there are a few atoms that were detected in both of them colored red, see text.

results in a second picture (Fig. 5.11c). After reconstruction, we obtain and compare the occupation matrices of the two images, see Fig. 5.11b. We find that the majority of the atoms appear either only in the first image (blue dots) or only in the second one (green dots). It implies that we imaged two different spin states in the same system with this method. The few individual atoms which appear in both images (red dots) may be a result of hopping or faulty reconstruction. Additionally, in the deconvolved images in Fig. 5.11, some weak signals appear which are not detected as atoms. We identify those as atoms that changed their spin state during imaging and thus did not scatter as many photons as atoms that remained in their initial spin state. We understand that this is probably a result of either off-resonant scattering or Raman scattering and can be suppressed by increasing the splitting between the m_{F_e} states as discussed in the previous section.

5.5 Conclusion

In this final experimental chapter, we presented single-atom-resolved imaging of fermionic strontium, with a first result of spin resolution. We discussed the challenges of single-atom-resolved imaging of fermionic strontium ^{87}Sr compared to bosonic strontium ^{84}Sr. While generating a blue fluorescence signal technically works, the method of cooling on the red narrow-linewidth transition fails due to the different light shifts of the hyperfine substates of the excited state. A careful investigation of the polarizabilities of the different m_{F_e} states for the hyperfine states F_e of $^3\mathrm{P}_1$ revealed that attractive Sisyphus cooling works for some of the spin states and repulsive Sisyphus cooling would have to be used for others. Performing imaging on the red transition only and exploiting the fluorescence photons for cooling, enabled us to image the fermionic atoms with a detection fidelity of 96.6 %. Even though the resolution is lower compared to the blue imaging due to the longer wavelength of the red imaging light, we showed that through deconvolution we can still reconstruct the images. In a last step, we discussed the experimental challenges due to Raman scattering and off-resonant scattering processes, which will be solved in the future by upgrading the magnetic-field coils of the apparatus. Finally, we demonstrated imaging of two different spin states in a thermal cloud of fermions with our microscope. Future steps for the system will extend the spin- and atom-resolved imaging scheme to more than two spin states which will empower us to realize and study spin correlations arising in SU(N) Fermi-Hubbard systems for up to ten different spin states.

Chapter 6

Conclusion and outlook

6.1 Thesis summary

This work presented the realization of a strontium quantum-gas microscope for the study of Bose- and Fermi-Hubbard systems. Strontium has both bosonic and fermionic isotopes, and the two-valence electrons provide a rich energy level diagram with a broad-linewidth blue transition and a narrow-linewidth red transition. Besides their application for laser cooling of strontium to microkelvin temperatures before performing evaporative cooling, we exploit the blue and the red transition for single-atom-resolved imaging of the strontium atoms in a Hubbard-regime optical lattice. This yields a resourceful tool box to study various physical problems.

In chapter 1, we introduced the goal and the topic of the thesis which is the realization of a quantum-gas microscope with strontium for quantum simulations of both Bose- and Fermi-Hubbard systems. In particular, we discussed the SU(N) Fermi-Hubbard model and some of the exotic magnetic phases it hosts. We also addressed the applications provided by the narrow-linewidth transitions, among which the long-lived clock state, which is a convenient tool for high-precision measurements. Additionally, an overview of the thesis is presented.

In chapter 2, we discussed the cooling sequence employed to generate ultracold atoms of strontium. We have discovered and studied a scheme to resonantly shield atoms from losses during the blue magneto-optical trap (MOT) and increases the atom number, which led to the publication [116]. The method relies on the narrow linewidth of the red transition at 689 nm, which forms a closed two-level system, in contrast to the broad-linewidth transition (461 nm) of the blue MOT, which is not closed. The method doubles our atom number and the increase is preserved through out all the consecutive cooling steps. While this method reduces the losses in the blue MOT, there are still atoms leaking into metastable states. Those can be recovered by introducing a repumper laser. The choice of the transition used for repumping is in particular important for the fermionic isotope due to its hyperfine structure. We settled with the 707 nm repumper laser combined with a 679 nm clock repumper because it promises recovery of atoms from the most hyperfine states. After the blue MOT, we switch to

the red transition for a narrow-line MOT. To this end, we implemented a first step of broadband cooling, where the frequency of the red laser is broadened to address more velocity classes, and then we employ a single-frequency cooling stage to reach microkelvin temperatures. The red MOT has additional challenges for the fermionic isotope which we discussed in detail in Sec. 2.3.3. We successfully implemented evaporative cooling in the far-detuned optical dipole trap (at 1064 nm) combined with a tightly focused light sheet beam at the clock-magic wavelength 813.4 nm. We demonstrated the Bose-Einstein condensation of ^{84}Sr and showed that quantum degeneracy of ^{87}Sr is within reach.

The ultracold strontium atoms are then loaded into a two-dimensional optical lattice. In chapter 3, we discuss the fourfold geometry and the setup of our optical lattice. We chose a bow tie configuration where one beam is overlapped four times with itself, resulting in a fourfold interference. The lattice is operated at the clock-magic wavelength which results in a lattice spacing of 575 nm. The band structure arising from our optical lattice is altered by power losses in the glass cell. However, the estimated values of the tunneling and the interaction parameters confirmed that we have realized a Hubbard system. The two-dimensional confinement is given by a tightly focused light sheet beam, which has a vertical beam waist of around 3.5 µm.

To study such systems, we implemented single-atom-resolved imaging. To this end, we implemented two different methods for the two different isotopes ^{84}Sr and ^{87}Sr. In chapter 4, for the bosonic isotope ^{84}Sr, we exploited blue fluorescence and realized for the first time attractive Sisyphus cooling in a lattice using the narrow-linewidth red transition of strontium. We used this method combined with momentum-space imaging, to detect and characterize a Bose-Hubbard superfluid by means of interference arising from the phase coherence of the superfluid phase. Besides that, we discussed the reconstruction of the occupation in the lattice and characterized the performance of the imaging, where we found a pinning fidelity of 96 %. Additionally, we exploited the spatial dependence of the attractive Sisyphus cooling on the harmonic confinement to characterize the trap potential during imaging. The results discussed in this chapter have been published in [220].

In chapter 5, we demonstrated imaging of the fermionic isotope ^{87}Sr on the red transition employing it for both fluorescence and cooling simultaneously. The substates of the hyperfine structure provide both a challenge and a tool. The different substates cannot be cooled at the same time due to the m_F-state-dependent differential light shift. We successfully imaged the fermionic atoms using one particular spin state, and characterize the imaging finding a detection fidelity of 96.6 %, despite the lower resolution of the red imaging scheme. However, we can split the substates of the excited hyperfine state $F = 11/2$ in energy and address all of the spin states individually. This sets the stage for spin resolved imaging on the narrow-linewidth transition, which we have shown for two different spin states.

In conclusion, we have successfully built an apparatus to routinely prepare ultracold strontium clouds for both the bosonic ^{84}Sr and fermionic ^{87}Sr isotopes. We have realized single-atom-resolved imaging for both of them and additionally spin resolution for the fermionic atoms. This combines the distinct properties of strontium with

the unprecedented access to local observables provided by quantum-gas microscopes, promising new insight into a variety of complex many-body systems.

6.2 Outlook

At the current stage, we have a quantum-gas microscope with single-atom resolution for bosonic ^{84}Sr and fermionic ^{87}Sr. Moreover, we have already loaded quantum-degenerate bosonic gases in an optical lattice and used our microscope to characterize Bose-Hubbard superfluids. However, we still need to achieve the strongly interacting regime, marked by the entrance into the Mott insulating phase. This will require an increase in the interaction with respect to the tunneling parameter. To this end, we will add a vertical lattice in the apparatus which will increase the two-dimensional confinement and consequently also the interaction. Once this is achieved, a diverse range of quantum experiments that can use the microscopic access provided by our apparatus will be studied.

6.2.1 The dissipative Bose-Hubbard model

The coupling of a quantum many-body system with the environment can lead to the destruction of the coherence of the system. However, well controlled dissipation can also be a tool to engineer phases of matter, providing an interesting research platform of open quantum many-body systems [256, 257]. To this end, ultracold atoms provide coherent systems and the desired control to induce dissipation and coherence. Narrow-linewidth transitions, as they occur naturally for alkaline-earth atoms, are beneficial for their use as well-controlled induced decoherence. In an experiment with ytterbium, the changes in the quantum phase transition between the superfluid and the Mott insulating phase have been studied under the influence of driven dissipation [258]. In another recent experiment, the decoherence of a strongly interacting Bose gas in lattices causes anomalous diffusion [259], similar to the results of the numerical study of the Bose-Hubbard model [260]

Quantum-gas microscopes provide a convenient platform to study dissipative quantum many-body systems, allowing access to local observables and manipulation of individual atoms [85, 261]. Our superfluid of ^{84}Sr in the quantum-gas microscope provides a well-controlled system in a coherent state, where dissipation can readily be implemented through the narrow-linewidth two-level transition between the ground state $^1S_0$ and $^3P_1$.

6.2.2 Frustrated quantum magnets with hardcore bosons

The quantum spin liquids describe an exotic phase of matter which exhibits topological order and long-range quantum entanglement [262]. They are exciting system in the context high-T_c superconductivity [2, 263] and topological quantum computing, as the topology improves the robustness of the qubits [264, 265]. In a simplified picture, quantum spin liquids can be considered systems that avoid ordering of the spin states

even at low temperatures [266]. Frustrated systems can exhibit properties of spin liquids [16]. For example, a two component system with antiferromagnetic coupling in a triangular lattice forms a geometrically frustrated system, where the three adjacent lattice sites cannot accommodate antiferromagnetic ordering of the spin states [52] and the spins may favor arranging in singlets across the lattice [16].

The challenges of numerical methods for those systems [267], make quantum simulations a desirable goal. The topological properties of quantum spin liquids have been studied by means of Rydberg atoms in tweezers arrays forming a kagome lattice [264]. A demonstration with ultracold atoms in optical lattices is still pending, despite various theoretical proposals [268, 269, 270].

In a Bose-Hubbard system, for large interactions $U/t \gg 1$ the occupation of the lattice sites can be mapped into pseudospins. For these systems quantum spin liquids are expected to form in triangular lattices [271]. As suggested in the master's thesis of M. Miranda [208], our quantum-gas microscope of ^{84}Sr is capable of investigating properties of those quantum spin liquid phases through clever mapping of a Bose-Hubbard model into the XX Hamiltonian and adiabadic preparation of the expected quantum spin liquid state. To this end, we will exploit the possibility of realizing a triangular geometry by adding an additional beam to our fourfold optical lattice, as discussed in Sec. 3.2.2.

6.2.3 Collective atom-photon scattering

The interaction between photons and an ordered array of atoms with subwavelength spacing exhibits collective phenomena [111]. In such an atomic array, the remission of absorbed light can lead to collective interference which can be constructive resulting in superradiance or destructive leading to subradiance. Subradiance atomic arrays are a promising tool to realize quantum memory through storage of light, discussed theoretically [113] and observed experimentally [114]. As a consequence of its subradiant nature, such systems display a narrowing of their intrinsic single-atom linewidth [112].

Strontium provides a convenient platform for studies of atom-photon interactions in the subwavelength regime due to the closed two-level system between ^{1}S$_0$ and ^{3}P$_1$ at a wavelength of 689 nm. Realizing these systems with our quantum-gas microscope for ^{84}Sr is straightforward. Our lattice spacing is subwavelength compared to the red transition and a unit-filled ordered array will be achieved once we realize the Mott insulating phase. Alternatively we could also attempt to produce ordered arrays exploiting the method of algorithmic cooling [219]. Moreover, exploiting the long-lived states in the ^{3}P$_J$ manifold combined with higher lying states unlocks interesting opportunities in the opposite regime, for superradiance [161]. The transition from the ^{3}P$_0$ clock state to the D-states is at micrometer wavelengths, which gives access to strongly subwavelength arrays [272].

While the bosonic isotope is a natural choice due to its simpler level structure, ordered arrays of ^{87}Sr can also be used for collective studies. Large magnetic fields will be required to address the transitions of the different spin states individually. For

example, R. B. Hutson *et al.* realized a spin-polarized system that can detect the frequency shifts resulting from dipole-dipole interactions in a cubic lattice by means of the clock transition [273]. It is a promising starting point for future experiments regarding collective atom-photon interactions.

6.2.4 SU(N) Fermi-Hubbard physics

The extension of a two-component Fermi-Hubbard system to N spin-component system exhibiting SU(N) symmetry provides access to new and exciting phenomena.

Of particular interest are the correlations and orders arising in the exotic quantum magnetic phases of those systems. While the SU(2) case has been studied extensively, systems with $N > 2$ are an interesting challenge. Long-range spin ordering and dimerization have been proposed and their dependence on N and the lattice geometry has been studied theoretically [75, 23]. For increasing number of spin flavors in the system, the formation of new phases of matter can emerge, such as chiral spin liquids, which results from the difference between singlets of SU(2) and SU(N) systems and exhibit topological order [76].

In experiments of ultracold atoms, antiferromagnetic ordering for SU(2) systems was first detected for short-range spin-correlations in three dimensions [49, 274]. The development of Fermi microscopes allowed one to go beyond that, and observe the antiferromagnetic correlations in a one-dimensional chain where they extend over three sites [91] and in two-dimensional systems, nearest-neighbour spin correlations have been observed and studied for doped systems [92, 93]. However, the first observation of long-range antiferromagnetic order has been achieved by A. Mazurenko *et al.* [50]. In contrast to systems with two-spin components, in larger spin systems only short-range correlations have been measured. A comparison between SU(4) and SU(2) was demonstrated exploiting the SU($N \leq 6$) symmetry of ytterbium [70]. More recently, short-range correlations have been studied in SU(6) systems in one-, two- and three-dimensional lattices [71]. The occurrence of long-range correlations in SU(N) Fermi systems has yet to be observed experimentally.

Our strontium quantum-gas microscope is in a very good position to achieve this goal. In this thesis, we have demonstrated a first spin-dependent single-atom-resolved imaging. Once we master the technique and cool the fermionic atoms to quantum degeneracy, we can readily realize SU($N \leq 10$) Fermi-Hubbard systems. To ensure we reach the strongly interacting energy regime, where long-range spin correlations emerge, we will implement techniques such as entropy redistribution [275, 276, 50]. Furthermore, such a SU(N) system can benefit from so-called Pomeranchuk cooling [277, 69, 70], in which spin states can absorb the entropy and reduce density fluctuations upon entering the Mott insulating phase. A first study could involve SU(3) Fermi-Hubbard systems and the observation of different phases therein, such as Mott insulators and antiferromagnetism [278]. Another very exciting research direction is the investigation of doped systems. In the SU(2) case, recent experiments were able to observe hole pairing. First theoretical investigations of the SU(3) case, albeit in the t-J model limit, show rich physics [279] that should be reachable with our setup.

6.2.5 Spin-orbit coupling and synthetic flux ladders

The realization of synthetic dimensions and synthetic gauge fields is a powerful tool in the research of novel material and complex solid state systems. The basic idea is to exploit the internal state of the atoms as a synthetic dimension, additional to the spatial ones of the system. These synthetic dimensions can be coupled through laser light, realizing a magnetic flux piercing the system [280]. Fermionic alkaline-earth atoms are a resourceful candidate for the realization of those systems [248, 281]: on the one hand, they have many nuclear spin states that can be connected via two-photon Raman transitions, and on the other hand they have long-lived clock states that can realize a spin-1/2 model by directly driving the clock transition. Both points benefit from the narrow-linewidth and the long coherence times, as measured for example for strontium [282].

Clock-driven spin-orbit-coupled systems have been demonstrated with fermionic ytterbium and strontium [283, 209], as well as with bosonic ytterbium [284]. They are equivalent to a two-leg synthetic ladder pierced by a magnetic flux. They allow to realize spin-orbit coupled systems where the interactions of the two different components are different, which leads to rich physics as investigated in the bosonic case in our group in another setup, both from the experimental [285] and the theoretical [286] point of view.

In our quantum-gas microscope, it will be possible to explore this situation once we have installed the clock laser, which is being prepared [287], to address the ultra-narrow transition between the ground and the clock state. Spin-orbit coupling involving more than two states could be already implemented using the nuclear spin states of the ground state, where all scattering lengths are equal, leading to a different regime [288, 289, 290]. In both cases, the combination of spin-orbit coupling with single-atom resolution will provide invaluable access to study the chiral currents predicted in those systems [281].

Appendix A

Details on fermionic strontium

In this appendix we discuss the hyperfine structure of the fermionic strontium isotope arising from the large nuclear spin $I = 9/2$. We summarize briefly the hyperfine splitting for the transitions relevant for laser cooling and imaging of strontium. We explain the splitting between m_F states caused by a small magnetic field. Additionally, we list the Clebsch-Gordan coefficients which describe the coupling between angular momenta of different atomic states.

A.1 Hyperfine structure and Zeeman shift

The challenges of laser cooling and imaging fermionic strontium arise mainly from the hyperfine states and their numerous sublevels. The large nuclear spin of $I = 9/2$ together with the total angular momentum J forms hyperfine states F with $|I - J| < F < I + J$. For the ground state $^1S_0$ with $J = 0$ this results in only one hyperfine state $F = 9/2$. For states with $J = 1$ such as the blue $^1P_1$ and the red $^3P_1$ transitions of strontium there are three hyperfine states: $F = 7/2$, $9/2$ and $11/2$, see Fig. A.1. For the blue transition, from the ground state $^1S_0$ to the excited state $^1P_1$, the splitting between the hyperfine states F is of the same order of magnitude as the linewidth of the transition ($\Gamma/2\pi \approx 30.5\,\mathrm{MHz}$), such that the different states cannot be excited independently. For the $^3P_1$ state, the energy difference between the three hyperfine states are several orders of magnitude larger than the linewidth ($\Gamma/2\pi \approx 7.4\,\mathrm{kHz}$), consequently all three F-states can be addressed independently, which we exploit during the preparation of the cloud by means of laser cooling, see Sec. 2.3.3.

Each hyperfine state has $2F+1$ sublevels: $m_F = -F, -F+1, ..., F-1, F$. External fields, magnetic or light fields, shift the energy of the m_F states. For the ground state $^1S_0$, the total angular momentum is purely nuclear. Hence, large fields are required to achieve splittings of the $m_F = -9/2, ..., +9/2$ states comparable to the ones of the excited states at $J = 1$, typically magnetic fields of around hundreds of Gauss [291]. Therefore, the splitting of the m_F states of the ground state can be neglected in the

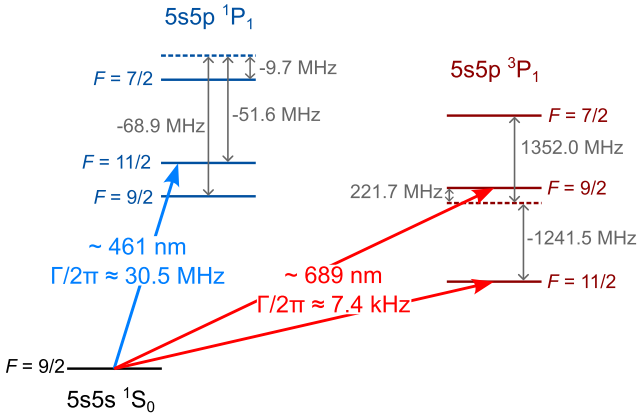

Figure A.1: Hyperfine splitting of the transitions relevant for laser cooling and imaging. The values are given with respect to the bosonic isotope ^{88}Sr [123, 125]. The blue transition from ^{1}S$_0$ to ^{1}P$_1$ at 461 nm is the same as the one for the blue MOT. The transitions at 689 nm from ^{1}S$_0$ to ^{3}P$_1$ are, on the one hand, the same as the red MOT ($F = 11/2$) and, on the other hand, the one of the stirring light ($F = 9/2$), see Sec. 2.3.3.

Hyperfine state	$g_F(^1\mathrm{P}_1)$	$g_F(^3\mathrm{P}_1)$
$F = 7/2$	$-2/9$	$-1/3$
$F = 9/2$	$4/99$	$2/33$
$F = 11/2$	$2/11$	$3/11$

Table A.1: Landé g-factors relevant for the Zeeman splitting (Eq. A.1). The values of g_F for the excited state of the blue transition ^{1}P$_1$ and the one of the red transition ^{3}P$_1$ are listed for the different hyperfine states F [291].

discussions of this work, because the applied fields are small and the m_F-splitting of the excited state dominates.

A.1.1 Zeeman splitting

At small magnetic fields, the frequency difference of the m_F states is proportional to the magnetic field amplitude B

$$\delta_F(B) = g_F \mu_\mathrm{B} B m_F / h \tag{A.1}$$

where μ_B is the Bohr magneton and h is Planck's constant. The Landé g-factor g_F depends on both the orbital and the spin angular momentum and therefore varies for the different hyperfine states, see Tab. A.1. The values of g_F are comparable for the excited states of the blue ^{1}P$_1$ and the red ^{3}P$_1$ transitions. In contrast, they vary significantly for different hyperfine states which directly affects the splitting of the m_F states, see in Fig. A.2 for the hyperfine states of the ^{3}P$_1$. For the red

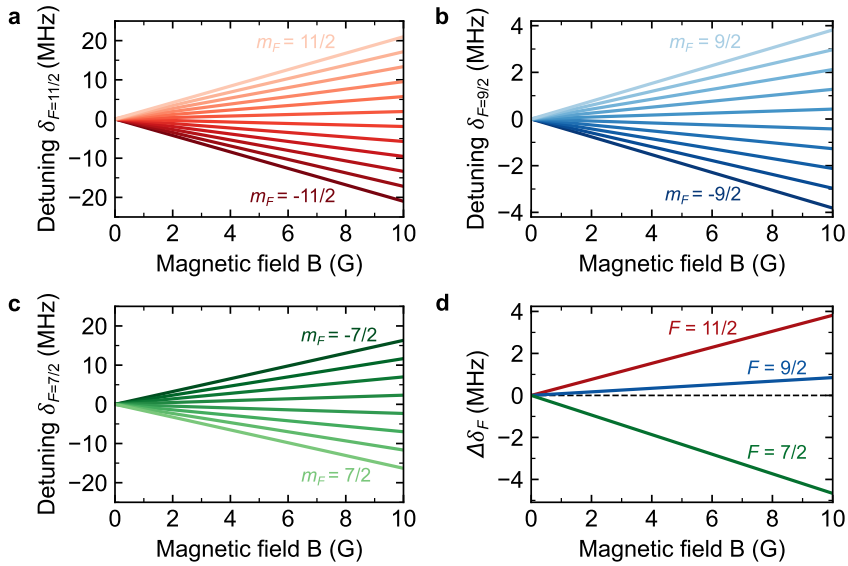

Figure A.2: Zeeman effect of different hyperfine states of $^3P_1$ at low magnetic fields. The relative splitting of the m_F states for **a** $F = 11/2$, **b** $F = 9/2$ and **c** $F = 7/2$ hyperfine states at magnetic fields up to 10 G. The hyperfine splitting is presented in Fig. A.1. **d** The energy difference between m_F and $m_F + 1$ states is linear at low fields and depends on the Landé g-factor in Tab. A.1. For large magnetic fields this linear approximation is invalid [126].

transition $^1S_0 \rightarrow ^3P_1$, a magnetic field of a few Gauss splits the m_F states hundreds of kilohertz, such that they can be addressed individually. This is not the case for the blue transition, where the larger linewidth prevents m_F selective excitation.

A.2 Clebsch-Gordan coefficients

The coupling between different levels $|F_g, m_{F_g}\rangle \rightarrow |F_e, m_{F_e}\rangle$ depends on the angular momenta of the states and the polarization of the laser addressing the transition. The probability of the transition is represented by the Clebsch-Gordan coefficients which describe the coupling between angular momenta:

$$C^{F_e,m_{F_e}}_{1,q,F_g,m_{F_g}} = \langle 1, q, F_g, m_{F_g} | F_e, m_{F_e} \rangle \tag{A.2}$$

for light with polarization $q = -1, 0, +1$ corresponding to σ^-, π and σ^+ polarization. For strontium the ground state $^1S_0$ with $F_g = 9/2$ has ten sublevels $m_{F_g} = -9/2, -7/2, ..., 7/2, 9/2$. For the excited state, we are mainly interested in $F_e = 11/2$, $F_e = 9/2$ and $F_e = 7/2$ because they are the hyperfine states of the $^3P_1$ excited state.

The Clebsch-Gordan coefficients of these three hyperfine states are shown in Fig. A.3, Fig. A.4 and Fig. A.5. The ground state m_{F_g} can be coupled to three different states $m_{F_e} = m_{F_g} + q$ with $q = -1, 0, +1$ depending on the polarization of the light. As shown in Fig. A.3, $|F_g = 9/2, m_{F_g} = -9/2\rangle$ is strongly coupled to

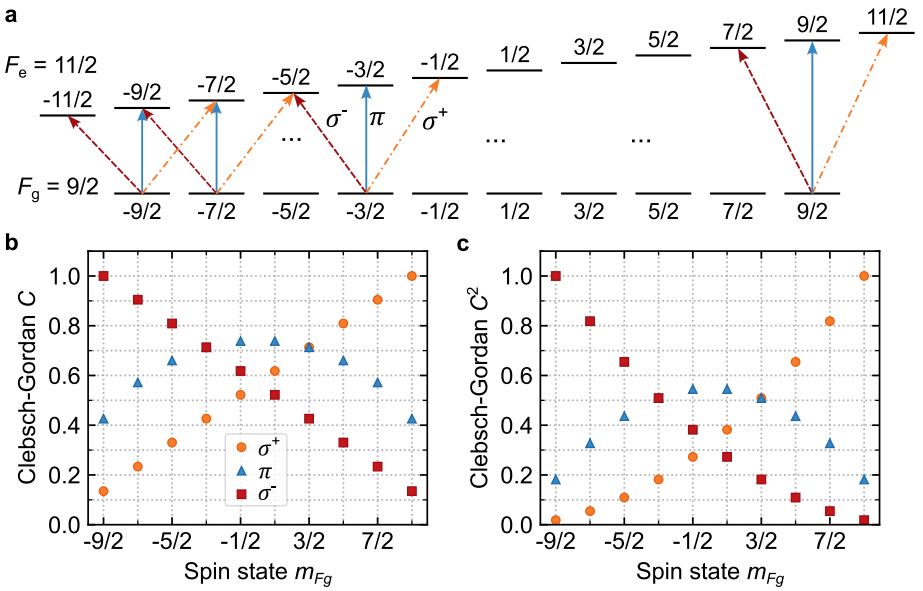

Figure A.3: Transitions of the hyperfine state $F_e = 11/2$. **a** Schematic of transitions from the ground state $^1S_0$ with $F_g = 9/2$ to the excited state $^3P_1$ $F_e = 11/2$ under the influence of an external field, thus the m_{F_e} states are non-degenerate. The blue solid arrows represent the π-transition, red dashed arrows the σ^- and orange dotted-dashed arrows the σ^+. **b** The Clebsch-Gordan coefficient $C = C^{F_e,m_{F_e}}_{1,q,F_g,m_{F_g}}$ where $m_{F_e} = m_{F_g} + q$ and $q = -1, 0, +1$ represents the polarization of the light σ^-, π and σ^+ respectively. **c** The square of the Clebsch-Gordan coefficient.

$|F_e = 11/2, m_{F_e} = -11/2\rangle$ through σ^- polarized light ($q = -1$), whereas the coupling through σ^+ to $|F_e = 11/2, m_{F_e} = -7/2\rangle$ is weak in comparison, see Fig. A.3b. Equivalently, the discussion can be continued for the other transitions and hyperfine states, although there are less excited m_{F_e} states for $F_e = 9/2$ and $7/2$ compared to $11/2$. Besides the relevance for understanding the probability of the different transitions, the coupling between the different states is relevant for the fermionic red MOT in Sec. 2.3.3 and for the calculation of the polarizability in Sec. 5.2.2.

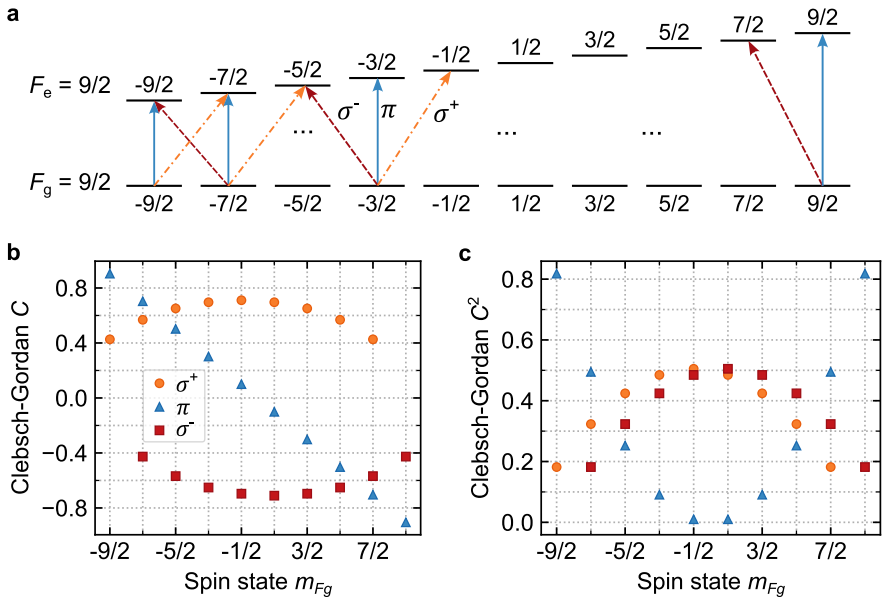

Figure A.4: Transitions of the hyperfine state $F_e = 9/2$. **a** The transitions are shown assuming a small external field. Between the ground state $^1S_0$ with $F_g = 9/2$ and the excited state $^3P_1$, $F_e = 9/2$ there is a total of ten resonance frequencies. The blue solid arrows represent the π-transition, red dashed arrows the σ^- and orange dotted-dashed arrows the σ^+. **b** The Clebsch-Gordan coefficient $C = C^{F_e,m_{F_e}}_{1,q,F_g,m_{F_g}}$ where $m_{F_e} = m_{F_g} + q$ and $q = -1, 0, +1$ represents the polarization of the light σ^-, π and σ^+ respectively. **c** The square of the Clebsch-Gordan coefficient.

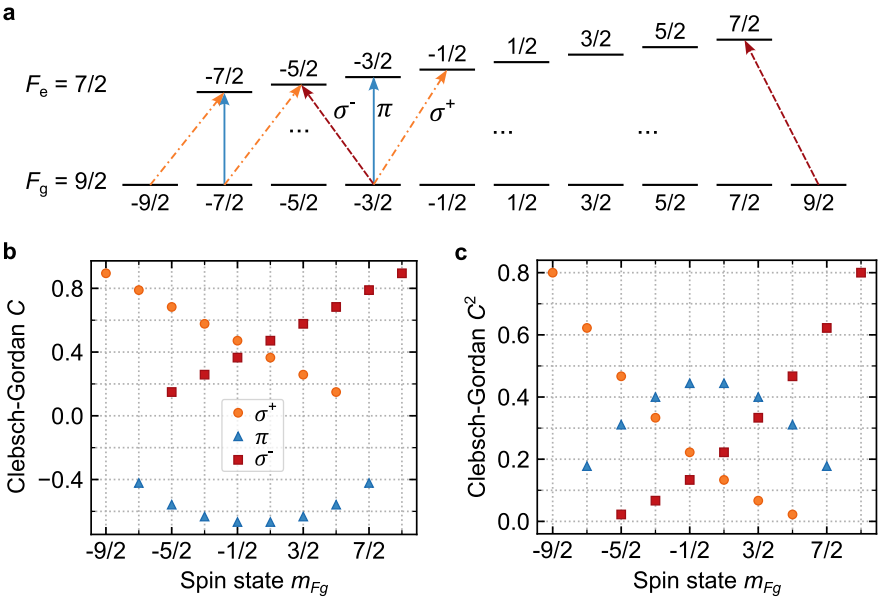

Figure A.5: Transitions of the hyperfine state $F_e = 7/2$. **a** There is a total of eight resonance frequencies for the excited state $^3\mathrm{P}_1$, $F_e = 7/2$, due to the splitting of the $m_{F_e} = -7/2, -5/2, ..., 7/2$ states upon applying an external field. The blue solid arrows represent the π-transition, red dashed arrows the σ^- and orange dotted-dashed arrows the σ^+. **b** The Clebsch-Gordan coefficient $C = C^{F_e, m_{F_e}}_{1,q,F_g,m_{F_g}}$ where $m_{F_e} = m_{F_g} + q$ and $q = -1, 0, +1$ represents the polarization of the light σ^-, π and σ^+ respectively. **c** The square of the Clebsch-Gordan coefficient. The $m_{F_g} = \pm 9/2$ can only be addressed by $\sigma^\mp$ respectively.

Appendix B

Polarizability

A potential formed by a laser beam depends on the intensity of the trapping light and the polarizability. In this appendix we discuss the polarizability and how it affect the trapping potential for different substates m_J and m_F. We start with a simplified discussion of the bosonic case, and explain how to expand it to fermions with their hyperfine states. For a detailed calculation we refer the reader to the work of I. H. Deutsch *et al.* [252] and the PhD thesis of A. A. Urech [292].

B.1 Polarizability and state-dependent light shift

For the calculation of the polarizability, first, we consider the atoms without hyperfine states, which describes well the polarizability for the bosonic isotope. The coupling between states J and J' is described by the polarizability operator [292]:

$$\begin{aligned}\hat{\alpha}_{q,q'}(J,J',\lambda) =& \frac{1}{\beta}\frac{\alpha_{\mathrm{FS}}}{\pi}\frac{|\langle J'||d||J\rangle|^2}{2J'+1}\frac{\nu_{J'}-\nu_J}{(\nu_{J'}-\nu_J)^2-\nu_\lambda^2}\times \\ & \sum_m C^{J',m+q}_{J,m+q-q'} C^{J',m+q}_{J,m} \left|J,m+q-q'\right\rangle\left\langle J,m\right|\end{aligned} \tag{B.1}$$

where q and q' are the polarization of the light, α_{FS} is the fine structure constant and $\beta = 5.29\times10^{-9}$ is a constant to change to the correct energy scale [292]. The polarizability operator includes the reduced transition dipole moment $\langle J'||d||J\rangle$ and the energy difference between the states $\nu_{J'}-\nu_J$ which, for strontium, are listed in [115]. Further, the sum runs over all m states, which describe the initial state m_i. The Clebsch-Gordan coefficients (Appx. A.2) describe the coupling between the angular momenta of the involved transitions $|J,m_i\rangle$, $|J',m_i+q\rangle$ and the final state $|J,m_f=m_i+q-q'\rangle$, see Fig. B.1.

To evaluate the polarizability operator, we define the quantization axis by choosing a basis for the polarization of the trapping light. Since our trapping light is linearly polarized in vertical direction (see Ch. 3), we chose a basis such that π-polarization is aligned with the z-direction in Cartesian coordinates. Applying the chosen basis and considering a set of m_i and m_f states the operator can be written as a rank-2-tensor $\hat{\alpha}^{(2)}_{m_i,m_f}(J,J',\lambda)$ of size $(2J+1)\times(2J+1)$, details in [252, 292]. In order to get the

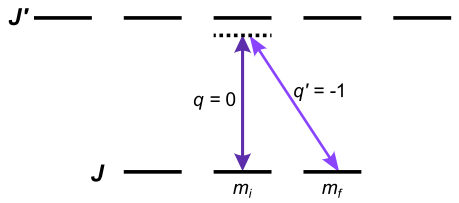

Figure B.1: Transition from J to J' described by the polarizability operator $\hat{\alpha}_{q,q'}(J, J', \lambda)$. This is an example for red-detuned light with non-pure polarization such that $q \neq q'$. The sum in Eq. (B.1) is over all initial states $m_J = m_i$ and the final state is determined through the polarization of the trapping light $m_f = m_i + q - q'$. The figure is adapted from [292].

State	a (a.u.)	b (nm × a.u.)	c (nm)
$^1S_0$	11.57	45.88	470.61
$^3P_0$	25.2832	2173.54	322.64
$^3P_1$	35.03	6011.86	355.61

Table B.1: The fit parameters of $\alpha_{\text{other}}(J, \lambda)$ from Eq. (B.3). The values of this table are optimized for $\lambda = 813\,\text{nm}$ and stem from [292]. The value of a is given in atomic units (a.u.).

polarizability for a given state J, we sum the matrix elements over all possible excited states J'. The total polarizability is then

$$\hat{\alpha}_{m_i,m_f,\text{tot}}(J, \lambda) = \sum_{J'} \hat{\alpha}^{(2)}_{m_i,m_f}(J, J', \lambda) + \alpha_{\text{other}}(J, \lambda) \tag{B.2}$$

where α_{other} accounts for non-dominant transitions and the effect of the ionic core. This correction is

$$\alpha_{\text{other}}(J, \lambda) = a + \frac{b}{\lambda - c} \tag{B.3}$$

where the wavelength of the trapping light λ is in nanometer, and the parameters a, b and c depend on the initial state of J, see Tab. B.1. The values originate from the PhD thesis of A. A. Urech [292] and are specific for wavelengths around 813 nm. The correction has to be adjusted and the fit parameters are no longer valid for other wavelengths for example around 500 nm, see [115].

With this knowledge, we can calculate the polarizabilities of the different states of strontium. For example, the polarizability of the ground state $^1S_0$ of bosonic strontium where $J = 0$. It depends on the contributions of the excited states $^1P_1$ with $J' = 1$ and $^3P_1$ with $J' = 1$, which are the dominant transitions. Other possible transitions are considered in the correction α_{other} Eq. (B.3). For the polarizability of the state $^3P_1$ with $J = 1$ numerous excited states J' contribute with comparable strength [115]. The polarizabilites of the bosonic isotope have been discussed in Sec. 4.3 in the context of Sisyphus cooling. The values in Fig. 4.11 show how α_e depends on m_J of the

$^3P_1$ state, in particular compared to the polarizability α_g of the ground state $^1S_0$: $\alpha_e(|m_J| = 1) > \alpha_g > \alpha_e(m_J = 0)$. This is the reason why attractive Sisyphus cooling only works for $|m_J| = 1$, and repulsive Sisyphus cooling would have to be used for $m_J = 0$.

For fermions the situation is more complicated compared to bosons. The hyperfine splitting adds an extra term in the equation of the polarizability operator, a prefactor $f_{F,F'}$ to the Clebsch-Gordan coefficients. It describes the relative oscillator strength for decays $|F'\rangle \rightarrow |F\rangle$ [252]. Additionally, due to the large F there are $2F+1 = 10$ m_F states for the ground state, and twelve for the hyperfine state $F = 11/2$ in contrast to the bosons where we had $2J + 1 \leq 3$ m_J states. The m_F dependent polarizabilities are discussed in Sec. 5.2.2.

Appendix C

Coating of dichroic mirror

In this appendix, we show the transmittance and reflectance curves of the custom dichroic mirrors which we have used to combine 813.4 nm light with other wavelengths. The coatings are custom-made from LaserOptik in order to fulfill the requirements of our applications.

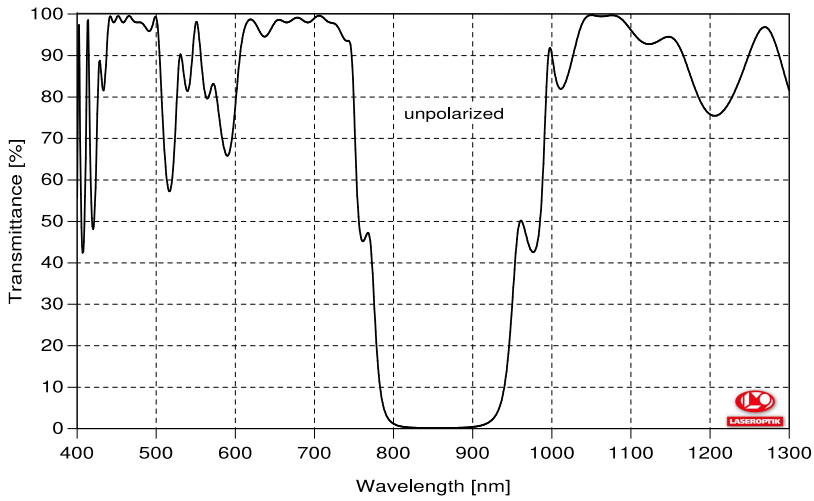

Figure C.1: Transmittance for unpolarized light.

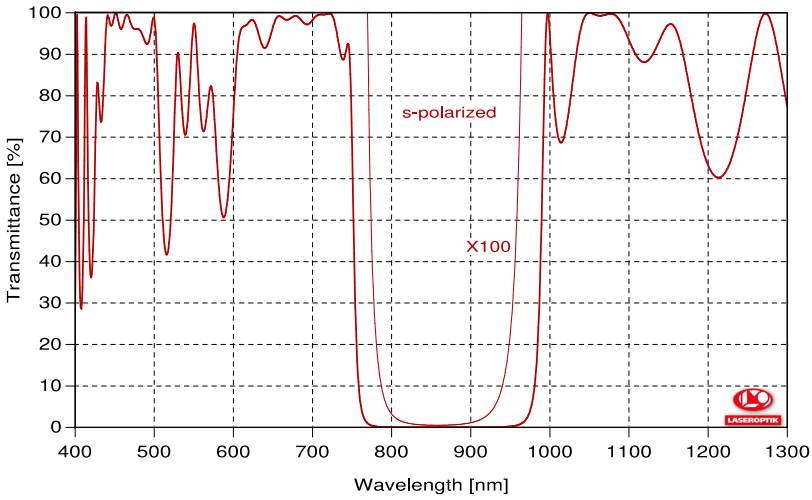

Figure C.2: Transmittance for s-polarized light.

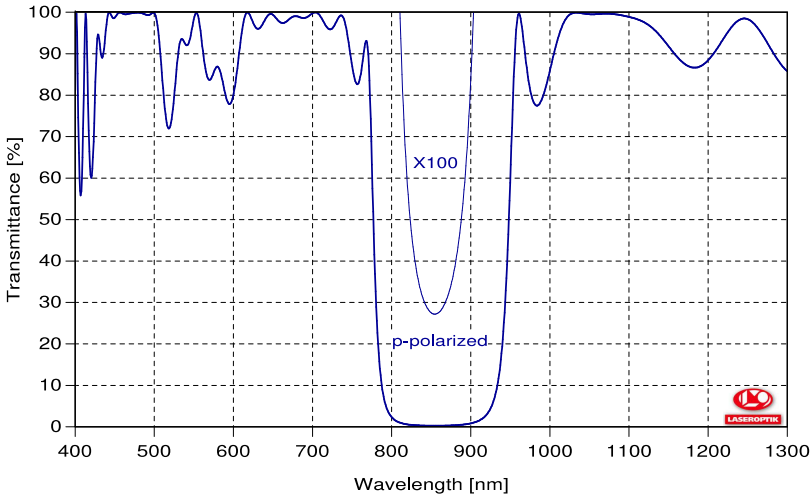

Figure C.3: Transmittance for p-polarized light.

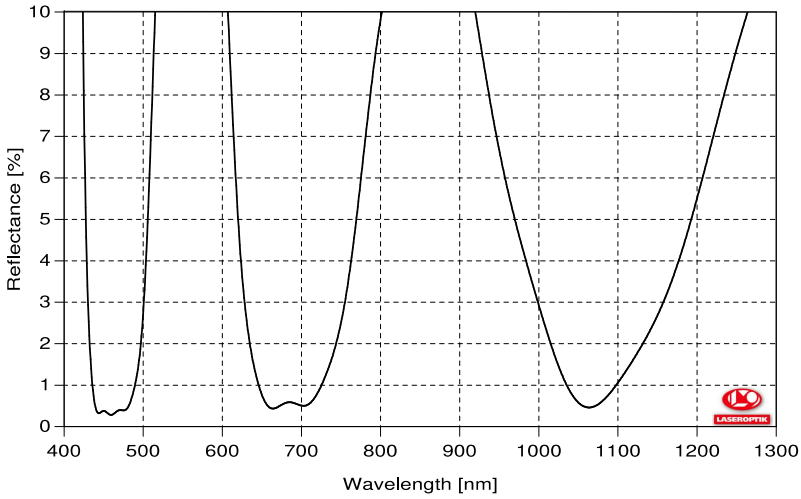

Figure C.4: Reflectance for unpolarized light.

References

[1] J. G. Bednorz and K. A. Müller. *Possible high-T_c superconductivity in the Ba–La–Cu–O system*. Z. Physik B - Condensed Matter **64**, 189–193 (1986) (Cited on page 1).

[2] P. W. Anderson. *The Resonating Valence Bond State in La_2CuO_4 and Superconductivity*. Science **235**, 1196–1198 (1987) (Cited on pages 1, 117).

[3] B. Keimer, S. A. Kivelson, M. R. Norman, S. Uchida, and J. Zaanen. *From quantum matter to high-temperature superconductivity in copper oxides*. Nature **518**, 179–186 (2015) (Cited on page 1).

[4] H. Xu, C.-M. Chung, M. Qin, U. Schollwöck, S. R. White, and S. Zhang. *Coexistence of superconductivity with partially filled stripes in the Hubbard model*. Science **384**, eadh7691 (2024) (Cited on page 1).

[5] A. Schilling, M. Cantoni, J. D. Guo, and H. R. Ott. *Superconductivity above 130 K in the Hg–Ba–Ca–Cu–O system*. Nature **363**, 56–58 (1993) (Cited on page 1).

[6] P. W. Anderson. *More Is Different: Broken symmetry and the nature of the hierarchical structure of science*. Science **177**, 393–396 (1972) (Cited on page 1).

[7] J. Hubbard. *Electron correlations in narrow energy bands*. Proc. Roy. Soc. (London), Ser. A **276**, 237–257 (1963) (Cited on page 2).

[8] J. Kanamori. *Electron Correlation and Ferromagnetism of Transition Metals*. Progress of Theoretical Physics **30**, 275–289 (1963) (Cited on page 2).

[9] M. C. Gutzwiller. *Effect of Correlation on the Ferromagnetism of Transition Metals*. Phys. Rev. Lett. **10**, 159–162 (1963) (Cited on page 2).

[10] J. Hubbard. *Electron correlations in narrow energy bands III. An improved solution*. Proc. Roy. Soc. (London), Ser. A **281**, 401–419 (1964) (Cited on page 2).

[11] *The Hubbard model at half a century*. Nat. Phys. **9**, 523–523 (2013) (Cited on page 2).

[12] O. Dutta, M. Gajda, P. Hauke, M. Lewenstein, D.-S. Lühmann, B. A. Malomed, T. Sowiński, and J. Zakrzewski. *Non-standard Hubbard models in optical lattices: a review*. Rep. Prog. Phys. **78**, 066001 (2015) (Cited on pages 2, 5).

[13] P. A. Lee, N. Nagaosa, and X.-G. Wen. *Doping a Mott insulator: Physics of high-temperature superconductivity*. Rev. Mod. Phys. **78**, 17–85 (2006) (Cited on page 2).

[14] A. Auerbach. *Interacting Electrons and Quantum Magnetism*. Springer-Verlag New York, Inc, 1994 (Cited on pages 2, 5, 6).

[15] S. Sachdev. *Quantum magnetism and criticality*. Nat. Phys. **4**, 173–185 (2008) (Cited on page 2).

[16] L. Balents. *Spin liquids in frustrated magnets*. Nature **464**, 199–208 (2010) (Cited on pages 2, 118).

[17] M. Fujihala, K. Morita, R. Mole, S. Mitsuda, T. Tohyama, S.-i. Yano, D. Yu, S. Sota, T. Kuwai, A. Koda, H. Okabe, H. Lee, S. Itoh, T. Hawai, T. Masuda, H. Sagayama, A. Matsuo, K. Kindo, S. Ohira-Kawamura, and K. Nakajima. *Gapless spin liquid in a square-kagome lattice antiferromagnet*. Nat. Comm. **11**, 3429 (2020) (Cited on page 2).

[18] D. Galanakis, E. Khatami, K. Mikelsons, A. Macridin, J. Moreno, D. A. Browne, and M. Jarrell. *Quantum criticality and incipient phase separation in the thermodynamic properties of the Hubbard model*. Phil. Trans. R. Soc. A. **369**, 1670–1686 (2011) (Cited on page 2).

[19] E. H. Lieb and F. Y. Wu. *Absence of Mott Transition in an Exact Solution of the Short-Range, One-Band Model in One Dimension*. Phys. Rev. Lett. **20**, 1445–1448 (1968) (Cited on page 2).

[20] M. Suzuki. *Quantum Monte Carlo methods in condensed matter physics*. World scientific, 1993 (Cited on page 2).

[21] A. Georges, G. Kotliar, W. Krauth, and M. J. Rozenberg. *Dynamical mean-field theory of strongly correlated fermion systems and the limit of infinite dimensions*. Rev. Mod. Phys. **68**, 13–125 (1996) (Cited on page 2).

[22] J. M. Zhang and R. X. Dong. *Exact diagonalization: the Bose–Hubbard model as an example*. Eur. J. Phys. **31**, 591 (2010) (Cited on page 2).

[23] T. Botzung and P. Nataf. *Exact Diagonalization of* SU(N) *Fermi-Hubbard Models*. Phys. Rev. Lett. **132**, 153001 (2024) (Cited on pages 2, 6, 7, 108, 119).

[24] H.-S. Zhong, H. Wang, Y.-H. Deng, M.-C. Chen, L.-C. Peng, Y.-H. Luo, J. Qin, D. Wu, X. Ding, Y. Hu, P. Hu, X.-Y. Yang, W.-J. Zhang, H. Li, Y. Li, X. Jiang, L. Gan, G. Yang, L. You, Z. Wang, L. Li, N.-L. Liu, C.-Y. Lu, and J.-W. Pan. *Quantum computational advantage using photons*. Science **370**, 1460–1463 (2020) (Cited on page 3).

[25] A. J. Daley, I. Bloch, C. Kokail, S. Flannigan, N. Pearson, M. Troyer, and P. Zoller. *Practical quantum advantage in quantum simulation*. Nature **607**, 667–676 (2022) (Cited on page 3).

[26] R. P. Feynman. *Simulating physics with computers*. International Journal of Theoretical Physics **21**, 467–488 (1982) (Cited on page 3).

[27] J. I. Cirac and P. Zoller. *Goals and opportunities in quantum simulation*. Nat. Phys. **8**, 264–266 (2012) (Cited on page 3).

[28] D. Porras and J. I. Cirac. *Quantum Manipulation of Trapped Ions in Two Dimensional Coulomb Crystals*. Phys. Rev. Lett. **96**, 250501 (2006) (Cited on page 3).

[29] J. Chiaverini and W. E. Lybarger. *Laserless trapped-ion quantum simulations without spontaneous scattering using microtrap arrays*. Phys. Rev. A **77**, 022324 (2008) (Cited on page 3).

[30] R. Schmied, T. Roscilde, V. Murg, D. Porras, and J. I. Cirac. *Quantum phases of trapped ions in an optical lattice*. New J. Phys. **10**, 045017 (2008) (Cited on page 3).

[31] E. Manousakis. *A Quantum-Dot Array as Model for Copper-Oxide Superconductors: A Dedicated Quantum Simulator for the Many-Fermion Problem*. Journal of Low Temperature Physics **126**, 1501–1513 (2002) (Cited on page 3).

[32] T. Byrnes, N. Y. Kim, K. Kusudo, and Y. Yamamoto. *Quantum simulation of Fermi-Hubbard models in semiconductor quantum-dot arrays*. Phys. Rev. B **78**, 075320 (2008) (Cited on page 3).

[33] A. van Oudenaarden and J. E. Mooij. *One-Dimensional Mott Insulator Formed by Quantum Vortices in Josephson Junction Arrays*. Phys. Rev. Lett. **76**, 4947–4950 (1996) (Cited on page 3).

[34] T. Yamamoto, M. Watanabe, J. Q. You, Y. A. Pashkin, O. Astafiev, Y. Nakamura, F. Nori, and J. S. Tsai. *Spectroscopy of superconducting charge qubits coupled by a Josephson inductance*. Phys. Rev. B **77**, 064505 (2008) (Cited on page 3).

[35] J. Q. You and F. Nori. *Atomic physics and quantum optics using superconducting circuits*. Nature **474**, 589–597 (2011) (Cited on page 3).

[36] X.-s. Ma, B. Dakic, W. Naylor, A. Zeilinger, and P. Walther. *Quantum simulation of the wavefunction to probe frustrated Heisenberg spin systems*. Nat. Phys. **7**, 399–405 (2011) (Cited on page 3).

[37] D. G. Angelakis, M. Huo, E. Kyoseva, and L. C. Kwek. *Luttinger Liquid of Photons and Spin-Charge Separation in Hollow-Core Fibers*. Phys. Rev. Lett. **106**, 153601 (2011) (Cited on page 3).

[38] X. Peng, J. Zhang, J. Du, and D. Suter. *Quantum Simulation of a System with Competing Two- and Three-Body Interactions*. Phys. Rev. Lett. **103**, 140501 (2009) (Cited on page 3).

[39] Z. Li, M.-H. Yung, H. Chen, D. Lu, J. D. Whitfield, X. Peng, A. Aspuru-Guzik, and J. Du. *Solving Quantum Ground-State Problems with Nuclear Magnetic Resonance*. Sci Rep **1**, 88 (2011) (Cited on page 3).

[40] J. Zhang, M.-H. Yung, R. Laflamme, A. Aspuru-Guzik, and J. Baugh. *Digital quantum simulation of the statistical mechanics of a frustrated magnet*. Nat. Comm. **3**, 880 (2012) (Cited on page 3).

[41] M. Lewenstein, A. Sanpera, V. Ahufinger, B. Damski, A. Sen De, and U. Sen. *Ultracold atomic gases in optical lattices: mimicking condensed matter physics and beyond*. Advances in Physics **56**, 243–379 (2007) (Cited on page 3).

[42] I. Bloch, J. Dalibard, and W. Zwerger. *Many-body physics with ultracold gases*. Rev. Mod. Phys. **80**, 885–964 (2008) (Cited on pages 3, 49).

[43] C. Gross and I. Bloch. *Quantum simulations with ultracold atoms in optical lattices*. Science **357**, 995–1001 (2017) (Cited on pages 3, 7).

[44] I. M. Georgescu, S. Ashhab, and F. Nori. *Quantum simulation*. Rev. Mod. Phys. **86**, 153–185 (2014) (Cited on page 3).

[45] D. Jaksch, C. Bruder, J. I. Cirac, C. W. Gardiner, and P. Zoller. *Cold Bosonic Atoms in Optical Lattices*. Phys. Rev. Lett. **81**, 3108–3111 (1998) (Cited on page 3).

[46] M. Greiner, O. Mandel, T. Esslinger, T. W. Hänsch, and I. Bloch. *Quantum phase transition from a superfluid to a Mott insulator in a gas of ultracold atoms*. Nature **415**, 39–44 (2002) (Cited on pages 3, 51, 68, 88).

[47] R. Jördens, N. Strohmaier, K. Günter, H. Moritz, and T. Esslinger. *A Mott insulator of fermionic atoms in an optical lattice*. Nature **455**, 204–207 (2008) (Cited on pages 3, 51).

[48] U. Schneider, L. Hackermüller, S. Will, T. Best, I. Bloch, T. A. Costi, R. W. Helmes, D. Rasch, and A. Rosch. *Metallic and Insulating Phases*

of Repulsively Interacting Fermions in a 3D Optical Lattice. Science **322**, 1520–1525 (2008) (Cited on pages 3, 51).

[49] D. Greif, T. Uehlinger, G. Jotzu, L. Tarruell, and T. Esslinger. *Short-Range Quantum Magnetism of Ultracold Fermions in an Optical Lattice*. Science **340**, 1307–1310 (2013) (Cited on pages 3, 119).

[50] A. Mazurenko, C. S. Chiu, G. Ji, M. F. Parsons, M. Kanász-Nagy, R. Schmidt, F. Grusdt, E. Demler, D. Greif, and M. Greiner. *A cold-atom Fermi–Hubbard antiferromagnet*. Nature **545**, 462–466 (2017) (Cited on pages 3, 7, 96, 119).

[51] C. Becker, P. Soltan-Panahi, J. Kronjäger, S. Dörscher, K. Bongs, and K. Sengstock. *Ultracold quantum gases in triangular optical lattices*. New J. Phys. **12**, 065025 (2010) (Cited on pages 3, 51).

[52] J. Struck, C. Ölschläger, R. Le Targat, P. Soltan-Panahi, A. Eckardt, M. Lewenstein, P. Windpassinger, and K. Sengstock. *Quantum Simulation of Frustrated Classical Magnetism in Triangular Optical Lattices*. Science **333**, 996–999 (2011) (Cited on pages 3, 51, 118).

[53] G. Jotzu, M. Messer, R. Desbuquois, M. Lebrat, T. Uehlinger, D. Greif, and T. Esslinger. *Experimental realization of the topological Haldane model with ultracold fermions*. Nature **515**, 237–240 (2014) (Cited on page 3).

[54] J. Léonard, S. Kim, J. Kwan, P. Segura, F. Grusdt, C. Repellin, N. Goldman, and M. Greiner. *Realization of a fractional quantum Hall state with ultracold atoms*. Nature **619**, 495–499 (2023) (Cited on page 3).

[55] P. Lunt, P. Hill, J. Reiter, P. M. Preiss, M. Gałka, and S. Jochim. *Realization of a Laughlin state of two rapidly rotating fermions*. arXiv: 2402.14814 (2024) (Cited on page 3).

[56] A. M. Kaufman, M. E. Tai, A. Lukin, M. Rispoli, R. Schittko, P. M. Preiss, and M. Greiner. *Quantum thermalization through entanglement in an isolated many-body system*. Science **353**, 794–800 (2016) (Cited on page 4).

[57] M. Schreiber, S. S. Hodgman, P. Bordia, H. P. Lüschen, M. H. Fischer, R. Vosk, E. Altman, U. Schneider, and I. Bloch. *Observation of many-body localization of interacting fermions in a quasirandom optical lattice*. Science **349**, 842–845 (2015) (Cited on page 4).

[58] J.-y. Choi, S. Hild, J. Zeiher, P. Schauß, A. Rubio-Abadal, T. Yefsah, V. Khemani, D. A. Huse, I. Bloch, and C. Gross. *Exploring the many-body localization transition in two dimensions*. Science **352**, 1547–1552 (2016) (Cited on page 4).

[59] M. P. A. Fisher, P. B. Weichman, G. Grinstein, and D. S. Fisher. *Boson localization and the superfluid-insulator transition*. Phys. Rev. B **40**, 546–570 (1989) (Cited on page 5).

[60] S. Trotzky, P. Cheinet, S. Fölling, M. Feld, U. Schnorrberger, A. M. Rey, A. Polkovnikov, E. A. Demler, M. D. Lukin, and I. Bloch. *Time-Resolved Observation and Control of Superexchange Interactions with Ultracold Atoms in Optical Lattices*. Science **319**, 295–299 (2008) (Cited on page 5).

[61] M. Gross, E. Sánchez-Velasco, and E. Siggia. *Ground-state properties of the two-dimensional antiferromagnetic Heisenberg model*. Phys. Rev. B **39**, 2484–2493 (1989) (Cited on page 5).

[62] C. Hofrichter, L. Riegger, F. Scazza, M. Höfer, D. R. Fernandes, I. Bloch, and S. Fölling. *Direct Probing of the Mott Crossover in the* SU(N) *Fermi-Hubbard Model*. Phys. Rev. X **6**, 021030 (2016) (Cited on page 6).

[63] D. P. Arovas, A. Karlhede, and D. Lilliehöök. SU(N) *quantum Hall skyrmions*. Phys. Rev. B **59**, 13147–13150 (1999) (Cited on page 6).

[64] Z. F. Ezawa, G. Tsitsishvili, and K. Hasebe. *Noncommutative geometry, extended W_∞ algebra, and Grassmannian solitons in multicomponent quantum Hall systems*. Phys. Rev. B **67**, 125314 (2003) (Cited on page 6).

[65] I. Affleck and J. B. Marston. *Large-n limit of the Heisenberg-Hubbard model: Implications for high-T_c superconductors*. Phys. Rev. B **37**, 3774–3777 (1988) (Cited on page 6).

[66] J. B. Marston and I. Affleck. *Large-n limit of the Hubbard-Heisenberg model*. Phys. Rev. B **39**, 11538–11558 (1989) (Cited on page 6).

[67] N. Read and S. Sachdev. *Valence-bond and spin-Peierls ground states of low-dimensional quantum antiferromagnets*. Phys. Rev. Lett. **62**, 1694–1697 (1989) (Cited on page 6).

[68] M. A. Cazalilla and A. M. Rey. *Ultracold Fermi gases with emergent SU(N) symmetry*. Rep. Prog. Phys. **77**, 124401 (2014) (Cited on pages 6, 14, 96).

[69] S. Taie, R. Yamazaki, S. Sugawa, and Y. Takahashi. *An SU(6) Mott insulator of an atomic Fermi gas realized by large-spin Pomeranchuk cooling*. Nat. Phys. **8**, 825–830 (2012) (Cited on pages 6, 96, 119).

[70] H. Ozawa, S. Taie, Y. Takasu, and Y. Takahashi. *Antiferromagnetic Spin Correlation of* SU($\mathcal{N}$) *Fermi Gas in an Optical Superlattice*. Phys. Rev. Lett. **121**, 225303 (2018) (Cited on pages 6, 119).

[71] S. Taie, E. Ibarra-García-Padilla, N. Nishizawa, Y. Takasu, Y. Kuno, H.-T. Wei, R. T. Scalettar, K. R. A. Hazzard, and Y. Takahashi. *Observation of antiferromagnetic correlations in an ultracold SU(N) Hubbard model*. Nat. Phys. **18**, 1356–1361 (2022) (Cited on pages 6, 96, 119).

[72] G. Pasqualetti, O. Bettermann, N. Darkwah Oppong, E. Ibarra-García-Padilla, S. Dasgupta, R. T. Scalettar, K. R. A. Hazzard, I. Bloch, and S. Fölling. *Equation of State and Thermometry of the 2D SU(N) Fermi-Hubbard Model*. Phys. Rev. Lett. **132**, 083401 (2024) (Cited on pages 6, 96).

[73] T. A. Tóth, A. M. Läuchli, F. Mila, and K. Penc. *Three-Sublattice Ordering of the SU(3) Heisenberg Model of Three-Flavor Fermions on the Square and Cubic Lattices*. Phys. Rev. Lett. **105**, 265301 (2010) (Cited on pages 6, 96, 108).

[74] P. Corboz, A. M. Läuchli, K. Penc, M. Troyer, and F. Mila. *Simultaneous Dimerization and SU(4) Symmetry Breaking of 4-Color Fermions on the Square Lattice*. Phys. Rev. Lett. **107**, 215301 (2011) (Cited on pages 6, 96, 108).

[75] P. Nataf and F. Mila. *Exact Diagonalization of Heisenberg* SU(N) *Models*. Phys. Rev. Lett. **113**, 127204 (2014) (Cited on pages 6, 7, 96, 108, 119).

[76] M. Hermele, V. Gurarie, and A. M. Rey. *Mott Insulators of Ultracold Fermionic Alkaline Earth Atoms: Underconstrained Magnetism and Chiral Spin Liquid*. Phys. Rev. Lett. **103**, 135301 (2009) (Cited on pages 7, 96, 119).

[77] M. Greiner and S. Fölling. *Optical lattices*. Nature **453**, 736–738 (2008) (Cited on pages 7, 48).

[78] K. B. Davis, M. O. Mewes, M. R. Andrews, N. J. van Druten, D. S. Durfee, D. M. Kurn, and W. Ketterle. *Bose-Einstein Condensation in a Gas of Sodium Atoms*. Phys. Rev. Lett. **75**, 3969–3973 (1995) (Cited on pages 7, 14).

[79] M. H. Anderson, J. R. Ensher, M. R. Matthews, C. E. Wieman, and E. A. Cornell. *Observation of Bose-Einstein Condensation in a Dilute Atomic Vapor*. Science **269**, 198–201 (1995) (Cited on pages 7, 14).

[80] B. DeMarco and D. S. Jin. *Onset of Fermi Degeneracy in a Trapped Atomic Gas*. Science **285**, 1703–1706 (1999) (Cited on page 7).

[81] T. Fukuhara, Y. Takasu, M. Kumakura, and Y. Takahashi. *Degenerate Fermi Gases of Ytterbium*. Phys. Rev. Lett. **98**, 030401 (2007) (Cited on page 7).

[82] B. J. DeSalvo, M. Yan, P. G. Mickelson, Y. N. Martinez de Escobar, and T. C. Killian. *Degenerate Fermi Gas of* ^{87}Sr. Phys. Rev. Lett. **105**, 030402 (2010) (Cited on pages 7, 14).

[83] M. K. Tey, S. Stellmer, R. Grimm, and F. Schreck. *Double-degenerate Bose-Fermi mixture of strontium*. Phys. Rev. A **82**, 011608 (2010) (Cited on pages 7, 14).

[84] M. Lu, N. Q. Burdick, and B. L. Lev. *Quantum Degenerate Dipolar Fermi Gas*. Phys. Rev. Lett. **108**, 215301 (2012) (Cited on page 7).

[85] W. S. Bakr, J. I. Gillen, A. Peng, S. Fölling, and M. Greiner. *A quantum gas microscope for detecting single atoms in a Hubbard-regime optical lattice*. Nature **462**, 74–77 (2009) (Cited on pages 7, 51, 68, 69, 77, 106, 117).

[86] J. F. Sherson, C. Weitenberg, M. Endres, M. Cheneau, I. Bloch, and S. Kuhr. *Single-atom-resolved fluorescence imaging of an atomic Mott insulator*. Nature **467**, 68–72 (2010) (Cited on pages 7, 68, 69, 77).

[87] W. S. Bakr, A. Peng, M. E. Tai, R. Ma, J. Simon, J. I. Gillen, S. Fölling, L. Pollet, and M. Greiner. *Probing the Superfluid–to–Mott Insulator Transition at the Single-Atom Level*. Science **329**, 547–550 (2010) (Cited on pages 7, 88, 90).

[88] L. W. Cheuk, M. A. Nichols, M. Okan, T. Gersdorf, V. V. Ramasesh, W. S. Bakr, T. Lompe, and M. W. Zwierlein. *Quantum-Gas Microscope for Fermionic Atoms*. Phys. Rev. Lett. **114**, 193001 (2015) (Cited on pages 7, 68, 69, 106).

[89] E. Haller, J. Hudson, A. Kelly, D. A. Cotta, B. Peaudecerf, G. D. Bruce, and S. Kuhr. *Single-atom imaging of fermions in a quantum-gas microscope*. Nat. Phys. **11**, 738–742 (2015) (Cited on pages 7, 68, 69, 106).

[90] G. J. A. Edge, R. Anderson, D. Jervis, D. C. McKay, R. Day, S. Trotzky, and J. H. Thywissen. *Imaging and addressing of individual fermionic atoms in an optical lattice*. Phys. Rev. A **92**, 063406 (2015) (Cited on pages 7, 51, 68, 69, 106).

[91] M. Boll, T. A. Hilker, G. Salomon, A. Omran, J. Nespolo, L. Pollet, I. Bloch, and C. Gross. *Spin- and density-resolved microscopy of antiferromagnetic correlations in Fermi-Hubbard chains*. Science **353**, 1257–1260 (2016) (Cited on pages 7, 119).

[92] M. F. Parsons, A. Mazurenko, C. S. Chiu, G. Ji, D. Greif, and M. Greiner. *Site-resolved measurement of the spin-correlation function in the Fermi-Hubbard model*. Science **353**, 1253–1256 (2016) (Cited on pages 7, 119).

[93] L. W. Cheuk, M. A. Nichols, K. R. Lawrence, M. Okan, H. Zhang, E. Khatami, N. Trivedi, T. Paiva, M. Rigol, and M. W. Zwierlein. *Observation of spatial charge and spin correlations in the 2D Fermi-Hubbard model*. Science **353**, 1260–1264 (2016) (Cited on pages 7, 119).

[94] C. S. Chiu, G. Ji, A. Bohrdt, M. Xu, M. Knap, E. Demler, F. Grusdt, M. Greiner, and D. Greif. *String patterns in the doped Hubbard model*. Science **365**, 251–256 (2019) (Cited on page 8).

[95] A. Bohrdt, C. S. Chiu, G. Ji, M. Xu, D. Greif, M. Greiner, E. Demler, F. Grusdt, and M. Knap. *Classifying snapshots of the doped Hubbard model with machine learning*. Nat. Phys. **15**, 921–924 (2019) (Cited on page 8).

[96] S. Hirthe, T. Chalopin, D. Bourgund, P. Bojović, A. Bohrdt, E. Demler, F. Grusdt, I. Bloch, and T. A. Hilker. *Magnetically mediated hole pairing in fermionic ladders of ultracold atoms*. Nature **613**, 463–467 (2023) (Cited on page 8).

[97] P. T. Brown, D. Mitra, E. Guardado-Sanchez, P. Schauß, S. S. Kondov, E. Khatami, T. Paiva, N. Trivedi, D. A. Huse, and W. S. Bakr. *Spin-imbalance in a 2D Fermi-Hubbard system*. Science **357**, 1385–1388 (2017) (Cited on pages 8, 68).

[98] P. T. Brown, D. Mitra, E. Guardado-Sanchez, R. Nourafkan, A. Reymbaut, C.-D. Hébert, S. Bergeron, A.-M. S. Tremblay, J. Kokalj, D. A. Huse, P. Schauß, and W. S. Bakr. *Bad metallic transport in a cold atom Fermi-Hubbard system*. Science **363**, 379–382 (2019) (Cited on page 8).

[99] M. A. Nichols, L. W. Cheuk, M. Okan, T. R. Hartke, E. Mendez, T. Senthil, E. Khatami, H. Zhang, and M. W. Zwierlein. *Spin transport in a Mott insulator of ultracold fermions*. Science **363**, 383–387 (2019) (Cited on page 8).

[100] J. Koepsell, J. Vijayan, P. Sompet, F. Grusdt, T. A. Hilker, E. Demler, G. Salomon, I. Bloch, and C. Gross. *Imaging magnetic polarons in the doped Fermi–Hubbard model*. Nature **572**, 358–362 (2019) (Cited on page 8).

[101] G. Ji, M. Xu, L. H. Kendrick, C. S. Chiu, J. C. Brüggenjürgen, D. Greif, A. Bohrdt, F. Grusdt, E. Demler, M. Lebrat, and M. Greiner. *Coupling a Mobile Hole to an Antiferromagnetic Spin Background: Transient Dynamics of a Magnetic Polaron*. Phys. Rev. X **11**, 021022 (2021) (Cited on page 8).

[102] S. Stellmer, R. Grimm, and F. Schreck. *Production of quantum-degenerate strontium gases*. Phys. Rev. A **87**, 013611 (2013) (Cited on page 8).

[103] C.-C. Chen, R. González Escudero, J. Minář, B. Pasquiou, S. Bennetts, and F. Schreck. *Continuous Bose–Einstein condensation*. Nature **606**, 683–687 (2022) (Cited on pages 8, 39).

[104] A. Urech, I. H. A. Knottnerus, R. J. C. Spreeuw, and F. Schreck. *Narrow-line imaging of single strontium atoms in shallow optical tweezers*. Phys. Rev. Res. **4**, 023245 (2022) (Cited on pages 8, 73, 102).

[105] B. J. Bloom, T. L. Nicholson, J. R. Williams, S. L. Campbell, M. Bishof, X. Zhang, W. Zhang, S. L. Bromley, and J. Ye. *An optical lattice clock with accuracy and stability at the* $10^{=18}$ *level*. Nature **506**, 71–75 (2014) (Cited on pages 8, 16).

[106] H. Katori, M. Takamoto, V. G. Pal'chikov, and V. D. Ovsiannikov. *Ultrastable Optical Clock with Neutral Atoms in an Engineered Light Shift Trap*. Phys. Rev. Lett. **91**, 173005 (2003) (Cited on pages 8, 52).

[107] J. Ye, H. J. Kimble, and H. Katori. *Quantum State Engineering and Precision Metrology Using State-Insensitive Light Traps*. Science **320**, 1734–1738 (2008) (Cited on pages 8, 52, 70).

[108] T. Bothwell, C. J. Kennedy, A. Aeppli, D. Kedar, J. M. Robinson, E. Oelker, A. Staron, and J. Ye. *Resolving the gravitational redshift across a millimetre-scale atomic sample*. Nature **602**, 420–424 (2022) (Cited on pages 8, 17).

[109] J. P. Covey, I. S. Madjarov, A. Cooper, and M. Endres. *2000-Times Repeated Imaging of Strontium Atoms in Clock-Magic Tweezer Arrays*. Phys. Rev. Lett. **122**, 173201 (2019) (Cited on pages 8, 9, 52, 70, 73).

[110] K. Barnes, P. Battaglino, B. J. Bloom, K. Cassella, R. Coxe, N. Crisosto, J. P. King, S. S. Kondov, K. Kotru, S. C. Larsen, J. Lauigan, B. J. Lester, M. McDonald, E. Megidish, S. Narayanaswami, C. Nishiguchi, R. Notermans, L. S. Peng, A. Ryou, T.-Y. Wu, and M. Yarwood. *Assembly and coherent control of a register of nuclear spin qubits*. Nat. Comm. **13**, 2779 (2022) (Cited on pages 8, 9, 17, 55, 96, 108).

[111] A. Asenjo-Garcia, M. Moreno-Cardoner, A. Albrecht, H. J. Kimble, and D. E. Chang. *Exponential Improvement in Photon Storage Fidelities Using Subradiance and Selective Radiance in Atomic Arrays*. Phys. Rev. X **7**, 031024 (2017) (Cited on pages 9, 118).

[112] J. Rui, D. Wei, A. Rubio-Abadal, S. Hollerith, J. Zeiher, D. M. Stamper-Kurn, C. Gross, and I. Bloch. *A subradiant optical mirror formed by a single structured atomic layer*. Nature **583**, 369–374 (2020) (Cited on pages 9, 118).

[113] G. Facchinetti, S. D. Jenkins, and J. Ruostekoski. *Storing Light with Subradiant Correlations in Arrays of Atoms*. Phys. Rev. Lett. **117**, 243601 (2016) (Cited on pages 9, 118).

[114] G. Ferioli, A. Glicenstein, L. Henriet, I. Ferrier-Barbut, and A. Browaeys. *Storage and Release of Subradiant Excitations in a Dense Atomic Cloud*. Phys. Rev. X **11**, 021031 (2021) (Cited on pages 9, 118).

[115] A. Cooper, J. P. Covey, I. S. Madjarov, S. G. Porsev, M. S. Safronova, and M. Endres. *Alkaline-Earth Atoms in Optical Tweezers*. Phys. Rev. X **8**, 041055 (2018) (Cited on pages 9, 16, 19, 23, 52, 70, 127, 128).

[116] J. Höschele, S. Buob, A. Rubio-Abadal, V. Makhalov, and L. Tarruell. *Atom-Number Enhancement by Shielding Atoms From Losses in Strontium Magneto-Optical Traps*. Phys. Rev. Appl. **19**, 064011 (2023) (Cited on pages 11, 20, 23, 27, 30, 31, 115).

[117] S. Stellmer, M. K. Tey, B. Huang, R. Grimm, and F. Schreck. *Bose-Einstein Condensation of Strontium*. Phys. Rev. Lett. **103**, 200401 (2009) (Cited on pages 12, 14, 16, 19, 22, 27, 30).

[118] Y. N. M. de Escobar, P. G. Mickelson, M. Yan, B. J. DeSalvo, S. B. Nagel, and T. C. Killian. *Bose-Einstein Condensation of* ^{84}Sr. Phys. Rev. Lett. **103**, 200402 (2009) (Cited on pages 12, 14, 16, 27).

[119] J. Höschele. *A strontium quantum-gas microscope*. PhD thesis. ICFO, Barcelona, Spain, 2024 (Cited on pages 13, 17, 27, 30, 31, 42, 43, 58, 76).

[120] D. Jacobs. *Design and construction of a new experimental apparatus for the laser cooling of strontium*. Master's thesis. ICFO, Barcelona and Universität Hamburg, 2019 (Cited on page 13).

[121] S. Stellmer, M. K. Tey, R. Grimm, and F. Schreck. *Bose-Einstein condensation of* ^{86}Sr. Phys. Rev. A **82**, 041602 (2010) (Cited on page 14).

[122] P. G. Mickelson, Y. N. Martinez de Escobar, M. Yan, B. J. DeSalvo, and T. C. Killian. *Bose-Einstein condensation of* ^{88}Sr *through sympathetic cooling with* ^{87}Sr. Phys. Rev. A **81**, 051601 (2010) (Cited on pages 14, 16, 19).

[123] J. E. Sansonetti and G. Nave. *Wavelengths, Transition Probabilities, and Energy Levels for the Spectrum of Neutral Strontium (SrI)*. Journal of Physical and Chemical Reference Data **39**, 033103 (2010) (Cited on pages 14, 15, 16, 87, 122).

[124] Y. N. Martinez de Escobar, P. G. Mickelson, P. Pellegrini, S. B. Nagel, A. Traverso, M. Yan, R. Côté, and T. C. Killian. *Two-photon photoas-*

sociative spectroscopy of ultracold ^{88}Sr. Phys. Rev. A **78**, 062708 (2008) (Cited on pages 14, 30, 87).

[125] S. Stellmer. *Degenerate quantum gases of strontium*. PhD thesis. University of Innsbruck, Austria, 2013 (Cited on pages 14, 16, 25, 26, 122).

[126] M. M. Boyd, T. Zelevinsky, A. D. Ludlow, S. Blatt, T. Zanon-Willette, S. M. Foreman, and J. Ye. *Nuclear spin effects in optical lattice clocks*. Phys. Rev. A **76**, 022510 (2007) (Cited on pages 14, 108, 123).

[127] X. Zhang, M. Bishof, S. L. Bromley, C. V. Kraus, M. S. Safronova, P. Zoller, A. M. Rey, and J. Ye. *Spectroscopic observation of SU(N)-symmetric interactions in Sr orbital magnetism*. Science **345**, 1467–1473 (2014) (Cited on page 14).

[128] N. Masuhara, J. M. Doyle, J. C. Sandberg, D. Kleppner, T. J. Greytak, H. F. Hess, and G. P. Kochanski. *Evaporative Cooling of Spin-Polarized Atomic Hydrogen*. Phys. Rev. Lett. **61**, 935–938 (1988) (Cited on page 14).

[129] C. Chin, R. Grimm, P. Julienne, and E. Tiesinga. *Feshbach resonances in ultracold gases*. Rev. Mod. Phys. **82**, 1225–1286 (2010) (Cited on pages 14, 49).

[130] H. G. C. Werij, C. H. Greene, C. E. Theodosiou, and A. Gallagher. *Oscillator strengths and radiative branching ratios in atomic Sr*. Phys. Rev. A **46**, 1248–1260 (1992) (Cited on pages 16, 19).

[131] S. G. Porsev, M. G. Kozlov, Y. G. Rakhlina, and A. Derevianko. *Many-body calculations of electric-dipole amplitudes for transitions between low-lying levels of Mg, Ca, and Sr*. Phys. Rev. A **64**, 012508 (2001) (Cited on pages 16, 19).

[132] A. Derevianko. *Feasibility of Cooling and Trapping Metastable Alkaline-Earth Atoms*. Phys. Rev. Lett. **87**, 023002 (2001) (Cited on page 16).

[133] R. Santra, K. V. Christ, and C. H. Greene. *Properties of metastable alkaline-earth-metal atoms calculated using an accurate effective core potential*. Phys. Rev. A **69**, 042510 (2004) (Cited on pages 16, 17).

[134] S. B. Nagel, C. E. Simien, S. Laha, P. Gupta, V. S. Ashoka, and T. C. Killian. *Magnetic trapping of metastable* $^3P_2$ *atomic strontium*. Phys. Rev. A **67**, 011401 (2003) (Cited on pages 16, 19).

[135] T. Loftus, J. R. Bochinski, and T. W. Mossberg. *Magnetic trapping of ytterbium and the alkaline-earth metals*. Phys. Rev. A **66**, 013411 (2002) (Cited on page 16).

[136] A. V. Taichenachev, V. I. Yudin, C. W. Oates, C. W. Hoyt, Z. W. Barber, and L. Hollberg. *Magnetic Field-Induced Spectroscopy of Forbidden*

Optical Transitions with Application to Lattice-Based Optical Atomic Clocks. Phys. Rev. Lett. **96**, 083001 (2006) (Cited on page 16).

[137] I. S. Madjarov. *Entangling, controlling, and detecting individual strontium atoms in optical tweezer arrays*. PhD thesis. Caltech, Pasadena, California, 2021 (Cited on pages 16, 72, 83, 106).

[138] M. Schioppo, N. Poli, M. Prevedelli, S. Falke, C. Lisdat, U. Sterr, and G. M. Tino. *A compact and efficient strontium oven for laser-cooling experiments*. Rev. Sci. Instrum. **83** (2012) (Cited on pages 17, 27).

[139] R. Senaratne, S. V. Rajagopal, Z. A. Geiger, K. M. Fujiwara, V. Lebedev, and D. M. Weld. *Effusive atomic oven nozzle design using an aligned microcapillary array*. Review of Scientific Instruments **86** (2015) (Cited on page 17).

[140] I. Nosske, L. Couturier, F. Hu, C. Tan, C. Qiao, J. Blume, Y. H. Jiang, P. Chen, and M. Weidemüller. *Two-dimensional magneto-optical trap as a source for cold strontium atoms*. Phys. Rev. A **96**, 053415 (2017) (Cited on page 17).

[141] M. Barbiero, M. G. Tarallo, D. Calonico, F. Levi, G. Lamporesi, and G. Ferrari. *Sideband-Enhanced Cold Atomic Source for Optical Clocks*. Phys. Rev. Appl. **13**, 014013 (2020) (Cited on pages 17, 27).

[142] J. Huckans, W. Dubosclard, E. Maréchal, O. Gorceix, B. Laburthe-Tolra, and M. Robert-de-Saint-Vincent. *Note on the reflectance of mirrors exposed to a strontium beam*. arXiv: 1802.08499 (2018) (Cited on page 17).

[143] L. R. Hunter, W. A. Walker, and D. S. Weiss. *Observation of an atomic Stark–electric-quadrupole interference*. Phys. Rev. Lett. **56**, 823–826 (1986) (Cited on page 19).

[144] J. Kwela, Z. Konefal, R. Drozdowski, and J. Heldt. *Observation of the electric-field-inducedE1 transition between $5s4d\,^1D_2$ and $5s2\,^1S_0$ levels in Sr I*. Z Phys D - Atoms, Molecules and Clusters **9**, 215–218 (1988) (Cited on page 19).

[145] X. Xu, T. H. Loftus, J. L. Hall, A. Gallagher, and J. Ye. *Cooling and trapping of atomic strontium*. J. Opt. Soc. Am. B, JOSAB **20**, 968–976 (2003) (Cited on pages 19, 20, 23).

[146] M. Yasuda and H. Katori. *Lifetime Measurement of the $^3P_2$ Metastable State of Strontium Atoms*. Phys. Rev. Lett. **92**, 153004 (2004) (Cited on page 19).

[147] S. Stellmer and F. Schreck. *Reservoir spectroscopy of* $5s5p\ ^3P_2$–$5snd\ ^3D_{1,2,3}$ *transitions in strontium*. Phys. Rev. A **90**, 022512 (2014) (Cited on pages 19, 20, 22, 24, 25).

[148] N. Poli, R. E. Drullinger, G. Ferrari, J. Léonard, F. Sorrentino, and G. M. Tino. *Cooling and trapping of ultracold strontium isotopic mixtures*. Phys. Rev. A **71**, 061403 (2005) (Cited on pages 20, 22).

[149] R. Senaratne. *Quantum Simulation of Strongly-Driven Systems Using Ultracold Lithium and Strontium*. PhD thesis. University of California, Santa Barbara, California, 2018 (Cited on pages 20, 22).

[150] P. G. Mickelson, Y. N. M. de Escobar, P. Anzel, B. J. DeSalvo, S. B. Nagel, A. J. Traverso, M. Yan, and T. C. Killian. *Repumping and spectroscopy of laser-cooled Sr atoms using the* $(5s5p)^3P_2$–$(5s4d)^3D_2$ *transition*. J. Phys. B: At. Mol. Opt. Phys. **42**, 235001 (2009) (Cited on pages 20, 22, 24, 25).

[151] R. Ding. *Narrow Line Cooling of* ^{84}Sr. PhD thesis. Rice University, Houston, Texas, 2016 (Cited on pages 20, 22).

[152] F. Hu, I. Nosske, L. Couturier, C. Tan, C. Qiao, P. Chen, Y. H. Jiang, B. Zhu, and M. Weidemüller. *Analyzing a single-laser repumping scheme for efficient loading of a strontium magneto-optical trap*. Phys. Rev. A **99**, 033422 (2019) (Cited on pages 20, 22).

[153] R. Finance. *Repumping Schemes for an Ultracold Strontium Experiment*. Internship Report. ICFO Barcelona, Spain, 2022 (Cited on pages 20, 22).

[154] T. P. Dinneen, K. R. Vogel, E. Arimondo, J. L. Hall, and A. Gallagher. *Cold collisions of* $\mathrm{Sr}^* - \mathrm{Sr}$ *in a magneto-optical trap*. Phys. Rev. A **59**, 1216–1222 (1999) (Cited on pages 20, 23).

[155] K. Patel, P. Gakkhar, K. Biswas, S. S. Maurya, P. Dutta, V. Lal, B. K. Mani, and U. D. Rapol. *Spectroscopy of the* $5s5p^3P_0 \rightarrow 5s5d^3D_1$ *transition of strontium using laser cooled atoms*. J. Phys. B: At. Mol. Opt. Phys. **57**, 105501 (2024) (Cited on pages 20, 23).

[156] S. Zhang, P. Ramchurn, M. Menchetti, Q. Ubaid, J. Jones, K. Bongs, and Y. Singh. *Novel repumping on* $^3P_0 \rightarrow {}^3D_1$ *for Sr magneto-optical trap and Landé g-factor measurement of* $^3D_1$. J. Phys. B: At. Mol. Opt. Phys. **53**, 235301 (2020) (Cited on pages 20, 23).

[157] J. Samland, S. Bennetts, C.-C. Chen, R. G. Escudero, F. Schreck, and B. Pasquiou. *Optical pumping of* $5s4d^1D_2$ *strontium atoms for laser cooling and imaging*. Phys. Rev. Res. **6**, 013319 (2024) (Cited on pages 20, 23, 24, 26).

[158] P. H. Moriya, M. O. Araújo, F. Todão, M. Hemmerling, H. Keßler, R. F. Shiozaki, R. C. Teixeira, and P. W. Courteille. *Comparison between 403 nm and 497 nm repumping schemes for strontium magneto-optical traps.* J. Phys. Commun. **2**, 125008 (2018) (Cited on page 22).

[159] V. Schkolnik, O. Fartmann, and M. Krutzik. *An extended-cavity diode laser at 497nm for laser cooling and trapping of neutral strontium.* Laser Physics **29**, 035802 (2019) (Cited on page 22).

[160] A. Henderson and R. Stafford. *Low threshold, singly-resonant CW OPO pumped by an all-fiber pump source.* Opt. Express **14**, 767–772 (2006) (Cited on page 22).

[161] S. J. Masson, J. P. Covey, S. Will, and A. Asenjo-Garcia. *Dicke Superradiance in Ordered Arrays of Multilevel Atoms.* PRX Quantum **5**, 010344 (2024) (Cited on pages 22, 118).

[162] D. Husain and G. Roberts. *Radiative lifetimes, diffusion and energy pooling of Sr(5s5p(3PJ)) and Sr(5s4d(1D2)) studied by time-resolved atomic emission following pulsed dye-laser excitation.* Chemical Physics **127**, 203–225 (1988) (Cited on page 23).

[163] M. A. Norcia, A. W. Young, and A. M. Kaufman. *Microscopic Control and Detection of Ultracold Strontium in Optical-Tweezer Arrays.* Phys. Rev. X **8**, 041054 (2018) (Cited on pages 23, 52, 70, 101).

[164] J. D. Whalen. *Probing nonlocal correlations with ultralong-range Rydberg molecules.* PhD thesis. Rice University, Houston, Texas, 2021 (Cited on pages 24, 25).

[165] T. Yang, K. Pandey, M. S. Pramod, F. Leroux, C. C. Kwong, E. Hajiyev, Z. Y. Chia, B. Fang, and D. Wilkowski. *A high flux source of cold strontium atoms.* Eur. Phys. J. D **69**, 226 (2015) (Cited on pages 25, 26, 27).

[166] Y. B. Ovchinnikov. *A permanent Zeeman slower for Sr atomic clock.* The European Physical Journal Special Topics **163**, 95–100 (2008) (Cited on page 27).

[167] W. Ketterle, K. B. Davis, M. A. Joffe, A. Martin, and D. E. Pritchard. *High densities of cold atoms in a dark spontaneous-force optical trap.* Phys. Rev. Lett. **70**, 2253–2256 (1993) (Cited on page 27).

[168] M. H. Anderson, W. Petrich, J. R. Ensher, and E. A. Cornell. *Reduction of light-assisted collisional loss rate from a low-pressure vapor-cell trap.* Phys. Rev. A **50**, R3597–R3600 (1994) (Cited on page 27).

[169] T. Nicholson, S. Campbell, R. Hutson, G. Marti, B. Bloom, R. McNally, W. Zhang, M. Barrett, M. Safronova, G. Strouse, W. Tew, and J. Ye.

Systematic evaluation of an atomic clock at $2 \times 10^{=18}$ *total uncertainty.* Nat. Comm. **6**, 6896 (2015) (Cited on pages 28, 29).

[170] J. Weiner, V. S. Bagnato, S. Zilio, and P. S. Julienne. *Experiments and theory in cold and ultracold collisions.* Rev. Mod. Phys. **71**, 1–85 (1999) (Cited on page 30).

[171] A. Stein, H. Knöckel, and E. Tiemann. *Fourier-transform spectroscopy of* Sr_2 *and revised ground-state potential.* Phys. Rev. A **78**, 042508 (2008) (Cited on page 30).

[172] M. A. Norcia, J. R. K. Cline, J. P. Bartolotta, M. J. Holland, and J. K. Thompson. *Narrow-line laser cooling by adiabatic transfer.* New J. Phys. **20**, 023021 (2018) (Cited on page 34).

[173] J. P. Bartolotta, M. A. Norcia, J. R. K. Cline, J. K. Thompson, and M. J. Holland. *Laser cooling by sawtooth-wave adiabatic passage.* Phys. Rev. A **98**, 023404 (2018) (Cited on page 34).

[174] M. A. Norcia. *New tools for precision measurement and quantum science with narrow linewidth optical transitions.* PhD thesis. University of Colorado, Boulder, California, 2017 (Cited on pages 35, 38).

[175] S. Snigirev, A. J. Park, A. Heinz, I. Bloch, and S. Blatt. *Fast and dense magneto-optical traps for strontium.* Phys. Rev. A **99**, 063421 (2019) (Cited on page 35).

[176] H. Katori, T. Ido, Y. Isoya, and M. Kuwata-Gonokami. *Magneto-Optical Trapping and Cooling of Strontium Atoms down to the Photon Recoil Temperature.* Phys. Rev. Lett. **82**, 1116–1119 (1999) (Cited on page 36).

[177] T. H. Loftus, T. Ido, A. D. Ludlow, M. M. Boyd, and J. Ye. *Narrow Line Cooling: Finite Photon Recoil Dynamics.* Phys. Rev. Lett. **93**, 073003 (2004) (Cited on page 36).

[178] T. H. Loftus, T. Ido, M. M. Boyd, A. D. Ludlow, and J. Ye. *Narrow line cooling and momentum-space crystals.* Phys. Rev. A **70**, 063413 (2004) (Cited on page 36).

[179] T. Mukaiyama, H. Katori, T. Ido, Y. Li, and M. Kuwata-Gonokami. *Recoil-Limited Laser Cooling of* ^{87}Sr *Atoms near the Fermi Temperature.* Phys. Rev. Lett. **90**, 113002 (2003) (Cited on pages 38, 39).

[180] S. Stellmer, B. Pasquiou, R. Grimm, and F. Schreck. *Laser Cooling to Quantum Degeneracy.* Phys. Rev. Lett. **110**, 263003 (2013) (Cited on page 39).

[181] R. Grimm, M. Weidemüller, and Y. B. Ovchinnikov. *Optical Dipole Traps for Neutral Atoms.* Advances In Atomic, Molecular, and Optical Physics **42**, 95–170 (2000) (Cited on pages 40, 48, 98).

[182] I. Bloch. *Ultracold quantum gases in optical lattices*. Nat. Phys. **1**, 23–30 (2005) (Cited on page 48).

[183] I. Bloch, J. Dalibard, and S. Nascimbène. *Quantum simulations with ultracold quantum gases*. Nat. Phys. **8**, 267–276 (2012) (Cited on page 48).

[184] P. B. Blakie and C. W. Clark. *Wannier states and Bose–Hubbard parameters for 2D optical lattices*. J. Phys. B: At. Mol. Opt. Phys. **37**, 1391–1404 (2004) (Cited on pages 49, 61).

[185] W. Zwerger. *Mott–Hubbard transition of cold atoms in optical lattices*. J. Opt. B: Quantum Semiclass. Opt. **5**, S9 (2003) (Cited on page 49).

[186] M. Köhl, H. Moritz, T. Stöferle, K. Günter, and T. Esslinger. *Fermionic Atoms in a Three Dimensional Optical Lattice: Observing Fermi Surfaces, Dynamics, and Interactions*. Phys. Rev. Lett. **94**, 080403 (2005) (Cited on page 49).

[187] A. J. Daley, M. M. Boyd, J. Ye, and P. Zoller. *Quantum Computing with Alkaline-Earth-Metal Atoms*. Phys. Rev. Lett. **101**, 170504 (2008) (Cited on pages 51, 52, 96).

[188] A. J. Daley. *Quantum computing and quantum simulation with group-II atoms*. Quantum Inf. Process. **10**, 865–884 (2011) (Cited on pages 51, 52).

[189] A. Heinz. *Ultracold Strontium in State-Dependent Optical Lattices*. PhD thesis. LMU, München, Germany, 2020 (Cited on page 51).

[190] M. Anderlini, P. J. Lee, B. L. Brown, J. Sebby-Strabley, W. D. Phillips, and J. V. Porto. *Controlled exchange interaction between pairs of neutral atoms in an optical lattice*. Nature **448**, 452–456 (2007) (Cited on page 51).

[191] S. Fölling, S. Trotzky, P. Cheinet, M. Feld, R. Saers, A. Widera, T. Müller, and I. Bloch. *Direct observation of second-order atom tunnelling*. Nature **448**, 1029–1032 (2007) (Cited on page 51).

[192] L. Tarruell, D. Greif, T. Uehlinger, G. Jotzu, and T. Esslinger. *Creating, moving and merging Dirac points with a Fermi gas in a tunable honeycomb lattice*. Nature **483**, 302–305 (2012) (Cited on page 51).

[193] S. Taie, H. Ozawa, T. Ichinose, T. Nishio, S. Nakajima, and Y. Takahashi. *Coherent driving and freezing of bosonic matter wave in an optical Lieb lattice*. Sci. Adv. **1** (2015) (Cited on page 51).

[194] G.-B. Jo, J. Guzman, C. K. Thomas, P. Hosur, A. Vishwanath, and D. M. Stamper-Kurn. *Ultracold Atoms in a Tunable Optical Kagome Lattice*. Phys. Rev. Lett. **108**, 045305 (2012) (Cited on page 51).

[195] M. N. Kosch, L. Asteria, H. P. Zahn, K. Sengstock, and C. Weitenberg. *Multifrequency optical lattice for dynamic lattice-geometry control*. Phys. Rev. Res. **4**, 043083 (2022) (Cited on page 51).

[196] K. Viebahn, M. Sbroscia, E. Carter, J.-C. Yu, and U. Schneider. *Matter-Wave Diffraction from a Quasicrystalline Optical Lattice*. Phys. Rev. Lett. **122**, 110404 (2019) (Cited on page 51).

[197] D. Shechtman, I. Blech, D. Gratias, and J. W. Cahn. *Metallic Phase with Long-Range Orientational Order and No Translational Symmetry*. Phys. Rev. Lett. **53**, 1951–1953 (1984) (Cited on page 51).

[198] R. Taïeb, R. Dum, J. I. Cirac, P. Marte, and P. Zoller. *Cooling and localization of atoms in laser-induced potential wells*. Phys. Rev. A **49**, 4876–4887 (1994) (Cited on pages 52, 70).

[199] V. V. Ivanov and S. Gupta. *Laser-driven Sisyphus cooling in an optical dipole trap*. Phys. Rev. A **84**, 063417 (2011) (Cited on pages 52, 70).

[200] R. Tao, M. Ammenwerth, F. Gyger, I. Bloch, and J. Zeiher. *High-Fidelity Detection of Large-Scale Atom Arrays in an Optical Lattice*. Phys. Rev. Lett. **133**, 013401 (2024) (Cited on pages 52, 70, 83, 98).

[201] M. Takamoto and H. Katori. *Spectroscopy of the $^1S_0$–$^3P_0$ Clock Transition of ^{87}Sr in an Optical Lattice*. Phys. Rev. Lett. **91**, 223001 (2003) (Cited on page 52).

[202] M. Takamoto, H. Katori, S. I. Marmo, V. D. Ovsiannikov, and V. G. Pal'chikov. *Prospects for Optical Clocks with a Blue-Detuned Lattice*. Phys. Rev. Lett. **102**, 063002 (2009) (Cited on page 52).

[203] T. Ido and H. Katori. *Recoil-Free Spectroscopy of Neutral Sr Atoms in the Lamb-Dicke Regime*. Phys. Rev. Lett. **91**, 053001 (2003) (Cited on pages 52, 59, 70, 101).

[204] G. Kestler, K. Ton, D. Filin, M. S. Safronova, and J. T. Barreiro. *Magic wavelengths of the Sr ($5s^2\,{}^1S_0$ to $5s5p^3P_1$) intercombination transition near the $5s5p\,{}^3P_1$ to $5p^2\,{}^3P_2$ transition*. Phys. Rev. A **105**, 012821 (2022) (Cited on page 52).

[205] M. S. Safronova, Z. Zuhrianda, U. I. Safronova, and C. W. Clark. *Extracting transition rates from zero-polarizability spectroscopy*. Phys. Rev. A **92**, 040501 (2015) (Cited on page 52).

[206] A. Heinz, A. Park, N. Šantić, J. Trautmann, S. Porsev, M. Safronova, I. Bloch, and S. Blatt. *State-Dependent Optical Lattices for the Strontium Optical Qubit*. Phy. Rev. Lett. **124** (2020) (Cited on page 52).

[207] M. Greiner, I. Bloch, O. Mandel, T. W. Hänsch, and T. Esslinger. *Exploring Phase Coherence in a 2D Lattice of Bose-Einstein Condensates.* Phys. Rev. Lett. **87**, 160405 (2001) (Cited on pages 53, 55).

[208] M. Miranda-Riaza. *Quantum spin liquid phases with ultracold bosonic atoms in optical lattices.* Master's thesis. ICFO and Universitat Autonoma de Barcelona, 2023 (Cited on pages 56, 58, 60, 61, 118).

[209] S. Kolkowitz, S. L. Bromley, T. Bothwell, M. L. Wall, G. E. Marti, A. P. Koller, X. Zhang, A. M. Rey, and J. Ye. *Spin–orbit-coupled fermions in an optical lattice clock.* Nature **542**, 66–70 (2017) (Cited on pages 55, 120).

[210] R. Bouganne, M. B. Aguilera, A. Dareau, E. Soave, J. Beugnon, and F. Gerbier. *Clock spectroscopy of interacting bosons in deep optical lattices.* New J. Phys. **19**, 113006 (2017) (Cited on page 55).

[211] L. Franchi, L. F. Livi, G. Cappellini, G. Binella, M. Inguscio, J. Catani, and L. Fallani. *State-dependent interactions in ultracold 174Yb probed by optical clock spectroscopy.* New J. Phys. **19**, 103037 (2017) (Cited on page 55).

[212] G. E. Marti, R. B. Hutson, A. Goban, S. L. Campbell, N. Poli, and J. Ye. *Imaging Optical Frequencies with* 100 μHz *Precision and* 1.1 μm *Resolution.* Phys. Rev. Lett. **120**, 103201 (2018) (Cited on page 55).

[213] T. Stöferle, H. Moritz, K. Günter, M. Köhl, and T. Esslinger. *Molecules of Fermionic Atoms in an Optical Lattice.* Phys. Rev. Lett. **96**, 030401 (2006) (Cited on page 61).

[214] B. Capogrosso-Sansone, Ş. G. ş. Söyler, N. Prokof'ev, and B. Svistunov. *Monte Carlo study of the two-dimensional Bose-Hubbard model.* Phys. Rev. A **77**, 015602 (2008) (Cited on pages 61, 87, 93).

[215] T. A. Savard, K. M. O'Hara, and J. E. Thomas. *Laser-noise-induced heating in far-off resonance optical traps.* Phys. Rev. A **56**, R1095–R1098 (1997) (Cited on page 63).

[216] S. Friebel, C. D'Andrea, J. Walz, M. Weitz, and T. W. Hänsch. CO_2*-laser optical lattice with cold rubidium atoms.* Phys. Rev. A **57**, R20–R23 (1998) (Cited on page 63).

[217] R. Jáuregui, N. Poli, G. Roati, and G. Modugno. *Anharmonic parametric excitation in optical lattices.* Phys. Rev. A **64**, 033403 (2001) (Cited on page 63).

[218] W. B. Case. *The pumping of a swing from the standing position.* Am. J. Phys. **64**, 215–220 (1996) (Cited on page 63).

[219] W. S. Bakr, P. M. Preiss, M. E. Tai, R. Ma, J. Simon, and M. Greiner. *Orbital excitation blockade and algorithmic cooling in quantum gases.* Nature **480**, 500–503 (2011) (Cited on pages 66, 118).

[220] S. Buob, J. Höschele, V. Makhalov, A. Rubio-Abadal, and L. Tarruell. *A Strontium Quantum-Gas Microscope.* PRX Quantum **5**, 020316 (2024) (Cited on pages 67, 116).

[221] K. D. Nelson, X. Li, and D. S. Weiss. *Imaging single atoms in a three-dimensional array.* Nat. Phys. **3**, 556–560 (2007) (Cited on page 68).

[222] O. Elíasson, J. S. Laustsen, R. Heck, R. Müller, J. J. Arlt, C. A. Weidner, and J. F. Sherson. *Spatial tomography of individual atoms in a quantum gas microscope.* Phys. Rev. A **102**, 053311 (2020) (Cited on page 68).

[223] R. Yamamoto, H. Ozawa, D. C. Nak, I. Nakamura, and T. Fukuhara. *Single-site-resolved imaging of ultracold atoms in a triangular optical lattice.* New J. Phys. **22**, 123028 (2020) (Cited on pages 68, 69).

[224] W.-Y. Zhang, M.-G. He, H. Sun, Y.-G. Zheng, Y. Liu, A. Luo, H.-Y. Wang, Z.-H. Zhu, P.-Y. Qiu, Y.-C. Shen, X.-K. Wang, W. Lin, S.-T. Yu, B.-C. Li, B. Xiao, M.-D. Li, Y.-M. Yang, X. Jiang, H.-N. Dai, Y. Zhou, X. Ma, Z.-S. Yuan, and J.-W. Pan. *Scalable Multipartite Entanglement Created by Spin Exchange in an Optical Lattice.* Phys. Rev. Lett. **131**, 073401 (2023) (Cited on page 68).

[225] A. Di Carli, C. Parsonage, A. La Rooij, L. Koehn, C. Ulm, C. W. Duncan, A. J. Daley, E. Haller, and S. Kuhr. *Commensurate and incommensurate 1D interacting quantum systems.* Nat. Commun. **15**, 474 (2024) (Cited on page 68).

[226] M. F. Parsons, F. Huber, A. Mazurenko, C. S. Chiu, W. Setiawan, K. Wooley-Brown, S. Blatt, and M. Greiner. *Site-Resolved Imaging of Fermionic* ^{6}Li *in an Optical Lattice.* Phys. Rev. Lett. **114**, 213002 (2015) (Cited on pages 68, 69).

[227] A. Omran, M. Boll, T. A. Hilker, K. Kleinlein, G. Salomon, I. Bloch, and C. Gross. *Microscopic Observation of Pauli Blocking in Degenerate Fermionic Lattice Gases.* Phys. Rev. Lett. **115**, 263001 (2015) (Cited on pages 68, 69).

[228] A. Impertro, J. F. Wienand, S. Häfele, H. von Raven, S. Hubele, T. Klostermann, C. R. Cabrera, I. Bloch, and M. Aidelsburger. *An unsupervised deep learning algorithm for single-site reconstruction in quantum gas microscopes.* Commun. Phys. **6**, 1–8 (2023) (Cited on pages 68, 69, 76, 108).

[229] J. Yang, L. Liu, J. Mongkolkiattichai, and P. Schauss. *Site-Resolved Imaging of Ultracold Fermions in a Triangular-Lattice Quantum Gas Microscope*. PRX Quantum **2**, 020344 (2021) (Cited on pages 68, 69).

[230] K. Kwon, K. Kim, J. Hur, S. Huh, and J.-y. Choi. *Site-resolved imaging of a bosonic Mott insulator of* ^{7}Li *atoms*. Phys. Rev. A **105**, 033323 (2022) (Cited on pages 68, 69).

[231] J. Verstraten, K. Dai, M. Dixmerias, B. Peaudecerf, T. de Jongh, and T. Yefsah. *In-situ Imaging of a Single-Atom Wave Packet in Continuous Space*. arXiv: 2404.05699 (2024) (Cited on page 68).

[232] M. Miranda, R. Inoue, Y. Okuyama, A. Nakamoto, and M. Kozuma. *Site-resolved imaging of ytterbium atoms in a two-dimensional optical lattice*. Phys. Rev. A **91**, 063414 (2015) (Cited on page 69).

[233] R. Yamamoto, J. Kobayashi, T. Kuno, K. Kato, and Y. Takahashi. *An ytterbium quantum gas microscope with narrow-line laser cooling*. New J. Phys. **18**, 023016 (2016) (Cited on page 69).

[234] L. Su, A. Douglas, M. Szurek, R. Groth, S. F. Ozturk, A. Krahn, A. H. Hébert, G. A. Phelps, S. Ebadi, S. Dickerson, F. Ferlaino, O. Marković, and M. Greiner. *Dipolar quantum solids emerging in a Hubbard quantum simulator*. Nature **622**, 724–729 (2023) (Cited on page 69).

[235] C. Gross and W. S. Bakr. *Quantum gas microscopy for single atom and spin detection*. Nat. Phys. **17**, 1316–1323 (2021) (Cited on pages 69, 96).

[236] S. M. Mansfield and G. S. Kino. *Solid immersion microscope*. Applied Physics Letters **57**, 2615–2616 (1990) (Cited on page 69).

[237] M. Sohmen, M. J. Mark, M. Greiner, and F. Ferlaino. *A ship-in-a-bottle quantum gas microscope setup for magnetic mixtures*. SciPost Phys. **15**, 182 (2023) (Cited on page 69).

[238] N. Schine, A. W. Young, W. J. Eckner, M. J. Martin, and A. M. Kaufman. *Long-lived Bell states in an array of optical clock qubits*. Nat. Phys. **18**, 1067–1073 (2022) (Cited on pages 70, 98).

[239] E. Hecht. *Optics*. Pearson education, Inc. Addison-Wesley, 2002 (Cited on page 75).

[240] W. H. Richardson. *Bayesian-Based Iterative Method of Image Restoration∗*. J. Opt. Soc. Am. **62**, 55–59 (1972) (Cited on pages 76, 106, 109).

[241] L. B. Lucy. *An iterative technique for the rectification of observed distributions*. Astronomical Journal **79**, 745 (1974) (Cited on pages 76, 106, 109).

[242] M. T. DePue, C. McCormick, S. L. Winoto, S. Oliver, and D. S. Weiss. *Unity Occupation of Sites in a 3D Optical Lattice*. Phys. Rev. Lett. **82**, 2262–2265 (1999) (Cited on page 77).

[243] N. Schlosser, G. Reymond, I. Protsenko, and P. Grangier. *Sub-poissonian loading of single atoms in a microscopic dipole trap*. Nature **411**, 1024–1027 (2001) (Cited on page 77).

[244] P. A. Murthy, D. Kedar, T. Lompe, M. Neidig, M. G. Ries, A. N. Wenz, G. Zürn, and S. Jochim. *Matter-wave Fourier optics with a strongly interacting two-dimensional Fermi gas*. Phys. Rev. A **90**, 043611 (2014) (Cited on page 89).

[245] N. Strohmaier, Y. Takasu, K. Günter, R. Jördens, M. Köhl, H. Moritz, and T. Esslinger. *Interaction-Controlled Transport of an Ultracold Fermi Gas*. Phys. Rev. Lett. **99**, 220601 (2007) (Cited on page 89).

[246] F. Gerbier, A. Widera, S. Fölling, O. Mandel, T. Gericke, and I. Bloch. *Phase Coherence of an Atomic Mott Insulator*. Phys. Rev. Lett. **95**, 050404 (2005) (Cited on page 90).

[247] A. Rubio-Abadal. *Probing Quantum Thermalization and Localization in Bose-Hubbard Systems*. PhD thesis. LMU, München, Germany, 2020 (Cited on page 90).

[248] A. V. Gorshkov, M. Hermele, V. Gurarie, C. Xu, P. S. Julienne, J. Ye, P. Zoller, E. Demler, M. D. Lukin, and A. M. Rey. *Two-orbital SU(N) magnetism with ultracold alkaline-earth atoms*. Nat. Phys. **6**, 289–295 (2010) (Cited on pages 96, 120).

[249] B. Ye, F. Machado, J. Kemp, R. B. Hutson, and N. Y. Yao. *Universal Kardar-Parisi-Zhang Dynamics in Integrable Quantum Systems*. Phys. Rev. Lett. **129**, 230602 (2022) (Cited on page 96).

[250] E. Ibarra-García-Padilla, S. Dasgupta, H.-T. Wei, S. Taie, Y. Takahashi, R. T. Scalettar, and K. R. A. Hazzard. *Universal thermodynamics of an* SU(N) *Fermi-Hubbard model*. Phys. Rev. A **104**, 043316 (2021) (Cited on page 96).

[251] D. González-Cuadra, D. Bluvstein, M. Kalinowski, R. Kaubruegger, N. Maskara, P. Naldesi, T. V. Zache, A. M. Kaufman, M. D. Lukin, H. Pichler, B. Vermersch, J. Ye, and P. Zoller. *Fermionic quantum processing with programmable neutral atom arrays*. Proceedings of the National Academy of Sciences **120** (2023) (Cited on page 96).

[252] I. H. Deutsch and P. S. Jessen. *Quantum-state control in optical lattices*. Phys. Rev. A **57**, 1972–1986 (1998) (Cited on pages 98, 127, 129).

[253] W. Huie, L. Li, N. Chen, X. Hu, Z. Jia, W. K. C. Sun, and J. P. Covey. *Repetitive Readout and Real-Time Control of Nuclear Spin Qubits in ^{171}Yb Atoms*. PRX Quantum **4**, 030337 (2023) (Cited on pages 102, 108, 110).

[254] S. Dörscher, R. Schwarz, A. Al-Masoudi, S. Falke, U. Sterr, and C. Lisdat. *Lattice-induced photon scattering in an optical lattice clock*. Phys. Rev. A **97**, 063419 (2018) (Cited on page 108).

[255] S. Stellmer, R. Grimm, and F. Schreck. *Detection and manipulation of nuclear spin states in fermionic strontium*. Phys. Rev. A **84**, 043611 (2011) (Cited on page 110).

[256] A. J. Daley. *Quantum trajectories and open many-body quantum systems*. Advances in Physics **63**, 77–149 (2014) (Cited on page 117).

[257] G. Kordas, D. Witthaut, P. Buonsante, A. Vezzani, R. Burioni, A. I. Karanikas, and S. Wimberger. *The dissipative Bose-Hubbard model: Methods and examples*. Eur. Phys. J. Spec. Top. **224**, 2127–2171 (2015) (Cited on page 117).

[258] T. Tomita, S. Nakajima, I. Danshita, Y. Takasu, and Y. Takahashi. *Observation of the Mott insulator to superfluid crossover of a driven-dissipative Bose-Hubbard system*. Science Advances **3**, e1701513 (2017) (Cited on page 117).

[259] R. Bouganne, M. Bosch Aguilera, A. Ghermaoui, J. Beugnon, and F. Gerbier. *Anomalous decay of coherence in a dissipative many-body system*. en. Nat. Phys. **16**, 21–25 (2020) (Cited on page 117).

[260] D. Poletti, P. Barmettler, A. Georges, and C. Kollath. *Emergence of Glasslike Dynamics for Dissipative and Strongly Interacting Bosons*. Phys. Rev. Lett. **111**, 195301 (2013) (Cited on page 117).

[261] C. Weitenberg, M. Endres, J. F. Sherson, M. Cheneau, P. Schauß, T. Fukuhara, I. Bloch, and S. Kuhr. *Single-spin addressing in an atomic Mott insulator*. Nature **471**, 319–324 (2011) (Cited on page 117).

[262] X.-G. Wen. *Colloquium: Zoo of quantum-topological phases of matter*. Rev. Mod. Phys. **89**, 041004 (2017) (Cited on page 117).

[263] S. A. Kivelson, D. S. Rokhsar, and J. P. Sethna. *Topology of the resonating valence-bond state: Solitons and high-T_c superconductivity*. Phys. Rev. B **35**, 8865–8868 (1987) (Cited on page 117).

[264] G. Semeghini, H. Levine, A. Keesling, S. Ebadi, T. T. Wang, D. Bluvstein, R. Verresen, H. Pichler, M. Kalinowski, R. Samajdar, A. Omran, S. Sachdev, A. Vishwanath, M. Greiner, V. Vuletić, and M. D. Lukin.

Probing topological spin liquids on a programmable quantum simulator. Science **374**, 1242–1247 (2021) (Cited on pages 117, 118).

[265] A. Kitaev. *Fault-tolerant quantum computation by anyons*. Annals of Physics **303**, 2–30 (2003) (Cited on page 117).

[266] P. Anderson. *Resonating valence bonds: A new kind of insulator?* Materials Research Bulletin **8**, 153–160 (1973) (Cited on page 118).

[267] S. A. Kulagin, N. Prokof'ev, O. A. Starykh, B. Svistunov, and C. N. Varney. *Bold Diagrammatic Monte Carlo Method Applied to Fermionized Frustrated Spins*. Phys. Rev. Lett. **110**, 070601 (2013) (Cited on page 118).

[268] A. Eckardt, P. Hauke, P. Soltan-Panahi, C. Becker, K. Sengstock, and M. Lewenstein. *Frustrated quantum antiferromagnetism with ultracold bosons in a triangular lattice*. Europhysics Letters **89**, 10010 (2010) (Cited on page 118).

[269] D. Yamamoto, T. Fukuhara, and I. Danshita. *Frustrated quantum magnetism with Bose gases in triangular optical lattices at negative absolute temperatures*. Commun. Phys. **3**, 56 (2020) (Cited on page 118).

[270] B.-Y. Sun, N. Goldman, M. Aidelsburger, and M. Bukov. *Engineering and Probing Non-Abelian Chiral Spin Liquids Using Periodically Driven Ultracold Atoms*. PRX Quantum **4**, 020329 (2023) (Cited on page 118).

[271] A. Celi, T. Grass, A. J. Ferris, B. Padhi, D. Raventós, J. Simonet, K. Sengstock, and M. Lewenstein. *Modified spin-wave theory and spin-liquid behavior of cold bosons on an inhomogeneous triangular lattice*. Phys. Rev. B **94**, 075110 (2016) (Cited on page 118).

[272] B. Olmos, D. Yu, Y. Singh, F. Schreck, K. Bongs, and I. Lesanovsky. *Long-Range Interacting Many-Body Systems with Alkaline-Earth-Metal Atoms*. Phys. Rev. Lett. **110**, 143602 (2013) (Cited on page 118).

[273] R. B. Hutson, W. R. Milner, L. Yan, J. Ye, and C. Sanner. *Observation of millihertz-level cooperative Lamb shifts in an optical atomic clock*. Science **383**, 384–387 (2024) (Cited on page 119).

[274] R. A. Hart, P. M. Duarte, T.-L. Yang, X. Liu, T. Paiva, E. Khatami, R. T. Scalettar, N. Trivedi, D. A. Huse, and R. G. Hulet. *Observation of antiferromagnetic correlations in the Hubbard model with ultracold atoms*. Nature **519**, 211–214 (2015) (Cited on page 119).

[275] J.-S. Bernier, C. Kollath, A. Georges, L. De Leo, F. Gerbier, C. Salomon, and M. Köhl. *Cooling fermionic atoms in optical lattices by shaping the confinement*. Phys. Rev. A **79**, 061601 (2009) (Cited on page 119).

[276] T.-L. Ho and Q. Zhou. *Universal Cooling Scheme for Quantum Simulation*. arXiv: 0911.5506 (2009) (Cited on page 119).

[277] F. Werner, O. Parcollet, A. Georges, and S. R. Hassan. *Interaction-Induced Adiabatic Cooling and Antiferromagnetism of Cold Fermions in Optical Lattices*. Phys. Rev. Lett. **95**, 056401 (2005) (Cited on page 119).

[278] E. Ibarra-García-Padilla, C. Feng, G. Pasqualetti, S. Fölling, R. T. Scalettar, E. Khatami, and K. R. A. Hazzard. *Metal-insulator transition and magnetism of SU(3) fermions in the square lattice*. Phys. Rev. A **108**, 053312 (2023) (Cited on page 119).

[279] H. Schlömer, F. Grusdt, U. Schollwöck, K. R. A. Hazzard, and A. Bohrdt. *Subdimensional magnetic polarons in the one-hole doped SU(3) $t-J$ model*. Phys. Rev. B **110**, 125134 (2024) (Cited on page 119).

[280] A. Celi, P. Massignan, J. Ruseckas, N. Goldman, I. B. Spielman, G. Juzeli ūnas, and M. Lewenstein. *Synthetic Gauge Fields in Synthetic Dimensions*. Phys. Rev. Lett. **112**, 043001 (2014) (Cited on page 120).

[281] M. Mamaev, T. Bilitewski, B. Sundar, and A. M. Rey. *Resonant Dynamics of Strongly Interacting* SU(n) *Fermionic Atoms in a Synthetic Flux Ladder*. PRX Quantum **3**, 030328 (2022) (Cited on page 120).

[282] R. B. Hutson, A. Goban, G. E. Marti, L. Sonderhouse, C. Sanner, and J. Ye. *Engineering Quantum States of Matter for Atomic Clocks in Shallow Optical Lattices*. Phys. Rev. Lett. **123**, 123401 (2019) (Cited on page 120).

[283] L. F. Livi, G. Cappellini, M. Diem, L. Franchi, C. Clivati, M. Frittelli, F. Levi, D. Calonico, J. Catani, M. Inguscio, and L. Fallani. *Synthetic Dimensions and Spin-Orbit Coupling with an Optical Clock Transition*. Phys. Rev. Lett. **117**, 220401 (2016) (Cited on page 120).

[284] A. Ghermaoui, M. B. Aguilera, R. Bouganne, R. Vatré, I. Fritsche, J. Beugnon, and F. Gerbier. *Many-Body Dephasing by Hole Motion in a Spin-Orbit-Coupled Mott Insulator*. arXiv: 2409.05828 (2024) (Cited on page 120).

[285] A. Frölian, C. S. Chisholm, E. Neri, C. R. Cabrera, R. Ramos, A. Celi, and L. Tarruell. *Realizing a 1D topological gauge theory in an optically dressed BEC*. en. Nature **608**, 293–297 (2022) (Cited on page 120).

[286] L. Barbiero, J. Cabedo, M. Lewenstein, L. Tarruell, and A. Celi. *Frustrated magnets without geometrical frustration in bosonic flux ladders*. Phys. Rev. Res. **5**, L042008 (2023) (Cited on page 120).

[287] J. Gonzalez-Sorribes. *A laser system for addressing the strontium clock transition*. Master's thesis. ICFO and Universitat Politecnica de Catalunya, 2024 (Cited on page 120).

[288] T.-W. Zhou, G. Cappellini, D. Tusi, L. Franchi, J. Parravicini, C. Repellin, S. Greschner, M. Inguscio, T. Giamarchi, M. Filippone, J. Catani, and L. Fallani. *Observation of universal Hall response in strongly interacting Fermions*. Science **381**, 427–430 (2023) (Cited on page 120).

[289] M. Mancini, G. Pagano, G. Cappellini, L. Livi, M. Rider, J. Catani, C. Sias, P. Zoller, M. Inguscio, M. Dalmonte, and L. Fallani. *Observation of chiral edge states with neutral fermions in synthetic Hall ribbons*. Science **349**, 1510–1513 (2015) (Cited on page 120).

[290] J. H. Han, J. H. Kang, and Y. Shin. *Band Gap Closing in a Synthetic Hall Tube of Neutral Fermions*. Phys. Rev. Lett. **122**, 065303 (2019) (Cited on page 120).

[291] M. M. Boyd. *High Precision Spectroscopy of Strontium in an Optical Lattice: Towards a New Standard for Frequency and Time*. PhD thesis. University of Colorado, Boulder, California, 2007 (Cited on pages 121, 122).

[292] A. A. Urech. *Single strontium atoms in optical tweezers*. PhD thesis. Universiteit van Amsterdam, Netherlands, 2023 (Cited on pages 127, 128).

Acknowledgements

My PhD has been a great adventure and supported by many people. At this point I would like to express my gratitude towards all the people that accompanied me on this journey, crossed my paths and left meaningful memories.

First, I would like to thank Prof. Dr. Leticia Tarruell for the opportunity to do my PhD in her team and the chance to build a strontium quantum-gas microscope. I am grateful for the support I have received, the knowledge and advice you shared about physics, technical things and how to become a better scientist. I appreciate that you always have an open door for any struggle that may occur during a PhD.

Another big THANK YOU goes to the strontium team, current as well as former members: my PhD colleagues Dr. Jonatan Höschele and Carlos Gas, and my postdocs Dr. Vasiliy Makhalov and Dr. Antonio Rubio Abadal. I have learned a lot while working with you and enjoyed the hours we have spent in the lab together; baking the vacuum chamber, setting up beam paths, making coils, capturing the first atoms and trying to keep the MOT alive, increasing the atom number, fixing water connections, getting the atoms colder and eventually seeing the first single-atom-resolved images. For the discussions, the ideas, the advice, the celebrations, the tough, the exciting and the fun times I want to thank you all.

I also appreciate the interactions I had with all the other members of the ultracold quantum gases group: the former PhD students Dr. Anika Frölian and Dr. Craig Chisholm, the former postdocs Dr. Elettra Neri and Dr. Ramón Ramos, the current PhD students Ana Pérez, Ignacio Pérez Ramos, Andreas Meyer and Roxana Wedowski as well as the current postdocs Dr. Sarah Hirthe and Dr. Rémy Vatré, the theorists led by Prof. Dr. Alessio Celi, in particular Marc Miranda for his collaboration. Thanks to all of you for the coffee breaks, the fruitful discussions and the exchange of ideas, knowledge and stories, but also the adventures we had outside the lab.

I couldn't have completed this thesis without the support from the different departments at ICFO. In particular my thanks goes to: Carlos Dengra Tineo and the facilities team for keeping the infrastructure running, which makes it possible to perform such complex experiments, Xavier Menino Pizarro and the mechanical workshop team for manufacturing various custom pieces for us, the electronical workshop team led by José Carlos Cifuentes González, Magdalena Lara Juárez and Santiago Martín Muñoz from the Purchasing Unit, the IT department led by Dr. Juli Céspedes Capdevila, the human resources team as well as the academic affairs officers and all the other departments and people that contributed in one or another way to the success of this work.

My thanks also go to my family and friends who supported me during the past four years. Thank you for always listening and giving me advice, for keeping me grounded and making this journey an even more memorable adventure.

Furthermore, I would like to thank my committee Prof. Dr. Tilman Esslinger, Prof. Dr. Christian Groß and Dr. Pablo Loza-Alvarez for evaluating my research and this dissertation.

During my PhD I have received funding from MCIN/AEI/10.13039/501100011033 and ESF (Grant No. PRE2020-094414).